15ᵀᴴ INTERNATIONAL CONFERENCE ON TURBOCHARGERS AND TURBOCHARGING

Institution of Mechanical Engineers

15TH INTERNATIONAL CONFERENCE ON
TURBOCHARGERS AND TURBOCHARGING

The Institution's International Conference on Turbochargers and Turbocharging (Twickenham, London, UK, 16-17 May 2023) returns to address the latest advances, research and developments in turbocharging system designs and boosting solutions.

This volume presents a peer-reviewed collection of papers which will address current and novel turbocharging system choices and components with a renewed emphasis to address the challenges posed by emission regulations and market trends. The latest developments leading to enhanced performance and efficiency, increased durability and reduced emissions in line with meeting Net-Zero and global emissions targets.

Topics include:

- Air management in powertrains: conventional, hybrids, fuel cells and novel configurations
- Alternate fuels and their needs in boosting (e.g. hydrogen, synthetic fuels)
- Electrification of turbochargers, compressors, and exhaust turbines
- Simulation and testing techniques, data analytics, including AI and digital twins
- Thermal management, waste heat recovery and expanders
- Turbomachinery aerodynamic: novel compressors & turbines and multi-stage systems
- Component fatigue life, bearing design, rotor-dynamics and durability prediction
- Mechatronics, control, sensors and power electronics
- High speed turbomachinery in propulsion and power systems Future Legislation needs for thermal propulsion systems

PROCEEDINGS OF THE 15TH INTERNATIONAL CONFERENCE ON TURBOCHARGERS AND TURBOCHARGING, TWICKENHAM, LONDON, 16–17 MAY 2023

15TH INTERNATIONAL CONFERENCE ON TURBOCHARGERS AND TURBOCHARGING

Edited by

Institution of Mechanical Engineers

Table of Contents

EXPERIMENTAL INVESTIGATIONS

Organising Committee

Powertrain Systems and Fuels Group

Member Credits

Ricardo Martinez-Botas	Imperial College London
Peter Davies	Garrett Motion
Jamie Archer	Cummins Turbo Technologies
Lutz Aurahs	MAN Energy Solution
Alan Baker	Jaguar Land Rover
Elias Chebli	Porsche
Colin Copeland	Simon Fraser University
Dietmar Filsinger	IHI Charging Systems International GmbH
Rogier Lammers	Mitsubishi Turbocharger and Engine Europe B.V.
Per-Inge Larsson	Scania
Herve Martin	Turbo Systems Switzerland Ltd
Nathan McArdle	BorgWarner
Anthony Morelli	Ford Motor Company
Takashi Otobe	Honda Racing Corporation
Prabhu Ramasamy	Perkins Engines
Professor Jörg Seume	Leibniz Universität Hannover
Stephen Spence	Trinity College Dublin

Compressor considerations

Experimental investigation on surge phenomena in small centrifugal compressors

S. Marelli, V. Usai

University of Genoa, Genoa, Italy

ABSTRACT

Centrifugal compressors are key components in propulsion and energy production systems. They are commonly adopted in fuel cells, internal combustion engines, small cogeneration plants and many other systems. The main limitation to obtaining high performance and high boost pressures in centrifugal compressors is due to the instability phenomenon that occurs at low mass flow rates. A better knowledge of this phenomenon can consistently improve the performance of the systems in which centrifugal compressors are installed. The analysis of compressor instabilities, i.e., surge, is an important topic: during surge occurrence the operating flow can assume a highly unsteady behaviour with large fluctuations in pressure and mass flow rate. The compressor can be seriously damaged by phenomena of surge instability due to vibrations and thermal stress. In standard application it is common practice to reduce the operating area of the turbomachinery working away from the surge line to avoid any risk of damage. Usually, to avoid the surge occurrence, the maximum boost pressure is controlled with a by-pass valve commonly called dump valve, it is clear that this solution reduces the mass flow rate provided by the machine and therefore its performance.

A better understanding of surge, which can be achieved through dedicated experimental investigations, is essential to develop simulation models capable of accurately predict compressor behaviour and surge occurrence. An in-depth experimental investigation was carried out on a small centrifugal compressor for automotive application at the test rig for components of propulsion system of the University of Genoa. A specific circuit adaptable in length and volume was set up to analyse the effect of different layout configurations on compressor performance with special reference to the low mass flow rate region. The instantaneous value of pressure and mass flow rate are measured in different sections upstream and downstream the compressor and along the circuit. Particular attention was paid in the transition from the steady to the unsteady operation of the compressor, considering different conditions and circuit configurations. Furthermore, the present work describes a methodology to analyse surge cycles, showing their variations with compressor speed and system configuration, applying time synchronous average of a large number of consecutive cycles to evaluate shapes and sizes of surge cycles. Then, this paper highlights the energy content of pressure and mass flow rate fluctuations considering the hysteresis loop during deep surge operations. Finally, a preliminary analysis on the surge precursor is performed by analysing the low and high frequency domain of the pressure fluctuations during the transition from the stable to the unstable zone.

1   INTRODUCTION

Turbochargers composed of a centrifugal compressor and a centripetal turbine are widespread all over the world and find applications in many sectors from energy generation systems to propulsion systems. The main technology that adopts turbochargers are internal combustion engines [1], fuel cells [2], small cogeneration plants [3] and refrigeration systems [4]. The main limit of dynamic compressors is related to the

instability region at low mass flow rate. This unstable phenomenon causes large pressure fluctuations that cause large vibrations and uncontrolled rise in temperature at the compressor inlet: a long period in this condition can lead to the failure of the compressor or of the entire plant [5]. One of the first scientific work on this topic was proposed by Emmons et al. [6] in 1955. It was found that the surge consists of two different types of phenomena and their interaction. The whole system could be unstable in the manner of a self-excited Helmholtz resonator and, moreover, these phenomena interact with the stalling of the flow through the rows of blades, which is usually assumed to be the origin of pulsations. 20 years later Greitzer in [7,8] developed a non-linear model to predict the transient response of a compression system subsequent to a perturbation from steady operating conditions. It was found that, for the system investigated, there is an important nondimensional parameter on which this response depends. Whether this parameter is above or below a critical value determines which type of compressor instability, rotating stall or surge, will be encountered. The experimental procedure was developed to evaluate pressure and mass flow rate during a compressor transient operation in the unstable zone. Then, the experimental data are compared to the results of the theoretical model showing a very high degree of accuracy. Following studies by Hansen et al. [9] confirmed the validity of Greitzer's model for centrifugal compressors. Hansen conducted a detailed experimental investigation on a small centrifugal compressor and compared the experimental data to the model calculations, validating Greitzer's model. Fink et al. [10] studied the turbocharger surge in a radial impeller-vaneless diffuser free spool-system considering two very different layout downstream the compressor. Experimental measurements shown that the impeller stall at the inducer tips is a key phenomenon in surge inception and it is more severe near the volute tongue. Another experimental and modelling work by Schleer et al. [11] analysed the effect of clearance effects on the onset of instability. Time-resolved measurements of the static pressures are performed by installing pressure sensors along the flow to detect clearance vortices and stall precursors. The work also analysed the sequence of events leading to rotating stall in the diffuser. A stability analysis revealed that inlet tip recirculation is triggered when the leakage vortex approaches the adjacent blade. This leads to a sudden increase of random pressure fluctuation in the inducer section and a change in the loading distribution. Instead, Galindo et al. [12] analysed the effect of the inlet circuit geometry on the performance of an automotive compressor with special reference to the surge line position. Four different compressor inlet circuit configurations were designed and tested showing a clear sensitivity of the compressor characteristic curves to the circuit geometry at the inlet.

Nowadays, many researchers adopt 3D high-fidelity compressor simulations to better understand phenomena leading to the unstable operation of centrifugal compressors. CFD models are universally used to study the inception and the development of stall [13,14]. For example, Cravero et al. [15] used an unsteady simulation with a complete 3D model to confirm that the adoption of ported shroud can effectively extend the operating range of the compressor. Miura et al. [16] develop a CFD model to predict the inception of rotating stall and its effects on shaft vibration. The model was experimentally validated, and two types of rotating stall are measured: one is a multiple-cell induced in the vaneless diffuser, the other is a one-cell induced in the impeller.

In this paper, an extensive experimental campaign developed at the test bench for components of propulsion system of the University of Genoa is described in order to analyse the behaviour of a radial centrifugal compressor during surge operation. Pressure and mass flow rate signals measured in different sections of the system are analysed and used to describe the phenomena that occur during deep surge behaviour not only in the compressor, but in the whole system. In order to highlight the behaviour that characterizes the interactions between the system and the compressor, a circuit

with modular volume and length is adopted. In particular, the energy content related to pressure and mass flow rate fluctuations is analysed considering the hysteresis cycle during the deep surge operation. All this information can be used to find precursors of surge occurrence to be set as control data (i.e., an on/off signal for a bleed valve) implemented in an on board engine control system.

2   EXPERIMENTAL SET-UP AND MEASURING EQUIPMENT

The experimental activity was developed on a small turbocharger fitted with an unshrouded vaneless centrifugal compressor (diameter of 40 mm) and a single-entry nozzle-less waste-gated centripetal turbine, used in automotive application on down-sized 4-cylinder spark ignition engines.

The experimental campaign was developed at the test bench for components of propulsion system of the University of Genoa (fully described in [17,18]). The test rig, particularly suited to test turbochargers in a wide operative range thanks to two independent feeding lines, is schematically shown in Figure 1. Three electric screw compressors deliver a maximum of 0.85 kg/s of dry air at 8 bar allowing tests on turbochargers for light and heavy-duty vehicles. Turbocharges can be tested in "cold" and "hot" conditions by controlling the thermal power of electrical air heaters capable of raising the turbine inlet temperature up to 750°C. Moreover, the test rig allows turbochargers to be tested under steady, transient and pulsating flow operation [19–21].

AF	Air Filter	LM	Laminar Flow Meter
AH	Air Heater	PC	Pressure Control
AR	Air Reservoir	SC	Screw Compressor
C	Compressor	T	Turbine
LC	Lubricating Circuit	TM	Thermal Mass Flow Meter
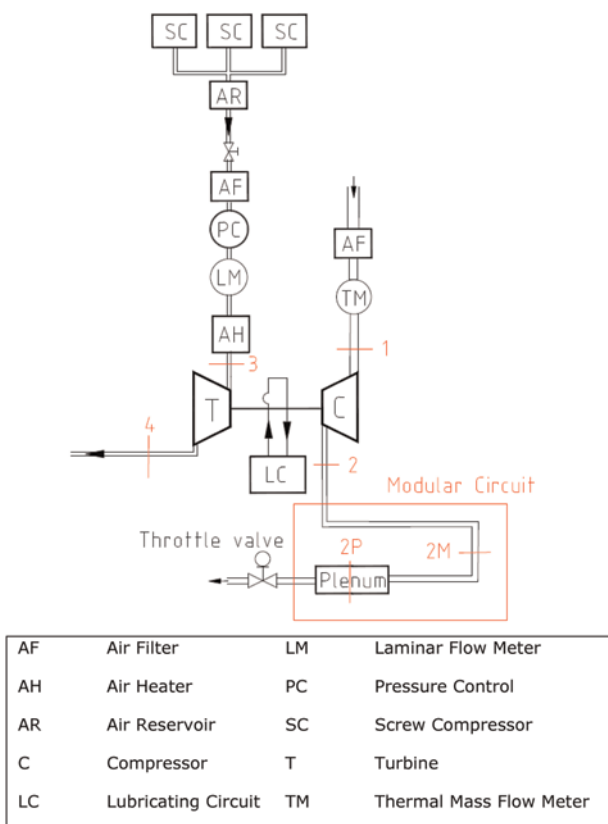
Figure 1. Test bench for components of propulsion system of the University of Genoa.

Since the aim of the experimental campaign is related to the analysis of the surge phenomenon, a modular circuit (red box in Figure 1) is installed downstream the compressor to evaluate the impact of different circuits on surge dynamics. The length of the pipe can be varied between 0, 2 and 4 metres, while the volume of the plenum can be varied between 2 and 6 litres. The variable volume plenum is followed by a motorized throttle valve used to change the pressure losses and control the external characteristic of the circuit. Figure 2 shows an overview of the test bench layout highlighting the position of the compressor and the modular circuit. In this paper, the nomenclature adopted refers to the configuration called VxLy, where x denotes the volume of the plenum expressed in litres and y refers to the length of the circuit expressed in metres. Table 1 shows the downstream configurations analysed.
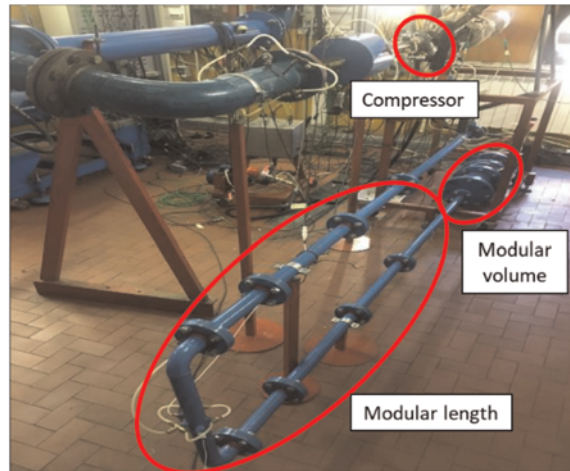
Figure 2. Overview of the test circuit layout.

Table 1. Downstream configurations.

Layout	V2L0	V2L2	V2L4	V6L0	V6L2	V6L4
Total Volume [litres]	3,7	5,8	7,9	7,7	9,8	11,9
V_{pipes}/V_{plenum}	0,84	1,89	2,95	0,28	0,63	0,98

In each measuring section, reported in red in Figure 1, the thermodynamic quantities are recorded through an automatic data acquisition system developed in LabVIEW® environment.

Average and instantaneous values of static pressure were measured with piezo-resistive probes (accuracy of $\pm0.10\%$ of full scale). The air temperature was measured with K type thermocouples (accuracy $\pm1.5°C$), and with platinum resistance thermometers Pt 100 class A (accuracy of $\pm0.15°C$ and $\pm0.2\%$ of measured value). The turbocharger rotational speed was recorded through an eddy current probe mounted close to the compressor wheel (accuracy of $\pm0.009\%$ of full scale). The average compressor mass flow rate is evaluated using a thermal mass flowmeter

(accuracy of $\pm0.9\%$ of the measured value and $\pm0.05\%$ of the full scale). High-frequency response piezoresistive probes are adopted to measure instantaneous values of pressure. Dynamic pressure transducers were installed in different sections of the compressor circuit, and in the compressor volute. To detect the onset of surge and determine the transition from stable to unstable operation, i.e. the surge line position, the compressor outlet pressure signal was used as the reference. By analysing the low-frequency component of the spectrum, the transition to unstable operation was then established when the amplitude of the peak crosses 0.6% of the mean value for each operating condition.

The instantaneous mass flow rate was recorded with a constant temperature anemometric system with a fibre film probe calibrated under steady flow conditions against the thermal mass flowmeter. Since the air temperature influences the output voltage of the probe, calibration curves were measured at four different temperature levels (20, 50, 75 and 100°C), selected to cover the field of interest of the experimental tests, as shown in Figure 3.
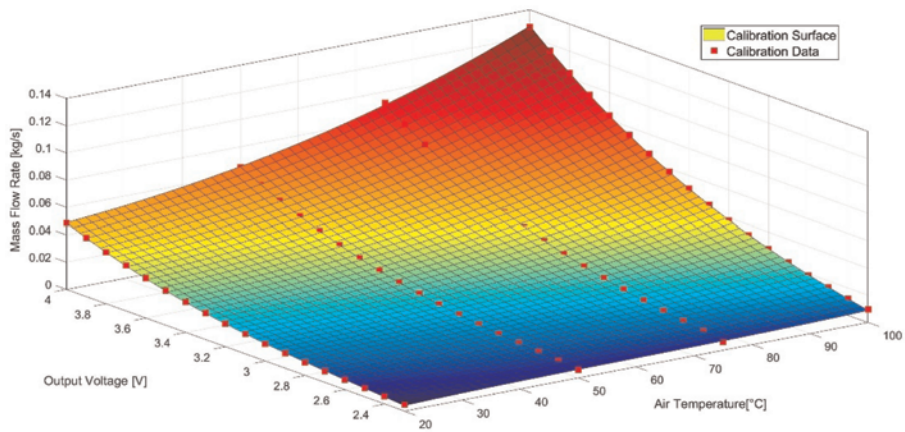
Figure 3. Hot fiber film probe calibration surface.

The fibre film probe was installed in the measuring section at the compressor outlet with its axis perpendicular to the flow direction. During deep surge operation, the flow direction reverses. This phenomenon cannot be captured by the unidirectional single fibre film probe, so the mass flow rate signal had to be properly post-processed. All the details on the post processing technique are reported in [22]. In Figure 4 the recorded signal (in orange) and the post-processed signal (in blue) are compared.
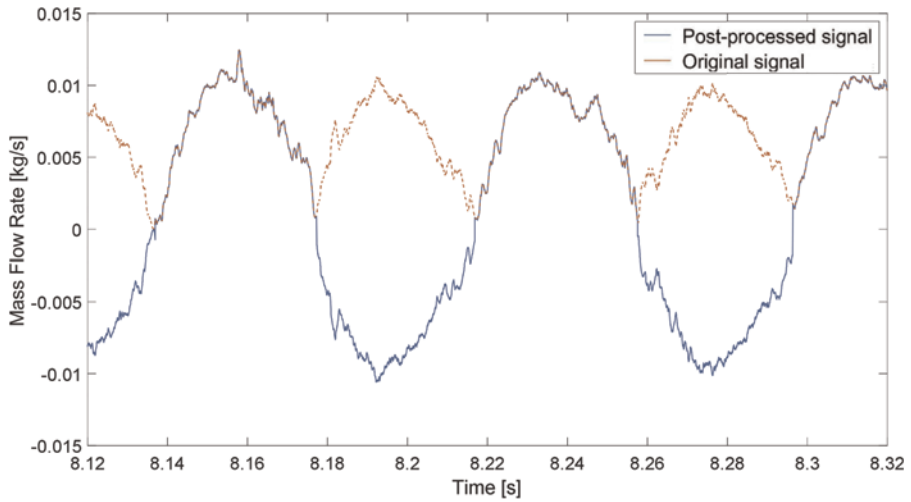
Figure 4. Mass flow rate signal before (in orange) and after (in blue) the post-processing technique.

The Fast Fourier Transform analysis applied on pressure and mass flow rate signals confirms the quality of this technique. Before the post-processing, the surge frequency of mass flow rate signal was double the frequency of pressure signal. After the post-processing technique, the surge frequency of mass flow rate and pressure signals matches.

In Figure 5 the FFT of the mass flow rate signal before (in orange), and after (in blue) the post-processing technique is reported, highlighting the energy contents located at 12 Hz.
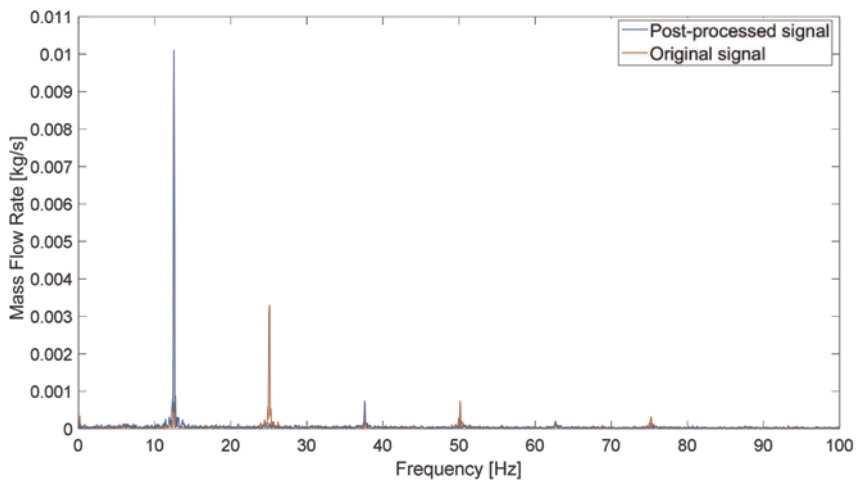
Figure 5. FFT analysis of mass flow rate signal in deep surge operation referring to raw data (in orange) and post processed data (in blue).

Furthermore, the significance of this approach can be observed in Figure 6 where a comparison between the cycle average hysteresis loop recorded (in orange) and post-processed (in blue) is reported for 118000 rpm in V2L0 configuration. It is clear that the shape of the curve is totally different in the extension of the area used here to evaluate the energy content of the surge cycles.
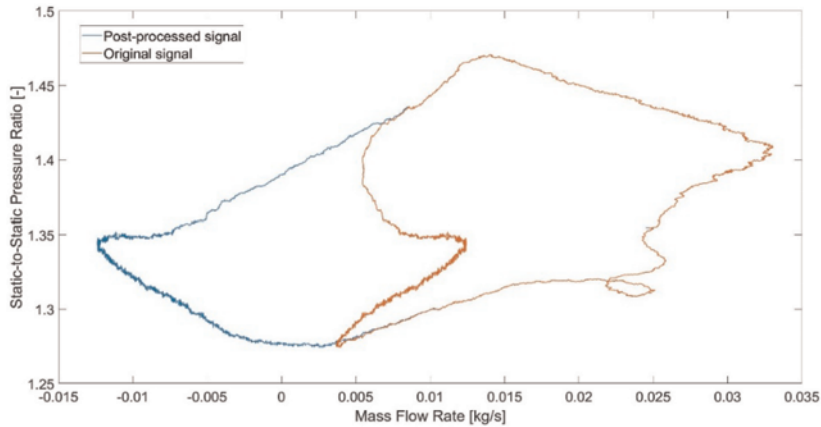
Figure 6. Deep surge hysteresis loop with mass flow rate signal before (in orange) and after (in blue) the post-processing technique.

In surge operation, all signals are processed calculating the time synchronous average over different complete cycles. As a slight pulse period variation was detected during the observation window, the real pulse period length was estimated cycle by cycle. Consequently, the calculation of the point-by-point average signal was referred to fixed relative positions in the pulse cycle. Finally, a low-pass filter was applied to reduce noise.

3   EXPERIMENTAL RESULTS

The first step of the experimental analysis is the evaluation of the compressor characteristic curves for each configuration reported in Table 1. In particular, the pressure ratio characteristic curves are shown in Figure 7a and 7b, respectively for a plenum volume of 2 and 6 litres with different circuit lengths (0, 2 and 4 metres). It can be observed that the position of the surge lines differs from each other with a maximum deviation of 5%, which is more evident at higher rotational speed levels due to higher inertial effects. In particular, the surge line position seems to be moderately affected by the different dumping effects related to the length and volume of the circuit [23].
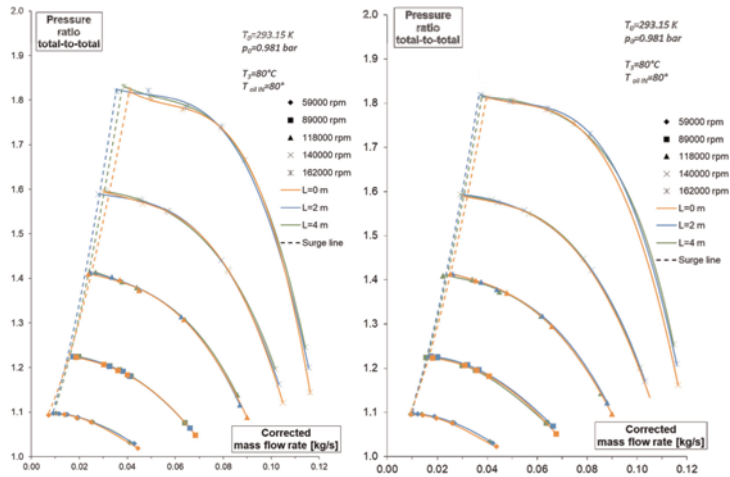
Figure 7. Compressor pressure ratio maps with reference to outlet plenum volume of 2 litres (left side) and 6 litres (right side).

Focusing on the unstable behaviour of the compressor, Figure 8 shows the cycle average hysteresis loop in surge operation for all the configurations analysed together with the corresponding steady state condition referring to static-to-static pressure ratio.
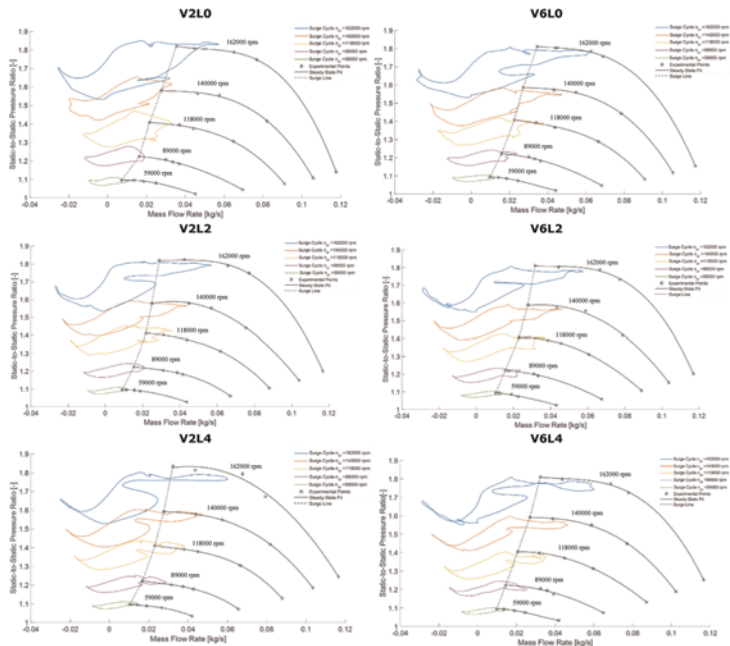
Figure 8. Unstable compressor performance compared with steady state for all arrangements.

Based on Figure 8, it can be observed that the area of the surge cycles increases as the turbocharger rotational speed increases for each configuration. In order to better understand the relationship between the surge cycle area and circuit volume and length, the analysis in the following section relates the experimental results with the Greitzer compressor surge theory [7,8].The Greitzer B parameter increases with the rotational speed and/or the volume rise, as shown in Equation 1. When B increases, the variation in mass flow rate increases (Equation 2), while the variation in pressure decreases (Equation 3).

$$B = \frac{u}{2a_p} \sqrt{\frac{V_p}{AL}} \tag{1}$$

$$\frac{d\dot{m}_c^*}{dt^*} = B\left(p_c^* - p_p^*\right) \tag{2}$$

$$\frac{dp_c^*}{dt^*} = \frac{1}{B}\left(\dot{m}_c^* - \dot{m}_v^*\right) \tag{3}$$

Where:

- u is the tangential speed of the rotor;
- a_p is the speed of sound in the plenum;
- V_p, A and L are the plenum volume and the area and length of the pipe system;
- $\dot{m}_c^*$ and $\dot{m}_v^*$ are the dimensionless compressor and throttle valve mass flow rates;
- p_c^* and p_p^* are the dimensionless compressor outlet and plenum pressures.

The circuit configuration affects the position and the shape of each cycle. With the increase in circuit volume, the cycles tend to get thinner and the negative portion of the cycle deviates less from the steady state characteristic. At higher speed, length or volume, the mass in the system increases, making the system slower during transitions. This behaviour moves the system to operate closer to the steady state characteristic also in the negative mass flow rate region. The shape of the steady state characteristic in the negative area has been measured and calculated by many researchers [24,25]: the pressure ratio, approximated as a third order polynomial, decreases moving from the minimum mass flow rate until the mass flow rate becomes zero. Therefore, in the negative flow rate region, the surge cycle tends to the steady state characteristic when the volume or length of the system increases.

The position of the cycle is also affected by inertial effects. When circuit volume and rotational speed increase, the delays in the propagation of mass flow rate and pressure waves from the point where instability generates to the measuring station increase. This delay affects the shift between the maximum value of mass flow rate and the maximum value of pressure. For this reason, the cycles at higher rotational speed and for higher configuration volumes shift below the steady state compressor characteristic.

In the following analysis, the area of each surge cycle is adopted as a method to evaluate the energy content of pressure and mass flow signals during surge operation. Figure 9 shows the surge cycle area for different rotational speed levels referring to each volume, while Figure 10 reports a comparison between each length.
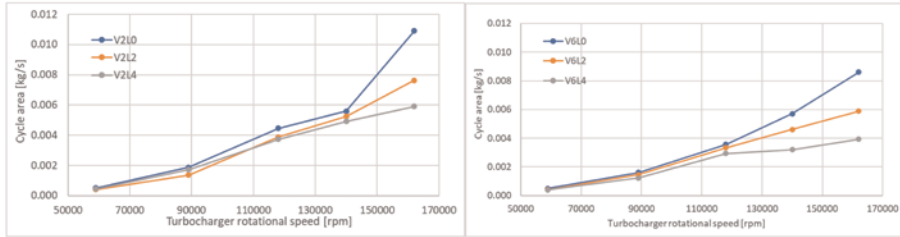
Figure 9. Effects of turbocharger rotational speed and piping lengths on surge cycles area for 2 litres volume (on the left) and 6 litres (on the right).
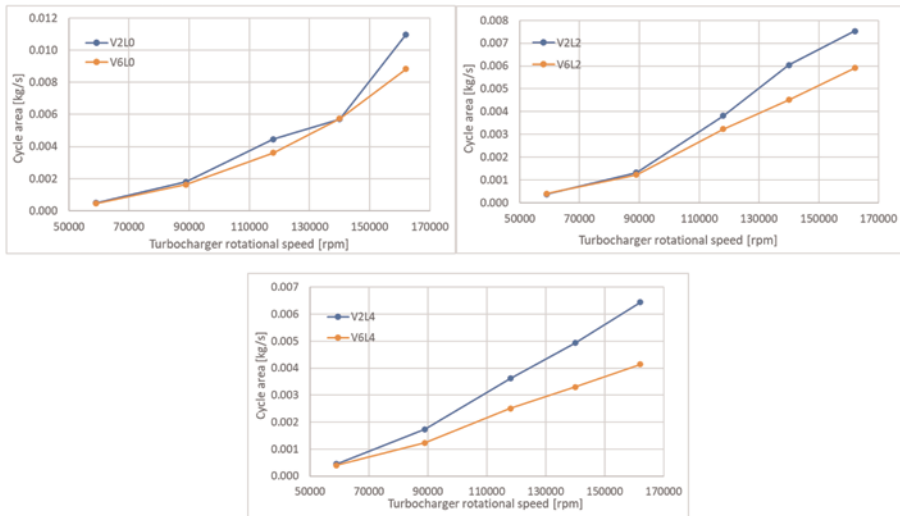
Figure 10. Effects of turbocharger rotational speed and volumes on surge cycles area for circuit lengths of 0, 2 and 4 metres.

The cycles area rises with the rotational speed, with a more significant deviation at higher rotational speed; as a matter of fact, the amplitude of the oscillations of pressure and mass flow rate signals increases with the turbocharger rotational speed due to the higher energy content in the system. The effect of the circuit lengths on the cycles area becomes more apparent at lower volume values, while inertial effects are less affected by circuit lengths at higher plenum volumes. In addition, the pressure oscillation amplitude is damped by the friction which rises with the pipe length increase. The same considerations can be addressed to Figure 10, where the energy content of the surge cycles is less significant due to the greater volume.

The pressure and mass flow rate oscillation amplitude becomes more important as the volume decreases. This aspect could be confirmed by the fundamental frequency of the mass flow and pressure signals in surge operation, evaluated through a Fast Fourier Transform analysis. In Figure 11 it is reported the fundamental frequency of surge operation for two different circuit configurations: V2L2 and V6L2. For the high volume configuration, the time required to complete a cycle is longer due to the more prominent inertial effects, causing a decrease of the surge frequency.

12
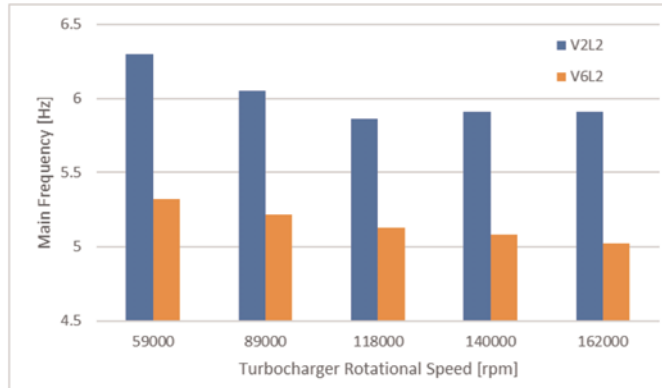
Figure 11. Main frequency in surge operation.

Moreover, an analysis of the main frequency is conducted comparing the last stable point with the corresponding unstable operation to evaluate the presence of surge precursors. In Figure 12 a comparison between the spectra of the compressor outlet pressure in the last stable point (in blue) and in surge operation (in orange) is reported. As expected, the oscillations in unstable operation are consistently higher than the last stable points and, as previously stated, the amplitude increases with the turbocharger rotational speed. The surge frequency appears to be independent by rotational speed, while an opposite behaviour is highlighted in the last stable point where higher frequencies components can be observed. It was observed that, if the working point of the compressor gradually moves towards the surge operation, the unstable behaviour can be detected by the occurrence of not negligible components at low frequency [26].
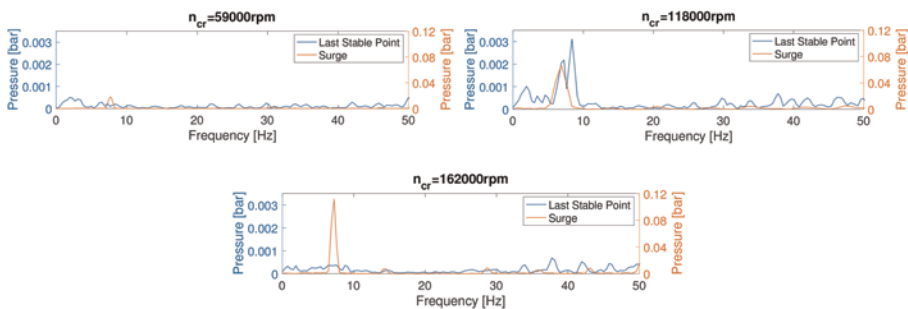
Figure 12. Pressure spectra in the last stable point (blue line) and in surge operation (orange line) for different turbocharger rotational speed (V6L0 layout).

Besides, the high-frequency domain is analysed to study the surge precursors. In Figure 13 the auto-power spectra of the pressure measured in the compressor volute are shown as a function of time in the high frequency domain. The stable part of the transient ends at second 35, which is the instant when surge occurs. To identify the blade passing frequency, the frequency of the auto-power spectra is divided by the

turbocharger rotational frequency. The normalized value of the blade passing frequency is 10, which is the number of blades in the compressor. During the transient, the amplitude of the blade passing frequency component increases when moving towards the surge line. In proximity to the surge limit, two other components appear at lower normalized frequencies. These components can be attributed to stall occurrence in the compressor, a phenomenon characterized by a frequency lower than the blade pass frequency. This behaviour can be detected only by the pressure transducer in the volute. When the flow reaches the compressor outlet pressure transducer, these components have been damped and are no longer detectable. The components that appear when moving closer to surge are caused by modulation effects. The modulation of the blade passing frequency component appears with the rotating stall component. These components occur when the operating point is close to the stability limit.
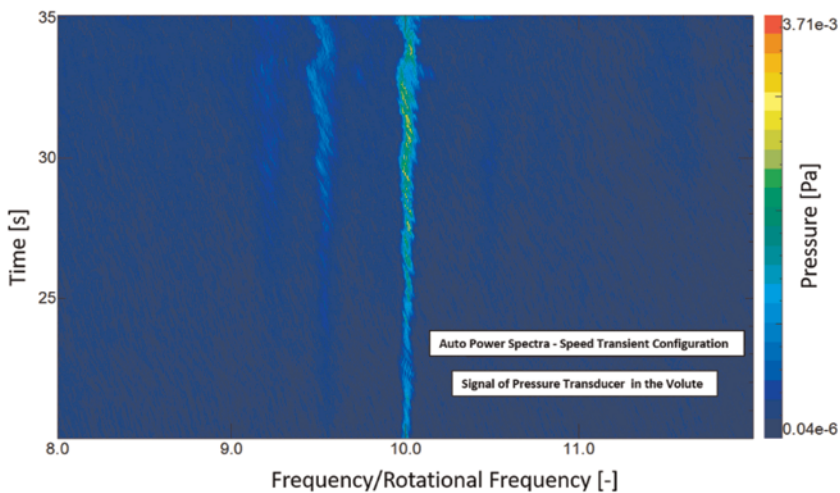
Figure 13. High frequency detail of the auto-power spectra evaluated in the compressor volute at 162000 rpm in V6L4 layout.

4   CONCLUSION

In this paper an experimental campaign developed at the test bench for components of propulsion system of the University of Genoa on a small centrifugal compressor of an automotive turbocharger is presented. A specific circuit with flexible length and volume was installed downstream the compressor to investigate the impact of different layouts. To evaluate the behaviour in the unstable region of the compressor, instantaneous signals of pressure and mass flow rate are recorded.

The behaviour of the compressor was investigated both in stable and unstable operation. At first, the characteristic curves of the compressor are analysed considering different circuit arrangements highlighting a deviation in surge line position, more prominent at higher rotational speed levels. Then, the cycle average hysteresis loops are measured in surge operation for each layout considered and compared to the corresponding steady state. It was observed that the circuit configuration strongly affects

the position and the shape of the cycles. Particular attention was paid to the energy content of the cycle average hysteresis loops considering the pressure and mass flow oscillation amplitude. Then, a preliminary analysis on the pressure signal in the low and in the high frequency domain was performed to highlight surge precursors during the transition from stable to unstable condition. A comparison between the spectra of the compressor outlet pressure in the last stable point and in surge is analysed. It seems that the last stable point and the surge operation do not share the same main frequency, but surge occurrence could be expected if an increase in the amplitude of the compressor outlet pressure spectrum is detected at low frequency domain. Besides, analysing the high frequency domain of a pressure signal in the compressor volute, a modulation effect, probably related to rotating stall, in the instants before the transition from stable to unstable operation can be detected.

The insight provided by the analysis of surge cycles can be adopted to validate CFD models for the analysis of surge occurrence and to develop physic-based control-oriented models to prevent surge occurrence.

REFERENCES

[1] Li, X., Zhao, Y., Liu, Z., Yao, H., Chen, H., "A New Method for Performance Map Prediction of Automotive Turbocharger Compressors with Both Vaneless and Vaned Diffusers," *Proceedings of the Institution of Mechanical Engineers, Part D: Journal of Automobile Engineering* Volume 235, Issue 6, Pages 1734–1747, 2021. DOI 10.1177/0954407020971252.

[2] Schoedel, M., Menze, M., Seume, J.R., "Experimentally Validated Extension of the Operating Range of an Electrically Driven Turbocharger for Fuel Cell Applications" *Machines* Volume 9, Issue 12, 2021. DOI 10.3390/machines9120331.

[3] Reggio, F., Silvestri P., Ferrari M.L., Massardo A.F., "Operation Extension in Gas Turbine-based Advanced Cycles with a Surge Prevention Tool," *Meccanica* Volume 57, Issue 8, Pages 2117, 2022. DOI 10.1007/s11012-022-01540-6.

[4] Yi, K., Zhao, Y., Yu, G., Yang, Q., Liu, G., Li, L., "Research on Performance of Refrigeration Centrifugal Compressor with Gas Bearings for Water Chillers," *Energy Reports* Volume 8, Pages 5562–5569, 2022. DOI 10.1016/j.egyr.2022.04.031.

[5] J. Galindo, J.R. Serrano, C. Guardiola, C. Cervelló, Surge Limit Definition in a Specific Test Bench for the Characterization of Automotive Turbochargers, *Experimental Thermal Fluid Science* 30 (5) 449–462, 2006. http://dx.doi.org/10.1016/j.expthermflusci.2005.06.002.

[6] Emmons, H.W., Emmons, H.W., Pearson, C.E., and Grant, H.P., "Compressor Surge and Stall Propagation," *Transactions of the ASME* 77(4):455–469, 1955. https://doi.org/10.1115/1.4014389.

[7] Greitzer, E.M., "Surge and Rotating Stall in Axial Flow Compressors. Part I: Theoretical Compression System Model," *Journal of Engineering for Power* 98 (2):190–198, 1976. https://doi.org/10.1115/1.3446138.

[8] Greitzer, E.M., "Surge and Rotating Stall in Axial Flow Compressors. Part II: Experimental Results and Comparison with Theory," *Journal of Engineering for Power* 98(2): 199–211, 1976. https://doi.org/10.1115/1.3446139

[9] Hansen, K.E., Jorgensen, P., and Larsen, P.S., "Experimental and Theoretical Study of Surge in a Small Centrifugal Compressor," *Journal of Fluids Engineering*, 103(3): 391–395, 1981. https://doi.org/10.1115/1.3240796

[10] Fink, D.A., Cumpsty, N.A., Greitzer, E.M., "Surge Dynamics in a Free-Spool Centrifugal Compressor System," *Journal of Turbomachinery* 114(2): 321–332, 1992. https://doi.org/10.1115/1.2929146

[11] Schleer, M., Jin Song S., Abhari, R.S. "Clearance Effects on the Onset of Instability in a Centrifugal Compressor," *Journal of Turbomachinery*, vol. 130, no. 3, p. 031002, 2008. DOI 10.1115/1.2776956.

[12] Galindo, J., Tiseira, A., Navarro, R., Tarì, D., Meano, C.M., "Effect of the Inlet Geometry on Performance, Surge Margin and Noise Emission of an Automotive Turbocharger Compressor," *Applied Thermal Engineering*, vol. 110, pp. 875–882, 2017. https://doi.org/10.1016/j.applthermaleng.2016.08.099.

[13] Yunfei, M., Xiaohua, L., Sun, D., Xiaofeng S., "Numerical Prediction of Stall Inception in Centrifugal Compressor Using Eigenvalue Method," in *ASME Turbo Expo 2015: Turbine Technical Conference and Exposition*, 2015. https://doi.org/10.1115/GT2015-42590.

[14] Vagani, M., Engeda, A., and Cave, M.J. "Prediction of Impeller Rotating Stall Onset Using Numerical Simulations of a Centrifugal Compressor. Part 1: Detection of Rotating Stall Using Fixed-Flow Transient Simulations," *Proceeding of the Institution of Mechanical Engineers, Part A: Journal of Power and Energy*, vol. 227, no. 4, pp. 403–414, 2013. DOI 10.1177/0957650912474386.

[15] Cravero, C., Leutcha, P.J., Marsano, D., "Simulation and Modelling of Ported Shroud Effects on Radial Compressor Stage Stability Limits," *Energies*, 2022, Vol.15, Issue 7, p. 2571. DOI: 10.3390/en15072571.

[16] Miura, T., Yamashita, H., Takeuchi, R., Sakai, N., "Numerical and Experimental Study on Rotating Stall in Industrial Centrifugal Compressor," *Journal of Turbomachinery*, 2022, Volume 143, Issue 8, Article number 081012. DOI: 10.1115/1.4050439.

[17] Marelli, S., Usai, V. "Experimental Analysis and 1D Simulation of an Advanced Hybrid Boosting System for Automotive Applications in Transient Operation," *International Journal of Engine Research*, 2021. DOI: 10.1177/14680874211060173.

[18] Marelli, S., Usai, V., Capobianco, M., "*Experimental Investigation on the Transient Response of an Automotive Turbocharger Coupled to an Electrically Assisted Compressor,*" 14th International Conference on Turbochargers and Turbocharging – Proceedings of the International Conference on Turbochargers and Turbocharging, 2021.

[19] Usai, V., Marelli, S., "Steady State Experimental Characterization of a Twin Entry Turbine Under Different Admission Conditions," *Energies*, 2021, Volume 14, Issue, Article number 2228. DOI 10.3390/en14082228

[20] Marelli, S., Usai, V., Capobianco, M., "*Experimental Investigation on the Transient Response of an Automotive Turbocharger Coupled to an Electrically Assisted Compressor,*" 14th International Conference on Turbochargers and Turbo charging – Proceedings of the International Conference on Turbochargers and Turbocharging, 2021, pp. 219 – 229. DOI 978-036767645-2.

[21] Marelli, S., Capobianco, M., Zamboni, G., "Pulsating Flow Performance of a Turbocharger Compressor for Automotive Application," *International Journal of Heat and Fluid Flow*, 2014, 45(1), pp. 158–165. DOI 10.1016/j.ijheatfluidflow.2013.11.001.

[22] Marelli, S., Misley, A., Ferrando, M., "Experimental Investigation in Turbocharger Compressors During Surge Operation," *Proceedings of the ASME Turbo Expo*, 2020, Volume 8. DOI: 10.1115/GT2020-15174.

[23] Marelli, S., Carraro, C., Moggia, S., Capobianco M., "Effect of Circuit Geometry on Steady Flow Performance of an Automotive Turbocharger Compressor" *Energy Procedia*, 2016. DOI: 10.1016/j.egypro.2016.11.080.

[24] Gravdahl, J.T., Willems, F., De Jager, B., Egeland, O., "Modeling of Surge in Free-Spool Centrifugal Compressors: Experimental Validation," *Journal of Propulsion and Power*, 2004, vol. 20, no. 5, pp. 849–857. DOI 10.2514/1.10052.

[25] J. Galindo, J. R. Serrano, H. Climent, A. Tiseira, "Experiments and Modeling of Surge in Small Centrifugal Compressors for Automotive Engines," *Journal of Experimental Thermal and Fluid Sciences*, 2008, vol. 32, no. 3, pp. 818–826. DOI 10.1016/j.expthermflusci.2007.10.001

[26] Marelli, S., Silvestri, P., Usai, V., Capobianco, M., "Incipient Surge Detection in Automotive Turbocharger Compressors," *SAE Technical Papers*, 2019. DOI: 10.4271/2019-24-0186.

An investigation on influence of inlet elbow on performance of a centrifugal compressor with vaned diffuser

X.C. Wang[1], M.Y. Yang[1]*, X.Y. Wang[2], W.L. Li[2], Y. Liu[3], C. Ma[3]

[1]Shanghai Jiao Tong University, Shanghai, China
[2]Weichai Power Co., Ltd., Weifang, China
[3]Kangyue Technology Co., Ltd., Weifang, China

ABSTRACT

The energy conservation and emission reduction requirements of internal combustion engines push turbochargers towards high efficiency and high compression ratio. Centrifugal compressors with vaned diffuser have significant efficiency advantages at high pressure ratio. Due to the compactness demand of internal combustion engine, the compressor inlet often has a prominent elbow structure. In this paper, the influence of inlet elbow on the performance of centrifugal compressor with vaned diffuser is studied. Firstly, the influence of elbow on compressor efficiency, pressure ratio and operating range is analyzed. The flow loss distribution differences of several inlet pipe geometries are compared and analyzed based on entropy generation method. The results show that the inlet elbow causes strong circumferential and radial flow distortion at the inlet of the impeller, which can lead to a significant deterioration of the performance of the centrifugal compressor. Furthermore, the influence of the elbow is highly dependent on its location relative to the volute, because the elbow-induce flow distortion is strongly coupled with the volute-induce flow distortion in the impeller and diffuser. Specifically, compared with the straight pipe, the efficiency reduces notably by 1.3% at inlet bending direction of 270 degree clockwise with the volute tongue, but increases by 0.6% at 180 degrees. Moreover, the operational range is also notably influenced by the location of the elbow. This study provides guidance for the layout and optimization of compressor inlet pipe geometry.

Keywords: Centrifugal compressor, Vaned diffuser, Flow distortion, Loss mechanism

---

*Corresponding Author

1   INTRODUCTION

Centrifugal compressor is one of the core components of internal combustion engine turbocharger. With increasingly strict emission regulations and pursuit of higher pressure ratio and higher efficiency, centrifugal compressor with vaned diffuser has attracted more and more attention due to its high single stage efficiency with high pressure ratio [1–2]. As the compact layout of internal combustion engine structures, compressor inlet will be constrained by other components, which will inevitably lead to bending and twisting of inlet.

The influence of inlet distortion on compressor performance has been studied. Total pressure distortion and velocity distortion in impeller inlet is studied by Ariga et al. [3–5] on the performance characteristics and surge margin of centrifugal compressor. As for the use of bent inlet, Kim[6] confirmed that inlet bent will cause upstream flow deformation of the compressor and non-uniformly enhanced flow angle, resulting in a reduction in compressor stage efficiency compared with straight intakes. Yamada et al. [7–8] use experiment find that at low mass flow point, inlet bend will cause the inlet of the compressor impeller to become a pre-eddy current, which inhibits the separation of the leading edge of the impeller tip side and improves the flow field inside the impeller.

Braembussche et al. [9] have made a remarkable study on the mechanism of the flow field in volute. The results show that the flow in the volute is negatively blocked and the pressure gradually increases in circumferential direction under low flow condition, while the result is opposite under high flow condition. Ceyrowsky and Zheng [10,11] further studied the influence mechanism of volute distortion on compressor performance. The propagation mode of circumferential distortion and its influence on impeller and diffuser are analyzed. The experimental work of Hagelstein [12] shows how the circumferential pressure distortion affect the discharge flow of the impeller under off-design conditions, and then lead to the impeller operating point changes in total pressure, temperature and flow angle. Niu et al. [13,14] reveal the rotating stall mechanism of vaneless diffuser compressor induced by volute and suggest to reduce pressure distortion along the circumferential direction in vaneless diffuser.

At the same time, several researches have been focused on changing compressor inlet geometry. Wang [15] studied the influence of the distance between bent pipe outlet and leading edge of impeller. In the case of large mass flow rate, longer bent inlet changes the distribution of blade load more obvious resulting in reduced efficiency. Yang [16] studied the influence of bent inlet of vaneless centrifugal compressor and get to the conclusion that bent inlet pipe enhances the sizes and ranges of the unsteady pressure fluctuation. The interaction between inlet vortex direction and impeller rotation direction is also studied by Hou [17]. The result confirmed that the influence is greatest when the direction of rotation between block vortex and impeller is the same.

In summary, there are some researches focusing on the influence of inlet piping on the compressor performance in recent years. And the influence has already been experimentally and numerically confirmed. However, most of these studies are based on centrifugal compressor with vaneless diffuser. In the centrifugal compressor with vaned diffuser, due to the existence of blade in diffuser, the volute-induce flow distortion has to penetrate the vaned diffuser before imposing on the impeller. Therefore, the flow distortion in the impeller is expected to be somewhat different from that of vaneless one. Furthermore, the rotor-stator interaction between the impeller and the vaned diffuser will be much strongly, and hence the flow distortion induced by both the volute and the inlet elbow can have more profound influence on the flow field and hence the performance. Therefore, it is necessary to study the coupling effect of volute distortion and inlet circumferential distortion in centrifugal compressor with vaned diffuser.

In this paper, the 3D simulation model of centrifugal compressor with vaned diffuser is established and verified. On this basis, the stability of compressor at low mass flow rate

and the entropy increase distribution are analyzed. Finally, according to the inlet flow distortion and the volute circumferential distortion, the influence of different inlet pipe bending directions on the overall performance of the compressor and the coupling effect with the volute circumferential distortion are analyzed.

2 THE CENTRIFUGAL COMPRESSOR AND NUMERICAL METHOD

2.1 Centrifugal compressor configurations

In this research, a centrifugal compressor with vaned diffuser is adopted. Geometries of impeller, diffuser and volute are shown in Figure 1-a. The angle when inlet bending direction coincides with volute tongue is defined as 0 degree, and four typical different angles of 0, 90, 180, 270 are taken clockwise, as shown in Figure 1-b. The bending angle and bending radius of inlet pipe is designed by engineering, which are 120 degree and 85mm separately, and keep constant in different orientations. Other parameters of the compressor and inlet model are shown in Table 1.

| (a) Impeller and vane | (b) Test elbow model |
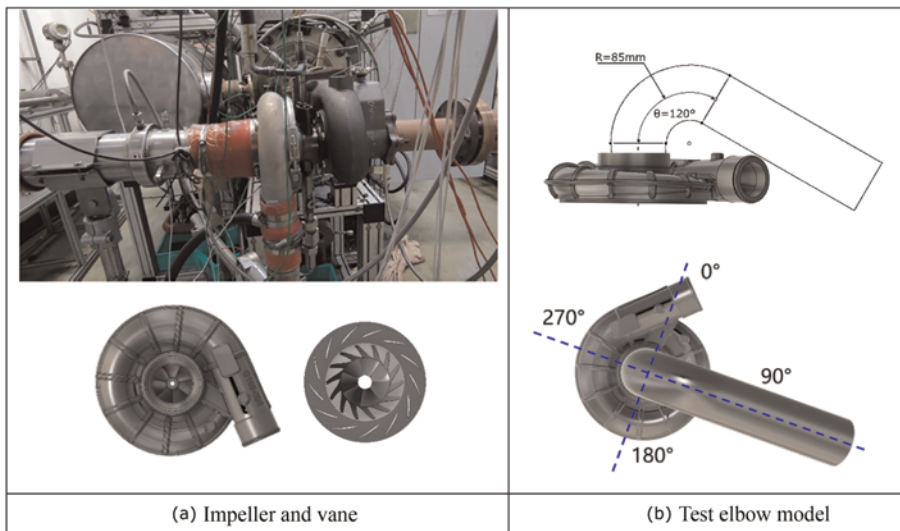
Figure 1. Centrifugal compressor and inlet elbow.

Table 1. Main geometries of the compressor.

Geometrical parameters	Values
Number of impeller blades	7
Number of diffuser blades	13
Bending angle of elbow	120deg
Bending radius of elbow	85mm
Inlet diameter of elbow	91.7mm
Inlet diameter of impeller	65.1mm
Outlet diameter of impeller	100mm
Outlet width of impeller	5.5mm

20

The centrifugal compressor has the characteristics of high single-stage pressure ratio and high efficiency. The operating speed range of this type of centrifugal compressor is between 87000 and 112000 RPM. Compressor speed when internal combustion engine is at optimum fuel economy is about 95500 RPM through experiment, which is selected in simulation study as rotating speed. The outlet pipe adopts straight shape in order to minimize the influence of outlet distortion effect as well as study coupling effect between volute and inlet bend more independently.

2.2 Numerical method and validations

In order to better study the performance and structural details of internal flow field of vaned diffuser compressor with inlet elbow, it is very necessary to use three-dimensional steady CFD simulation techniques. The three-dimensional fluid simulation software adopted in this paper is ANSYS-CFX. The model flow field needs to be meshed before simulation by different domains. The flow domains of the centrifugal compressor are shown in Figure 2-a, which are divided into five parts: inlet bend, impeller, vaned diffuser, volute and outlet straight pipe. Among them, impeller and diffuser use structured grid and are completed by Ansys TurboGrid module. Near-wall surface with high flow velocity gradient is specially encrypted in order to guarantee a relatively small y+, as shown in Figure 2-b and 2-c, the first layer thickness can reach 2.5×10^{-5}m. The inlet bend, volute and outlet pipe are made of unstructured mesh, which is completed by Ansys Mesh module. After grid independence verification, total grid number of five parts reaches 7.73 million, among which the impeller grid number is 3.8 million and diffuser grid number is 3.2 million.
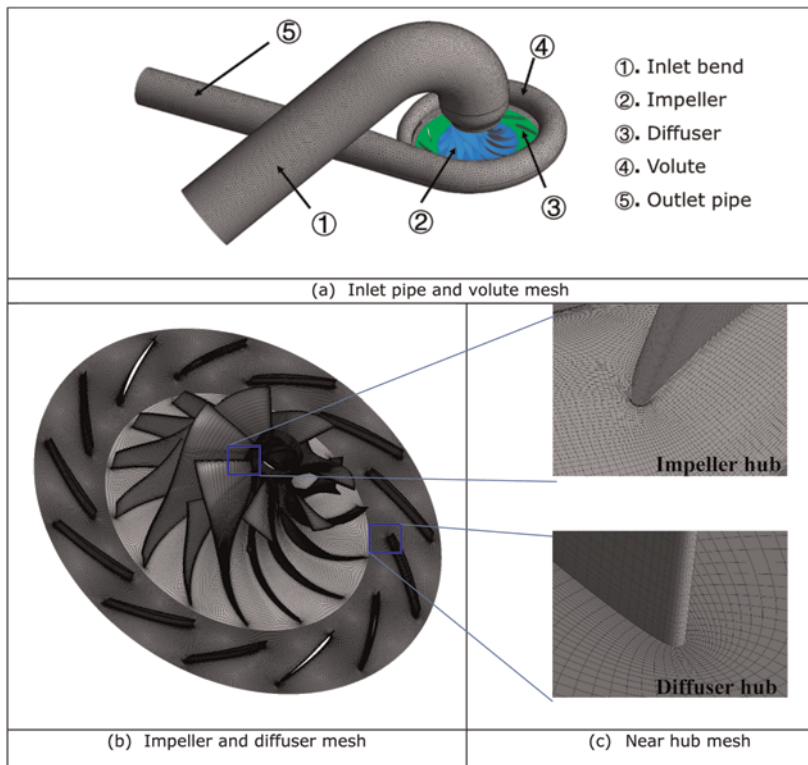
Figure 2. Computational domain and mesh.

Among the above five parts, the impeller is rotating while the rest are fixed. So, there is a problem of rotation and static conversion between grids. In this paper, Frozen Rotor method is adopted to deal with the interface of inlet – impeller and impeller – diffuser. Spalart-Allmaras turbulence model (S-A model), which is a one equation model, has high calculation accuracy for free shear turbulence, attached boundary layer turbulence and moderately separated turbulence flow, which can meet the requirements of engineering calculation accuracy. Meanwhile, it is faster than two-dimensional model, therefore it has been widely used in aerodynamics. In terms of inlet and outlet boundary, total pressure outlet is adopted in large flow condition because of the stable working condition. When flow rate is low and close to compressor stall, mass flow outlet is used to ensure convergence.

For purpose of ensuring reliability of simulation results, experimental results are compared with simulation results. Due to the confidentiality requirements of the enterprise, the pressure ratio and efficiency are processed in a normalized way which are shown in Figure 3. The results illustrate that pressure ratio and efficiency of simulation results fit well with the data measured by actual experiment. It is worth mentioning that the pressure ratio measured by simulation is slightly higher while the efficiency is perfectly matched with the experimental map line. This result proves the reliability and stability of simulation model and gives us confidence to use simulation data to predict actual compressor working conditions. Subsequent work will be carried out based on this model.
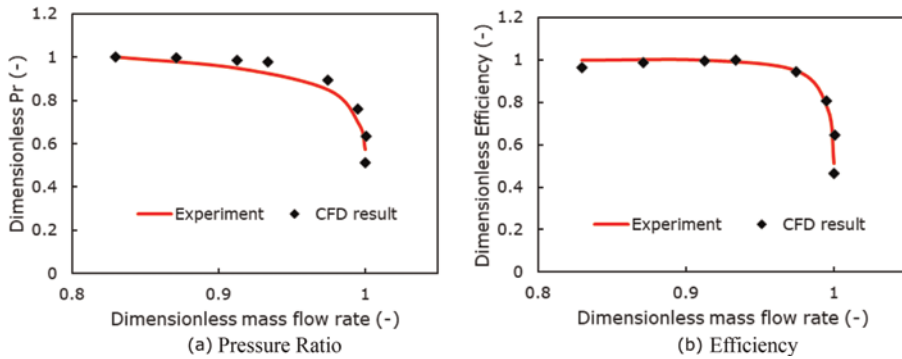
Figure 3. Experimental normalized PR and mass flow rate via CFD results.

3 PERFORMANCE OF INLET STRAIGHT PIPE AND DIFFERENT BENDING DIRECTIONS

Due to the compactness demand of internal combustion engine, compressor inlet pipe is usually not an ideal straight structure but may bend in any directions, which is bound to cause flow field distortion at impeller inlet. This distortion spreads downstream with incoming flow, and then affects flow field structure inside impeller and diffuser. At the same time, due to the influence of asymmetric structure of volute, the flow field distortion caused by volute will also propagate upstream, they two distortions are tightly coupled, resulting in changes in flow range, performance and pressure ratio of the compressor. However, the coupling mechanism between the two has not been studied in centrifugal compressor with vaned diffuser yet. Therefore, it is very necessary to analyze the performance variation mechanism of inlet elbow distortion and volute distortion of centrifugal compressor with vaned diffuser and the coupling mechanism of flow field.

3.1 Compressor performance at different inlet bending directions

In order to analyze the inlet elbow influence, three points, normalized mass flow rate at 0.871, 0.913 and 0.934, with the smallest difference between their simulation performance and actual compressor experimental parameters in straight inlet condition are selected. The flow conditions of inlet elbow are analyzed based on these three points. In order to check the application scope of elbow model, two points at relatively large mass flow rate with low pressure ratio are also simulated as auxiliary verification, and results were shown in Figure 4.

The variation curves of efficiency in different bending directions are analyzed, as shown in Figure 4 upper part. In order to more significantly display and analyze the differences between various angles, three relatively lower mass flow rate points are selected to make Figure 4 lower part.

As is shown in Figure 4, when normalized mass flow rate is greater than 0.913, the straight pipe is superior. When flow is less than or equal to 0.913, the performance of elbow in 0 degree direction and 180 degree is better than other cases, the 90 degree direction is similar to straight pipe. The performance of elbow in 270 degree direction, however, is much lower than others under any kind of flow case. For example, compared with 0 degree condition at normalized mass flow point 0.87, the 270 degree condition is 1.9% lower in normalized efficiency, and in position 0.913 the 270 degree condition is 2.1% lower.
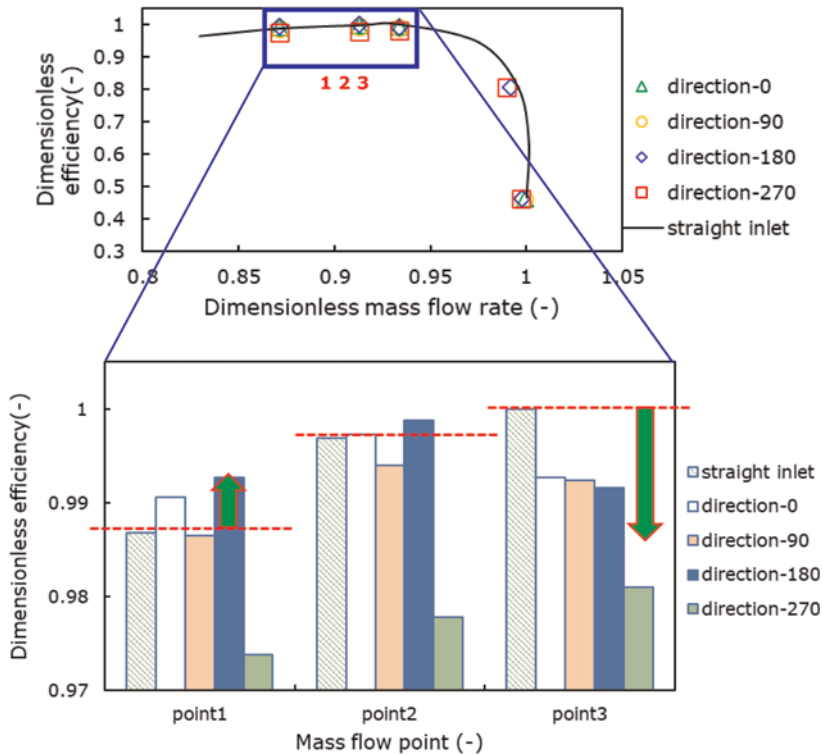
Figure 4. Efficiency in different bending directions.

In addition, there are also significant differences in compressor stability. Point 1 and point 2 at 90 degree and 270 degree working conditions have fluctuated in the steady-state simulation, while the remaining 0 degree, 180 degree and straight pipe converge very smoothly. In fact, mesh model and time step used between different bending directions are the same and just orientations are different.

To facilitate the analysis in next section, it is necessary to determine the unstable parts of the compressor. In fact, the instability of compressor can be judged by the following stability parameter (SP) indicators [18]:

$$SP_i = -\frac{1}{PR_i}\frac{\partial PR_i}{\partial m} \tag{1}$$

The overall condition for stability is:

$$SP_{tot} = SP_{comp} + SP_{diff} \tag{2}$$

Here the subscript tot means the whole compressor stability, comp and diff represent compressor and vaned diffuser respectively. The SP formula indicates compressor's stability, and the larger the value, the more stable it is. Parameters such as pressure ratio and flow rate in straight pipe are selected as input conditions. By inputting each parameter and calculating partial derivative, the stability parameter table of centrifugal compressor with vaned diffuser of this type can be obtained as shown in Figure 5. According to the data, the position of instability and the unstable components can be easily judged. It can be seen that fluctuation of diffuser's SP parameter is almost above the 0 line, and only the left-most point is a little below 0. It can be inferred that the diffuser is basically in stable working range, while the impeller is unstable near normalized mass flow rate of 0.84. This corresponds to the fact that straight pipe shown by black line in Figure 4 is still stable near normalized mass flow rate of 0.87. In fact, it does become difficult for straight pipe to converge near relative flow rate of 0.83, which will inevitably bring in error. This is also the reason why steady-state simulation has a little numerical difference with experimental value at this point. Unsteady simulation can be used in later study to expand calculation accuracy of these unsteady points in order to obtain more reliable calculation results.
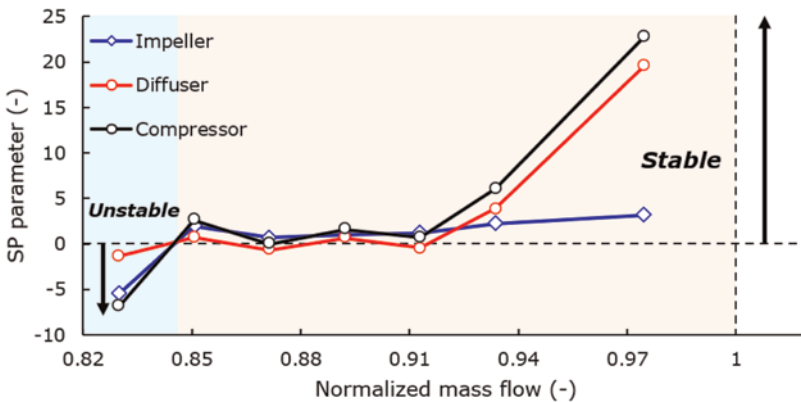
Figure 5. SP for vaned centrifugal compressor.

3.2 Coupling mechanism

According to the SP parameter in the previous section, it can be found that the impeller firstly becomes unstable when the mass flow is small. In this section, the causes of impeller instability are analyzed from the perspective of flow field. The working conditions under different bending directions are also compared.

The volute of compressor is generally designed according to the optimal performance point, thus at the optimal performance, the change in cross-sectional area of volute is exactly consistent with the flow increment it can withstand. However, this is not the case at lower mass flow point and higher mass flow conditions far from optimal performance. In the case of high mass flow, the mass flow increment is greater than the ideal design load of volute. Leading to the condition that the volute is equivalent to a gradually shrinking nozzle. The static pressure of volute decreases gradually from volute tongue along circumference. However, the lower mass flow condition is exactly the opposite, the flow increment is smaller than the incremental change in cross-sectional area of volute, which makes the volute equal to a gradually expanding nozzle, and static pressure increases gradually from the volute tongue to the outlet of volute in circumferential direction. This is also verified by the section pressure distribution in Figure 6, which takes the flow field with a normalized mass flow rate of 0.87 as the analysis object. The flow field analyzed below is also based on the small flow point of 0.87. In a clockwise sequence, eight volute sections as shown in Figure 6-a are placed clockwise starting from the volute tongue, and the average static pressure distribution on the obtained sections is shown in Figure 6-b. It can be seen that compared with ideal pressure distribution, there is an obvious area of static pressure uplift, namely section 3 to section 6. The corresponding circumferential degree ranges from $90°$ to $225°$. In this case, although the diffuser as a whole does not become unstable, flow separation phenomenon still occurs in some areas. As shown in Figure 6-c, large separation vorticity is generated in the blade of the diffuser with a blade near $180°$ while the air flow is very smooth at Point 2. The two different phenomena are mainly caused by the change of pressure in diffuser outlet. The diffuser outlet pressure is relatively constant when volute pressure remains uniform, ensuring that the pressure side (PS) and suction side (SS) in the vaned diffuser are in normal design state, as shown in Figure 6-f (point 2). When the pressure inside the volute has the divergent nozzle effect caused by small mass flow, the outlet pressure of diffuser tends to increase circumferentially, resulting in a large pressure increase at original suction side, and even resulting in the phenomenon that the pressure at suction side is higher than pressure side as shown in Figure 6-e. The positions of suction side and pressure side are switched and unloaded, and fluid cannot cling to the blade. Then flow separation occurs.

(a) Location of volute cross section

(b) Normalized static pressure of volute

(c) Separation vortex near cross section 5

(d) Smooth flow near cross section 7

(e) Static pressure near cross section 5

(f) Static pressure near cross section 7
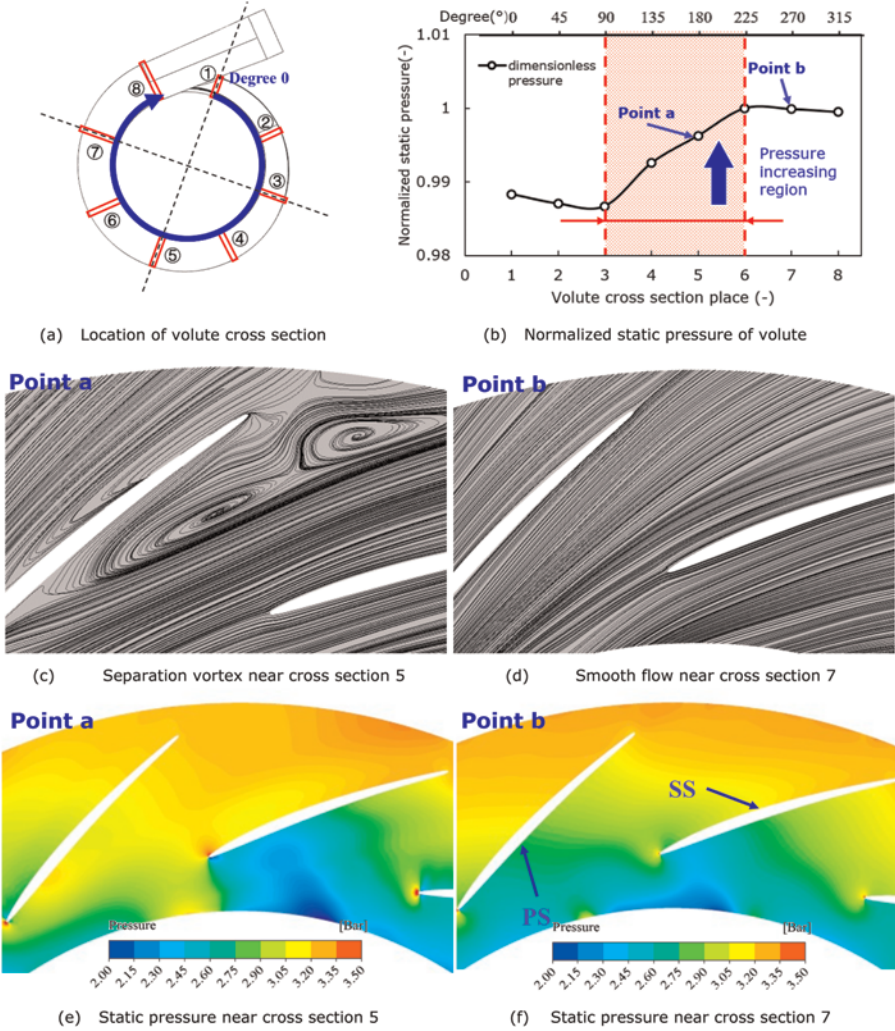
Figure 6. Distortion area of volute.

It is well known that the compressor efficiency is closely related to irreversible flow loss. This key indicator can be quantitatively analyzed by the entropy generation rate, which is a good way to measure the heat loss and the viscous dissipation.

The entropy generation is expressed by the thermodynamic parameters of the inlet and outlet of different components:

$$\Delta S_I = m\left(c_p \ln\left(\frac{T_2}{T_1}\right) - R\ln\left(\frac{P_2}{P_1}\right)\right) \tag{3}$$

26

And the parameters are made with normalized processing. As can be seen from Figure 7, the straight inlet pipe and inlet elbow with bending direction of 180 degree have small entropy generation rate. The total entropy generation of 270 degree is the largest, 0 degree and 90 degree cases have the generation rate between maximum and minimum. In terms of the constituent structure of entropy generation, the main parts are impeller, vaned diffuser and volute, and the entropy generation in both inlet pipe and outlet pipe are small. Due to the existence of inlet elbow, the entropy generated by inlet elbow is greater than that in straight pipe section, and the partial distortion will continue to be transmitted downstream. The impeller region occupies a dominant position of entropy increase, among which, when the inlet bending direction is 270 degree, the entropy increase in impeller is much larger than other cases, indicating that the internal flow field is rapidly deteriorating at this time.
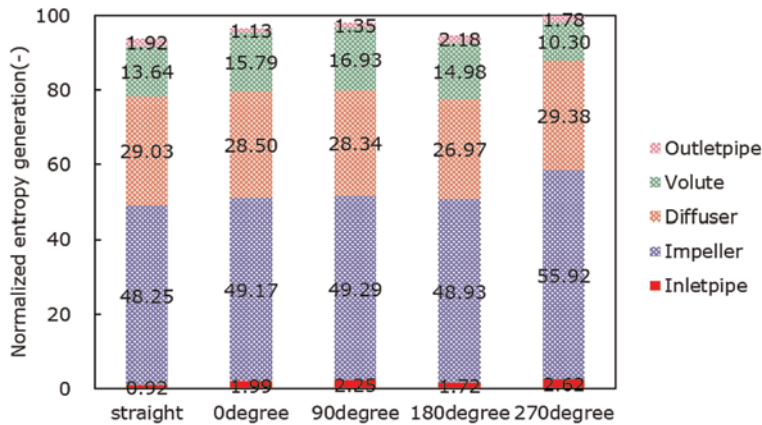
Figure 7. Static entropy increase in different parts.

In addition, the distortion caused by volute can also be displayed through the pressure distribution at the inlet of impeller, as shown in the left half of Figure 8. It can be seen from the figure that the flow field at the inlet of the impeller distributes relatively evenly in the circumferential direction, but the static pressure increases at opposite angle to the volute tongue direction. After inlet elbow is applied, the pressure distribution at inlet of the impeller is obviously different, as shown in the right half of Figure 8. The dual vortices caused by elbow can be clearly observed, which are located in the blue area with low static pressure. At bending direction of 180 degree, the strength of the dual vortices are obviously weakened and become different sizes. In other three bending angles, strength of the two vortices is similar. After the elbow is applied, the region of high static pressure is located on the other side of the dual vortex as a whole. However, due to the influence of the pressure change caused by the circumferential distortion of volute, the region of high static pressure at 0° and 270° is obviously expanded. But the phase is off by about 30°∼ 90°. It is worth mentioning that although the volute and inlet bend bring some parts of the impeller inlet static pressure increase, the mechanism is different. The volute increases inlet static pressure mainly because the volute pressure distribution leads to increase of inverse pressure gradient. The static pressure of the inlet bend is increased because of the stagnation effect caused by the bend.
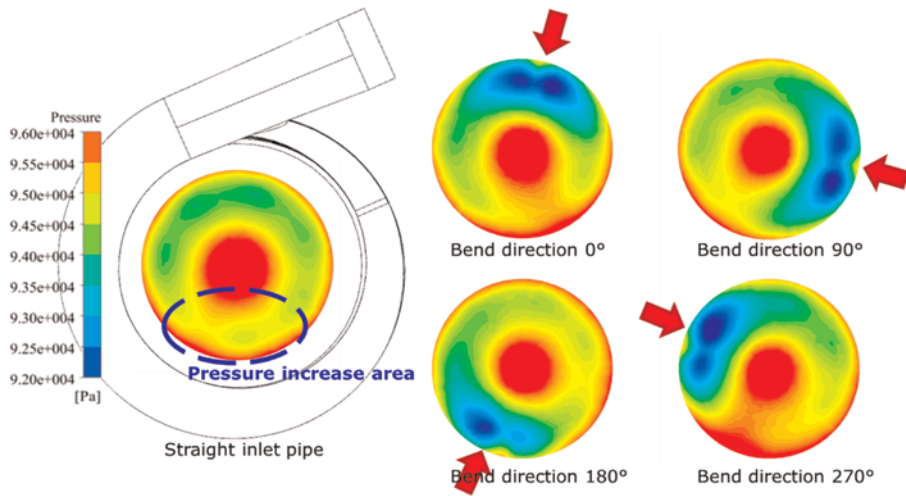
Figure 8. Impeller inlet pressure distortion.

Therefore, it is necessary to further explore the relationship between distortion caused by inlet and flow field distortion of diffuser. Figure 9 shows the comparison between straight pipe inlet and bending direction of 0 degree,180 degree and 270 degree. The counter at inlet of impeller is static pressure while the counter at constant span 0.9 in impeller and diffuser domain are set to Mach counter. The two different counters are distinguished by a black circle. Figure 9-a compares straight pipe inlet and inlet at bending direction of 180 degree which has the maximum efficiency. In the straight pipe condition, the high static pressure area of inlet and diffuser distortion position are at the same angle. In condition where bending direction is 180°, there is still a low Mach number area inside diffuser. However, the low Mach number area is located in different position with the straight one, and the low static pressure region at impeller inlet counteract the origin high pressure position. In Figure 9-b, the expansion of the high static pressure area appears at inlet of the impeller in both 0 degree and 270 degree inlet bending direction. Due to the phase difference, when the bending direction of inlet elbow is 0 degree, the area caused by the circumferential distortion of the volute is "exactly" avoided. However, when the bending direction of the inlet elbow is 270 degree, the superposition of the distortion is realized, which leads to great decrease of efficiency and advance of surge.

(a) Cases of straight inlet and bending direction 180°

(b) Cases of bending direction 0°and bending direction 270°
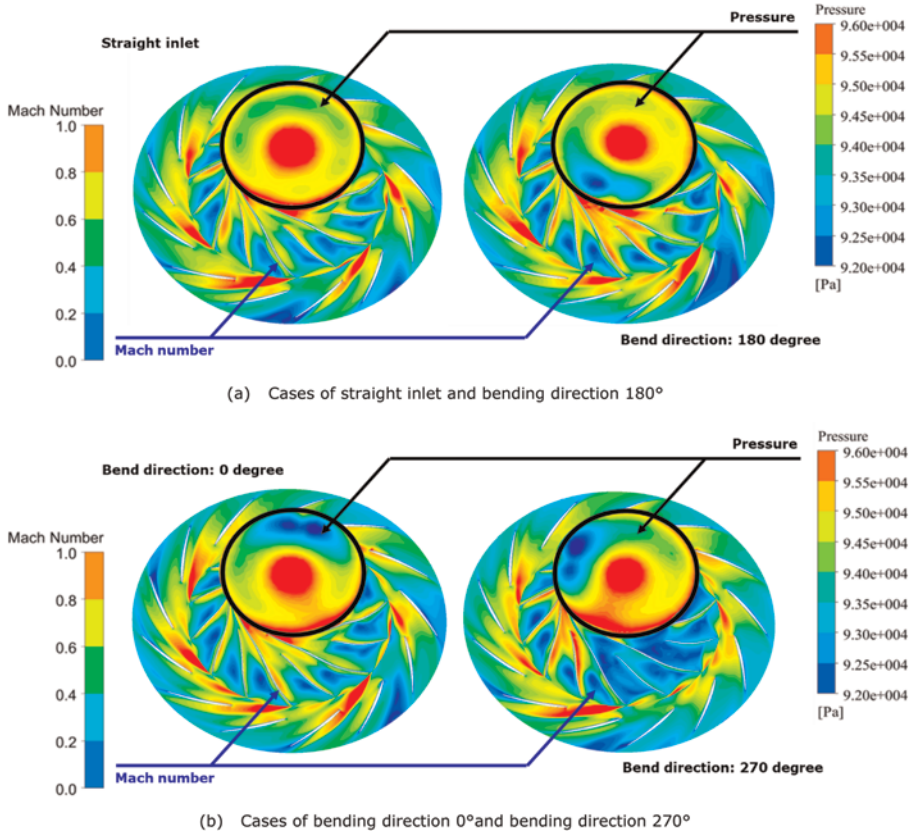
Figure 9. Relationship between inlet pressure distortion and vaned diffuser distortion.

The flow field inside the impeller and diffuser is further analyzed. As shown in Figure 10-a, the flow field inside the impeller is relatively stable when the inlet is a straight pipe section, and no obvious stall phenomenon or large eddy current mass is observed. The low mach number area inside the diffuser is mainly concentrated around $120°$ to $180°$, and the diverting field in the rest parts is relatively stable. When the inlet bending direction is $180°$, as shown in Figure 10-b, the low mach number area inside the diffuser changes to $60°$ to $120°$, and the flow field inside the impeller and diffuser remains stable. When the bending direction is $270°$, as shown in Figure 10-c, the distortion position at the inlet of the impeller overlaps with the circumferential distortion position of the volute, and obvious stall phenomenon appears inside the impeller, and the stall channel is not only one, but extends to three channels counterclockwise, making all the flows in the three channels unstable, resulting in a substantial decrease in efficiency. That's why the entropy inside the impeller generats so much at 270 degree.
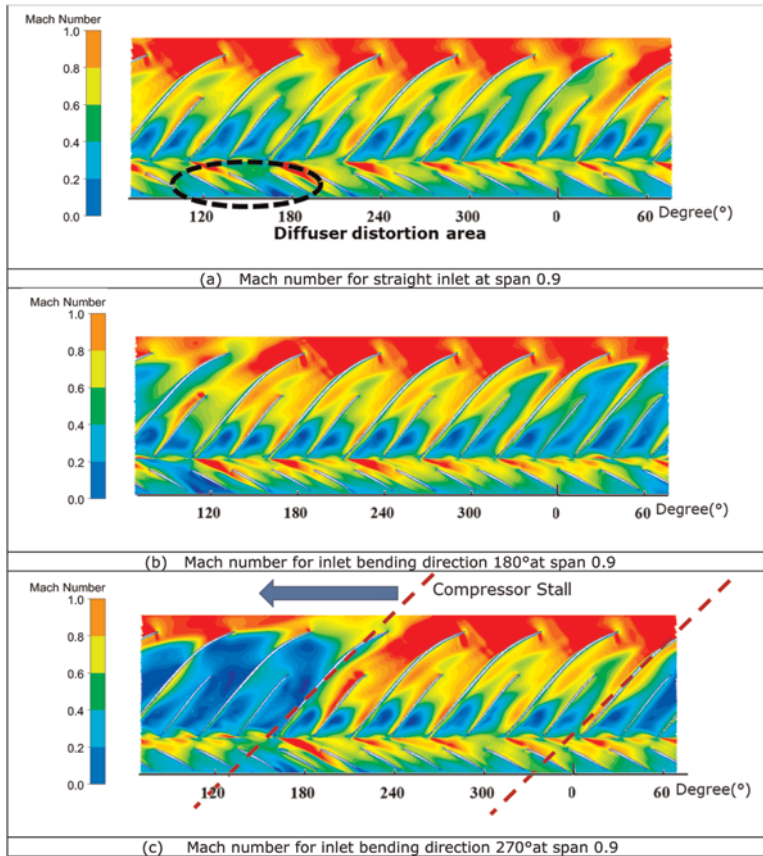
Figure 10. Mach number in straight inlet and bending direction 180° & 270°.

When the bending direction is 270°, the distortion position of inlet is exactly consistent with the distortion position of straight pipe inlet, resulting in the effect of distortion superposition, which makes the area with negative flow angle difference of inlet at 270° much larger than the other three bending directions. At other angles, the inlet distortion position is different from circumferential distortion position of volute, which ensures the stability of flow field inside impeller.

The impeller stall is mainly caused by inlet flow angle. With decrease of incidence angle, there is no longer enough air sticking to the blade surface, and the boundary layer begins to separate prematurely from blade surface.

As has been mentioned above, the volute distortion will not only affect the inside of vaned diffuser, but also affect the upstream of impeller blade due to the change of pressure. Without the influence of volute, the angle of impeller inlet will be relatively periodic and uniform. However, due to the existence of volute, the flow angle of the leading edge of impeller inlet will also change. As shown in Figure 11, it is the flow angle of inlet at the height of 0.9 blade. At this time, it can be judged that the impeller and diffuser are in a stable working range through SP diagram. The upper part of Figure 11-a shows the flow angle at 0.9 blade height in the working condition of inlet straight pipe.

30

Due to the distortion caused by volute, the inlet angle decreases at 60° to 240° in circumferential direction, making it easier for instability to occur. But most places of inlet flow angle are above the incidence angle shown by red dotted line. However, the working condition with inlet bending direction of 270 degree is completely different. Due to the superposition of the volute circumferential distortion and the inlet bend area, the flow angle near 180 degree is greatly reduced, and the flow angle is even less than the blade incidence angle as shown in lower part of Figure 11-a, thus causing the compressor instability. The same conditions at 0.9 blade height are calculated respectively in bending directions of 0 degree, 90 degree, 180 degree and 270 degree and are shown in Figure 11-b. The figure can reflect difference in direction and magnitude between inlet elbow and straight inlet. It can be seen from figure that the position of airflow angle distortion caused by four inlet elbows of 0 degree, 90 degree, 180 degree and 270 degree is totally different. The bending direction of 180 degree has the lowest distortion even less than straight pipe inlet.
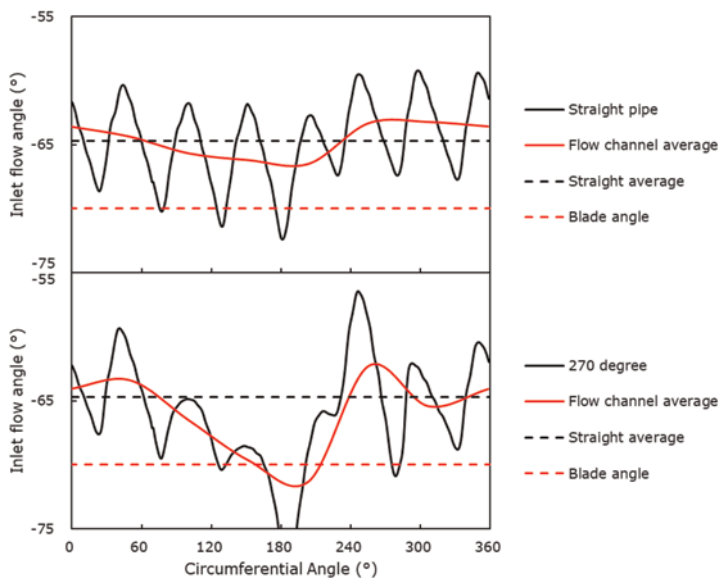
(a) Comparison of flow angle in straight pipe and bend direction 270 degree
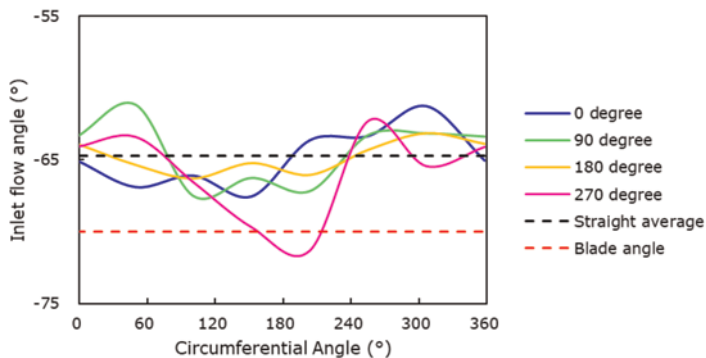
(b) Comparison of flow passage average flow angle in 4 bending directions

Figure 11. Impeller inlet flow angle at span 0.9.

Figure 12 further illustrates a sketch of the interpretation of the flow interaction between the elbow and the volute. The distortion caused by the volute is to reduce the incidence angle at entrance, as shown by black line.

The distortion caused by inlet bend includes both the area of incidence angle increasing and decreasing area, which are shown by dashed lines in the figure. Due to different orientations of inlet bend, the distortion caused by inlet bend also has phase difference. The red and blue dashed lines in the figure represent two typical inlet distortions with phase change due to different bent directions.

When the area of the inlet distortion reduces incidence angle coincides with volute distortion (as shown in solid red line), the distortion will be greatly enhanced. On the contrary, if the area where inlet distortion increases the incidence coincides with the volute distortion (as shown in solid blue line), the distortion will weaken and the flow field will be homogenized.
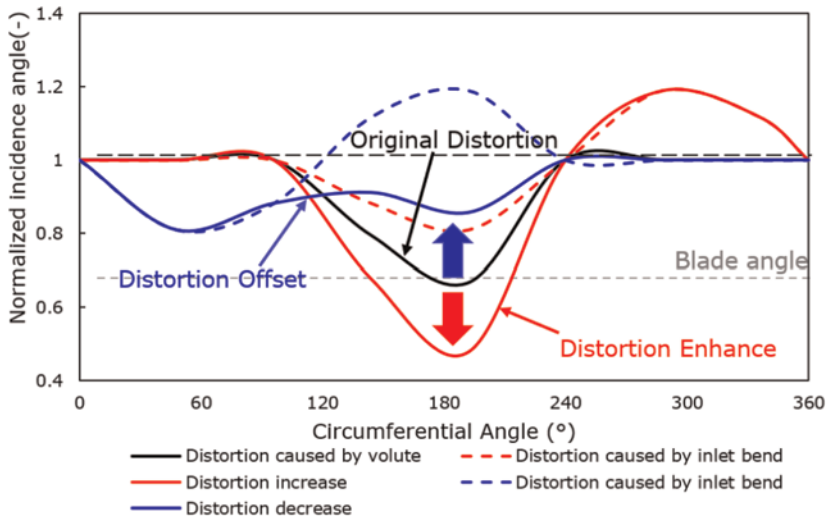
Figure 12. Practical coupling effect and theoretical mechanism.

4   CONCLUSIONS

The vaned centrifugal compressor has become an important part of the internal combustion engine supercharger because of its high efficiency and high single stage pressure ratio. In this paper, the compressor performance characteristics and flow mechanism of centrifugal compressor with inlet elbow in compact structure are studied, and the coupling mechanism of inlet distortion and volute distortion is analyzed. Three main conclusions are drawn as following:

1. Inlet elbow has a great influence on the efficiency of centrifugal compressor with vaned diffuser, and it varies with different bending directions. Specifically, the efficiency in small mass flow situation is much lower than straight tube when the angle is 270° while at 180° the efficiency will be higher than straight pipe.
2. According to the entropy generation method, the specific loss domain is analyzed. Compared with straight pipe inlet in small mass flow situation, the inlet bend at 180 degree will lead to a decrease in entropy generation in vaned diffuser, while the inlet

bend at 270 degree significantly increases the entropy generation in impeller, indicating that the internal flow field is rapidly deteriorating here.
3. The coupling relationship between the flow field distortion caused by inlet elbow and the circumferential distortion caused by volute is studied in small mass flow situation. The research shows that the existence of volute will lead to a distortion of impeller and result in high static pressure area, which is located in the opposite direction of the volute tongue. When the area of high static pressure generated by volute overlaps the area of high static pressure generated by the stagnation effect of inlet bend, the incidence angle is greatly reduced, resulting in deterioration of performance and advance of surge, as in the 270 degree inlet bend case in this paper. When the large flow and low static pressure area caused by inlet bend overlaps the high static pressure area caused by volute, the inlet flow angle will be more uniform and the performance will be improved.

According to the results of this research, it is confirmed that the configuration of the inlet pipe has notable influence on the performance of centrifugal compressor. The influence is resulted from the interaction between the flow distortion induced by volute and the inlet pipe. However, these results are based on the steady simulation. Further simulation will be carried out in an unsteady way for follow-up research and get more accurate relationships between the flow field distortion caused by inlet elbow and the circumferential distortion caused by volute.

NOMENCLATURES

CFD	Computational Fluid Dynamic	
C_p	Specific heat	J/(kg·°C)
m	Mass flow rate	kg/s
P	Pressure	Pa
PR	Pressure ratio	-
SS	Suction side	
PS	Pressure side	
SP	Stability parameter	-
T	Temperature	K
ΔS	Entropy generation	J/(kg·K)
Subscripts		
comp	Compressor	
diff	Vaned diffuser	
tot	Total	

REFERENCES

[1] Came, P. M., & Robinson, C. J. (1998). Centrifugal Compressor Design. Proceedings of the Institution of Mechanical Engineers, Part C: *Journal of Mechanical Engineering Science*, 213(2), 139–155.

[2] Krain, H. (2005). Review of Centrifugal Compressor's Application and Development. *J. Turbomach.*, 127(1), 25–34.

[3] Ariga, I., Kasai, N., Masuda, S., Watanabe, Y., & Watanabe, I. (1983). *The Effect of Inlet Distortion on the Performance Characteristics of A Centrifugal Compressor*.

[4] Naseri, A., Boroomand, M., & Sammak, S. (2016). Numerical Investigation of Effect of Inlet Swirl and Total-Pressure Distortion on Performance and Stability of an Axial Transonic Compressor. *Journal of Thermal Science*, 25(6), 501–510.

[5] Hah, C., Rabe, D. C., Sullivan, T. J., & Wadia, A. R. (1998). *Effects of Inlet Distortion on the Flow Field in a Transonic Compressor Rotor*.

[6] Kim, Y., Engeda, A., Aungier, R., & Amineni, N. (2002). A Centrifugal Compressor Stage With Wide Flow Range Vaned Diffusers And Different Inlet Configurations. Proceedings of the Institution of Mechanical Engineers, Part A: *Journal of Power and Energy*, 216(4), 307–320.

[7] Yamada, K., Furukawa, M., Arai, H., & Ito, S. (2019, June). Effects of Upstream Bend on Aerodynamic Performance of a Transonic Centrifugal Compressor. In *Turbo Expo: Power for Land, Sea, and Air* (Vol. 58561, p. V02BT44A014). American Society of Mechanical Engineers.

[8] Engeda, A., Kim, Y., Aungier, R., & Direnzi, G. (2003). The Inlet Flow Structure of A Centrifugal Compressor Stage and Its Influence on the Compressor Performance. *J. Fluids Eng.*, 125(5), 779–785.

[9] Van den Braembussche, R. A., & Hände, B. M. (1990). *Experimental and Theoretical Study of the Swirling Flow in Centrifugal Compressor Volutes*.

[10] Ceyrowsky, T., Hildebrandt, A., & Schwarze, R. (2018, June). Numerical Investigation of the Circumferential Pressure Distortion Induced By A Centrifugal Compressor's external volute. In *Turbo Expo: Power for Land, Sea, and Air* (Vol. 51005, p. V02BT44A015). American Society of Mechanical Engineers.

[11] Zheng, X., Jin, L., & Tamaki, H. (2013). Influence of Volute Distortion on the Performance of Turbocharger Centrifugal Compressor with Vane Diffuser. *Science China Technological Sciences*, 56(11), 2778–2786.

[12] Hagelstein, D. H. K. V., Hillewaert, K., Van den Braembussche, R. A., Engeda, A., Keiper, R., & Rautenberg, M. (2000). Experimental and Numerical Investigation of the Flow in a Centrifugal Compressor Volute. *J. Turbomach.*, 122(1), 22–31.

[13] Niu, Z., Sun, Z., Wang, B., & Zheng, X. (2020, September). Effects of Non-Axisymmetric Volute on Rotating Stall in the Vaneless Diffuser of a Centrifugal Compressor. In *Turbo Expo: Power for Land, Sea, and Air* (Vol. 84102, p. V02ET 39A015). American Society of Mechanical Engineers.

[14] Frigne, P., & Van Den Braembussche, R. (1984). *Distinction Between Different Types of Impeller and Diffuser Rotating Stall In A Centrifugal Compressor With Vaneless Diffuser.*

[15] Wang, L., Yang, C., Zhao, B., Lao, D., Ma, C., & Li, D. (2013). The Change of the Inlet Geometry of a Centrifugal Compressor Stage and its Influence on the Compressor Performance. *Journal of Thermal Science*, 22(3), 197–208.

[16] Yang, C., Zhao, B., Ma, C. C., Lao, D., & Zhou, M. (2013, June). Effect of Different Geometrical Inlet Pipes on a High Speed Centrifugal Compressor. In *Turbo Expo: Power for Land, Sea, and Air* (Vol. 55249, p. V06CT40A004). American Society of Mechanical Engineers.

[17] Hou, H., Wang, L., Wang, R., & Yang, Y. (2017). Effects of Bending-torsional Duct-induced Swirl Distortion on Aerodynamic Performance of a Centrifugal Compressor. *Journal of Thermal Science*, 26(2), 97–106.

[18] Dean, R. C. (1974). The Fluid Dynamic Design of Advanced Centrifugal Compressors. Von Karman Inst. for Fluid Dyn. *Advanced Radial Compressors* 99 p (SEE N 79-22506 13–37).

Electrification/Driven

Taylor & Francis
Taylor & Francis Group
http://taylorandfrancis.com

Comparison of the transient performance of a motorsport ICE first fitted with an e-turbocharger and then with a conventional turbocharger with added P1-hybrid electric machine

O. Le Roux de Bretagne, M.F. Harrison

School of Aerospace, Transport and Manufacturing, Cranfield University, Bedfordshire, UK

ABSTRACT

This paper discusses ways of deploying electrical machines (EM) on a turbocharged internal combustion engine and assesses their energy effectiveness. Inspired by the 2026 Formula One^{TM} regulations, the simulation software AVL Boost^{TM} is used to investigate the use of an EM attached to the turbocharger rotor (eTC) and that of a powerful EM at the engine crankshaft (MGU-K). Both improve powertrain performance, with the 350kW MGU-K achieving the best transient performance despite its limited impact on the responsiveness of a non-eTC turbocharger (turbo lag), while the eTC yields the best engine efficiency control and is the most energy efficient solution.

1   INTRODUCTION

From fully the electric to the electric-hybrid vehicle, electric motors have already been used to power cars and race cars, nevertheless fully electric race cars do not yet have the energy capacity for extended distance racing at the speeds expected from elite racing series. Early 'push-to-pass' hybrid motorsport powertrains, such as KERS [1], have been replaced with 'torque-fill' architectures where the power output of the electric motor (EM) is sufficient to significantly enhance the acceleration of the vehicle at a range of road and internal combustion engine (ICE) speeds. However, electrical storage on such vehicles is limited by weight, and package considerations or by regulations meaning that the ICE and EM must work as an inter-dependent system in order to be competitive in a race.

In order to assess how ICE and EM combine best to improve race car acceleration, this paper examines two alternative uses of the EM. Firstly, on the end of the turbocharger (TC) rotor to minimise turbo lag and secondly as a P1 hybrid architecture [2] to torque-fill, namely propel the car using electric power when the engine does not produce enough torque to meet the driver's demand. The obvious combination of both e-turbo (eTC) and P1 hybrid are not included for brevity, but comments are offered on how the assessments reported here extend to those systems.

This paper is inspired by the publication of the proposed changes in Formula One^{TM} power unit technical regulations in 2026 [3]. Looking back to the 1980s, the first turbo era in Formula One^{TM} featured engines with conventional turbochargers which were air-limited by intake manifold pressure regulators and reliant on high-octane fuels. After regulations excluded turbocharged engines for several decades, turbocharging returned to Formula One^{TM} in 2014 [4] under a different form. The engine was now part of hybrid-powertrain alongside two motor-generator units (MGU), one linked to the

crankshaft of the engine (MGU-K – P1 position) and the second connected to the tur-bocharger (MGU-H) allowing for complex energy management. In addition, the 2014 regulations introduced a fuel mass flow limit which changed the engine design philo-sophy. Previously, efficiency was of secondary importance and if engine power output could be increased by using more fuel and could overcome the addition weight handicap caused by a bigger tank, the solution was viable. However, as the fuel flow is now lim-ited, engine designers must make the most out of the limited energy available which makes fuel conversion efficiency a primary target. Even if the engine geometry and power output will stay the same, 2026 will see several major changes, namely the switch to 100% sustainable fuel (thereby changing the combustion characteristics), a change in thermal/electric power balance by increased MGU-K power and reducing fuel flow limit, leading to reduced local tailpipe emissions, and the removal of the MGU-H.

The latter change is the inspiration for this study. By removing the MGU-H, the 2026 engine will feature a conventional turbocharger, not electrically assisted. In the 2014 regulations, the turbocharger rotor speed was controllable with the MGU-H and any imbalance between the compressor work requirements and turbine supply could be supported by this EM. Furthermore, any excess turbine work could be used to charge the electrical system. In 2026, the turbocharger rotor speed will only be a function of the exhaust enthalpy, turbocharger design and wastegate strategy, meaning that the engine will again be subject to turbo lag making rapid changes in power (load) demand challenging.

Turbo lag refers to the delay between driver's load demand and engine delivery [5]. Typically, when the engine is operated at part-throttle / part-load, exhaust enthalpy is low leading to a reduction in turbocharger rotor speed. As turbocharged engine power output relies on high intake boost pressure, when the driver suddenly demands max-imum torque, it takes time for the engine to increase exhaust enthalpy, speed up the turbine and to build up appropriate boost pressure in the intake manifold and hence increased engine performances. The longer the delay, the higher the turbo lag, with obvious impact on racing performance.

To reduce turbo lag as much as possible, the aim is to minimise the change in turbocharger rotor speed over time or at least to be able to speed up the turbocharger rotor rapidly. This phenomenon is very well known, and the literature proposes a range of solutions. These solutions can be classified in four different categories as shown in Table 1:

Table 1. Categorisation of turbo lag reduction solutions.

Category	Solutions	Description
Minimise turbo-charger moment of inertia	Reduce turbocharger rotor mass and size (inertia) (5), (6), (7)	Reduce turbocharger rotating dimensions and use of low-density material (ceramic for instance) to reduce the rotor moment of inertia
	Reduce turbocharger friction losses (5)	Modify turbocharger bearings to reduce friction loses
	Use of axial turbine (6)	Use axial turbine rather than radial to benefit from their inher-ent lower moment of inertia (only featured in research engines to date)

(*Continued*)

Table 1.   (*Continued*)

Category	Solutions	Description
	Turbochargers in parallel (5)	If the engine architecture allows it, use several turbochargers in parallel (for example one for each bank of a V-shaped engine) leading to smaller and more responsive turbocharges than if only one was used
Turbine aspect ratio	Reduce turbine aspect ratio (5), (8)	Reduce the capacity of the turbine to increase the pressure drop and thus the energy recovered providing that the turbine is not choked, and that the engine back-pressure does not exceed reasonable limits
	Variable turbine geometry (5), (8)	Modifying the inclination of turbine nozzle vanes to modify the effective turbine aspect ratio and improve the turbine efficiency over a range of operating conditions
	Twin-scroll or twin-entry turbine (9)	Use multi-entry turbine to make better use of the interacting pulse flow of the engine cylinders
	Multiple stage turbocharger (5)	Use several turbochargers in series, each adapted to different operating conditions
Increased exhaust enthalpy	Late combustion or Early exhaust valve opening (10)	Retard ignition or early exhaust gas release so that most of the fuel energy is not used for work production but is sent in the exhaust system as high-temperature gas
	Exhaust manifold fuel injection	Fuel injection in the exhaust manifold. Due to the very high temperature, the mixture ignites with the whole fuel energy dedicated to increase exhaust enthalpy (no work production)
	Mixture fuel enrichment	Reduce the mixture air/fuel ratio to increase exhaust enthalpy
	Appropriate exhaust pipes material and insulation	Reduce thermal inertia of exhaust manifold and reduce heat loss upstream of the turbine

Table 1. (*Continued*)

Category	Solutions	Description
External assist	Electrically assisted turbo-charged (8)	Control the turbocharger rotor speed with an electric motor
	Hydraulic assisted turbo-charged (7)	Control the turbocharger rotor speed using high pressure oil using hydraulic turbine and pump mounted on the turbocharger rotor
	Compressed air assist (5)	High-pressure air injected either in the compressor wheel, turbine wheel or exhaust manifold
	Reduce compressor load during gear changes and off-throttle operation	Deliberately reduce compressor aerodynamic load using upstream throttle valves and use compressor/turbine momentary imbalance to speed up the rotor

In addition to the above, and linked at least indirectly, are the turbocharger matching techniques commonly employed such as internal or external wastegates and pressure-release valves in the intake manifold.

However, several of the above technical solutions are not allowed under the published 2026 Formula One™ regulations, either because of the regulations (variable turbine geometry and e-turbo not permitted [3]) or engine philosophy as the engine is fuel-energy limited.

This paper is investigating how the use of an EM can help the engine to mitigate turbo lag effect.

2 ENGINE MODEL, SIMULATION SETTINGS AND PERFORMANCE INDICATOR

2.1 Engine model and simulation settings

The engine model used for this study has been developed using AVL Boost™, a 1D internal combustion engine simulation software. For this work, AVL Boost is used in transient mode, the engine state is computed cycle by cycle with a user-defined crank angle step for each cycle and the results reported are the average values of each parameter over the cycle. The model is based on the 2026 Formula One™ Power Unit Regulations published on the FIA website on the 16th of August 2022 [3].

The data used for the creation of the 2026 engine model comes from the Cranfield F1 Design Sprint, an extra-curricular project run every year by students of the Advanced Motorsport Engineering / Mechatronics MSc at Cranfield University. Advanced simulation is used to provide an independent assessment of the performance capabilities of current and future Formula One™ powertrains. The students receive no engine data from the industry and therefore remain free to talk about their learning openly. However, the simulated performance results are scrutinised by people within the industry and through successive rounds of presentation, comment and improvement, confidence in the authenticity of the models is generated. In addition, sensitivity

analyses have been conducted on the parameters which values have been estimated in the above manner to assess their impact on engine performance and be confident that any difference with industry-used values would not significantly change the conclusions drawn in this paper.

The main characteristics of the engine are summarized in Table 2 and the model initialisation is done using results from constant speed simulation:

Table 2. Engine model parameters.

Parameter	Unit	Value
Bore	mm	80
Stroke	mm	53.052
Number of cylinders	–	6
Engine moment of inertia	kg.m^2	0.034
Turbocharger moment of inertia	kg.m^2	6.55e-5

To run transient simulations, an energy consumer is required, in this case a vehicle representing Formula One^{TM} type car that isn't being limited by a lack of tyre grip. The settings of this notional vehicle can be found in Table 3:

Table 3. Vehicle model parameters.

Parameter	Unit	Value
Mass	kg	936
Rolling radius	mm	360
Vehicle load	N	578.5 + 0.76*V^2
Drivetrain moment of inertia	kg.m^2	0.1
Gear ratios	–	2.65/2.29/1.975/1.7/1.46/1.255/1.08/ 0.93:1
Final gear ratio	–	5.35:1
Gear upshift/downshift RPM	RPM	9000/12000
Gear shifting time	ms	12

The turbocharger moment of inertia has been estimated via a self-created CAD model of the rotor based on the dimensions of the Garrett G30-770-58mm turbocharger [11] using nickel for the rotor and turbine wheel and titanium for the compressor wheel. The engine and drivetrain moments of inertia have been determined using methods published in the literature [12].

The turbocharger is also equipped with wastegates whose opening is defined via an ECU model by a user-defined map which is a function of turbocharger rotor speed and compressor intake mass flow. The aim to is open the wastegate when the turbine is about to reach its maximum swallowing capacity to avoid excessive back-pressure build-up and to control turbocharger rotor speed.

The vehicle load considers simplified rolling resistance (not vehicle speed dependent) and drag [13].

As the model is set to run transient simulation, it is controlled via an ECU model. The ECU dictates the load demand and accordingly controls fuel injection, waste gate and throttle position, using user-defined maps.

To model a situation in which turbo lag occurs, the engine is kept at 10% load for 0.9s at the beginning of the simulation with an initial speed of 10,000 RPM in 3rd gear before switching from 10% to 100% in 0.1s and maintaining 100% for the rest of the simulation. The simulation is set to run for 250 engine cycles which is equivalent to around 2.9s (depending on how engine speed evolves through the length of the simulation).

The engine is first assessed without any electric assistance, meaning that turbo lag will not be deliberately compensated for to provide the baseline assessment case.

Then the engine will feature one electric motor either linked to the turbocharger (referred later as eTC case) or later to the engine crankshaft (MGU-K case). Details of both electric motors deployed in the models are shown in Tables 4 and 5 respectively.

Table 4. eTC electric motor model parameters.

Parameter	Unit	Value
Maximum power	kW	30
Peak electrical efficiency	–	0.98
Moment of inertia	kg.m^2	0.005
Mechanical connection mechanical efficiency	–	0.97
Mechanical connection gear ratio	–	1:1

Table 5. MGU-K model parameters.

Parameter	Unit	Value
Maximum power	kW	350
Maximum torque	Nm	500
Peak electrical efficiency	–	0.98
Moment of inertia	kg.m^2	0.042
Mechanical connection mechanical efficiency	–	0.97
Mechanical connection gear ratio	–	4:1

The MGU-K settings have been derived for the CTSM242 electric motor developed by Helix [14] while the eTC EM values are also derived from this motor.

For the eTC case, the EM power is controlled by a virtual ECU throughout the entire simulation with the target to keep the turbocharger rotor speed at 125,000 RPM whatever the engine load demand. The MGU-K is only activated during full-throttle operation and then at its maximum available power.

2.2 Performance indicators

Turbo lag can be a feature in two distinct scenarios: during acceleration following a period of part-throttle operation or during gear shifting at full load. This study only focuses on the first scenario which has the most impact of competitive advantage in motorsport as current Formula One[TM] shifting delay are very short and that race car lap times are mostly sensible to low-speed power variation.

Each of the three models used in this study (reference non eTC, eTC, MGU-K) will be assessed in terms of acceleration capability of the vehicle between the moment 100% load is demanded (t = 0.9s) and the first gear shift. For more accurate comparison, vehicle acceleration in g divided by energy consumed in MJ (electric + fuel), as defined below:

$$I_{performaces}\ (g/MJ) = \frac{\left(\frac{V_{gearshift}\ -\ V_{t=0.9}}{t_{gearshift}\ -\ 0.9}\right) * \frac{1}{g}}{\int_{t=0.9s}^{t_{gearshift}} \left(\frac{dE_{electric}\ +\ Q_{lvh}*dm_{fuel}}{dt}\right) * dt} \tag{1}$$

Considering the time taken to reach the first gearshift as the performance indicator was another possibility. Nevertheless, as the Formula One powertrain is energy limited, efficiently using the limited available energy is key, the fastest solution might not allow the car to reach the end of the race if it consumes too much energy, that is why the energy consumed by the powertrain is integrated into the performance indicator for this study. However, manoeuvre times are also considered.

3   SIMULATION RESULTS – HOW DOES AN ETC IMPROVE ENGINE EFFICIENCY?

As seen in Figure 1, for the first 0.9s of the simulation, the engine speed decreases because of the total engine friction losses (including pumping losses) being higher than the torque produced by the engine at 10% load. It can be noted that the engine speed drops less for the eTC than for the reference. This is one of the effects of the eTC being kept spinning at high rotor speed where the compressor provides the engine with more mass flow, leading to higher in-cylinder pressure and thus more power produce by the engine. This, of course, may need compensation from the driver using brakes or MGU-K to regulate vehicle speed.

After the 75th cycle, the engine speed starts increasing in response to the load change from 0 to 100% until reaching 12,000 RPM where the model simulates a gear change.
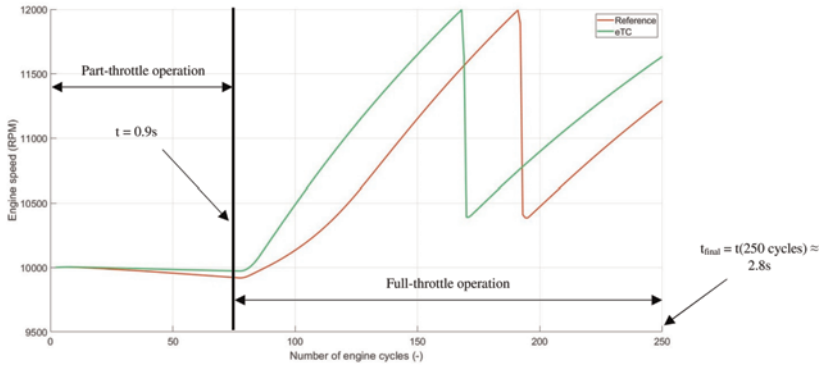
Figure 1. Engine speed evolution for the reference and eTC cases.

As previously mentioned, and as seen in Figure 2, the electric motor in the eTC case is controlled to keep the turbocharger rotor speed at a 125,000 RPM target (top graph – green line).

One can notice in Figure 2 that the compressor mass flow and boost pressure for the eTC case is very erratic at the beginning of the simulation suggesting that the compressor is operating around the surge line. This is due to the compressor spinning at high speed while the engine mass flow is limited by the throttle. To avoid this, the throttle angle could be increased to let more air flow through the compressor and the excess air could be recirculated using a dedicated valve.

On the other hand, looking at the red lines (top graph in Figure 2), it can be noted that turbo lag is being modelled realistically. All values are dropping during the first cycles as the turbine is supplied with very little exhaust enthalpy. Then, when full load is demanded (at the 75th cycle), it takes time to build up rotor speed and thus boost pressure and air mass flow.
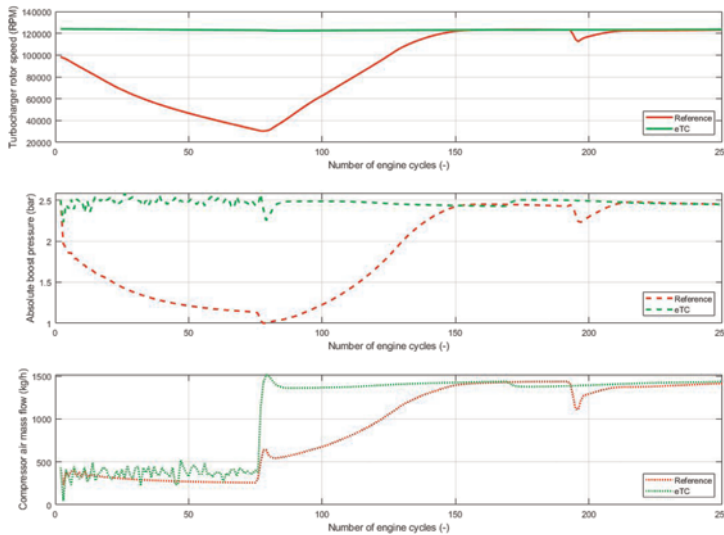
Figure 2. Reference vs eTC cases – Turbocharger rotor speed (top – solid lines), absolute boost pressure (middle – dashed lines) and compressor air mass flow (bottom – dotted lines).

As the turbocharger is made to spin at optimal speed during part-throttle operation in the eTC case, when the throttle is fully opened and 100% load is demanded, Figure 2 shows that the turbocharger is nearly immediately capable of supplying the engine with the requisite mass flow at the required pressure. As a result, the engine can maintain a higher air/fuel ratio than with a conventional turbocharger and reach higher efficiency.

In both the reference and the eTC cases, when 100% load is demanded, the model uses the maximum amount of fuel it is allowed to use under the published 2026 regulations (3000MJ/h above 10,500RPM [3]), but because the eTC engine operation yields higher efficiency, the engine can accelerate faster than in the reference case.

In addition to being useful when the engine 'tips in' to full load, the eTC also brings advantages during gear shifts. Fuel injection is cut during gear shift in these models meaning that the exhaust enthalpy briefly drops as there is no combustion to release fuel energy. The turbine is thus not able to recover sufficient energy and the turbocharger rotor slows down. Because of the higher moment of inertia of the eTC compared to a regular turbocharger, a smaller reduction in rotor speed is observed, i.e. less turbo lag during gear shift. Plus, the electric motor is capable of momentarily modify its power supply to ensure constant speed operation, as can be seen in Figure 2.

Nevertheless, it is important to highlight that current Formula One[TM] shifting time are very short, taken here to be 12 ms, compared to more conventional manual gearboxes meaning that turbo lag is less of a concern as the exhaust enthalpy is not reduced over a long period of time.

4   SIMULATION RESULTS – IMPACT OF THE MGU-K ON TRANSIENT BEHAVIOUR OF THE ENGINE AND TURBOCHARGER

As seen in Figure 3, the MGU-K case offers the shortest manoeuvre time despite a higher drop in engine speed than the eTC case for the opening segment of part throttle operation. In the MGU-K case, as the turbocharger is not electrically assisted, its speed will decrease during part-throttle operation due to low exhaust enthalpy (Figure 4) leading to lower air/fuel ratios and hence lower fuel conversion efficiency (Figure 5) and thus lower torque produced to counter total engine friction and pumping losses. As evident in Figures 4 and 5, the evolution of the turbocharger behaviour is very similar for the reference and MGU-K cases.
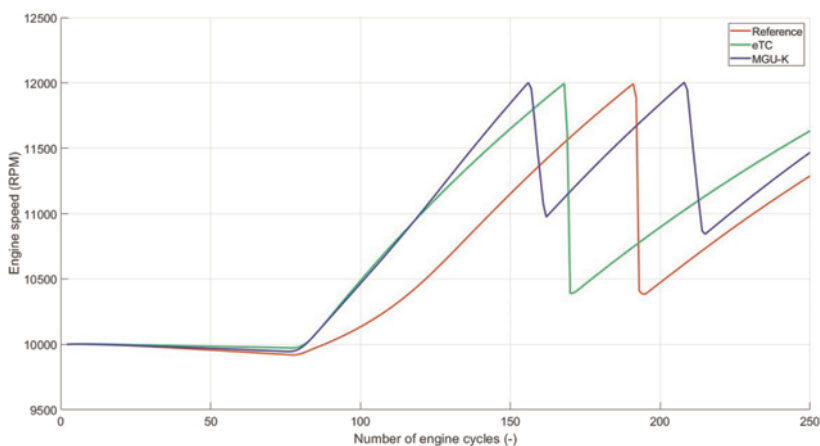

Figure 3. Reference vs eTC vs MGU-K cases – Engine speed evolution.

However, the engine speed drop in the MGU-K case is lower than that of the reference one because of the higher moment of inertia of the engine/electric motor assembly.

The higher inertia could also be a disadvantage for acceleration performance but thanks to the high MGU-K power (350 kW [3]), this configuration yields the faster manoeuvre time. The other big impact of the MGU-K added moment of inertia, as observable in Figure 3, is that the engine speed drop during gear shift is reduced compared to the other cases.

Inspecting Figure 4, it is interesting to note that the reference (red lines) and MGU-K (blue lines) cases are nearly identical when displaying the number of engine cycles as x-axis. However, as the engine is accelerating faster in the MGU-K case, it means that the engine cycle durations are shorter than that of the reference therefore in actuality the turbocharger rotor speed is increasing faster.
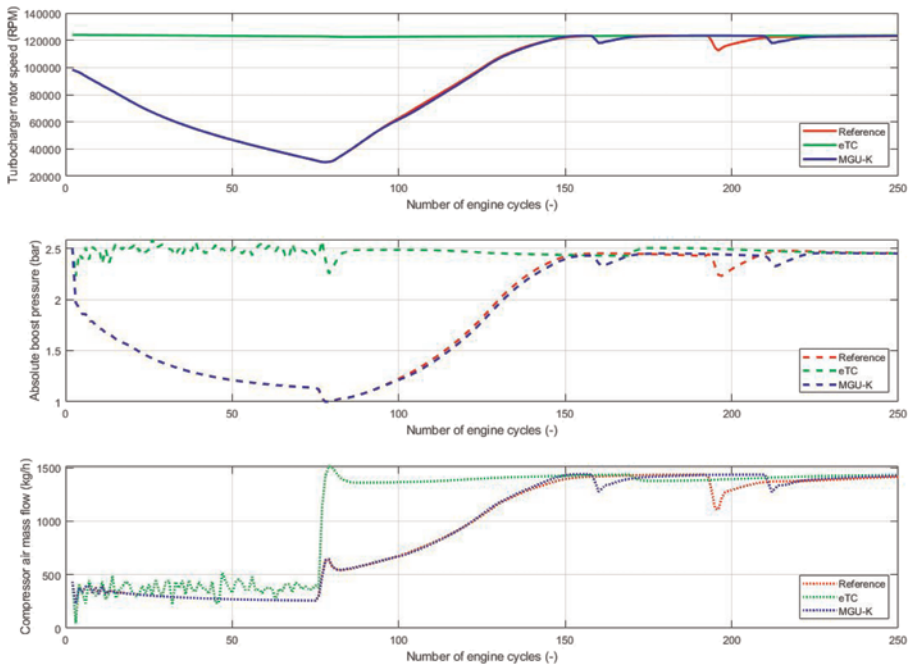
Figure 4. Reference vs eTC vs MGU-K cases – Turbocharger rotor speed (top – solid lines), absolute boost pressure (middle – dashed lines) and compressor air mass flow (bottom – dotted lines).

This can be explained by looking at Figure 5 on the right-hand side graph, the MGU-K case has the lowest excess air ratio values between 90 and 120 engines cycles. As seen in Figure 4, for these cycles, the turbocharger is spinning at the same speed for both the reference and MGU-K cases meaning that the boost pressures and compressor mass flow are also similar. However, as the engine is spinning faster in the MGU-K case due to the additional torque brought by the EM, the fuel mass flow increases at a faster rate than the air mass flow leading to momentarily lower air/fuel ratio and efficiency values (Figure 5).

However, because of this faster increase in fuel flow rate, the exhaust enthalpy is higher in the MGU-K case than that in the reference. And in consequence of the higher exhaust enthalpy, the turbine can achieve more work and thus spin the turbocharger rotor faster with the drawback of operating momentarily the engine at lower efficiency (Figure 5).

In the strategy chosen in this study, the fuel enrichment discussed above is not deliberate, it is a consequence of determining the fuel mass flow only based on the load demand and not considering compressor air mass flow supply. When the ECU instructs full load from the engine, the fuel supply is thus automatically set to the maximum. This strategy works very well with the eTC which is capable of immediately supplying the engine the right air mass flow and thus allows to operate at maximum efficiency most of the time as shown in Figure 5.
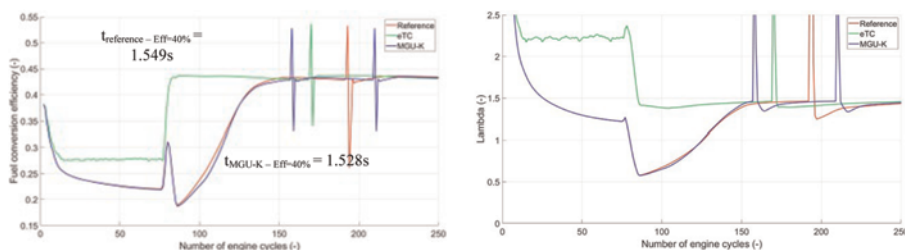
Figure 5. Reference vs eTC vs MGU-K cases – Fuel conversion efficiency and excess air ratio (lambda) evolution.

Even though it results in lower fuel conversion efficiency at the beginning of the acceleration, this strategy in the MGU-K case leads to shorter acceleration time for the turbocharger rotor, enabled by the higher exhaust enthalpy, which then allows for higher fuel conversion efficiencies to be subsequently achieved faster thanks to the turbocharger delivering high boost pressure and mass flow earlier. As shown in Figure 5, both the reference and MGU-K cases achieve 40% efficiency around the 130th engine cycle but in the time domain, because of the difference in engine speed evolution, the MGU-K achieves it faster than the reference case by 20ms (at t = 1.528s vs t = 1.549s).

Despite this behaviour, the MGU-K case remains less efficient than the eTC during this specific manoeuvre as seen in Figure 5. As the turbocharger rotor speed is kept constant, when 100% load is demanded, the eTC immediately provides the engine with the right air mass flow leading to lean operation and an efficiency advantage over more than 75 engine cycles compared to the MGU-K case.

5   DISCUSSION

As discussed, the MGU-K option is the fastest route to increased engine speed compared to the other cases (Figure 3) and this is obviously also the case when considering vehicle speed, see Figure 6, as the gear ratios are the same for all cases. The vehicle model used for these simulations assumes that the tyres can transmit all torque produced by the power unit without breaking traction. To test this assumption, the average acceleration for the MGU-K case from t = 0.9s to the end of the simulation is of 10.63 m/s^2 (1.08g) which is commonplace for current Formula One^{TM} cars and therefore the assumption is taken as robust.

Note in Figure 6 the very sudden increase in vehicle speed when the clutch is reengaging after a gear change for the MGU-K case. This behaviour is unrealistic and due to the way the clutch was modelled in AVL Boost^TM. The higher the moment of inertia, the bigger the step, explaining why this phenomenon is particularly visible for the MGU-K case and not the two others. But, because the period of interest for this study stops right before the gear change, this phenomenon does not influence the results presented here.

Regarding powertrain performance, because of the difference in power between the electric motor of the eTC and the MGU-K, the vehicle performance comparison can be biased. As visible in Figure 6 (dashed lines), the difference between the MGU-K and the eTC's EM power is very large with respective peak power of 350kW and 7.7kW. Table 6 shows how much energy is consumed in each case and the manoeuvre time.

For the eTC case, keeping the turbocharger rotor speed constant during the part throttle operation is a fundamental control goal so, in Table 6, the electric energy used in this period is also accounted whereas for the MGU-K and for fuel energy, only the period between full load demand (t = 0.9s) and the first gear shift is considered.

Table 6. Reference vs eTC vs MGU-K cases – Energy consumption during acceleration.

Case	Time between full load demand and first gear shift (s)	Fuel energy (kJ)	Electric energy (kJ)	Total energy (kJ)
Reference	1.293	1,020	0	1,020
eTC	1.019	799	10.8	809.8
MGU-K	0.896	696	291.7	987.7

Importantly, even though it is the fastest solution, the MGU-K case also consumes more energy than the eTC which a consequence of the very high-power output of the MGU-K.

The reference case is only relying on fuel to accelerate the engine and because of the initial drop in air/fuel ratio and efficiency, it requires the most time and total energy to reach 12,000 RPM. It must also be highlighted that at t = 0.9s, this is the case for which the engine speed is the lowest, so the delta in engine speed is greater than for the other cases.
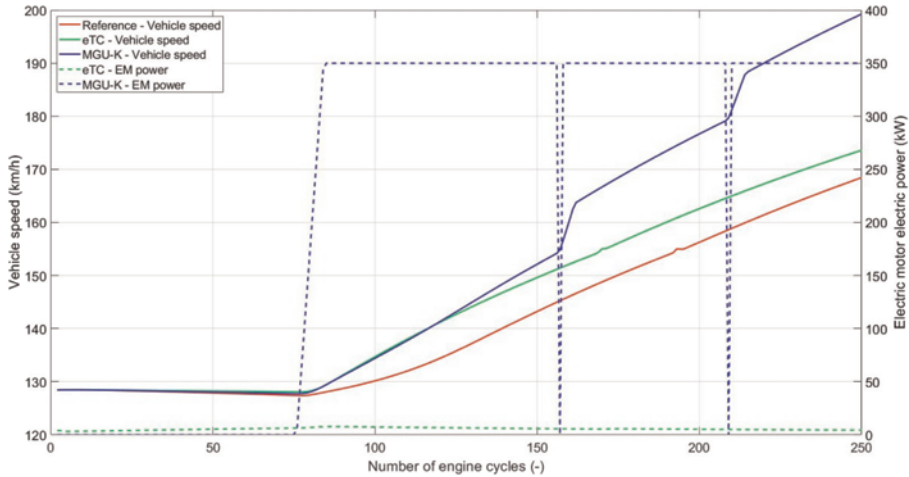
Figure 6. Reference vs eTC vs MGU-K cases – Vehicle speed (solid lines) and electric motor power (dashed lines) evolutions.

For the eTC case, the fuel energy is the only source of propulsion for the vehicle with the electric energy being solely used to control the turbocharger speed. However, thanks to the constant speed control regime, the fuel energy is more efficiently converted into work as demonstrated in Figure 5, leading to lower manoeuvre time compared to the reference case. However, even though the eTC case requires more fuel energy than the MGU-K case, the huge difference in electrical energy consumption must be highlighted, the MGU-K requiring nearly thirty times more electrical energy than the eTC for a 0.12s gain in manoeuvre time.

In addition, the 2026 Formula One™ Power Unit Regulations [3] states that a maximum of 9MJ can be recovered each lap and that the difference between the maximum and the minimum state of charge of the battery cannot be greater than 4MJ at any time the car is on track meaning that the vehicle can deploy a maximum of 13MJ for a given lap. In the general and simplified case where the acceleration manoeuvre studied in this paper is repeated on subsequent segments of the track, the MGU-K can only operate for 39.9s within the 13MJ limit against 1226.6s for the eTC before consuming all the energy available for a lap (considering the data in Table 6). Or put another way, the MGU-K manoeuvre can be undertaken around a dozen times.

As defined in section **2.2**, the performance indicators have been calculated for each case and are shown in Figure 7. The performance of the reference case is much lower than the two others showing how impacting turbo lag is on vehicle performance.

The performance of the eTC and MGU-K cases are very close. However, using the vehicle acceleration effectiveness indicator (Equation 1), the eTC solution makes better use of the energy. Even when accounting for the energy required to keep the turbo-charger spinning during the part-throttle operation, the fact that the engine efficiency is kept high any time during full load demand makes a big difference, allowing the powertrain to accelerate the car only using a small amount of electric energy and making the most of the available fuel energy.
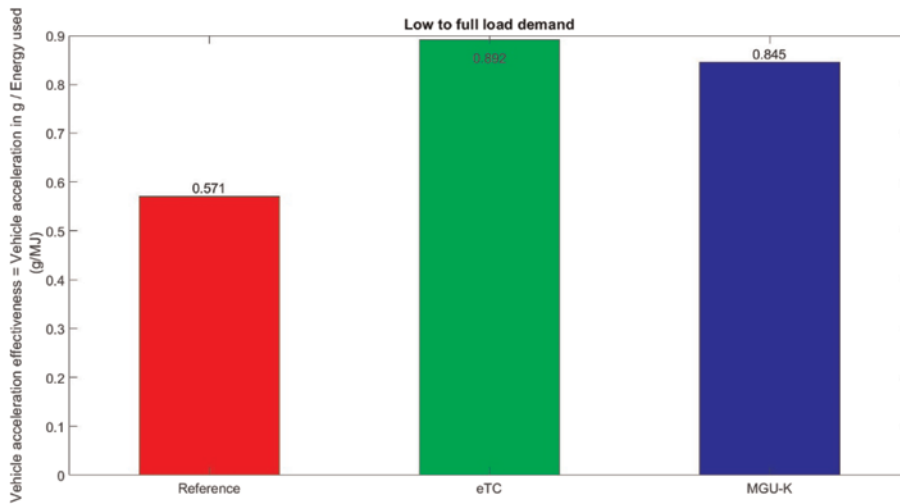
51

Figure 7. Energy normalised performance indicators.

6   CONCLUSIONS

The simulations reported here demonstrate that coupling a single electric motor to a turbocharged internal combustion engine, either by connecting it to the crankshaft or to the turbocharger rotor, helps to improve the transient behaviour of the powertrain and vehicle and more importantly for motorsport applications, enhances vehicle acceleration performance. The reference case, which does not feature any electric motor, is subject to turbo lag without any compensation and yields the highest time and total energy consumption for the sudden acceleration manoeuvre studied.

The electrically assisted turbocharger (eTC) enables the direct control of the rotating speed of the turbocharger rotor independently of the conditions at the turbine and thus to effectively eliminate turbo lag. As demonstrated in this study, this method is very effective as it maintains air/fuel ratio and engine fuel conversion efficiency high allowing to make the most of the limited amount of fuel available and that only by using a small amount of electric energy. This device is without doubt a contributor to the 50% efficiency reportedly achieved by the current Formula One[TM] power units [15] and seen in the Cranfield F1 Design Sprint.

On the other hand, the 350kW MGU-K proved to be the most useful device to accelerate the vehicle. Even though the engine simulations showed that the engine suffers from turbo lag during the first phase of acceleration, the 'torque-to-fill' capacity of the MGU-K allows rapid acceleration of the vehicle despite delay in the turbocharger response, but this is at the expense of low fuel conversion efficiency at the beginning of the manoeuvre. However, the MGU-K can also be used during braking events to recover kinetic energy, which is not investigated and considered in this study.

In addition, it was demonstrated that the non-deliberate fuel enrichment allowed by the applied fuel strategy and the engine speed increase due to the MGU-K leads to higher exhaust enthalpy and thus a more responsive behaviour of the turbocharger. However, to operate, the MGU-K requires a significant amount of electric energy meaning that given the electric consumption dictated by the regulations, it can only be used for circa 30s per lap for the specific manoeuvre studied here. Furthermore, when comparing the

acceleration performance normalised by the total amount of energy used, the MGU-K is less efficient than the eTC.

Even though, the MGU-K will be of high-importance for vehicle performances in 2026, the Formula One^TM engine manufacturers will have to implement additional solutions to mitigate the effect of turbo lag considering the quantum of energy that must be drawn out of the battery to power the MGU-K in the case studied.

The fuel strategy implemented in this study was interesting to compare the eTC and MGU-K cases but will not be viable for 2026 because of the significant drop in air/fuel ratio and efficiency at the manoeuvre. Engine manufacturers need to find a balance between achieving high fuel conversion efficiency and rapidly accelerating the turbo-charger rotor. For instance, it can be useful to briefly sacrifice fuel conversion efficiency, to a less extend than what observed in thus study, to speed up the turbocharger and achieving high efficiencies faster.

Energy management strategies are not discussed in this paper but due to their hybrid nature, the Formula One^TM powertrain must be developed as a system to maximise the efficiency of the overall system to make the best use of the limited energy. For example, the MGU-K can be used to 'torque-to-fill' as investigated in this paper but also to 'torque-consume' during low torque demand from the driver. The idea of 'torque consuming' is to run the engine at higher load than demanded by the driver or acceptable at the tyre contact patch. This keeps exhaust enthalpy, turbocharger speed and fuel conversion efficiency high and the excess energy is recovered using the MGU-K. In this way, the MGU-K is used 'against' the engine when the battery is not fully charged, or the vehicle is grip limited preventing more torque from the engine to be used for propulsion and/or the MGU-K is not already recovering energy at full power. This is a way to recharge the battery and to nearly eliminate turbo lag when the driver demands full load as the engine is already operating at optimal condition. However, there is a circa 10% energy conversion penalty to pay each time heat energy is transferred to electrical energy and vice versa.

In a more general context, coupling the ICE with an electric motor helps to improve performances. If the aim of the power unit is to maximise efficiency, the electric assisted turbocharger is the solution to select, and it only requires modest electric energy supply. If the objective is highest vehicle acceleration performance, high-power MGU-K is preferred, but at the cost of high electric energy consumption and lower average fuel conversion efficiency than with an eTC. Obviously, if allowed, the best solution for efficiency and vehicle performance is to combine both solutions with a simple electrically assisted turbocharger which is not able to re-charge the battery for simplicity reasons. Any of the electrical hybrid solutions outperform the powertrain that has no electrical assistance.

NOMENCLATURE

V	Vehicle speed (m/s)
$I_{performance}$	Acceleration performance indicator: acceleration/energy consumption (g/MJ)
$V_{gearshift+}$	Vehicle speed at which the first gear upshift occurs (m/s)
$V_{t = 0.9}$	Vehicle speed at t = 0.9s (m/s)

(*Continued*)

(*Continued*)

$t_{gearshift}$	Simulation time at which the first gear upshift occurs (s)
g	Earth's gravity acceleration taken as 9.81 (m/s²)
$E_{electric}$	Electric energy consumption (MJ)
Q_{lvh}	Fuel lower heating value taken as 41 (MJ/kg)
m_{fuel}	Consumed fuel mass (kg)
dt	Differential of time (s)
t_{final}	Total simulation time (s)
$t_{reference - Eff = 40\%}$	Simulation time at which 40% efficiency is reached in the reference case (s)
$t_{MGU-K - Eff = 40\%}$	Simulation time at which 40% efficiency is reached in the MGU-K case (s)

REFERENCES

[1] Yoshida, M., Kita, M. and Atarashi, H. (2009) *'Development of Hybrid System for Formula One', Honda R&D Technical Review F1 Special (The Third Era Activities)*, pp. 225–238.

[2] Dahodwala, M., Joshi, S., Dhanraj, F. N. U., Ahuja, N., Koehler, E., Franke, M. and Tomazic, D. (2021) 'Evaluation of 48V and High Voltage Parallel Hybrid Diesel Powertrain Architectures for Class 6–7 Medium Heavy-Duty Vehicles', *SAE Technical Papers*, (2021), pp. 1–11. doi: 10.4271/2021-01-0720.

[3] *Fédération Internationale de l'Automobile* (FIA) (2022) *2026 Formula One Power Unit Technical Regulations, FIA Technical Regulations*.

[4] *Fédération Internationale de l'Automobile* (FIA) (2014) 2014 Formula One Technical Regulations, FIA Technical Regulations.

[5] Barman, J., Patchappalam, K. and Gambhir, H. (2019) 'Compressed Air in Engine Exhaust Manifold to Improve Engine Performance and Fuel Economy', *SAE Technical Papers*, 2019-26–00. doi: 10.4271/2019-26-0043.

[6] Baietta, L., Alshammari, M., Pesyridis, A. and Gohil, D. (2020) 'Design of an Axial Turbine for Highly Downsized Internal Combustion Engines', *Applied Sciences*, 10 (17). doi: https://doi.org/10.3390/app10175935.

[7] Zeng, T., Upadhyay, D., Sun, H., Curtis, E. and Zhu, G. G. (2018) 'Regenerative Hydraulic Assisted Turbocharger', *ASME. J. Eng. Gas Turbines Power*, 140(10). doi: 10.1115/1.4039937.

[8] Katrasnik, T., Rodman, S., Trenc, F., Hribernik, A. and Medica, V. (2003) 'Improvement of the Dynamic Characteristic of an Automotive Engine by a Turbocharger Assisted by an Electric Motor', *ASME. J. Eng. Gas Turbines Power*, 125(2), pp. 590–595. doi: 10.1115/1.1563246.

[9] Walkingshaw, J., Iosifidis, G., Scheuermann, T., Filsinger, D. and Ikeya, N. (2015) 'A Comparison of a Mono-, Twin-, and Double-Scroll Turbine for Automotive

Applications', *ASME. J. Eng. Gas Turbines Power*, 138(5). doi: https://doi.org/10.1115/1.4031449.

[10] Spessa, E. and Baratta, M. (2009) 'Turbocharged CNG Engines for Urban Transportation: Evaluation of Turbolag Reduction Strategies by Means of Computational Analyses', in *Proceedings of the ASME Internal Combustion Engine Division 2009 Spring Technical Conference*. Milwaukee, Wisconsin, USA, 3–6 May: ASME, pp. 573–582.

[11] Garrett Motion Inc. (2022) *G-Series G30-770 58mm*. Available at: https://www.garrettmotion.com/racing-and-performance/performance-catalog/turbo/g-series-g30-770/ (Accessed: 22 November 2022).

[12] Harrison, M. (2004) *Vehicle refinement: controlling noise and vibration in road vehicles*. Oxford: Elsevier.

[13] Seward, D. (2014) Race Car Design. London: Palgrave.

[14] Integral Powertrain Limited (2022) *CTSM242 Platform*. Available at: https://ehelix.com/products/ctsm242-electric-motor/ (Accessed: 22 November 2022).

[15] AMG Petronas Formula One Team (2022) *Insight: Five Examples Why F1 Is Accelerating the Future*. Available at: https://www.mercedesamgf1.com/en/news/2018/10/insight-five-examples-why-f1-is-accelerating-the-future/ (Accessed: 22 November 2022).

Benefits of a driven-turbo for hydrogen internal combustion engines

T. Waldron, J. Brin

SuperTurbo^{TM} Technologies, USA

ABSTRACT

Restrictive future CO_2 emission regulations are incentivizing evaluation of carbon-free fuels. This is particularly true in the difficult to electrify heavy commercial vehicle segment. The reemergence of hydrogen internal combustion (H_2 ICE) for large displacement engines can both expedite hydrogen adoption and reduce total cost of ownership. This paper will cover how the application of a Driven-Turbo can address challenges unique to H_2 ICE. The research being presented is joint simulation conducted by AVL List GmbH and SuperTurbo Technologies on a 13L H_2 ICE. The GT Power model is calibrated from dyno testing at AVL of an operational engine and then modified with known and tested data from a mechanically variable Driven-Turbo. The first H_2 ICE challenge that will be addressed is the requirement for the engine to maintain a lean-burn combustion strategy. Maintaining H_2 lean-burn is key to controlling NO_x formation and minimizing aftertreatment requirements. The high lambda requirement can create challenges for turbocharges when available turbine power is insufficient for the desired compressor power. The on-demand air functionality of the Driven-Turbo negates this problem and can be used to optimize air-fuel ratio in steady-state and transient cycles. The simulation will show low NO_x formation through combustion optimization and time to torque transients equivalent to diesel. The second H_2 ICE challenge that will be addressed is how to maintain highest BMEP and BTE for hydrogen internal combustion engines with a Driven-Turbo in order to close the gap to diesel and FCEV respectively. The availability of Driven-Turbo enabled exhaust energy recovery through turbo-compounding, in combination with combustion optimization, will demonstrate an ability to improve H_2 ICE BMEP/BTE/BSFC. SuperTurbo and AVL have completed full WHTC cycle comparisons for the mechanically Driven-Turbo versus both VGT and Two-Stage Turbo configurations, and those results will be highlighted. The WHTC cycle results will show the compromises between engine response (total cycle work) versus engine-out NOx (both peak transient NOx and accumulated cycle NOx). The Driven-Turbo is showing the potential to eliminate NOx peaks and reach Euro6 compliance levels without aftertreatment. The engine being evaluated through the WHTC is port injected with no EGR, and applicability to other engine configurations will be discussed. Physical engine testing to validate all of these findings is upcoming. Inclusion of the dyno test results will be made available via this paper and/or conference presentation, depending on test completion and material submission deadlines.

1   INTRODUCTION

The SuperTurbo is a mechanically driven turbocharger that has been developed for commercial diesel engines to improve efficiency, emissions and performance. When presented with the unique challenges for hydrogen as an engine fuel, it became apparent that the Driven-Turbo could specifically address several of the challenges seen on these engines. *Rapid response and precise delivery of airflow can allow a H_2 ICE to maintain a desired air fuel ratio (AFR) throughout dynamic operating conditions.*

This paper will primarily focus on a study of the 13L engine operating with port fuel injection (PFI) and zero exhaust gas recirculation (EGR). Understanding the performance and limitations with this architecture is a key starting point, as it represents the most expedient and cost-effective approach to early implementation of H_2 ICE. This paper will cover the WHTC cycle analysis and then more specific studies related to steady-state maps and load step transients. The effects of adding EGR will also be discussed. The baseline evaluated for the study is a VGT, however ongoing analysis of alternative boosting systems will also be discussed.

High excess Air Ratio (or Lambda) is critically necessary to prevent an exponential rise in engine NOx emissions for hydrogen engines [5]. Figure 1 below shows this relation as tested on the 13L engine. *Holding an optimal Lambda prevents NOx creation and also can prevent unwanted hydrogen slip conditions often seen with excessively high Lambda.* The Driven-Turbo, by design, is an on-demand air system that is well suited to consistently control ideal Lamba conditions. This paper will show the challenges faced by traditional turbochargers when exhaust enthalpy is not adequate to maintain high compressor power, especially in transient cycles.
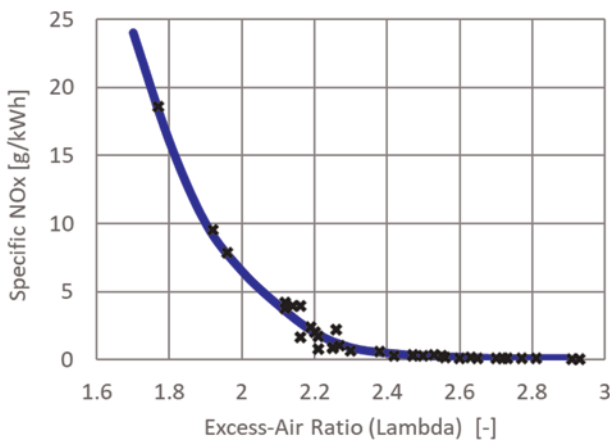

Figure 1. NOx vs Lambda from 13L H2 ICE testing.

In addition to the problems created by the necessity to maintain lean-burn operation, there are several other areas that must be addressed for H_2 ICE. Reaching high BMEP levels is important for truck and equipment engines that require high relative power

versus displacement. Maximizing BTE and BSFC to lower operating costs and extend vehicle range is also important.

2   BACKGROUND

2.1   Engine and model

AVL has successfully demonstrated the possibility to convert a 13L CNG heavy duty engine into a hydrogen engine [4]. The demonstrator has proved the feasibility to reach a BMEP of 21bar with BTE of 42% and single stage turbocharger. To achieve more flexibility on engine tests in view of boost pressure demands a turbocharger with variable turbine geometry was used.

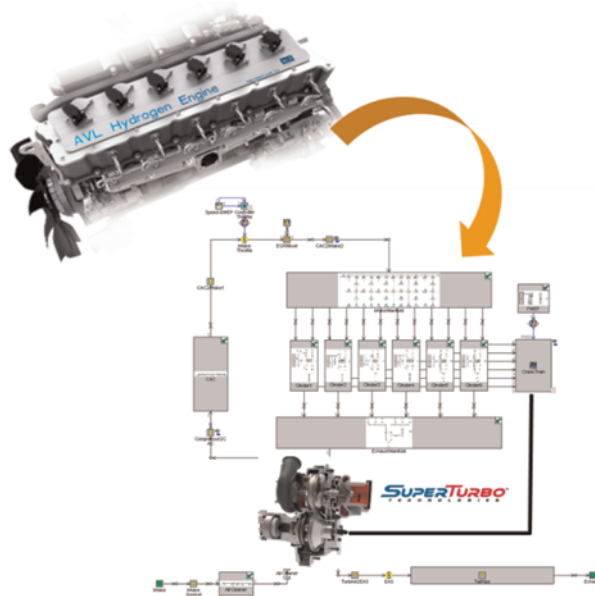**Figure 2. AVL 13L + SuperTurbo engine model.**

Table 1. 13L baseline engine specification.

Base Engine	HD IL6 CNG Application	
Properties	**Unit**	**Value**
Bore	mm	130,0
Stroke	mm	161,0
Volume/cylinder	ltr	2,14
Swept volume	ltr	12,82
Charging System	–	Single Stage TC/Intercooled
EGR System	–	Cooled high pressure

In order to show the benefits of the Driven-Turbo technology on a hydrogen engine, investigations by means of 1D simulation were performed. A GT-Power (GTP) engine model with H2 combustion (MPI gas injection) was created and *calibrated to AVL's hydrogen engine test results*. This simulation model was the baseline for the investigations with the Driven-Turbo charging technology. The model can calculate a complete engine map (from full load to low engine load of 4bar BMEP) for the investigation of different charging concepts. The hydrogen combustion is modelled based on test data and AVL experience. An engine data based NOx emission prediction is applied in place of GT Power NOx prediction for accuracy.

2.2 SuperTurbo

The SuperTurbo designed for commercial vehicles covers an engine displacement range from 7L to 15L. It combines and improves upon the capabilities of a supercharger, turbocharger and turbo-compounder. The internal components are common across this range while the turbine and compressor designs are changed based upon the individual engine requirements. With 90% part commonality, the device is designed to economically scale and cover most of the heavy commercial industry. *In order to maximize benefits, this large SuperTurbo is specified with a continuous power limit of 30 kW (primarily for compounding) and an instantaneous power limit of 50kW (primarily for supercharging).* The SuperTurbo is designed to mechanically integrate with the engine through connections at either the PTO or FEAD. The mechanical connection includes a controlled clutch and torsional damper. The core components or subassemblies are designed as cartridge-like units that are contained in a common housing. The two core components are the speed reducing fixed ratio planetary which controls the turbo shaft and the CVT which allows for overall ratio adjustment [8]. The primary control centers around delivering precise boost pressure and MAF. While following air commands the SuperTurbo will be supercharging when turbine power is less than compressor power (example: transient) and likewise compounding when turbine power exceeds compressor power (example: highway cruise or higher engine power).
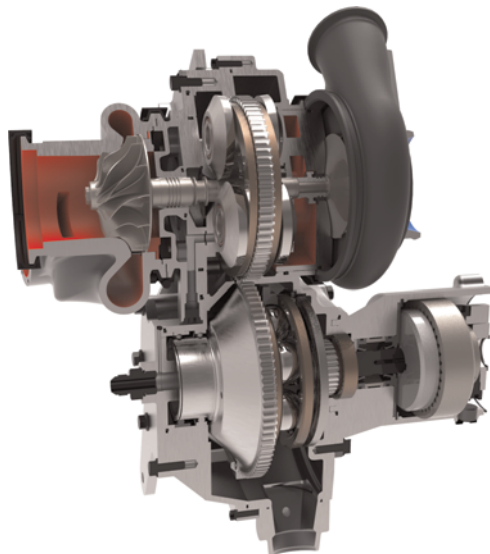

Figure 3. SuperTurbo cross section.

3   WHTC SIMULATION RESULTS

With future regulations focused on cycle-based compliance, the most important simulation result from this study is the comparative World Harmonized Transient Cycle (WHTC). Figure 4 shows a comparison of the VGT (from both engine test and calibrated simulation) with two different Driven-Turbo control strategies. Future NOx regulations (Euro7, China7, CARB, EPA) [1,3] are focused on ultra-low NOx emissions and hydrogen engines will need to meet or exceed the most stringent standards.

The peaks of instantaneous NOx output during WHTC transient sections with the VGT highlight a fundamental challenge. Holding high Lambda during transient sections is difficult given available turbine power in comparison to desired compressor power. This results in large peaks of NOx creation as shown in Figure 4. The accumulated NOx is also shown in total grams through the cycle.

The Driven-Turbo was simulated with two different control strategies. The 'recovery' cycle as shown in blue emphasizes turbo-compounding and has less aggressive Lambda targets and supercharging response. The 'boosting' control strategy emphasizes aggressive supercharging response and higher Lambda targets to eliminate cycle NOx peaks. These strategies were controlled by adjusting minimum Lambda constraints as well as targets with the Driven-Turbo controller.

Also shown in Figure 4 is the total WHTC cycle work performed by the VGT and the two different Driven-Turbo control strategies. This metric will translate to vehicle driveability. As could be expected, access to supercharging power will increase cycle work for a given Lambda. For an H_2 ICE equipped with a Driven-Turbo this increase in cycle work does not come with a correlating NOx penalty, as high Lambda values are maintained through the cycle. If the VGT was pushed to increase cycle work, it would require a drop in Lambda and correlating rise in NOx.
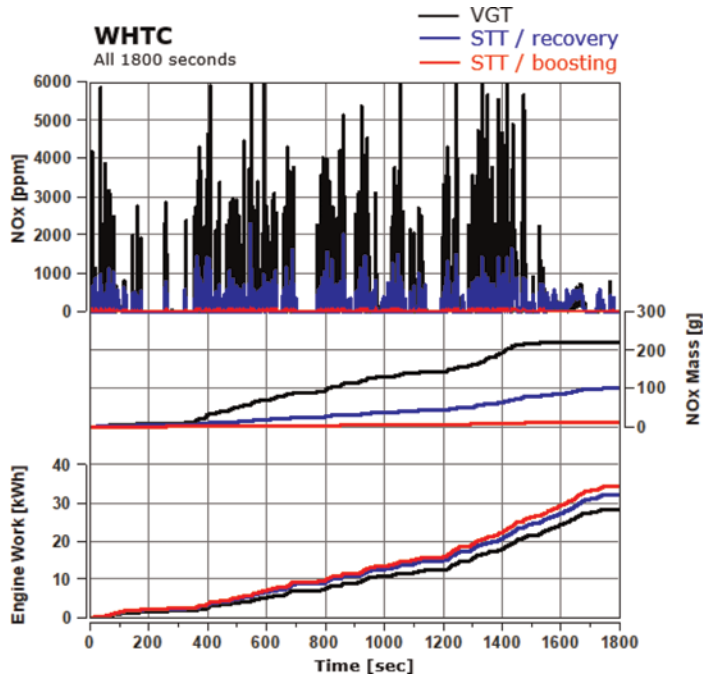
Figure 4. Comparative WHTC NOx and engine work.

Access to supercharging power has demonstrated the ability to lower NOx and increase transient response + engine work. It could be assumed that pulling supercharging power from the engine would have a negative net effect on engine efficiency. However, this simulation, and subsequent OEM analysis has shown that efficiency actually improves when utilizing the Driven-Turbo in the more aggressive 'boosting' mode.

When supercharging the Driven-Turbo is only taking power from the engine to over-come inertia and compensate for inadequate turbine power. The turbine is still actively feeding the transient rise and thus the Driven-Turbo is combining exhaust power and crankshaft power to 'efficiently' supercharge.

Table 2 below shows a summary of NOx emissions and fuel consumption through the WHTC for the different boosting systems and strategies. It is not surprising that more boosting equates to higher Lambda and thus lower NOx. *Interestingly, more boosting from the Driven-Turbo also equates to the lowest fuel consumption.* This higher efficiency comes from several sources. The Driven-Turbo does turbo-compound through much of the cycle, which mostly negates the cumulative supercharging power draw. The maintenance of lean-burn conditions keeps temperatures lower and reduces heat transfer. Most importantly the control over AFR facilitates improved combustion and closed cycle efficiency. In cylinder efficiency should be the primary objective for air handling and is fundamental to on-demand air systems like the Driven-Turbo.

Table 2. WHTC BSNOx and BSFC.

	BSNOx [g/kWh]	BSFC [g/kWh]
VGT	7.8	85.4
STT / more recovery	3.1	83.1
STT / more boosting	0.28	79.7

Table 2 shows that conceptually the 'boosting' strategy applied to the Driven-Turbo can result in Euro6 complaint NOx on the WHTC without aftertreatment. It is still advisable to consider an SCR for different cycles and real-world driving. Euro7 and similar standards will require NOx aftertreatment, although they could be significantly simplified with these low levels of engine out NOx.

To further understand what the Driven-Turbo is doing through the cycle, Figure 5 outlines both the power and accumulated work of the device. The 'recovery' cycle with a less aggressive Lambda target has smaller supercharging power peaks and higher levels of turbo compounding. The net effect is >1 kWh recovered back to the engine over the cycle. The 'boosting' cycle with a higher Lambda target has large supercharging peaks into the ~35kW range and less compounding. Again, the SuperTurbo mechanical specification is 50kW of instantaneous supercharging power and 30kW of continuous compounding. The 'boosting' control strategy results in a more balanced, yet slightly negative total Driven-Turbo cycle work. Given the overall results as shown in Figure 4 and Table 2, this appears to be the optimal strategy despite not having net positive compounding work, as the benefits to in-cylinder efficiency outweigh the drop in compounding work.
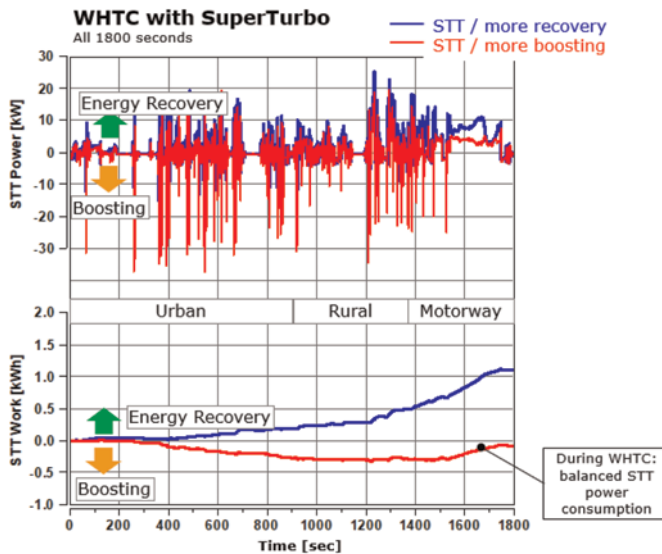

Figure 5. WHTC SuperTurbo power and work.

To better understand the full cycle results, it's also necessary to analyse specific sections of the cycle in more detail. Figure 6 highlights the 460-488 second section of the WHTC. This section of the WHTC was chosen to highlight intensive gradient load increases. The result compares how the VGT and Driven-Turbo respond with different Lambda limiters applied.

The VGT (as shown in black) has a Lambda lower limit applied at 1.8. Referencing back to Figure 1, this limit is justified as a minimal value for this engine, given the excessive NOx production at lower Lambdas. With that limit in place, the VGT struggles to follow the WHTC demand curve for BMEP. There are also large NOx peaks created when Lambda drops to that limitation. This result highlights the challenges when there is no access to external power, other than exhaust power, to increase boost pressure. Thus, the fundamental trade-off between engine response and NOx creation is more clearly shown for exhaust driven turbochargers.

The Driven-Turbo (as shown in red) is able to apply a Lambda lower limit at 2.4. This higher Lambda limit results in near elimination of the NOx peaks in this transient section. Additionally, the Driven-Turbo is able to better follow the BMEP demand trace of the cycle. This section of the WHTC as shown in Figure 6 is demonstrative of the full cycle results that were previously shown in Figure 4.
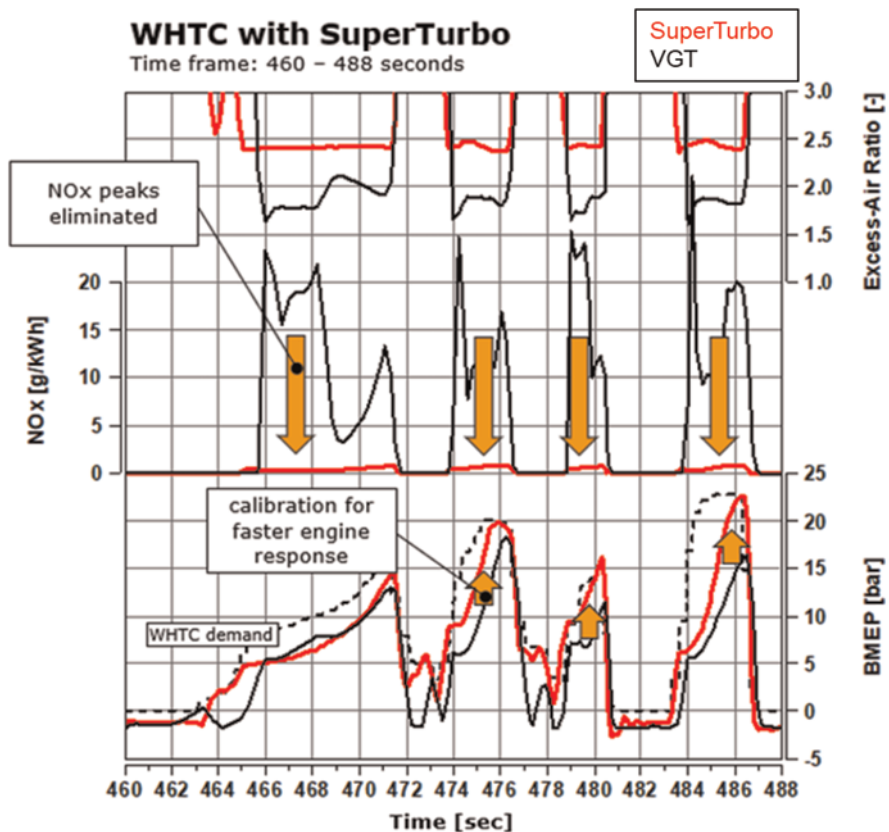

Figure 6. WHTC transient section.

The conclusions drawn from the full WHTC H_2 ICE simulation are that having a driven-turbo like the SuperTurbo can:

– *Achieve ultra-low cycle NOx*
– *Improve total engine work and driveability*
– *Improve fuel efficiency*

4 TRANSIENT SIMULATION ANALYSIS

The project also included a variety of specific transient response evaluations, some of which will be shared in this paper. Looking at individual transients in more detail can be helpful to understand the full cycle results. The primary constraints and variables to balance against each other in transient scenarios are: Lambda limits, NOx creation, and torque/power response. Figure 7 below shows the VGT sensitivity to Lambda limits from 1.8 to 2.2 and compares them against the Driven-Turbo at the highest 2.2 Lambda target.
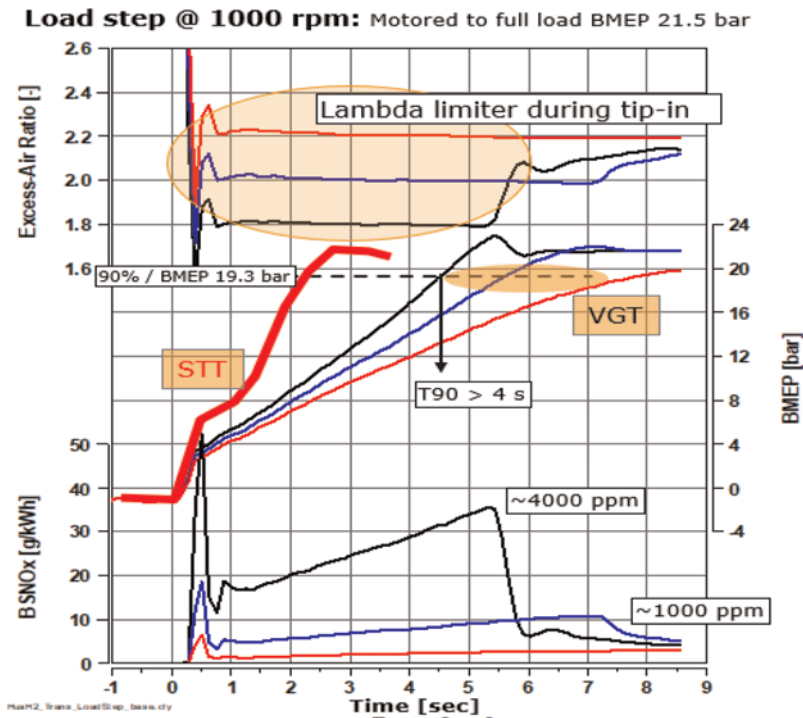
Figure 7. Variable Lambda transients VGT vs Driven-Turbo.

In these scenarios the Driven-Turbo is able to hold a Lambda target of 2.2 and achieve time to 90% BMEP in 2.2 seconds. The VGT, with a similar Lambda target is stretched to an 8 second transient. Decreasing the transient response time of the VGT requires relaxation of the Lambda limiter which results in the expected rise in NOx creation. Further reduction of transient response to achieve Driven-Turbo like response would result in unacceptable NOx levels.

Another transient sensitivity test was run just on the Driven-Turbo and can be seen in Figure 8. In this scenario the time to torque/BMEP for the transient was held constant at ~2.8 seconds. For the Driven-Turbo to meet this response time at Lambda 2.2 it requires ~13kW or supercharging draw. To push NOx down to significantly lower levels, the Driven-Turbo can target a Lambda of 2.6, which would require ~32kw of super-charging draw. As the minimum Lambda limit is increased, the engine transient response does not suffer, as the Driven-Turbo can simply compensate through increased supercharging power.

Analysis like these (and others) were completed to show both the flexibility and limits of a controllable driven-turbo. These results show how one can target a transient response time and adjust a NOx output within a given power limit (and correlating boost response) from an on-demand air system.
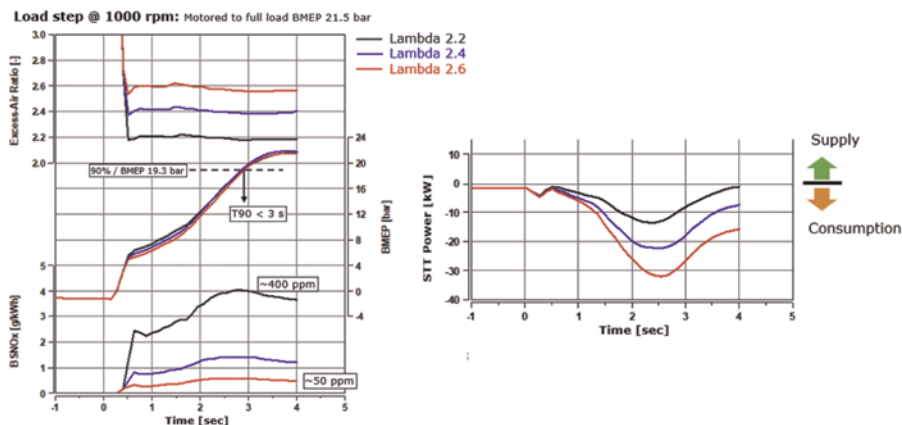

Figure 8. Utilization of Driven-Turbo power to lower NOx.

5   STEADY STATE ANALYSIS

Simulation of steady state conditions is fundamental to building the full drivecycle analysis and establishing those models. Properly matching turbine and compressor maps all begin in the steady state environment. The simulation project included several iterations of different turbine and compressor options. The turbine design balances compounding power, pumping losses, turbine efficiency and pressure ratio (and ability to drive EGR if desired). The turbine can be designed to target compounding and effi-ciency at different engine operating points which then have correlating sacrifices at other points. Example: a more restrictive turbine will increase compounding power at lower engine power and speeds, but will have higher pumping losses at rated power. A more free flowing turbine will perform well at rated power, but not maximize exhaust power collection for on-highway cruise conditions. Since the Driven-Turbo has reduced concerns over turbine weight and inertia and no concern for overspeed, it allows a dif-ferent approach to efficient turbine design [7]. Compressor maps for H_2 ICE and their need for high Lambda operation are uniquely stressed. Single stage compressors need to maximize pressure ratio and mass flow to facilitate lean-burn along the lug curve, especially for high BMEP applications [8].

The tuning of the turbine and compressor maps for the 13L engine were focused on the mid rpm ranges with power in the 75–100% range. Figure 9 below shows a comparison

of BTE for the Driven-Turbo vs. baseline VGT. Peak BTE gain aligns with maximum turbo compounding power, however turbine design was specifically modified to add benefits to areas central to on-highway vehicle operation. BTE benefits are the result of both compounded exhaust energy recovery and the ability to tune optimal air flow for combustion efficiency.
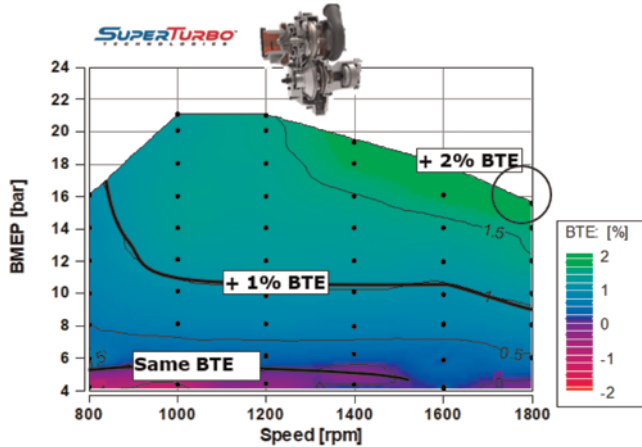
Figure 9. BTE comparison of VGT vs Driven-Turbo.

Understanding the source of steady state efficiency gains also requires clarity on one of the unique functions of the Driven-Turbo. The compounding of exhaust power back to the engine is predictable in the steady state environment, and obviously more dynamic in a transient cycle. The simulation study has shown that there is available exhaust enthalpy to create compounding conditions on the 13L hydrogen engine.

Figure 10. Driven-Turbo steady state maps.

As noted in section 2.1, the baseline VGT equipped engine had a peak BTE of 42%. The Driven-Turbo steady state analysis broadened the efficiency region and improved it to 43% while also increasing the full load BTE as seen in Figure 9. Of course, these steady state results can be adjusted based on a variety of aero changes and specific strategies. Figure 11 contains steady state maps showing BTE, Lambda, MFB50, and NOx. Steady state Lambda is well controlled and l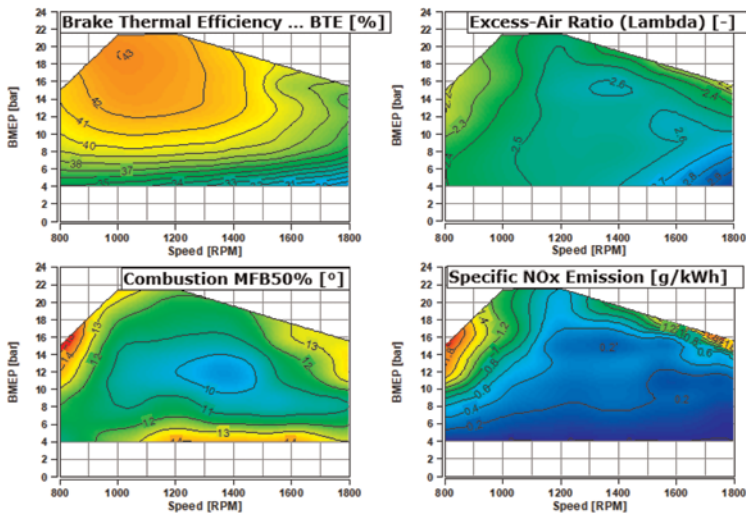ug curve NOx is low. However, it is always of note that steady state NOx is not the fundamental challenge for H_2 ICE. Transient cycle NOx is the paramount problem to be addressed.

All of the simulation results shown up to this point have been based on PFI with no EGR. MPI is performed through port fuel injection (PFI) and the terms will be used inter-changeably. By design this simulation project was focused on proven and tested architectures for H_2 ICE which could also translate to expedient implementation and low total system cost.

6   BOOSTING SYSTEM COMPARISONS

The simulation is now being utilized to map a variety of different boosting archi-tectures through WHTC analysis. While these results and simulation details will be discussed more in subsequent publication, a summary is provided in Figure 11. The results show the compromise between transient response and cycle NOx. The load step is a 1000rpm time to torque (x axis) and cycle NOx is translated into required EAS conversion to reach .04 g/kWh. Different power and voltage electrified architectures are also included.
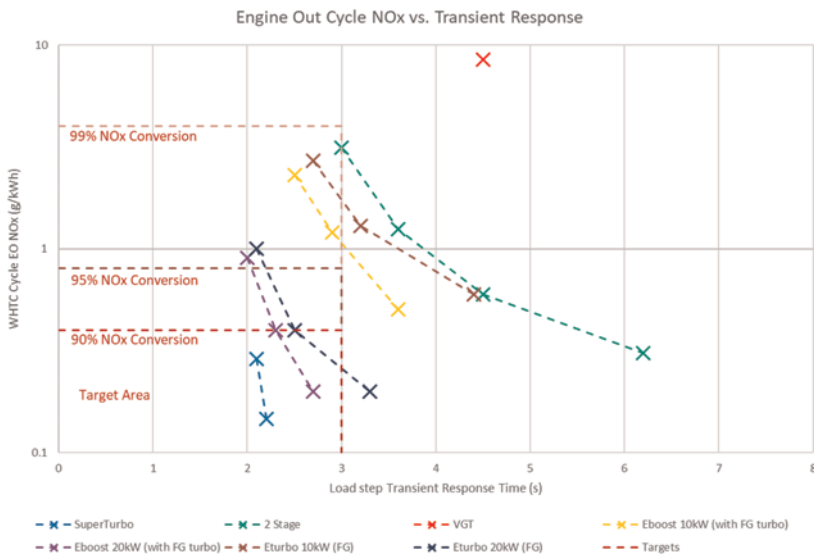

Figure 11. Boosting system cycle NOx vs engine response.

7   SUMMARY

The results presented here are select portions of current knowledge developed over a year of joint simulation efforts by SuperTurbo and AVL on hydrogen combustion.

The conclusions of the work is that a mechanically Driven-Turbo with SuperTurbo specifications shows:

- *Faster, Diesel-like torque build up can be achieved, even at high Lambda*
- *NOx peaks during acceleration can be fully eliminated*
- *Significant raw NOx reduction towards EURO VI emission requirements can be demonstrated*
- *Simplifications in the EAS system are feasible (single stage SCR, less Urea consumption)*
- *Lowest fuel consumption in the WHTC is achieved*

ACKNOWLEDGEMENTS

REFERENCES

[1] Boriboonsomsin, K., Johnson, K., Scora, G., Sandex, D. *et al.*, *Collection of Activity Data from On-Road Heavy-Duty Diesel Vehicles. Final Report, California Air Resources Board and the California Environmental Protection Agency*, May 2017.

[2] Brown, J., and Waldron, T., *"Drivecycle Benefits of Controlling Airflow with the SuperTurboTM,"* SAE Technical Paper 2018-01-0970, 2018, https://doi-org/10.4271/2018-01-0970.

[3] California Air Resources Board (CARB), *"California Air Resources Board Staff Current Assessment of the Technical Feasibility of Lower NOx Standards and Associated Test Procedures for 2022 and Subsequent Model Year Medium-Duty and Heavy-Duty Diesel Engines,"* White Paper, April 2019. https://ww3.arb.ca.gov/msprog/hdlownox/white_paper_04182019a.pdf

[4] Dreisbach, R.; Arnberger, A.; Zukancic, A.; Wieser, M.; Kunder, N.; Plettenberg, M.; Raser, B.; Eichlseder, H. *The heavy-duty hydrogen engine and its realization until 2025*. In Proceedings of the 42nd International Vienna Motor Symposium, Vienna, Austria, 29–30 April 2021.

[5] Ebert, T., Koch, D., Keyou GmbH *et al.*, Effectiveness of H2-specific operating strategy in dynamic engine operation, IVT 18th Symposium '*Sustainable Mobility, Transport and Power Generation'*, Graz Austria, September 2021.

[6] Manufacturers of Emission Controls Association (MECA), *"Technology Feasibility for Heavy-Duty Diesel Trucks in Achieving 90% Lower NOx Standards in 2027,"* White Paper, February 2020. http://www.meca.org/resources/MECA_2027_Low_NOx_White_Paper_FINAL.pdf

[7] Sherrill, R., Brown, J., and Waldron, T., *"Design and Testing of a Mechanically Driven Turbocharger for Improved Efficiency and Drivability,"* in 13th International Conference on Turbochargers and Turbocharging, London, 2018.

[8] Waldron, T., Brin, J. D'Orsi, N., *"Cycle benefits for commercial diesel engines utilizing a SuperTurbo"* Aufladetechnische Konferenz, Dresden Germany, September 2020.

Secondary air injection with E-Boosting devices

S.K. Yadla[1], D. Terber[2], J. Keuler[1], P. Davies[3]

[1]Garrett Motion Germany, GmbH, Holzgerlingen, Germany
[2]Garrett Motion Czech Republic s.r.o, Prague, Czech Republic
[3]Garrett Motion, Thaon-les-Vosges, France

ABSTRACT

Future emission norms will focus on reduced idle and more aggressive driveaway strategies to further limit the cold start emissions of Gasoline engines in all geographies. Europe will likely be the first with EU7 RDE and will be followed by China VII and revisions to SULEV standards in the USA.

One promising solution is the use of Secondary Air Injection (SAI) for "cold start". The current industry standard is to use low power secondary air pumps, which are limited to catalyst heating strategies under engine idling conditions. However, for dynamic boundary conditions, the SAI source should be controllable precisely to regulate the exhaust lambda and at the same time be powerful enough to operate against high exhaust back pressure.

Electric boosting products, E-Compressors & E-Turbos, fulfil the SAI requirements of future emission regulations comfortably. Once the catalyst heating strategy is completed, they function as regular electric boosting devices, to improve engine efficiency and reduce emissions under normal operation.

In this paper, the various layouts of E-Compressors & E-Turbo enabling SAI and electric boosting are discussed.

1   INTRODUCTION

Hybridization of vehicle powertrains is accelerating due to the increasing pressure on the automotive industry to introduce greener vehicles, tightening emission limits and the challenging CO2 fleet average targets. EU7 is expected to be introduced between 2025 & 2027 and as per the current market forecasts and the majority will be hybridized in some way. Hybridization improves efficiency but also allows an additional degree of freedom to apply faster catalyst light-off strategies and to tackle cold start emissions. One way of reducing cold start emissions is by using the E-Machine for electric-assist, either by reducing the engine load depending upon the type of powertrain layout or also by completely driving the vehicle electrically with a decoupled engine performing its cold start strategy. This alone reduces the absolute level of cold start emissions significantly, provided that the battery SOC is intelligently managed to cover all possible driving & environmental scenarios.

Another benefit of hybridized powertrains is the availability of High-Voltage architecture for auxiliary devices. There is an increasing trend to decouple engine/powertrain auxiliaries and electrify them for better efficiency & flexibility of operation. (e.g., electrical AC compressor, active vehicle stability control, electric boosting, electrically heated catalysts, etc.)

2   CHALLENGES & REQUIREMENTS OF NEW EMISSION REGULATIONS

With the introduction of EU7, the proposal is to further tighten the emission limits and to extend the testing boundary conditions. The latest proposal for EU7 introduced by European Commission [1] focusses on fuel-neutral emission limits, robustness/durability of emission compliance, lower emission limits along with the introduction of new emission species amongst others. For the Real-Driving Emissions (RDE) regulation in Europe starting from 2017, emission tests are performed on-road with the help of Portable Emission Measurement Systems (PEMS). There is no fixed driving profile considered for the test, rather only a few guidelines to define the valid test boundary conditions. As a result, the vehicle driveaway could occur immediately after engine start and the engine idling phase could be considerably shorter. It is also a similar case in the USA with the ongoing discussions of ACCII regulation, where the idling time of the FPT75 cycle could be shortened from 20 sec to 8 sec. Additionally, CARB has proposed six special test cycles for High-Power Cold-Starts.
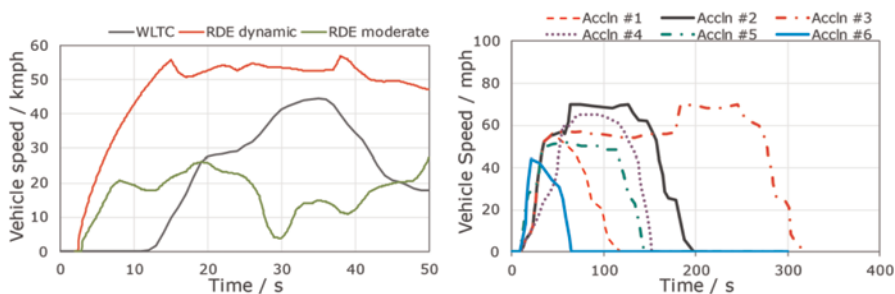

Figure 1. Cold start driving cycles/conditions [2].

The proposed emission limits can be achieved by breaking down the key requirements in the following categories:

- Cold start emission reduction
- **Faster Catalyst Light-Off**
- **Emission robustness under normal operation**
- Optimized control strategies – Engine & Powertrain
- Advanced After-Treatment Systems

In this paper, faster catalyst light-off measures & emission robustness under normal operation in combination with E-Boosting devices are addressed. Short urban trips will pose the biggest challenge for Gasoline powertrains, since most gaseous emissions occur within the first 30 seconds of operation after a cold start, until the catalyst has reached sufficient conversion efficiency. Under warm engine conditions or normal operation, it is essential for Gasoline powertrains in the future to maintain stoichiometric combustion throughout the engine operation area to ensure emission robustness. Electric Boosting devices such as E-Compressor and E-Turbo are key enablers of Lambda 1 operation, while maintaining or enhancing engine power density.
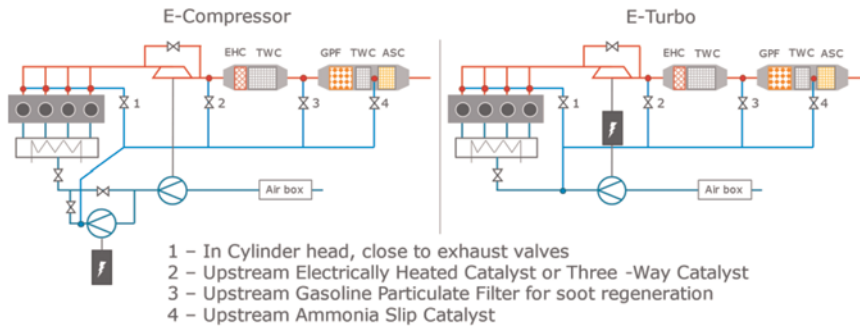
Figure 2. SAI layouts with E-Boosting components.

Figure 2 shows two alternative layouts of E-Compressor and E-Turbo systems combined with advanced EATS technologies considered for EU7 applications. In these configurations the E-Machines can provide both E-Boost and Secondary Air Injection functionality.

Another technology to improve cold start emissions is by using an electrically heated catalyst (EHC). With the help of an EHC, the catalyst can be brought to light-off temperature independent of engine operation. In HEV/PHEV architectures, the EHC can be deployed prior to engine start to heat up the catalyst and also to maintain the light-off temperature in the catalyst during overrun or long engine stop phases, by using intelligent operation strategies. The metallic substrate heats up rapidly achieving light-off after a few seconds. However, an engine start followed by cold exhaust gas flowing across the electrically heated catalysts would drop their temperature be-low the level needed for sufficient conversion efficiency. Therefore, an external air supply through the electrically heated catalysts is necessary prior to the engine start in order to achieve sufficient convective heat transfer to heat up the main catalyst as well. Since the main catalyst has a higher thermal inertia, it is more robust against the temperature drop resulting from the cold exhaust gas in the first seconds of engine operation. At the same time, the higher thermal inertia requires some time until the catalyst is heated up sufficiently [3]. Therefore, a pre-heating strategy is mandatory before starting the engine. The duration & intensity of the pre-heating strategy is strongly dependent on the type of powertrain and OEM driveability strategy. However, for extreme conditions such as cold ambient conditions or low battery SOC scenarios combined with moderate power request from the driver, the driveability of the vehicle could be heavily restricted.

3   SECONDARY AIR INJECTION WITH E-COMPRESSOR

Garrett's new generation E-Compressor offers industry-leading motor power & efficiency, speed capability and aerodynamic performance. It is offered in 48 V and will be available in 400 V. Advanced power electronics design and thermal management allows the compressor to operate under a wide range of engine operation conditions. The system adopts a sealed ball bearing design capable of running at 90 kRPM and is very compact to ease system integration. The high efficiency electric motor and power electronics are paired with bespoke aerodynamics based on the type of application.

A normal operation strategy for SAI requires low mass flow rates at high pressure ratios. Especially, under driveaway conditions, the SAI operation points are shifted towards even higher-pressure ratio compared to a typical 12 V SAI pump operation range. Advanced development tools are used within Garrett, to design dedicated aerodynamics for different SAI applications [5]. The typical aerodynamics of the E-Compressor targeting wide engine operation window for E-Boosting & SAI is called the 'Performance' wheel and it is paired with the 7.5 kW$_{DC}$ E-Motor. This wheel covers PR up to 1.8 and mass flow rates up to 0.17 Kg/s. For dedicated SAI application targeting high power density or large displacement engines, a special wheel has been developed which targets pressure ratios up to 2.1. This wheel can also enable E-Boosting up to medium engine speeds. By adapting the compressor wheel further, the surge margin can be optimized for EU7 boundary conditions by limiting the flow capacity of the wheel.

3.1 SAI layouts with E-Compressor

The more common SAI layouts use electric pumps in the "p1" position (Figure 3, A) where inlet to the pump is located downstream the air filter and up-stream the compressor. The pump outlet is connected to the exhaust system, typically to the exhaust ports. In this layout, both a traditional side channel blower or an E-Compressor can be utilized. Typically, an on/off valve "a" is used to open or close the SAI channel. The SAI pump is used to precisely control the amount of SAI flow to the exhaust system to ensure stable stochiometric (or lean) operation upstream the catalyst. Alternatively, a fully controllable valve "a" can also be used. Additionally, a reed valve is used to prevent any potential backflow from the exhaust to the intake system. Valve "b" represents an engine throttle.
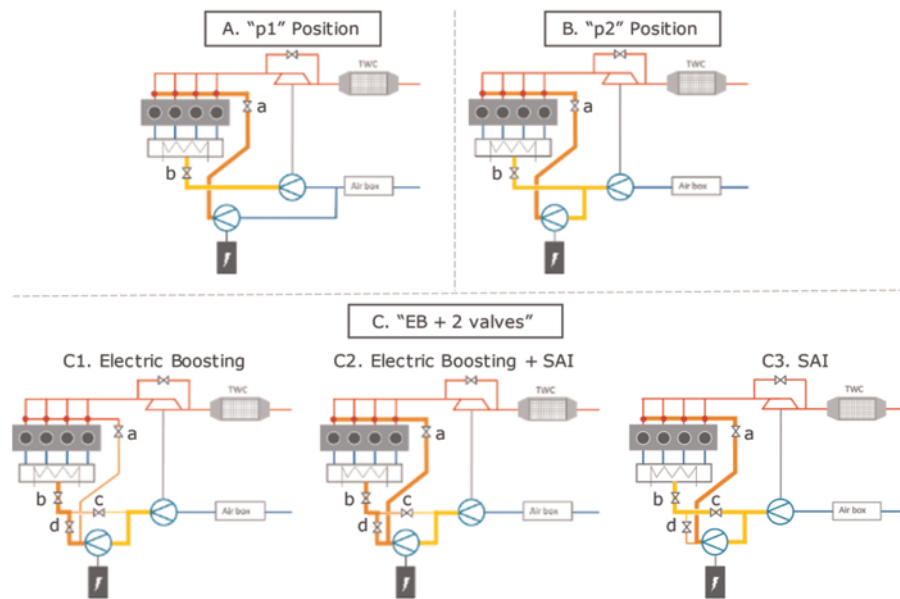

Figure 3. E-Compressor layouts.

The pressure at SAI pump inlet is slightly lower than ambient pressure, due to the air filter losses. The pump needs to compress fresh air to a pressure level sufficient to compensate the pressure drop in the SAI channel & also the higher exhaust pressure.

The "p1" position is therefore only suitable for low engine load applications with open wastegate. Higher loads and closed wastegate would lead to higher pressures upstream of the turbine and therefore higher demand on the pump's power and pressure ratio capability.

This configuration might not be capable of fulfilling 'extended' RDE boundary conditions [1]. Dynamic driveaway events or PHEV engine starts at high loads could be particularly challenging and SAI could help shorten the time to catalyst light-off, as well as reduce raw NOx emissions through in-cylinder enrichment. To address such high engine load scenarios, two-stage compression can be used by including the turbo-compressor in the SAI path. This is especially convenient when placing the pump inlet at the turbo-compressor outlet which is named as the "p2" position. Although this layout imposes new challenges in terms of packaging and bearing sealing, the performance gain in terms of SAI operation range is significantly increased by running at higher pressure in the SAI channel. The "p2" layout (Figure 3, B) does not require additional valves in comparison to "p1" position. Furthermore, "p2" position can enable electric boosting by adding valve "c" (EB with one valve). To further optimize both electric boosting and SAI operations, one more valve "d" (EB with two valves) can be introduced. With this layout, three control strategies are possible: Electric boosting only (Figure 3, C1), SAI only (Figure 3, C3), and electric boosting with SAI combined (Figure 3, C2).

For electric boosting, control valve "c" needs to be placed downstream of the branch point leading to the pump. Valve "c" is an on/off valve that can be either electrically controlled or more conveniently, it can be a passive valve opened by a positive pressure difference upstream and downstream the valve. A passive valve is lower cost and is often more compact since it does not require an actuator. By closing the valve "c", all the air compressed in main turbo compressor is forced to the SAI pump for second stage compression.

Electric boosting can also be used together with SAI, if valve "a" and valve "d" are opened while valve "c" is closed. In this case, the throttle controlling the engine power ensures that the compressors can deliver sufficient secondary air flow by limiting the engine transient response. This may result in increased calibration and control efforts but on the other hand, valve "d" is not mandatory for electric boosting nor SAI. The benefit of having valve "d" is to separate SAI channel from the engine intake manifold. It allows the same operation as "p2" when valve "d" is closed, and valve "c" is opened. This improves power requirements as well as controllability of the pump. It also prevents the throttle, charge cooler and intake piping from operating at relatively high pressure which is needed to drive enough SAI during high engine load operation.

Table 1. Comparison of SAI layouts.

No.	Parameter	"p1" No EB	"p2" No EB	"p2" EB with one valve	"p2" EB with two valves
1	Packaging	++	+	0	–
2	Additional Valves	+	+	0	–
3	Power Requirement	–	++	+	++
4	SAI Operation Range	–	++	+	++
5	EB Capable	NA	NA	++	++
6	Controllability	+	+	–	+
7	Sealing	++	–	–	–
8	System cost*	+	+	0	–

Assumption: SAI pump specification remains unchanged for all layouts.

4   SECONDARY AIR INJECTION WITH E-TURBO

Garrett's 48V 5kW$_{DC}$ E-Turbo is a series production proven solution that enables full engine map lambda 1 at high power density and offers transient performance improvement. It's also suitable and beneficial to be used as SAI pump to utilize the full advantage of the electric machine. Hence, this device was selected for more detailed SAI capability investigation through 1D simulations in chapter 5. As made reference to in chapter 2, E-Boosting devices such as the E-Turbo can help heating electrically heated catalysts heat up quicker. This operation is being investigated by Garrett in the course of ongoing test campaign within the EU project "PHOENICE" [4].

4.1 SAI layout with E-Turbo

As shown in Figure 4, SAI can be realized with the E-Turbo by adding introducing a valve 'a' between the compressor outlet and the SAI path. Upgrading an existing ICE with an E-Turbo requires to increase turbine size to reduce p3. LET is then maintained by using the electric machine. This leads to reduced residuals, PMEP and improved SAI flow. Furthermore, compressor can be updated for high PR which further improves SAI flow, especially in high engine loads. The Figure 4 shows possible SAI layout with an E-Turbo as well as comparison of envelopes of the baseline compressor with the E-Turbo compressor optimized for high load SAI operation.
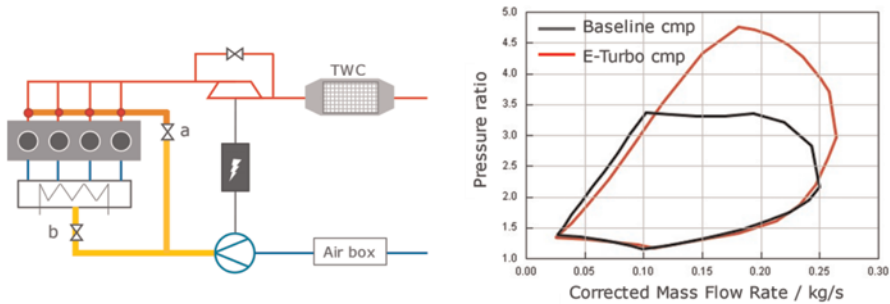
Figure 4. E-Turbo with SAI.

4.2 SAI Operation with E-Turbo

E-Turbo SAI layout from the Figure 4 requires 4 controllable parts to control the SAI flow and engine air flow: Wastegate; Throttle; SAI valve & E-motor.

Control strategy of all these parts need to be adapted during the SAI operation to prioritize sufficient and stable SAI flow. From previous investigation on SAI with E-compressor [5], it was discovered that it is beneficial for SAI flow to operate with closed wastegate. The downside of increased p3 is outweighed by elevated p2. This was also confirmed in the case of E-Turbo via simulations.

The throttle strategy is to control the engine performance, although the priority during transient operation needs to be the SAI flow. Therefore, acceleration during engine cold start which is enhanced by the EB machine must be limited. The full throttle opening leads to reduced secondary air pressure while p3 increases. This leads to reduced SAI flow even if SAI valve and E-motor is saturated at their maximum limit. This is also the case for E-Compressor in "EB plus one valve" layout. The "p1" and "p2" layouts don't offer EB functionality and therefore the acceleration is not as fast. But since their SAI channels are separated from the engine intake system, this allows higher secondary air pressure than throttle inlet pressure.

The SAI flow itself can be controlled in two ways. If an on/off SAI valve is used, then E-motor controls the SAI flow through regulating the SAI pressure. If fully variable SAI valve is used, then the E-motor can be controlled to its maximum power. SAI valve then regulates the SAI flow.

5   SAI OPERATION – E-COMPRESSOR VS. E-TURBO

The following sections are dedicated to the comparison of SAI performance with E-Compressor and E-Turbo through 1D simulation results. Chapter 5.1. describes the simulation model configuration and its boundary conditions. Steady state results in chapter 5.2. show comparison of expected engine map coverage of SAI with E-Compressor and E-Turbo, as well as maximum achievable engine power with SAI for different SAI layouts. Transient SAI performance comparison is simulated on RDE acceleration to full-load power in section 5.3.

5.1   Boundary conditions – E-Compressor vs. E-Turbo

A 1D gas-exchange simulation model was setup in GT-POWER for comparing Garrett's 48 V 7.5 kW$_{DC}$ E-Compressor in "EB plus 1 valve" layout with Garrett's series production 48 V 5 kW$_{DC}$ E-Turbo. The scenario is an upgrade of an existing engine to become EB capable and high load SAI capable with minimum hardware changes. Therefore, the

baseline TC was carried over for simulations with E-Compressor, while updated wheels were used for the E-Turbo. The E-Compressor is capable of 90 krpm and uses high flow "performance" wheel.

The baseline model for the simulations is a 4 cylinder, 2.0L TGDI engine adapted for SAI application. The secondary air channels in the cylinder head are connected to the exhaust ports and the diameter of the secondary air passages is limited, so that the structural integrity of the cylinder head is not compromised. This leads to a high pressure drop of 650 mbar at 100 kg/h of steady state flow. Standard ambient conditions and steady-state temperature solver (instead of transient) were used in the simulations, which results in higher temperature in both, intake and exhaust geometry, leading to higher volumetric flows and therefore higher pressure drops. This can be considered as a conservative approach for the SAI performance. The 50% burn point is retarded to 30°ATDC for oxidation stability in the exhaust system [6] as well as to increase enthalpy to improve catalyst light-off time. However, combustion optimization on the testbed is required to get a full MFB50% map for SAI operation. Retarded combustion leads to a higher air mass flow requirement for the same load and therefore higher demand on SAI pump for the same in-cylinder enrichment. The target for enrichment is lambda = 0.8, which corresponds to secondary air mass flow of 25% compared to the main engine flow.

All the boundary conditions for the simulations are listed in Table 2.

Table 2. Simulation boundary conditions.

No.	Parameter	Description
1	Engine	2.0TGDI, 4 cylinders, 20 bar BMEP, 135 kW
2	Temperature solver	Steady-state wall temperature solver
3	EATS	Secondary oxidation model, TWC model
4	Ambient conditions	1 bar, 25°C
5	SAI channel Δp	650 mbar at 100 kg/h steady flow (flow bench)
6	SAI Layout	"EB plus 1 valve" and E-Turbo
7	SAI Valve	On/Off
8	SAI Pump	E-Compressor and E-Turbo
9	SAI Control	Compressor speed, SAI valve fully opened
10	Electrical efficiency	85%
11	Combustion strategy	MFB50% = 30°ATDC (retarded)
12	Valve phasing	Advanced exhaust valve opening
13	Wastegate strategy	Closed
14	Turbocharger(TC)	Twin scroll baseline/E-Turbo (optimized wheels)

5.2 Steady state simulations – E-Compressor vs. E-Turbo

The following study is a steady-state comparison of maximum engine load which can be achieved with 25% of SAI with using E-Compressor and E-Turbo. The Figure 5 shows maximum achievable BMEP with SAI up to engine speed of 4000 rpm. The E-Turbo is

capable to support the engine with SAI to full load operation up to ∼3000 rpm. At 4000 rpm, 25% of SAI can be achieved up to 14.4 bar BMEP. The E-Compressor covers slightly smaller area by ∼2 bar BMEP at 3000 rpm and ∼1 bar BMEP at 4000rpm compared to the E-Turbo, even with the power advantage of 2.5 kW. This is caused by the difference between baseline TC wheels and E-Turbo wheels. While the baseline TC needs to start opening the wastegate from 3000rpm to stay within its compressor speed limit, the E-Turbo keeps the wastegate closed and the p3 is still significantly lower due to the high permeable turbine.

The Figure 5 also shows all the described SAI layouts in terms of maximum achievable power with 25% SAI. While the E-Compressors are using 7.5 kW_{DC} peak e-motor and baseline TC, the E-Turbo uses 5 kW_{DC} peak machine and optimized wheels.

- The layouts "p1" and "p2" use the dedicated SAI wheel as these layouts are not EB capable.
- The "EB plus 2 valves" also uses the dedicated wheel and therefore offers transient support only in low engine speeds.
- The results show that "p1" is not a suitable layout if high load SAI operation is required.
- "p2" benefits from pre-compressed air from the main compressor and achieves the best SAI performance.
- "EB plus two valves" brings the full benefit of "p2" layout and offers EB capability.
- The E-Turbo and E-Compressor in "EB plus 1 valve" layout offers the best EB capability but with slightly lower SAI performance, especially at high engine speeds and loads.
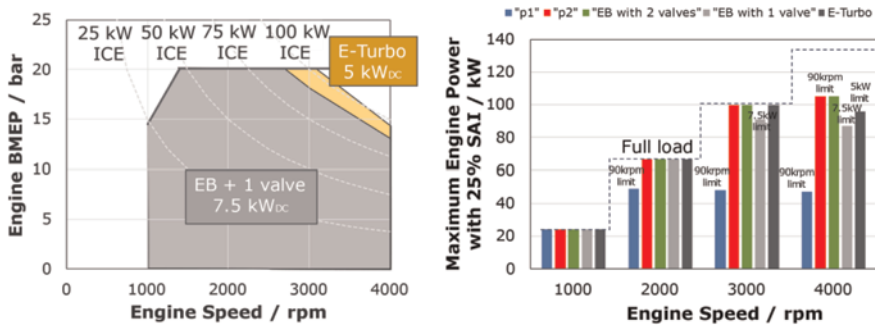

Figure 5. Maximum ICE steady-state achievable performance with 25% of SAI.

5.3 Transient simulations – E-Compressor vs. E-Turbo

As discussed in chapter 2, SAI operation under RDE conditions is essential. Hence another part of the comparison of E-Compressor and E-Turbo is a transient driveaway scenario with SAI operation. The boundary conditions are as in Table 2 with a few exceptions. The E-Motors are requested to run at peak transient power and the secondary air mass flow is controlled by an SAI valve. MFB50% is targeted for optimal combustion and drivability. A transient wall temperature solver to predict the warm-up behavior was used, with an initial temperature of 25°C. An in-cylinder lambda of 0.8 is targeted and is switched to stochiometric combustion if lambda upstream catalyst drops below 1. This condition also triggers SAI operation shut-off. The in-cylinder lambda behavior in Figure 6 is an indicator of how long E-Compressor and E-Turbo sustain requested SAI mass flow. The driveaway scenario with SAI can be supported by

E-Compressor for around 3.2 s, reaching engine power of around 106 kW. This is more than the steady-state results show and it's caused by the transient temperature solver and optimised combustion used for this study.
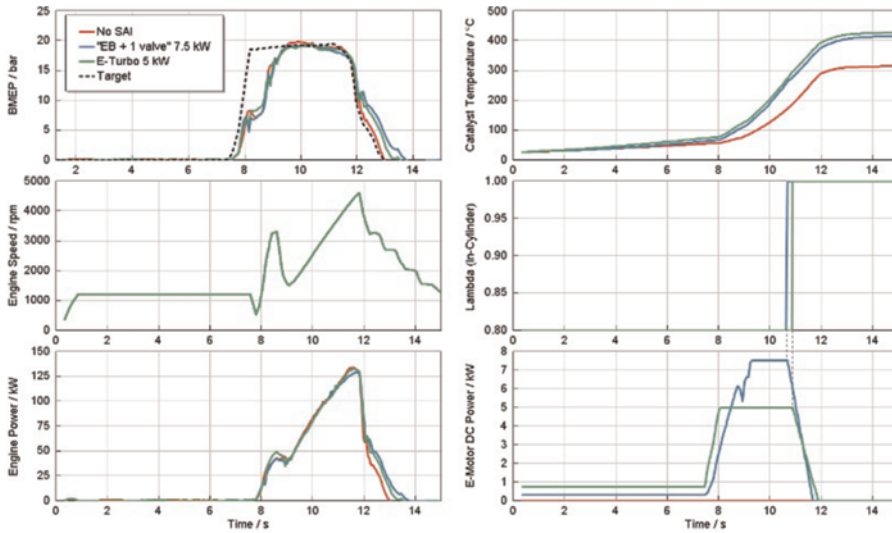

Figure 6. RDE acceleration to full load with SAI.

The E-Compressor can increase the temperature by 100°C by the end of the maneuver in comparison with acceleration without SAI. The E-Turbo can support SAI operation 0.2 s longer, achieving engine power of around 114 kW and increasing the catalyst temperature by another 12°C by the end of the maneuver in comparison with the E-Compressor. During this driveaway event, NOx emissions are reduced by 6 times due to SAI. Even higher engine powers with SAI are possible by optimizing the pressure drops in the system, such as in the SAI channel and SAI valves.

6   CONCLUSION

Future emission norms will focus on reduced engine idling times and more aggressive driveaway scenarios to further limit the cold start emissions of gasoline engines in all geographies. Europe will likely lead the way with EU7 and RDE (over extended boundary conditions) and will be followed by China VII and revisions to SULEV standards in the USA.

Garrett's simulations suggest that while the current SAI pumps in the power range of $800W_{DC}$ to $1kW_{DC}$ do a good job for applications homologated to the current SULEV norm, where a 20s idle warm up is allowed, this will not be satisfactory in the future.

Both 7.5 kW_{DC} E-Compressor in "EB plus 1 valve" layout with the baseline TC and 5 kW_{DC} E-Turbo with optimized wheels are capable of similarly significant reduction of catalyst light-off duration by maintaining SAI even at high engine load and speed operation. The E-Compressor performs very well even with the baseline TC with low PR compressor and relatively low permeable turbine. We can expect even better SAI per-formance with optimized baseline TC. The E-Turbo on the other hand takes full benefit of

optimized wheels and delivers similar SAI performance as the E-Compressor with lower maximum power needed.

NB: This paper is based on simulation studies and the findings are being tested in a vehicle environment at the time of writing this paper. The authors look forward to presenting actual test results at a future date. All simulations presented here were also performed at sea-level ambient conditions. This study will be extended to high altitude conditions in the very near future, but logic and initial investigations suggest that the SAI compressors would have to operate at even higher powers and duty cycles under such aggravated conditions.

REFERENCES

[1] *Regulation of the European Parliament and of the Council on type-approval of motor vehicles and engines with respect to emissions from motor vehicles* (Euro 7) and repealing Regulation (EC) No 715/2007 and Regulation (EC) No. 595/2009.

[2] Pham, A. and Jeftic, M., *"Characterization of Gaseous Emissions from Blended Plug-In Hybrid Electric Vehicles during High-Power Cold-Starts,"* SAE Technical Paper 2018-01-0428, 2018, doi:10.4271/2018-01-0428.

[3] S. Yadla, A. Balazs, M. Thewes, V. Walter, T. Uhlmann, R. Maurer, "Zero Impact Emission Vehicle", 32nd International AVL Conference "*Engine & Environment*", May 25th – 29th, 2020.

[4] PHOENICE EU – funded project [Agreement No. 101006841] "*Horizon 2020 – PHev Towards zerO EmissioNs & Ultimate ICE Efficiency*".

[5] S. Yadla, D. Terber, J. Keuler, M. Maniar, P. Davies *"The Role of E-Boosting in Future Emission Legislations"*, 26th Supercharging conference, Dresden, September 2022.

[6] D. Lee and J. B. Heywood, "*Effects of Secondary Air Injection During Cold Start of SI Engines*", SAE Technical Paper 2010-01-2124, 2010.

Taylor & Francis
Taylor & Francis Group
http://taylorandfrancis.com

Modelling and simulation

Validation and assessment of a mathematical model for centrifugal compressor surge

K. Powers[1], H. Wang[2]*, C. Wilson[2], J. Horsley[2], D. Wood[2], C. Copeland[1], J. Archer[2]

[1]School of Sustainable Energy Engineering, Simon Fraser University, Burnaby, Canada
[2]Cummins Turbo Technologies, Huddersfield, UK

ABSTRACT

The operation of centrifugal compressors is limited by the surge instability at low mass flow rates. Being able to predict the surge limit during early compressor design stages would save manufacturers time and reduce the need for costly experimental testing. In this paper, we assess the mathematical model by Powers *et al.* [1] for its ability to predict the directional change in the surge limit when geometric dimensions are varied. The model is able to match the predicted directional change in surge limits from a data-driven model, and so shows good promise for being a useful tool.

1   INTRODUCTION

Turbochargers are now a common component of many vehicle engine systems. With the drive towards cleaner technology, turbochargers are being combined with down-sized engines in order to achieve the latest emissions regulations. Therefore, it is usual to see turbochargers in a range of applications from large heavy-duty articulated lorries to small passenger cars.

Turbochargers consist of a turbine and a compressor connected by a shaft. The role of the compressor is to raise the pressure (and once cooled, the density) of the air prior to the engine cylinders, thus increasing the amount of oxygen per unit volume. The turbine uses energy from the vehicle exhaust to drive the compressor.

One of the main limitations of compressor operation is compressor surge. Surge is an instability that occurs at low mass flow rates. It is characterised by pressure and flow oscillations that can unbalance the compressor impeller and cause damage to the compressor and its surrounding installation. Even mild forms of surge are undesirable because the noise produced would be off-putting to any vehicle operator.

Predicting the surge limit of a compressor is therefore very important for turbocharger manufacturers and engine designers. Having information about the location of the surge limit and how it is influenced by geometric changes would be especially useful during the early design stages. Often, the surge limit of a new compressor design is only discovered during later design stages, once a prototype has been built and experimentally tested. Therefore, having knowledge of the surge limit to influence design decisions earlier in the design process would save time and money.

---

*Corresponding Author: haizhu.wang@cummins.com

For a surge model to be useful during early design stages it needs to be fast-running. The computation efficiency can to some extent take priority over the quantitative accuracy at this point in the design process; however, it is essential that the model has a good qualitative predictive ability. For example, an early-design surge tool should be able to confidently tell designers whether a surge limit improves or worsens between designs.

Over the past 50 years, there have been many approaches to modelling turbocharger compressors and predicting surge limits.

Computational Fluid Dynamics (CFD) has been a popular tool for assessing flow dynamics because of its ability to model complex 3D flow structures with good accuracy. However, the computational cost of high-fidelity CFD can be extremely high. Conducting a transient CFD simulation of a compressor near surge is of the order of a day per revolution using hundreds of cores running in parallel [2].

There are ways to help reduce this cost, for example, Karim *et al.* [3] reduced the computational time of a transient CFD surge simulation by ensuring the model pipework had a small inlet volume so that the surge was high-frequency and less revolutions were needed to capture it. Also, Righi *et al.* [2] developed a 3D model for an axial compressor that used empirical correlations to predict the performance of the blade-row to reduce the computational cost. However, none of the current approaches would reduce the computational cost of a CFD surge simulation to the point it could be used as a predictive tool in early-design stages.

Recently, machine learning has become a popular modelling approach. This approach means that you train a model on a large data set, then use this model to predict future events or new cases. For example, Hipple *et al.* [4] used a Recurrent Neural Network (RNN) to develop a real-time surge predictor. They trained the model on approximately 60,000 data points to teach it to identify when the turbine rotor speed indicates surge has been reached.

This modelling approach can also be used to predict compressor performance maps and the corresponding surge limit. For example, Ghorbanian and Gholamrezaei [5] used a Rotated General Regression Neural Network (RGRNN) and other machine learning approaches to predict the performance curves of axial compressors based on geometry. They stated that the results of the RGRNN prediction were limited to interpolation, so are not reliable for predicting the performance of a compressor with geometry outside the range of the training set.

Internally within Cummins Turbo Technologies, a similar study has been done to predict how the surge limit for radial compressors changes with geometry. An artificial neural network was trained on a set of more than 600 experimental compressor map data points, and was able to predict surge limits with good accuracy. However, the main limitation of the work is that any future design needs to be within the range of the training dataset to achieve the desired level of accuracy. Also, the model runtime is under 1 hour for training and less than 1 minute for producing predictions, which is very good in comparison to CFD but something even faster could be beneficial for early-design stages.

Often when looking for fast-running models, reduced-order physical models produce good results. Most reduced-order models are based on the work by Greitzer in 1976 [6]. He developed a quasi-steady 1D model that could simulate surge in an axial compressor but this type of model has been used for radial compressors too.

Greitzer's model has been updated and improved upon over the years. For example, both De Bellis and Bontempo [7] and Powers *et al.* [1] have developed 1D models that can capture compressor surge by simulating experimental facilities. In both cases, an unsteady model for the pipework is combined with a steady-state model for the compressor applied as a boundary condition.

The steady-state compressor model by De Bellis and Bontempo [7] has several tuning parameters that are found by minimising the error between the simulated and experimental compressor map for the specific compressor of interest. The full unsteady model is then used to simulate the dynamics of surge, and they get good agreement to experimental data.

Powers *et al.* [1] had a different approach. They developed their steady-state compressor model so that it would have a minimal number of parameters that needed tuning, and attempted to discover universal relations for these so that the compressor model, and hence the surge model, could be fully predictive. They were also able to capture both mild and deep surge dynamics which had not been done before using reduced-order surge models.

Since the model by Powers *et al.* [1] has been developed with the aim of being a predictive model for surge, and the runtime for the model is around 15 secs for a quasi-steady simulation, this is a good candidate for a surge tool for early design stages.

In this paper we will assess the model developed by Powers *et al.* [1] for its potential as a tool to predict how the surge line changes with geometry. In Section 2, we will summarise the model and find relations for two unknown parameters and, in Section 3, we will compare the model with experimental compressor map data to assess its validity. In Section 4, we will conduct a study where some geometric parameters are changed to see the influence this has on the simulated surge limit. These plots are compared with the results from the internal Cummins Turbo Technologies neural network model to determine if the model by Powers *et al.* is capturing the changes in the surge limit correctly. Finally, in Section 5, we will outline our conclusions and any directions for future work.

2 MATHEMATICAL MODEL

Powers *et al.* [1] developed a fast-running model for radial compressors with the capability of simulating both mild and deep surge. They modelled a gas-stand test facility via the schematic shown in Figure 1.
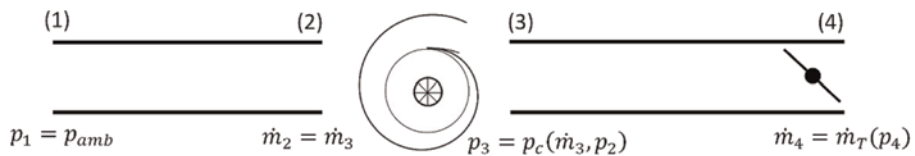

Figure 1. Schematic showing how an experimental facility was modelled mathematically in Powers *et al.* [1]. The inlet and outlet pipe of the compressor were modelled with unsteady flow equations, and steady-state models for the compressor and throttle valve were applied as boundary conditions at (3) and (4) respectively.

They simulated air flow through the test facility pipework via two Partial Differential Equations (PDEs):

$$\frac{\partial p}{\partial t} + \frac{\gamma \kappa^{\frac{1}{\gamma}}}{A} p^{\frac{\gamma-1}{\gamma}} \frac{\partial \dot{m}}{\partial x} = 0,$$

$$\frac{\partial \dot{m}}{\partial t} + A\frac{\partial p}{\partial x} + \frac{\kappa^{\frac{1}{\gamma}}}{A}\frac{\partial}{\partial x}\left(\frac{\dot{m}^2}{p^{\frac{1}{\gamma}}}\right) + \frac{fS\kappa^{\frac{1}{\gamma}}}{2A}\frac{\dot{m}^2}{p^{\frac{1}{\gamma}}} = 0,$$

where p is pressure, and $\dot{m}$ is the mass flow [1].

The behaviour of the compressor was included by developing a steady-state model and applying this as a boundary condition to the pipe. This steady-state compressor model was developed from first-principles. Powers *et al.* began with the equations for conservation of mass, momentum (in a rotating frame), and energy [1]. They then assumed the flow was adiabatic, an ideal gas ($p = \rho R T$), a perfect gas ($\gamma =$const.), had no dissipation losses apart from skin friction, and had only small variations in the axial direction, so the equations could be reduced to a single Ordinary Differential Equation (ODE) for the impeller,

$$\frac{\partial \rho}{\partial r} = \frac{-\rho q^2\left(\frac{1}{r}+\frac{1}{h}\frac{\partial h}{\partial r}\right) - \gamma\Omega^2 r^3 h^2\rho^3 + \gamma f\rho q^2\left(\frac{n_b}{2\pi r}+\frac{1}{h}\right)}{\left(\frac{\gamma+1}{2}\right)q^2 - (\gamma-1)E_I r^2 h^2 \rho^2},$$

for the diffuser,

$$\frac{\partial \rho}{\partial r} = \frac{-\frac{\rho q^2}{r} - r^2 h^2\rho^3\left(\gamma\frac{u_\theta^2}{r}+(\gamma-1)u_\theta\frac{\partial u_\theta}{\partial r}\right) + \gamma\frac{f}{h}\rho q^2}{\left(\frac{\gamma+1}{2}\right)q^2 + (\gamma-1)\left(\frac{u_\theta^2}{2}-E_D\right)r^2 h^2\rho^2},$$

and for the volute,

$$\frac{\partial \rho}{\partial s} = \frac{\dot{m}^2\rho fS - 2\rho\dot{m}^2\frac{dA}{ds}}{(3-\gamma)\dot{m}^2 - 2(\gamma-1)E_V\rho^2 A^2},$$

where ρ is the density, r is the radial direction through the impeller or diffuser, and s is the arclength through the volute [1]. Here,

$$E = \frac{|\boldsymbol{u}|^2}{2} + \frac{\gamma}{\gamma-1}\frac{p}{\rho}$$

is the specific total energy,

$$u_\theta = \frac{\Omega r_{tip}^2}{r} e^{-\frac{f}{h}(r-r_{tip})},$$

is the tangential velocity, and $q = \dot{m}/2\pi$ is mass flow per radian [1].

Finally, Powers *et al.* modified the above formulation in order to simulate some of the physical phenomenon that couldn't be captured by the simplified 1D model. In reverse flow, a shear loss was included at the impeller-diffuser interface to account for the large sudden change in tangential velocity when the flow makes contact with the impeller

blades [1,8]. This was included as an instantaneous pressure loss,

$$p_D = p_I - v(u_{\theta I} - u_{\theta D})^2,$$

where subscripts I and D denote the impeller and diffuser side of the interface respectively [8].

In forward flow, stall functions were included in the definition of mass flow rate

$$\dot{m} = \xi(\beta)\eta(\alpha)A\rho u_r$$

to account for incidence and recirculation losses [1]. Powers *et al.* developed an impeller inlet stall function of

$$\xi(\beta) = \frac{1}{\frac{1}{2}\left(\frac{\tan\beta_B}{\tan\beta} + \frac{\tan\beta}{\tan\beta_B}\right) + \widehat{a}\left(1 + \frac{1}{2}\frac{\tan\beta}{\tan\beta_B}\right)\left(\frac{\tan\beta_B}{\tan\beta} - 1\right)^2},$$

where β_B is the average inlet blade angle and β is the flow angle into the impeller [8]. This stall function represents the fraction of the impeller channel available to the flow [1,8]. For example, $\xi(\beta_B) = 1$, so when the flow angle perfectly matches the blade angle (zero incidence), there is no stall and the entire channel is available to the flow. However, $\xi \to 0$ as $\beta \to 90^\circ$, so as the flow enters more tangentially, stalling occurs that effectively blocks the impeller channel, restricting the area available to the flow.

In this paper, we propose an alternative stall function of

$$\xi(\beta) = \frac{1}{1 + \widehat{a}\left(1 + 2\frac{\tan\beta}{\tan\beta_B}\right)\left(\frac{\tan\beta_B}{\tan\beta} - 1\right)^2}.$$

Mathematically, the difference between the stall function in Powers *et al.* [8] and the stall function proposed here is a change from the assumption that the gradient of the stalled velocity is zero at zero flow ($du_r/d\dot{m}(0) = 0$) to

$$\frac{d^2 u_r}{d\dot{m}^2}(0) = 0.$$

Since we do not know physically what happens to the stalled velocity as we approach zero mass flow, both of these assumptions are equally likely to reflect the truth.

The reason behind the suggested change is that now $\xi(\beta) \equiv 1$ when $\widehat{a} = 0$. This means that the stall parameter, $\widehat{a}$, has a clearer definition because it now directly controls the level of stalling.

For consistency, we also propose that the diffuser stall function, which accounts for diffuser flow recirculation, becomes

$$\eta(\alpha) = \frac{1}{1 + \widehat{b}\left(1 + 2\frac{\tan\alpha}{\tan\alpha^*}\right)\left(\frac{\tan\alpha^*}{\tan\alpha} - 1\right)^2},$$

where α^* is the critical angle for recirculation in the diffuser, α is the flow angle into the diffuser, and stall parameter $\widehat{b}$ now directly controls the level of stalling.

2.1 Parameter relations

In the model presented above, there are some parameters that change with different compressors but do not directly relate to geometry. For example, the friction factor f also encompasses losses associated with 3D effects that the 1D model cannot capture. Therefore, the value of the friction factor changes for different compressors and impeller rotational speeds. Parameters like these need relations so the model can predict the surge limit accurately with just geometric inputs.

To find these parameter relations we collected geometric data and corresponding compressor maps for eight different compressors. The model presented above does not simulate any effects of casing treatments, so compressors selected had no casing treatments. To try and capture the full range of compressors, we selected a large range of sizes (wheel diameter ranged from 52mm to 193mm).

To find a relation for the friction factor, the steady-state compressor model was run using the specified geometry to generate a simulated compressor map. For each speed line in the compressor map. Figure 2 plots these values for f against the tip-speed of the impeller as circles. The colours correspond to the size of the compressor.

From this a statistical relation for the friction factor was found

$$f = f_1 \left(\left(f_2 \Omega r_{tip} \right)^2 + \frac{1}{r_{tip}} \right)$$

where the fitting factors $f_1 = 0.0022 \cdot m$, and $f_2 = 0.0153 \cdot s \cdot m^{3/2}$, which gave an R^2 value of 0.9484. Curves showing this relation have been added to Figure 2 to show the fit.
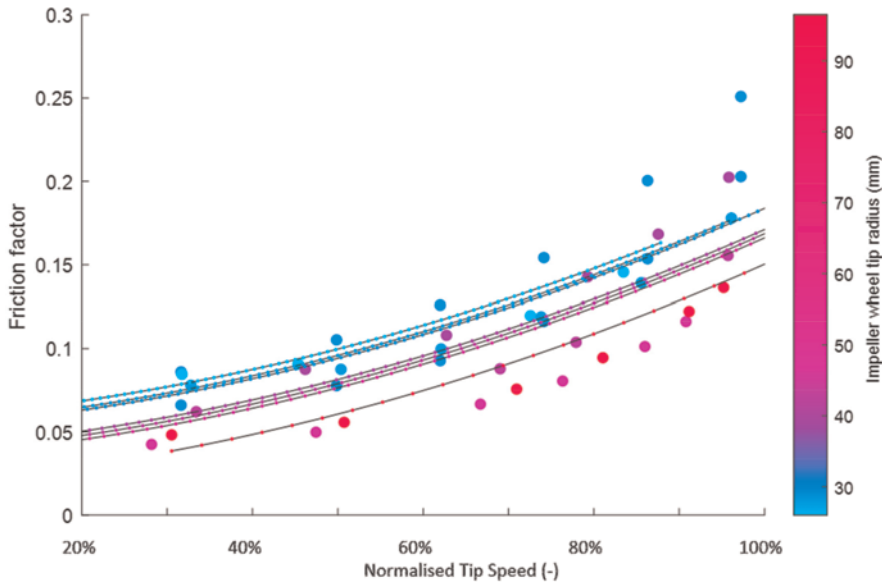

Figure 2. Lines showing curves of predicted values for friction factor, f. Circles show optimal values of f found via least-squares fits of simulated individual speed lines and experimental compressor map data. The colour scale shows how the relation changes with compressor size.

Similarly, relations need to be found for the impeller and diffuser stall factors, $\widehat{a}$ and $\widehat{b}$, and the critical angle α^*. For the stall factors, Powers *et al.* [1,9] used the amplitude of mild and deep transient surge data to find suitable values or relations. Unfortunately, due to resource and time constraints, we only have access to the steady-state compressor map data so cannot do the same here. Instead, we choose $\widehat{a}$ so that the minimum pressure seen in the deep surge cycle is close to the choked flow limit. Mathematically, this means that

$$\widehat{a} = \frac{\tan\beta_B u_{choke}}{2\Omega r_{hub}}$$

where u_{choke} is the radial velocity at the choked flow limit. For the diffuser stall factor, we know that this is less than the impeller stall factor, and by setting $\widehat{b} = 0.5\widehat{a}$ we got good results.

However, for the critical angle α^*, we can use the steady-state compressor map data to give us an idea of a relation. Again, we run the steady-state compressor model using the specified geometry to generate a simulated compressor map. We then compare the surge limit to the surge limit of the experimental compressor map to give an estimate for the optimal value of the critical angle.

Plots these estimates against the tip-speed of the impeller as circles. The colours correspond to the size of the compressor.

Consider the flow angle entering the diffuser, α. We know that $\tan\alpha = u_\theta/u_r$ at the impeller tip. This means there is a simple relation between the tangential velocity, u_θ, at the impeller tip (the tip-speed) and the flow angle. Therefore, it appears sensible to look for a relation between $\tan\alpha^*$ and the tip-speed.
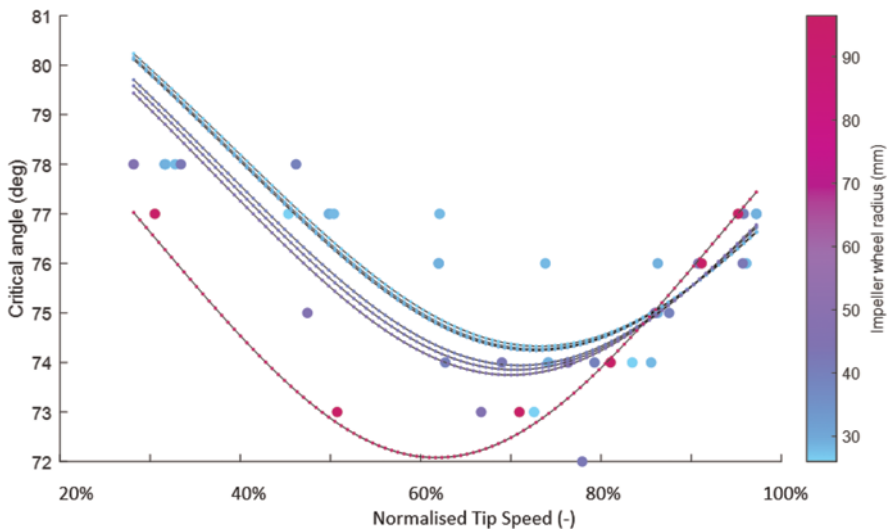

Figure 3. Lines showing curves of predicted values for the critical angle, α^*, at which stalling occurs in the diffuser for different impeller wheel sizes. Circles show estimates for the optional value of α^* found by minimising the error between experimental and simulated surge limits. The colour scale shows how things change with compressor size.

After statistical analysis to find the coefficients, the relation we propose is

$$\tan\alpha^* = f_3\left(f_4\Omega r_{tip} - \left(f_5 - 812r_{tip}\right)\right)^2 + \left(3.738 - f_6 r_{tip}\right)$$

where the fitting factors $f_3 = 4.432 \times 10^{-5} \cdot \text{m}^{-2}$, $f_4 = 1 \cdot \text{s}$, $f_5 = 487 \cdot \text{m}$, $f_6 = 6.69 \cdot \text{m}^{-1}$, which gives an R^2 value of 0.6933. Curves showing this relation have been added to. The fit is better for the larger compressors, but this reflects experimental data that diffuser stall is more significant in larger compressor and at high rotational speeds.

3   MODEL VALIDATION

We can now compare the mathematical model for surge against the compressor map data of a variety of different compressors to assess its validity.

As shown in Powers *et al.*'s first paper, the surge limit can be approximated by taking the local maximum of the compressor characteristics [9]. In their later work, they demonstrated that this limit might be conservative because the unsteady pipework model identified a surge limit to the left of the local maxima [1]. However, we are prioritising a fast-running model and therefore have chosen to run the steady-state compressor model and locate the local maxima as an approximate surge limit because this is the quickest approach computationally.

The compressor map data we use in the comparison is all from compressors without any casing treatments, and for impeller wheel diameters within the range of 52mm to 193mm.

Figure 4 shows the resulting comparisons between the steady-state mathematical model and experimental data. It is clear that the fit between the simulated map and experimental data has some issues. The choke limit is often not approximated well, especially for the small compressors, and the model struggles to capture the correct pressure values for the highest speed lines of the largest compressors.

It was stated in Powers *et al.* [9] that the model had some difficulty when the flow approaches sonic velocities. The equation for rate of change of density with respect to radius has an asymptote at sonic velocity when the Mach number of the flow approaches one, so any numerical solver will have problems in accurately resolving the solution, improved numerical methods are being investigated to address this issue. In choked flow conditions the radial velocity approaches sonic conditions, and for high impeller rotational speeds (particularly for large impellers) the tangential velocity approaches sonic conditions. Therefore, the current version of the model will have issues matching experimental data in these regions.

However, this is a very simple fast-running model with only two fitted parameters. Therefore, the fact that the model is able to capture the general shapes of the compressor maps is a good achievement. Moreover, there appears to be a good fit for the surge limit for all of the compressor sizes, which is the main importance because we are aiming to use this model as a tool to predict changes in the surge limit as we alter geometry.
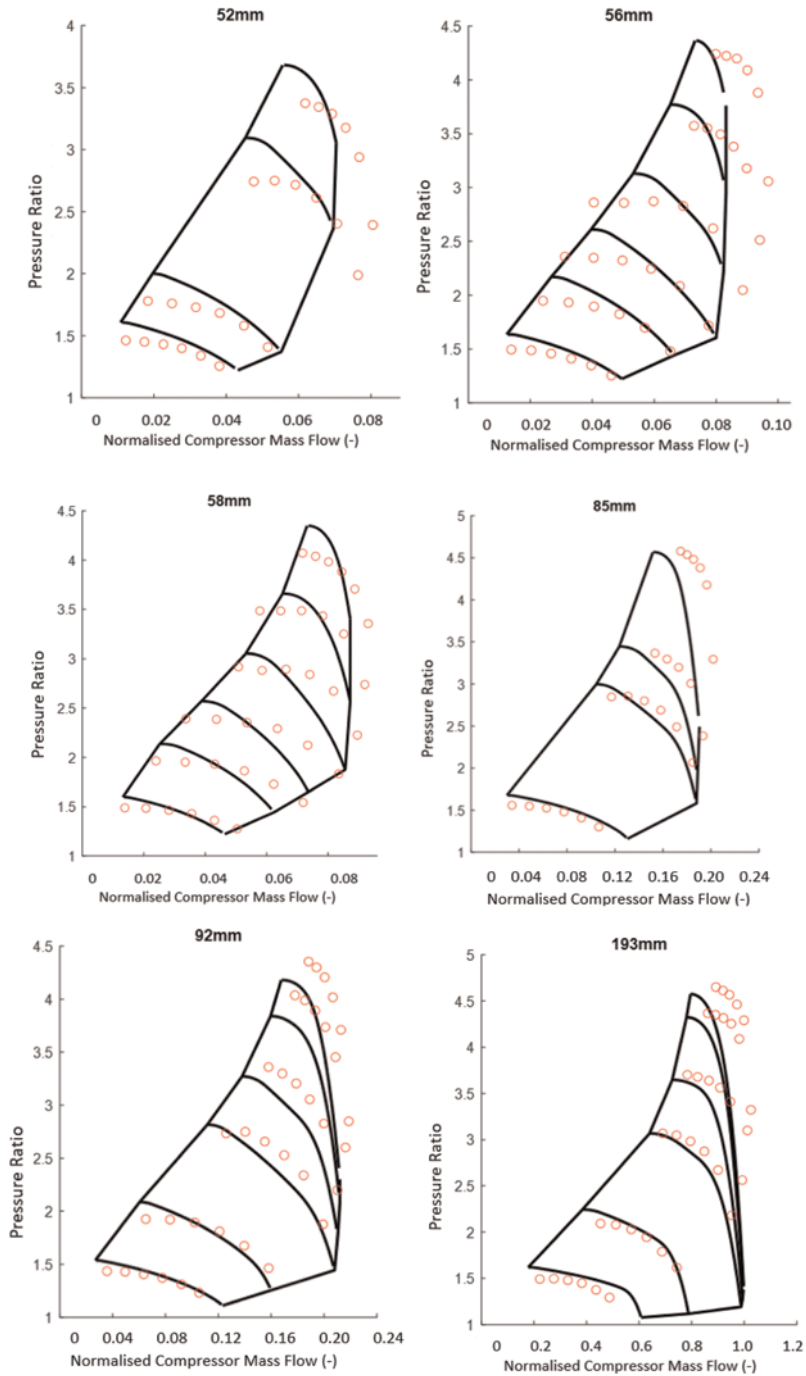
Figure 4. Comparison between simulated compressor map using steady-state mathematical model and parameter relations from Section 2 (solid lines) and experimental data (red circles).

4   MODEL ASSESSMENT

As stated in the introduction, a data-driven model for predicting how the surge limit changes with geometric considerations has been developed internally within Cummins Turbo Technologies. This model was trained by back-propagation of artificial neural network consisting of five hidden fully connected layers with an Adam optimizer, using a dataset of more than 600 physical compressor surge points from gas stand experimental testing. All of the compressors used in the training dataset had casing treatments, and the impeller wheel diameter ranged from 64mm to 98mm.

The mean absolute percentage error (MAPE) for the model is 3.7% and 0.5% for mass flow parameter and pressure ratio, respectively – provided predictions are made within the training range.

In order to assess the mathematical model presented in this paper for its potential as a tool for indicating how the surge line shifts with geometric changes, we will vary individual geometric inputs and compare the results to the same change in the data-driven model.

We will use the 85mm compressor from Section 3 as the baseline geometry in both models, and vary the following five inputs to see the effect on the surge limit: impeller hub diameter, impeller inlet shroud diameter, impeller tip diameter, diffuser gap, and diffuser diameter (see Figure 5).
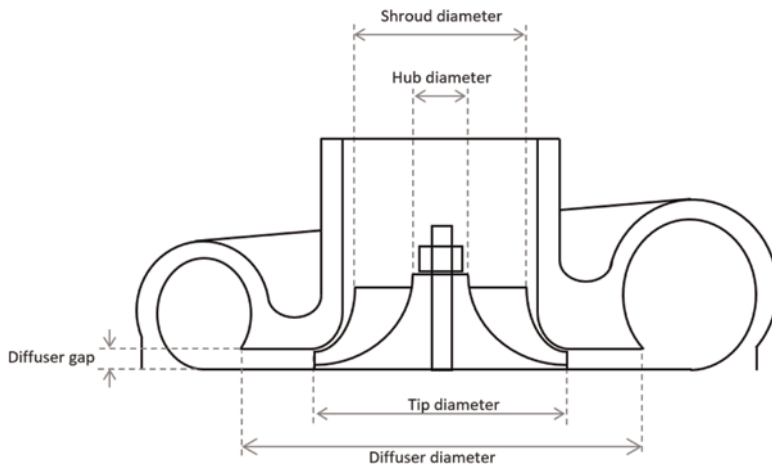

Figure 5. Diagram showing the five geometric input that are changed individually to see the effect of the surge limit.

It is important to know that in the development of their mathematical model, Powers *et al.* [1,9] made an assumption that the impeller wheel did not turn the flow from axial to radial but remained fully in the radial direction. Therefore, changing the hub and shroud diameters in this model is different to a typical impeller. Figure 6 shows this difference.
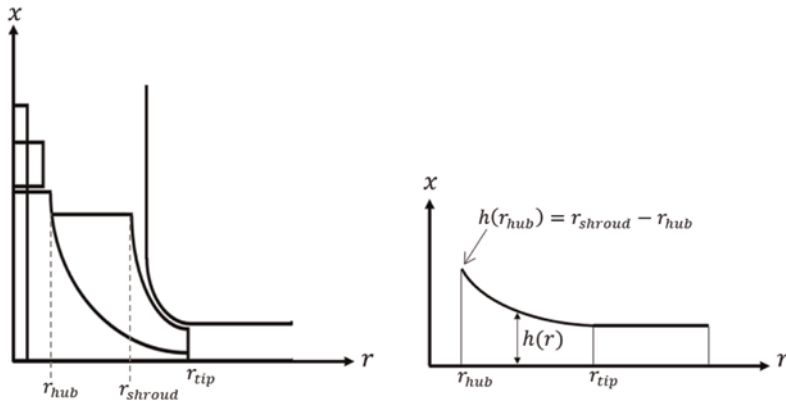
Figure 6. Diagram showing a standard impeller geometry (left) and the impeller geometry in Powers *et al.*'s [1] mathematical model. Powers *et al.* assume the flow is purely radial instead of turning from axial to radial, so the geometry is different to account for this.

The results of varying the five geometric dimensions for the mathematical model and the data-driven model are shown in Figure 7.
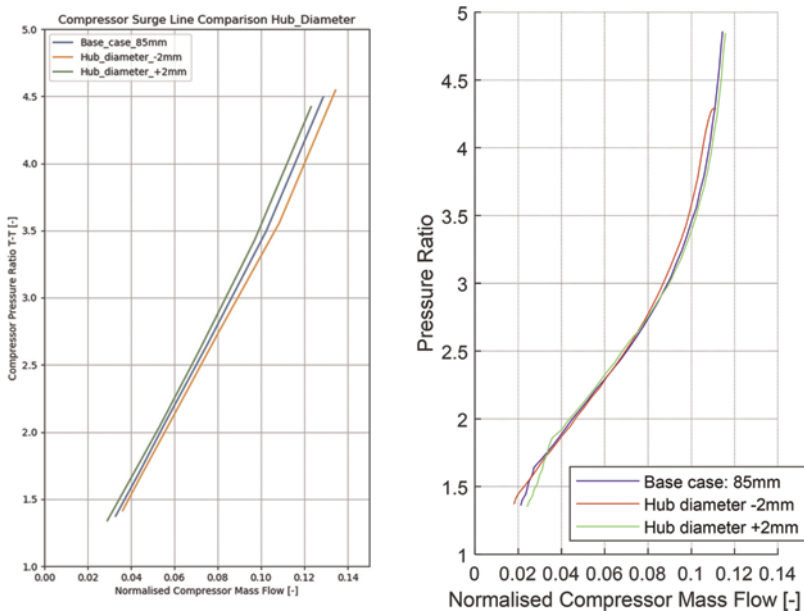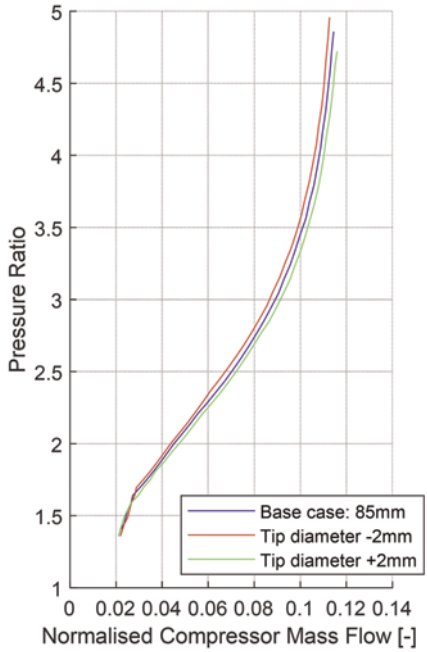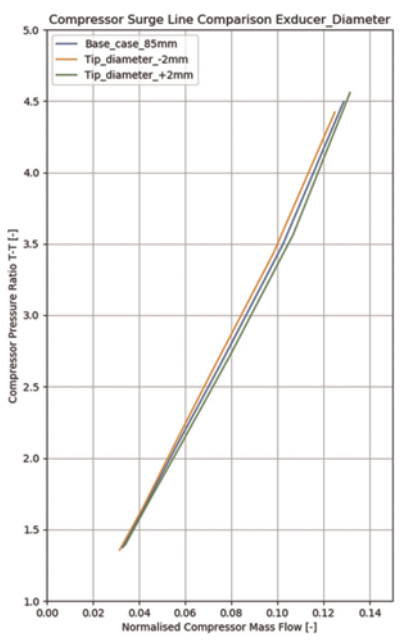

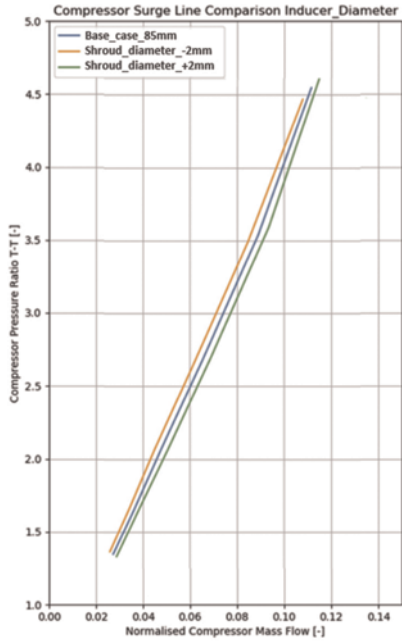**Figure 7. Comparison between data-driven model (left) and mathematical model (right).**
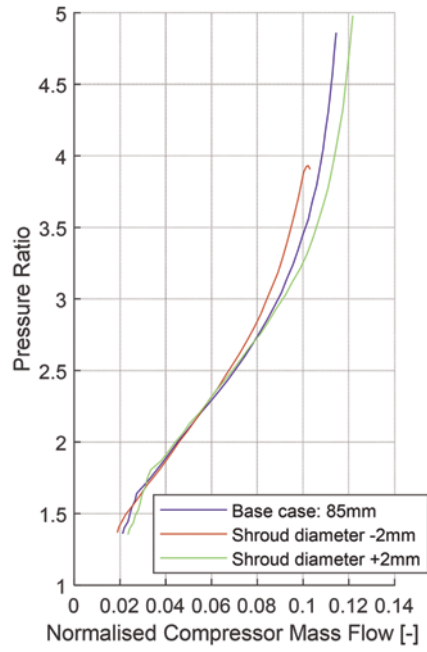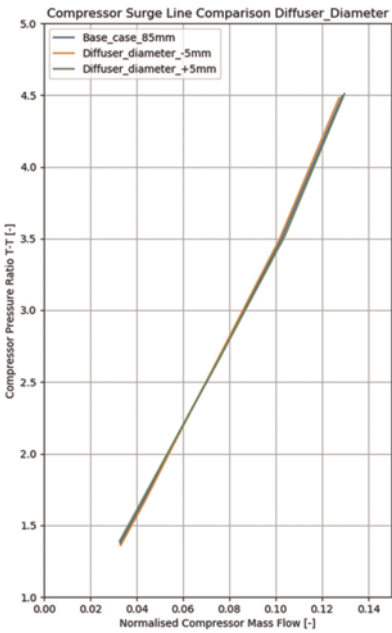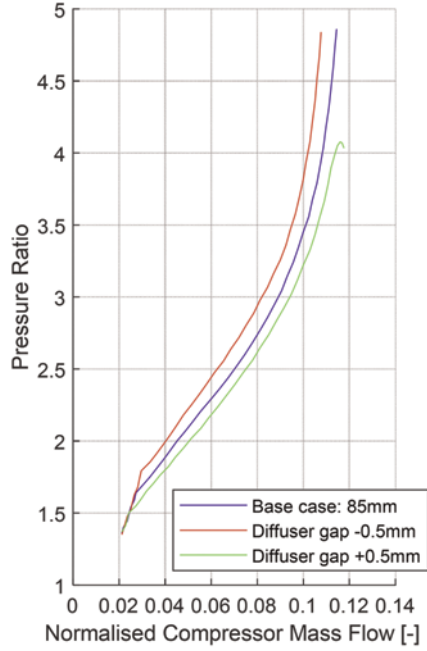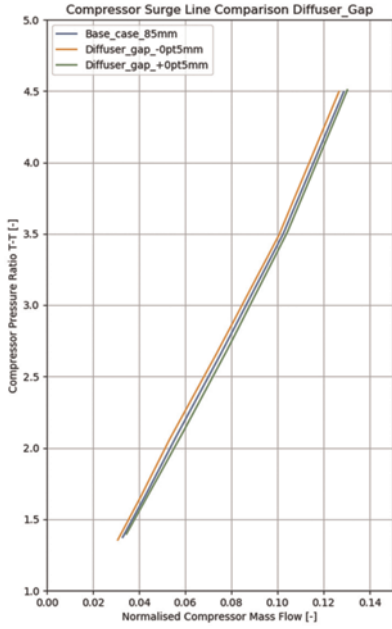
Figure 7. (Continued)
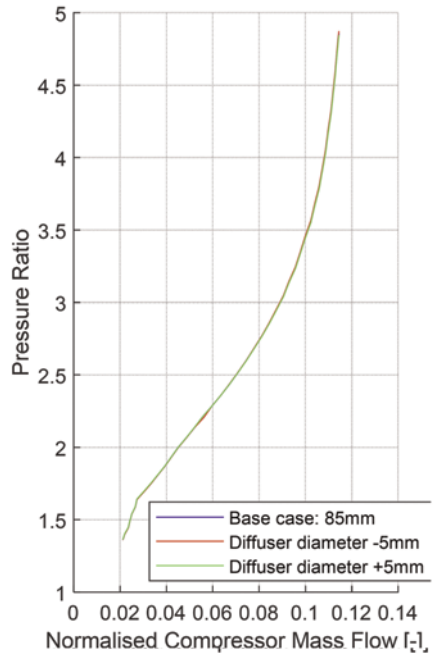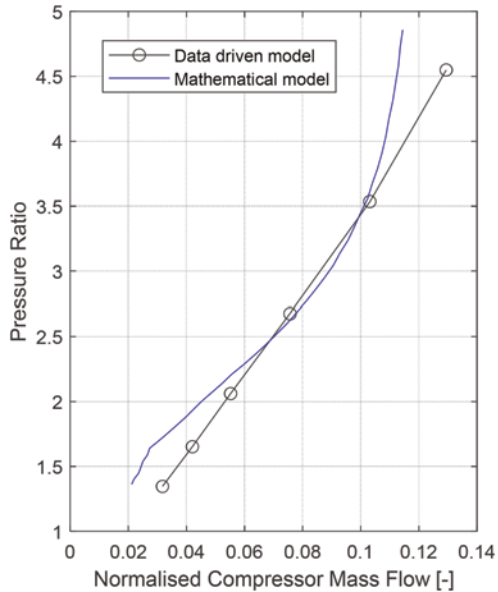
Figure 7.   (Continued)

Figure 8. Comparison between surge limit for the 85mm base case between the mathematical model (blue) which assumed no casing treatments, and the data-driven model (black circles) which assumes there is casing treatments.

In all cases, the mathematical model agrees with the data-driven model in terms of the directional shift in the surge limit as we change individual parameters. Therefore, this gives us confidence that the model by Powers *et al.* [1] can be used as a tool to help designers understand the implications of changing geometry on the surge limit.

As can be seen in Figure 8, the surge limits in the data-driven model are more linear than the surge limit curves of the mathematical model. However, we believe this is due to the difference between compressors with and without casing treatments. The mathematical model predicts the surge limit for a compressor without any casing treatments, whereas the data-driven model has been trained on data consisting of compressors that all include casing treatments.

Comparing the plots showing the change in hub diameter, we see that the effect on the surge limit is relatively small, with a larger shift at higher pressure ratios. The data-driven model predicts a larger change in surge limit than the mathematical model. Also, the mathematical model predicts the surge limits crossing, but this doesn't occur in the data-driven model.

This is the case where we have the worst match between the data-driven model and the mathematical model. For the mathematical model, changing of hub diameter will result in a change in the 'meridional length' through the impeller as well as the change in inlet area. We can see this in Figure 6 because the inlet of the impeller is defined to be at radius r_{hub} so changing this will change the overall size of the impeller, not just the inlet area through $h(r_{hub})$. Therefore, this miss-match is not a surprise because this effect will not occur in the data driven model.

When studying the shroud diameter plots, we can see that the directional change of the surge limits match, but the extent of the change in surge limit is different. In the data-driven model, the shift in surge limit is pretty constant at all pressure ratios, however, in the mathematical model, the shift in surge limit is larger at higher pressure ratios. Again, this could be due to the difference in modelled impeller geometry shown in Figure 6.

When changing the tip diameter in the mathematical model, the diffuser and volute will also change in size because the diffuser radius ratio, and the ratio between the radius to the centroid of the volute and the tip, are kept constant. Also, the tip width was left unchanged, so the wheel exit area will change with the tip diameter. These conditions were repeated to obtain the equivalent results for the data-driven model. As can be seen, we get a good agreement between the two models for this case. Both models predict that the change in the surge limit is more significant at higher pressure ratios.

We also get good agreement for the variation in diffuser gap. Again, both models predict that the shift in surge limit is more significant at higher pressure ratios. In the mathematical model, the tip width is set to the same value as the diffuser gap, so the tip width was changed to replicate this in the data-driven model results.

Finally, for the change in diffuser diameter, both models agree and seem to suggest this has very little influence on the surge limit on its own. Therefore, any real effects of changing this would be due to a combination of effects instead.

5 CONCLUSIONS

In this paper we have assessed the mathematical model developed by Powers *et al.* [1] for its ability to create a surge tool during early compressor design stages. The idea is that this tool has the ability to qualitatively predict how the surge limit shifts between different geometric designs.

To use the model by Powers *et al.*, we first found relations for two unknown parameters (the friction factor and the critical angle at which stall occurs in the diffuser) and validated the model against a range of compressors.

We then varied geometric inputs for the model and compared the shift in the resulting surge limit to equivalent results from a data-driven model. The two models agree with the directional change of the surge limit within the confidence intervals of the training dataset for the data-driven model. Therefore, this gives us confidence that the mathematical model is also correctly predicting the expected directional shift in the surge limit.

The results in this paper have indicated that the model by Powers *et al.* [1] is a good candidate for a fast-running, predictive surge tool. However, future work is still necessary to achieve this goal. We have been investigating ways to deal with the numerical instability of the solvers as we approach sonic flows to improve the compressor model in regions of choked flow and high impeller rotational speeds. We plan to improve the model by Powers *et al.* so that it can capture the effects of backsweep and diffuser recirculation more accurately. We also plan to include casing treatments and the option of a vaned diffuser, so that the tool would have more versatility. Finally, we would need to perform more surge limit investigations to assess validity and improve confidence in such a tool.

NOMENCLATURE

A	Cross-sectional area
$\hat{a}$	Impeller stall parameter
$\hat{b}$	Diffuser stall parameter
E	Specific total energy
f	Friction factor
h	Height
$\dot{m}$	Mass flow rate
n_b	Number of blades
p	Pressure
q	Mass flow per radian
r	radius or radial direction
R	Specific gas constant
s	Arclength
t	Time
T	Temperature
u	Velocity
x	Distance
α	Flow angle into the diffuser
β	Flow angle into the impeller
γ	Specific heat ratio
η	Diffuser stall
κ	Isentropic constant
ν	Shear loss coefficient
ξ	Impeller stall
ρ	Density
Ω	Impeller rotational speed
Subscripts:	
amb	Ambient
B	Blade
c	Compressor
D	Diffuser
hub	Impeller hub

(*Continued*)

(*Continued*)

Subscripts:	
I	Impeller
r	radial
T	Throttle
tip	Impeller tip
V	Volute
θ	Tangential
*	Critical value

REFERENCES

[1] Powers K., Kennedy I., Archer J., Eynon P., Horsley J., Brace C., Copeland C. and Milewski P., "A New First-Principles Model to Predict Mild and Deep Surge for a Centrifugal Compressor," *Journal of Energy*, vol. 244, p. 123050, April 2022.

[2] Righi M., Pachidis V., Konozsy L., Giersch T. and Schrape S., "Experimental Validation of a Three-dimensional Through-flow Model for High-speed Compressor Surge," *Journal of Aerospace Science and Technology*, vol. 128, p. 107775, September 2022.

[3] Karim A., Miazgowicz K. and Lizotte B., "Automotive Turbochargers Compressor Onset of Surge Prediction using Computational Fluid Dynamics," in *SAE World Congress & Exhibition*, Detroit MI, 2015.

[4] Hipple S., Bonilla-Alvarado H., Pezzini P., Shadle L. and Bryden K., "Using Machine Learning Tools to Predict Compressor Stall," *Journal of Energy Resources Technology*, vol. 142, p. 070915, April 2020.

[5] Ghorbanian K. and Gholamrezaei M., "An Artificial Neural Network Approach to Compressor Performance Prediction," *Journal of Applied Energy*, vol. 86, pp. 1210–1221, July 2009.

[6] Greitzer E., "Surge and Rotating Stall in Axial Flow Compressors – Part I: Theoretical compression system model," *Journal of Engineering for Power*, vol. 98, pp. 190–198, 1976.

[7] De Bellis V. and Bontempo R., "Development and validation of a 1D model for turbocharger compressors under deep-surge operation," *Journal of Energy*, vol. 142, pp. 507–517, January 2018.

[8] Powers K., Kennedy I., Brace C., Milewski P. and Copeland C., "Development and Validation of a Model for Centrifugal Compressors in Reversed Flow Regimes," *Journal of Turbomachinery*, vol. 143, p. 101001, October 2021.

[9] Powers K., Brace C., Budd C., Copeland C. and Milewski P., "Modeling Axisymmetric Centrifugal Compressor Characteristics from First Principles," *Journal of Turbomachinery*, vol. 142, p. 091010, September 2020.

Novel shroud treatment for turbocharger centrifugal compressor surge enhancement

M.E. Barrera-Medrano, P. Ale Martos

Imperial College London, London, UK

Y. Hayashi

Mitsubishi Heavy Industries Ltd, Japan

R. Martinez-Botas

Imperial College London, London, UK

ABSTRACT

A turbocharger when operating at low speed and high load has a limitation given by compressor, due to surge [1–8]. The surge limit of the turbocharger compressor will limit the minimum flow at which the engine can operate [1,6–8]; therefore, compressor surge margin is a significant constraint at low-end torque operating area of the engine, corresponding to full load at very low engine speed. This paper presents a novel turbo-compressor inlet shroud treatment for surge limit enhancement. This innovative shroud design aims to "accommodate" the flow when flow-separation happens by re-conducting the reverse flow back to inflow direction by means of the presence of an annular cavity in the vicinity of the compressor impeller tip. Numerical results obtained from the initial computational assessment of this concept suggest that the axial flow distortion, commonly encountered when compressor stalls, is retarded by the presence of the annular cavity, which "corrects" the flow direction, and thus retarding stall propagation when operating at low flow rates, near surge.

Furthermore, an experimental campaign was carried out at Imperial College London experimental facilities to proof the feasibility of the presented shroud treatment on a turbocharger centrifugal compressor for automotive application. Experimental results suggest that the presence of a cavity at compressor inlet facilitates the re-entering of flow reversal at compressor inlet when compared to equivalent traditional compressor shroud design.

1   INTRODUCTION

The operating range of a centrifugal compressor is generally restricted by the inception of surge and rotating stall [1,2,5–7]. The main difference between rotating stall and surge lies in the severity of the disruption occurring to the flow. Compressor stall is a two-dimensional (2-D) or three-dimensional (3-D) instability characterized by pressure distortions and circumferential mass flow that revolve around the compressor [2,6,7]. However, during stall, the distorted flow remains in the forward direction at all times; and the averaged flow through the compressor is steady. Moreover, surge is a one-dimensional instability characterized by oscillations in area-averaged mass ow and pressure rise, resulting in a complete flow disruption through the compressor. During surge, the mass flow variations and the flow passing through the compressor pulses, therefore the compressor is no longer under stable operation. Surge and stall lead to flow and pressure oscillations in the centrifugal compressor and consequently the

aerodynamic performance and efficiency of the centrifugal compressor are negatively affected [6–8]. During the last decades, many studies have been conducted to improve the operating stability of centrifugal compressors. Both passive and active methods have been suggested to enhance compressor stability, mainly focused on surge margin enhancement.

As a passive method for stall control, casing treatment is usually applied by changing the shape of the shroud or the inlet duct, generating a recirculation area that reduces the blockage close to the shroud wall. This approach is known to considerably extend the operating range of compressors by controlling the trajectory of the tip leakage flow. Passive methods are usually quite efficient in improving the operating stability of centrifugal compressors but reduce the efficiency by inducing additional aerodynamic losses. The ported shroud concepts presented in this study propose to minimize the reduction in efficiency of a centrifugal compressor by a recirculation of the flow in the normal direction of the main flow stream.

This study presents a new shroud design concepts linked to an annular cavity, to achieve better surge margin. To assess the effects of the new designs on the compressor performance, four different concepts were evaluated. The angle and width of the cavity port and the location of the ported shroud were selected as the design variables. The aerodynamic performance of a compressor with ported shroud is analysed by using 3-D Reynolds-averaged Navier Stokes (RANS) equations.

1.1 Hypothesis behind the idea – Annular shroud treatment

This novel compressor ported shroud design arose from the analysis of the CFD simulation carried out on the reference compressor used in this study. The numerical analysis was focused on near surge operation operating condition when flow reversal is prompt to occur. When analysing the streamlines at the vicinity of impeller inlet at near surge operation, two main flow separation regions were identified – near blade tip and near splitter tip. It is based on this observation that the authors suggested that the presence of an annular cavity located near impeller tip region around the compressor shroud casing might "accommodate" the flow when flow-separation happens by re-directing the reverse flow back to inflow by means of the "annular shroud treatment".

As a result, axial flow distortion, commonly encountered when compressor stalls, is retarded by the presence of this ported shroud, thus retarding stall propagation when operating at low flow rates, near surge. Therefore, this hypothesis suggests that the presence of a ported shroud at compressor inlet facilitates the re-entrance of possible flow reversal prior compressor inlet by reducing the incidence angle at the impeller blade leading edge due to the ported shroud. This "surge enhancement" concept idea arose from the analysis of the results of the CFD simulation carried out using the original MHI centrifugal compressor geometry and with a pulsating outlet boundary condition of 66.67Hz pulse frequency, being the reference operating condition in the current study. When analysing the unsteady CFD results for the reference case original compressor and pulsating outlet boundary, two main areas of flow separation were identified blade tip and splitter tip. Figure 1 shows a sketch of these flow-separation locations based on the obtained streamlines for the reference condition.

Based on the streamlines and the general flow behaviour when stall inception occurs (low flow rates), this research led to an innovative passive solution/new shroud concept for compressor surge enhancement – "Compressor Cavity Treatment".
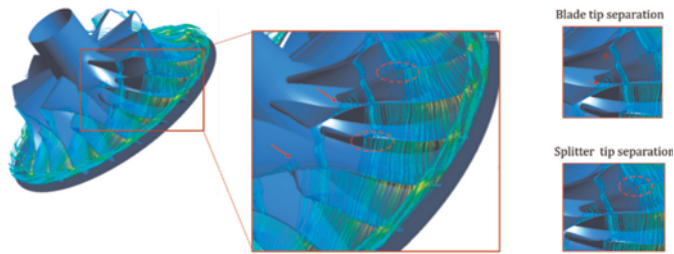
Figure 1. Reference compressor rotor - Streamlines at near surge operation.

In a previous work on vaneless centrifugal compressor surge, Uchida et al [11] developed a casing treatment that featured a curved wall cavity. The aims of the investigation were to study the surge characteristic of a turbocharger compressor, and how different dimensions of the casing treatment cavity effects on the compressor efficiency and the surge limit. As a result, it was found that the optimum casing treatment configuration reduced the surge flow rate by 30 % relative to a conventional compressor. Observing the fluid dynamics in more detail, it was identified the existence of a big vortex region in the shroud side after and before the impeller leading edge in operating points close to surge, Figure 2. Based on this, it was concluded that it is important to control these vortices to improve both, the surge limit and the efficiency of the compressor. The casing treatment suggested on this research aimed to reduce the low-pressure region (the recirculating region) created after the leading edge.

Uchida et al. [11] designed a casing treatment concept with six cavities delimited by spoon-like curved wall, and two slits located in the shroud of the compressor housing, see Figure 3. The shape of the cavities was designed to smoothly change the
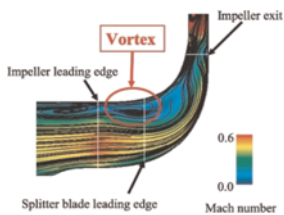

Figure 2. Streamlines and Mach number at one compressor passage at near surge point [11].
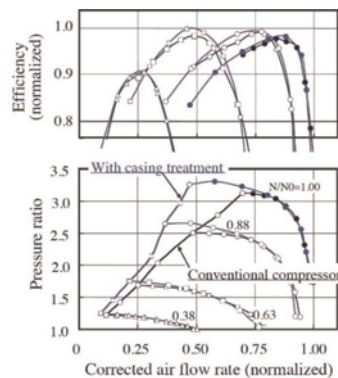

Figure 4. Compressor map and efficiency plotted for no casing treatment case (in black) and best case with casing treatment (in blue) [11].
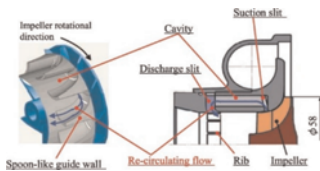

Figure 3. Geometry for a casing treatment concept with six cavities develop by [11].

recirculation flow velocity from the circumferential to the axial direction. The location and the width of the two slits in the casing treatment were investigated experimentally to improve the surge margin of the compressor. Compared to a conventional compressor, with no casing treatment, they found an improvement on the surge limit over the entire range of pressure ratios. They did not observe any decrease in efficiency. In fact, efficiency increased for all four-line speeds studied. These correlations can be seen in Figure 4 where the compressor map and its efficiency lines are plotted for the case without casing treatment (in black) and the case where the best of the casing treatment geometries studied is included (in blue).

By analysing the flow field at the impeller channel, one can see how the vortex created upstream of the suction slit disappears. However, the large vortex that occurs downstream of the suction slit cannot be controlled with the casing treatment, see Figure 2. For that reason, in this work the cavities are studied in two different locations, the impeller leading edge and the splitter blade leading edge.

Halawa et al. [10] presented a numerical study of a casing treatment grooves focused on optimizing the parameters which can enhance the centrifugal compressor performance during stall. The authors considered three parameters defining the casing grooves, cross section aspect ratio (the groove height to width ratio), groove location and number of grooves. They found that the best location for the groove is at the full blades leading edge because the stall area can be minimized and controlled. Also, it was found that by increasing the number of grooves, the surge margin (SM) increases and the isentropic efficiency decreases, but the stall area at the shroud surface decreases in size and its location is shifted toward the blades trailing edge. The values of the compressor performance can be seen in Figure 5 where in the left is shown the pressure ratio again the mass flow, and on the right side the efficiency for each case.
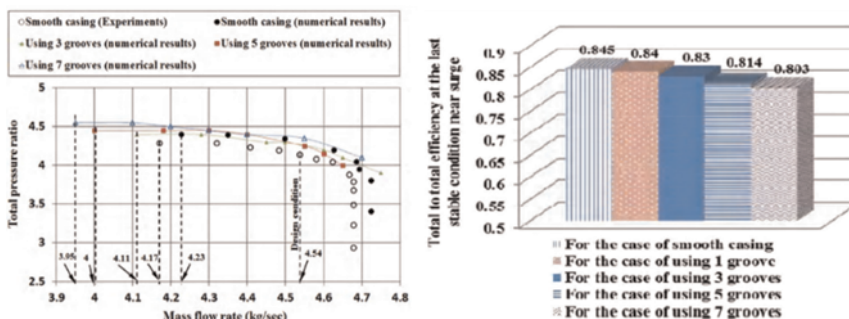

Figure 5. Compressor performance in PR (left) and efficiency (right) [10].

To prove the hypothesis behind the ported shroud concept considered in this study – "soothing" axial flow distortion (incidence angle) by accommodating/redirecting the reverse flow back to main inflow - four different ported shroud designs (cavities) have been prototyped and tested at Imperial College facilities. The four cavity designs (shape) and locations were defined based on the analysis of the flow structure and streamlines obtained from CFD simulation. Figure 6 shows a sketch of the four tested concepts:

Looking at Figure 6, one can observe that the cavity design/shape is slightly different when comparing "Blade Cavity" cases to "Splitter Cavity" cases. The reason behind

these different cavity shapes at the different locations is based on the analysis of the streamlines showing the behaviour of the flow within the impeller passage when compressor operates near surge.
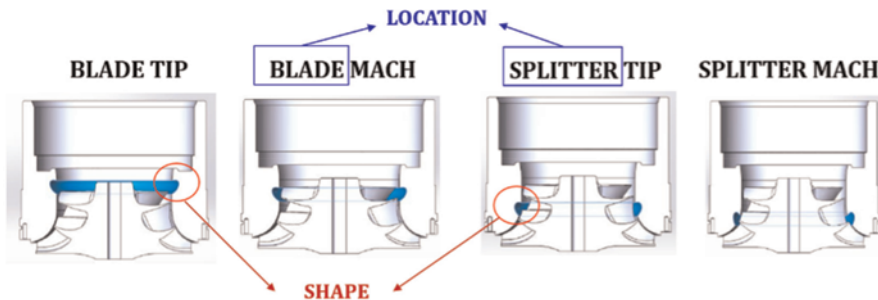

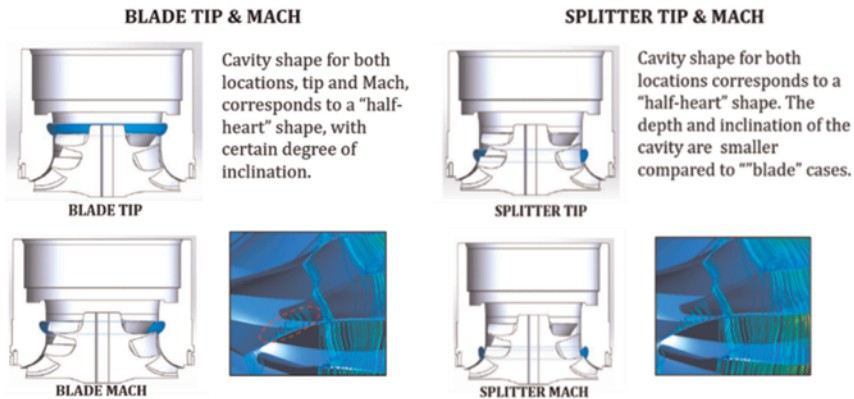**Figure 6. Location and shape for the four tested cavities tested.**

Figure 7. Details on blade (left) and splitter (right) cavity locations and resulting flow streamlines.

Figure 7 summarise the key differences, in terms of cavity location and shape, among the four tested cavity concepts – Blade cavity and Splitter cavity designs. The names "Tip" and "Mach" have been used to give the reader a reference to the location of the cavity, those with Tip in their name are located at the height of the blade and splitter tip. On the other hand, those with Mach in the name refer to cavities located at the rear of the blade tip and splitter. The name Mach refers to the low Mach number region that is created due to the flow separation in the tips.

2   EXPERIMENTAL FACILITY AND TEST MATRIX

To prove the surge enhancement potential of the cavity concept, an experimental campaign was carried out. This experimental benchmark considers four different cavity concepts under steady conditions and at five different pulse frequencies (unsteady exit state). The different test cases and pulse frequencies carried out are summarized in Table 1.

In this experimental campaign, the onset of surge was identified by the increase in compressor inlet temperature as well as by the sudden change in volume flow rate measured by the hot wire. Additionally the typical buffeting sound when surge occurs was noticed.

To compare the performance of the different conditions and configurations, one parameter is introduced: Surge Margin Improvement (SMI), defined as follows:

- **Surge Margin Improvement** – It is assumed cavity surge flow to be lower (better) than original surge flow. Thus, a negative value indicates surge margin is deteriorated.

$$SMI(\%) = \frac{Q_{surge,\ original} - Q_{surge,\ cavity}}{Q_{surge,\ original}} \cdot 100$$

Where $Q_{(surge,\ original)}$ and $Q_{(surge,\ cavity)}$ indicates the resulting surge flow with original compressor and cavity compressor, respectively.

SMI parameter is evaluated for each cavity concept to assess the effectiveness of this novel compressor shroud treatment ("cavity") on surge margin enhancement, when compared to original (reference) compressor under same operating conditions–steady and unsteady scenarios. For the unsteady evaluation (induced outlet pulsing condition), a range of pulse frequencies have been tested and are described in Table 1, ranging from low pulse frequencies (30Hz) to high pulse frequency values (100Hz, in this study).

Table 1. Experimental benchmark for the four tested cases.

Cavity Concept – BLADE MACH			Cavity Concept – SPLITTER MACH		
Pulse Freq [Hz]	**Speed [rpm]**	**Plenum [m3]**	**Pulse Freq [Hz]**	**Speed [rpm]**	**Plenum [m3]**
30	900	0.01661 – Inter. Vp	30	900	0.01661 – Inter. Vp
43	1300	0.01661 – Inter. Vp	43	1300	0.01661 – Inter. Vp
66.67	2000	0.01661 – Inter. Vp	66.67	2000	0.01661 – Inter. Vp
80	2400	0.01661 – Inter. Vp	80	2400	0.01661 – Inter. Vp
100	3000	0.01661 – Inter. Vp	100	3000	0.01661 – Inter. Vp

Cavity Concept – BLADE TIP			Cavity Concept – SPLITTER TIP		
Pulse Freq [Hz]	**Speed [rpm]**	**Plenum [m3]**	**Pulse Freq [Hz]**	**Speed [rpm]**	**Plenum [m3]**
30	900	0.01661 – Inter. Vp	30	900	0.01661 – Inter. Vp
43	1300	0.01661 – Inter. Vp	43	1300	0.01661 – Inter. Vp
66.67	2000	0.01661 – Inter. Vp	66.67	2000	0.01661 – Inter. Vp
80	2400	0.01661 – Inter. Vp	80	2400	0.01661 – Inter. Vp
100	3000	0.01661 – Inter. Vp	100	3000	0.01661 – Inter. Vp

2.1 Experimental facility

The compressor test facility used in this study was designed to include effects that can be observed under real engine conditions, such as pulsating effects and system volume effects. Both are generated in the compressor exhaust stream caused by the engine inlet valve train motion, and they alter the inertia of the system, a parameter which is closely related to the stability of the compressor and surge triggering [9]. The pulse can be defined by its frequency and amplitude and the volume effect is defined by vessel reproducing the piston volume of the engine. A schematic diagram of the centrifugal compressor test facility developed in this study is shown in Figure 8.
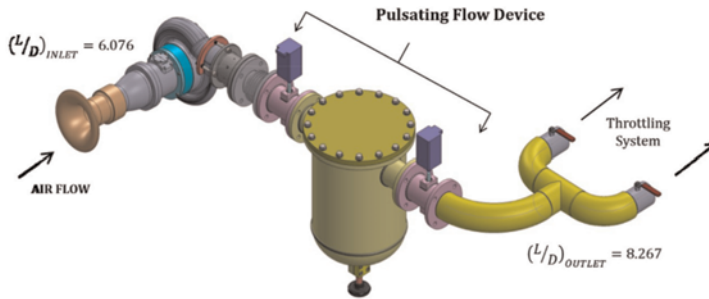

Figure 8. Experimental test bench at Imperial College London [9].

In this facility, air is drawn into the compressor through a bell mouth from ambient conditions, it then flows through a straight pipe (L/D = 6.076) ahead the compressor. After leaving the compressor, the airflow encounters the pulsating flow device. The airflow leaving the pulsating flow device encounters a 90-degree elbow followed by a pipe with an L/D = 8.267 ratio leading to the throttle system at exit (shown here as two exit valves). The compressor rig is driven at a constant speed by an 110kW ABB electric motor through a 27:1 step-up double epicycle gearbox designed and manufactured by Compact Orbital Gears. For a more detailed description of the compressor test bench, please refer to Dr. Barrera Medrano's thesis [9]. It describes in detail the instrumentation of the rig and the different components that compose it.

2.2 "Cavity" inserts

For the experimental phase of this work, four different cavity inserts have been prototyped in high temperature resin (Somos PerFORM resin) and fitted into a metallic modular compressor provided by MHI (Figure 9). This plastic resin printing allows a quick and reliable solution to get an idea of the potential that each cavity location had on the performance of the compressor. As can be seen in Figures 9 and 10, the different ported shroud models (cavities) were attached to the modular casing by means of eight short screws. In addition, adhesive tape was used in four regions of the connection in order to verify the tip clearance measurement at the junction of the two pieces, as can be seen in the marked area of the picture.

Based on the "coefficient of linear thermal expansion" (CTE, Table 2) and the location of the inserts, and assuming a maximum temperature of 100°C at the end of the insert (diffuser inlet), it was assumed the material thermal expansion was small enough to not be considered as an issue in its own.

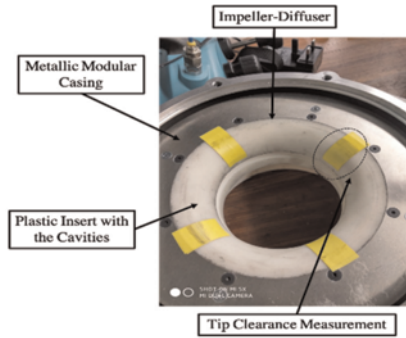**Figure 9. Modular metal casing with cavity insert.**

Figure 10. Metallic modular casing and cavity. Insert connection.

Table 2. Thermal properties for the cavity insert material.

Thermal/Electrical Properties		UV Postcure		Thermal Postcure	
ASTM Method	Property Description	Metric	Imperial	Metric	Imperial
E831-05	C.T.E. -40 - 0°C (-40 - 32°F)	29.9 µm/m°C	16.6 µin/in°F	26.4 µm/m°C	14.7 µin/in°F
E831-05	C.T.E. 0 - 50°C (32 - 122°F)	49.4 µm/m°C	27.4 µin/in°F	34.3 µm/m°C	19.1 µin/in°F
E831-05	C.T.E. 50 - 100°C (122 - 212°F)	79.1 µm/m°C	43.9 µin/in°F	59.9 µm/m°C	33.3 µin/in°F
E831-05	C.T.E. 100 - 150°C (212 - 302°F)	80.9 µm/m°C	45.0 µin/in°F	94.7 µm/m°C	52.6 µin/in°F

This design and manufacturing strategy was fast, and it combines different materials can lead to changes in the geometry due to surface continuity and temperature effects. The transition between resin inserts and metallic components was smooth, however the presence of flat screws and the additional metallic ring to fit compressor on bearing housing might affect the flow.

The modular compressor required a metallic ring to be fitted between compressor backface and bearing housing in order to ensure the correct diffuser height. The cavity size was rather big, therefore affecting the compressor efficiency at low flow regions due to extra losses generated within the large cavity. All the above effects can contribute to the measured reduction in efficiency.

3   EXPERIMENTAL RESULTS – UNSTEADY AND STEADY OUTLET CONDITIONS

3.1   Analysis of unsteady experimental results – Surge margin enhancement with cavity treatment under pulsating conditions

This section presents the analysis of the unsteady experimental results for each cavity concept. The resulting surge margin and calculated efficiency at surge (based on experimental measurement) for each cavity concept are compared to the experimental results of the original compressor at the same operating condition.

The analysis below is focused on SMI parameter, defined in the previous section. Figure 11 shows the Surge Margin Improvement (SMI) for all cavity concepts – Blade Mach/Tip and Splitter Mach/Tip; at all frequencies – 30Hz, 43Hz, 66.67Hz, 80Hz and 100Hz. From these figures it can be observed that the location of the cavity impacts the

SMI. The Blade cavity cases (blade Mach and blade tip) shows the largest SMI when compared to original case for all tested frequencies. Among the blade cavity concepts, Blade Mach cavity is the best option when looking onto SMI potential. At the typical engine speed range (43–80Hz), the SMI for the Blade Mach cavity improves in the range 6–12%, showing the potential of this innovative surge enhancement concept. In the case of the splitter cavity cases (splitter tip and splitter Mach), there is a surge margin penalty when compared to original case under the same operating condition as presented by the splitter Mach (green) and splitter tip (pink) cases in Figure 11.

Table 3 summarizes the results for SMI of each cavity concept at each tested frequency. For SMI, it is assumed cavity surge flow to be lower (better) than original surge flow, thus, a negative value indicates surge margin deteriorates.
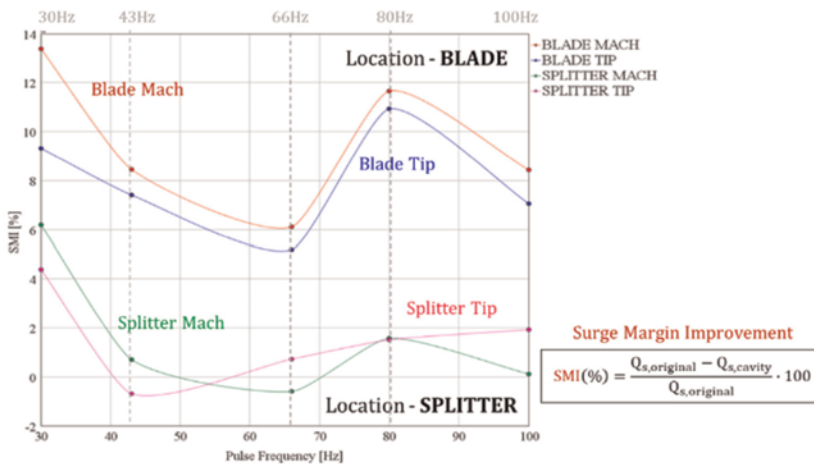

Figure 11. Surge margin improvement (SMI) at all frequencies.

$$SMI(\%) = \frac{Q_{s,original} - Q_{s,cavity}}{Q_{s,original}} \cdot 100$$

Table 3. Results for SMI and ED of each cavity concept at each tested frequency.

Cavity Case	Pulse Frequency	SMI [%]
BLADE MACH	30 Hz	13.4
BLADE TIP	30 Hz	9.3
SPLITTER MACH	30 Hz	6.2
SPLITTER TIP	30 Hz	4.4
BLADE MACH	43 Hz	8.4
BLADE TIP	43 Hz	7.4
SPLITTER MACH	43 Hz	0.7
SPLITTER TIP	43 Hz	−0.7
BLADE MACH	66.67 Hz	6.1

(*Continued*)

Table 3. (*Continued*)

Cavity Case	Pulse Frequency	SMI [%]
BLADE TIP	66.67 Hz	5.2
SPLITTER MACH	66.67 Hz	−0.6
SPLITTER TIP	66.67 Hz	0.7
BLADE MACH	80 Hz	11.7
BLADE TIP	80 Hz	10.9
SPLITTER MACH	80 Hz	1.6
SPLITTER TIP	80 Hz	1.5
BLADE MACH	100 Hz	8.4
BLADE TIP	100 Hz	7.1
SPLITTER MACH	100 Hz	0.1
SPLITTER TIP	100 Hz	1.9

Based on these results and to understand the physics behind these concepts, it was decided to investigate the cases numerically for the best cavity case in steady state (Blade Mach).

3.2 Performance maps for all pulse frequencies
Figures 12 to 16 show both the performance map and the isentropic efficiency for the four cavity models and the original, at all frequencies studied.
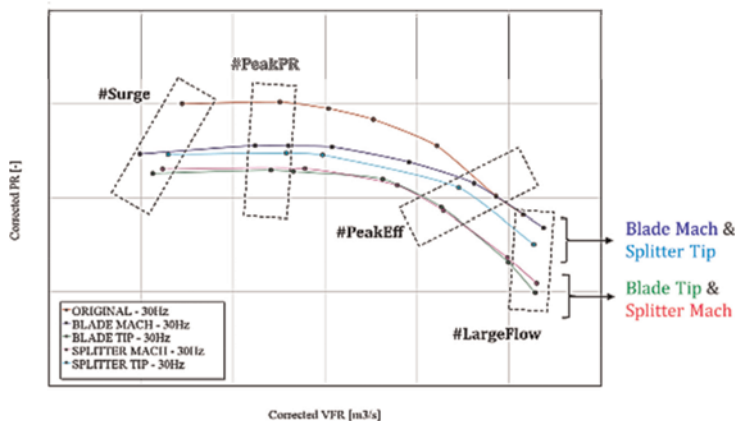

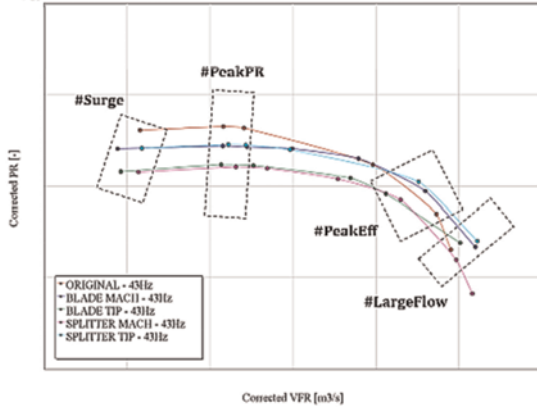**Figure 12. Compressor performance with unsteady outlet boundary condition−30Hz.**

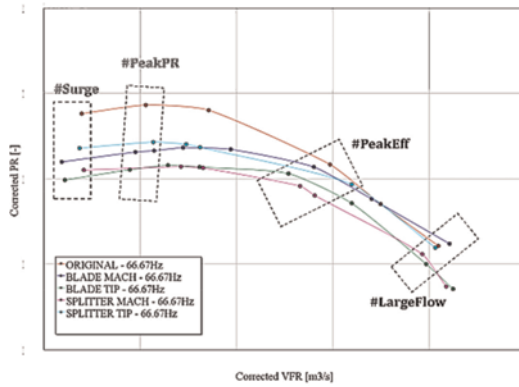**Figure 13. Compressor performance with unsteady boundary condition–43Hz.**

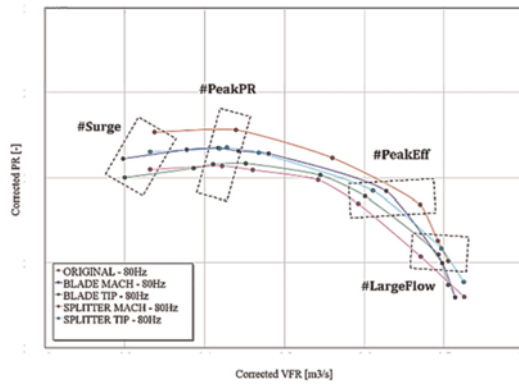**Figure 14. Compressor performance with unsteady boundary condition– 66.67Hz.**

Figure 15. Compressor performance with unsteady boundary condition–80Hz.
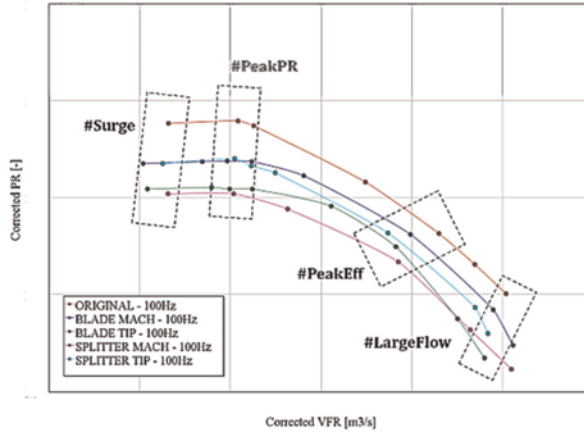
Figure 16. Compressor performance with unsteady boundary condition–100Hz.

All cavity designs show an improvement in surge margin when compared to the original compressor (reference), under the same operating conditions. When looking at compressor performance trends for the four tested cavity concepts, one can observe a similarity in the performance curves among the following pairs: (i) Blade Mach and Splitter Tip cavity concepts; (ii) Blade Tip and Splitter Mach cavity concepts. These pairs seem to follow the same behaviour for all operating points.

3.3   Analysis of steady experimental results – Surge margin enhancement with cavity treatment under steady conditions

Even though the focus of the "cavity" concept relates to compressor surge enhancement under pulsating outlet conditions, an experimental evaluation of the concepts under steady flow was carried out. Table 4 summarizes the results for SMI of each cavity concept under steady conditions. Looking into SMI, it is seen that the Blade Tip cavity case shows the highest potential for compressor surge enhancement with an 8% when compared to original compressor (no cavity), under steady conditions. The second-best SMI is achieved by Blade Mach Cavity case, presenting a surge margin enhancement of 3.5% when compared to reference (original) case. Generally, all tested cavity concepts show a surge margin improvement apart from Splitter Tip concept.

Table 4. SMI for the four cavity concepts when compared to original compressor.

Cavity Case	SMI [%]
BLADE MACH	3.5
BLADE TIP	8.1
SPLITTER MACH	1.45
SPLITTER TIP	−0.24

To understand the flow mechanism behind the observed improvement on surge margin during the experimental campaign, the original compressor design and the best two cavity cases – Blade Tip and Blade Mach designs have been explored computationally. The key findings from this numerical assessment are presented in the next section.

4   CFD ASSESSMENT OF THE CAVITY CONCEPT – LOOKING INTO THE FLOW MECHANISM

To characterise compressor behaviour and flow instabilities developed under off-design conditions, it is necessary to build up data for a high number of operating conditions. This requires creating a mesh capable of reproducing the fluid field under these circumstances. Figure 17 shows the domain of the compressor. The compressor inlet consists of a straight pipe of 250 mm in length to ensure a fully developed flow prior impeller inlet. Figure 18 shows a summary of the computational domain as well as a sectional view of the inlet mesh. The number of mesh elements was 1,93 million approx. with an orthogonal quality parameter of 0.85 (0 being a poor-quality mesh and 1 being a high-quality mesh).

The boundary conditions at the inlet in the analysis correspond to total pressure and total temperature (T_0 = 293.15K, P_0 = 1 atm), with an angle normal to the surface and turbulence intensity of 5%. Area-averaged static pressure was imposed as outlet boundary condition. A Frozen-rotor interface was used for the rotor/stator region located between the diffuser and the impeller. In this method, the relative location of the rotor to volute tongue is assumed to be "frozen" and calculations at two sides of the interface are carried out in different frames. The flow distortion at either side can be passed through the interface without being circumferentially averaged. Smooth solid walls were set to be no-slip and adiabatic. The fluid was set as ideal gas. $k - Epsilon$ turbulence model was used. the average dimensionless near-wall distance y+ was also nearly constant for each mesh with values of y+> 30, using the scalable wall function.

To validate the model, the steady-state simulations were run until a converged solution was achieved. Thereby, the numerical results can give an accurate performance prediction from choke to points near surge. The operation point which achieved the lowest mass flow rate while still converging is taken to be the numerical surge point [11]. The appearance of oscillations in the flow patterns indicate an unstable operating point. These unstable fluctuations cannot be resolved with the steady-state approach by this model and were therefore not part of this simulation. Therefore, the lower mass flow limit is referred to as the surge limit of the CFD calculations, a procedure common for the investigation of surge limit [12,13]. The solution convergence was evaluated by calculating the total pressure ratio, isentropic efficiency, and the imbalances for each component of the compressor at each iteration. The simulation was considered as converged if:

- The RMS residuals were lower than 10^{-4}.
- All imbalances were less than 1% for each compressor component.
- The mass flow rate fluctuations were lower than 0.5% at the inlet and outlet of the compressor.
- Isentropic efficiency fluctuated by less than 0.5\%.

To improve the quality of the simulation, a mesh refinement near the walls has been implemented using the inflation technique. This inflation has been carried out by using "First Layer Thickness", with number of layers of 10 with a growth ratio of 1.7.

The diffuser is a vaneless diffuser with an inlet diameter of 152mm and an outlet diameter of 200mm. The channel height is 8.06 mm at the inlet and 8.24 mm at the outlet.

This configuration in which the channel is gaining height enhances the static pressure gain of the diffuser. Figure 18 shows a sectional view of the diffuser mesh. The number of mesh elements was 1,3 million approx. with an orthogonal quality parameter of 0.88. A refinement of the mesh near the walls has been implemented with several layers of 10 with a growth ratio of 1.7.
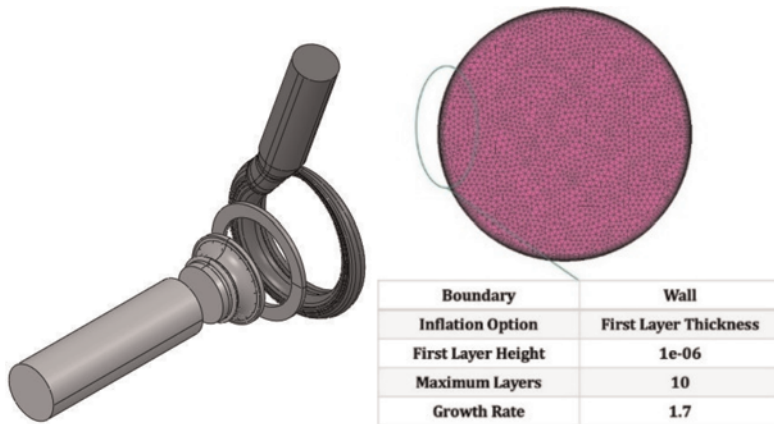

Boundary	Wall
Inflation Option	First Layer Thickness
First Layer Height	1e-06
Maximum Layers	10
Growth Rate	1.7

Figure 17. Fluid domain for numerical analysis (left) and inlet pipe mesh details (right) of the numerical assessment.

Figure 19 shows the geometrical design of the volute used in this study. The number of mesh elements was 5,41 million approx. with an orthogonal quality parameter of 0.85.

For the impeller domain, three different configurations were created, the first of which corresponds to the original compressor, i.e., without ported shroud. The other configurations correspond to the experimental model that has shown the best potential on the experimental phase. These are Blade Tip and Blade Mach. Figure 19 shows the CAD domain of the original and both cavity cases, respectively.

In the CFD analysis for the best cavity cases, no downstream volume is included in the simulation. Bearing this in mind, one can expect differences among experimental and numerical results, as the compression system volumes/lengths play a key role in stall inception. Nevertheless, the aim of this numerical analysis is to understand how the presence of a cavity in the compressor shroud affects flow physics and resulting stall inception.

A validation study of the mesh and its dependence on the number of cells in the solution presented here. The validation of the meshes has been conducted on the impeller component, as this is the one in charge of capturing the effects caused by the new shroud design. For this purpose, three meshes were created with an increasing number of cells, as well as with a different treatment in the approximation of the mesh to the walls. Table 5 shows the number of elements that each of the meshes has for the rotor and for the complete compressor domain. These figures vary from approximately 14 million elements for what can be considered a coarse mesh to 22 million for a fine mesh.
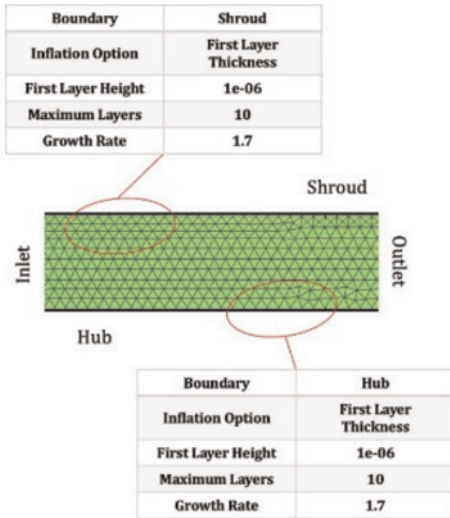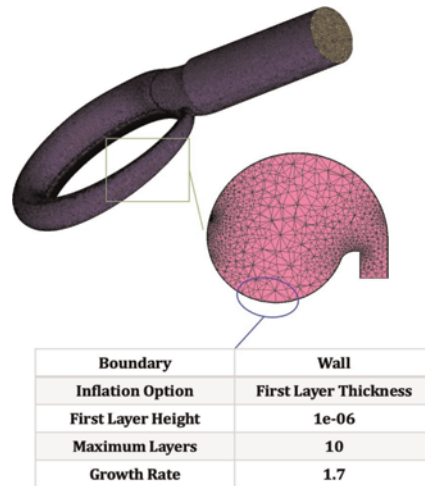
Boundary	Shroud
Inflation Option	First Layer Thickness
First Layer Height	1e-06
Maximum Layers	10
Growth Rate	1.7

Boundary	Hub
Inflation Option	First Layer Thickness
First Layer Height	1e-06
Maximum Layers	10
Growth Rate	1.7

Figure 18. Diffuser mesh details.

Boundary	Wall
Inflation Option	First Layer Thickness
First Layer Height	1e-06
Maximum Layers	10
Growth Rate	1.7

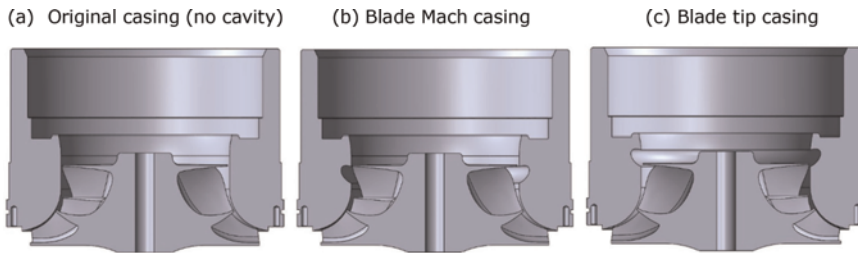**Figure 19. Scroll mesh details.**

Figure 20. CAD domain comparison for 3 configurations: (a) original, (b) Blade Mach, (c) Blade tip.

Table 5. Number of elements for each compressor component.

Mesh	Rotor Cell no.	Compressor Cell no.	Description
Mesh1	4,108,696	14,935,662	No inflation layer close to impeller blades (poor accuracy near the impeller blade, Hub and shroud walls)
Mesh2	7,140,161	17,925,872	Course inflation layers close to impeller blades (the inflation improve the accuracy near the impeller blade, hub and shroud walls)
Mesh3	13,988,723	22,632,094	Fine inflation layers close to impeller blades (the inflation improve the accuracy near the impeller blade, hub and shroud walls)

In addition to the information presented in Table 5, the differences of the meshes can be seen in detail in Figure 21. Figures 22 shows the results on predicted performance and efficiency of the three meshes described in Table 5. The results suggest that *Mesh3* (red line) can reproduce the behaviour of the compressor in the tested performance range (black line) for both, thus, it will be used for the numerical assessment of this study. The same parameters of inflation and mesh density were used to create the mesh for the Blade Mach and Blade Tip cases.
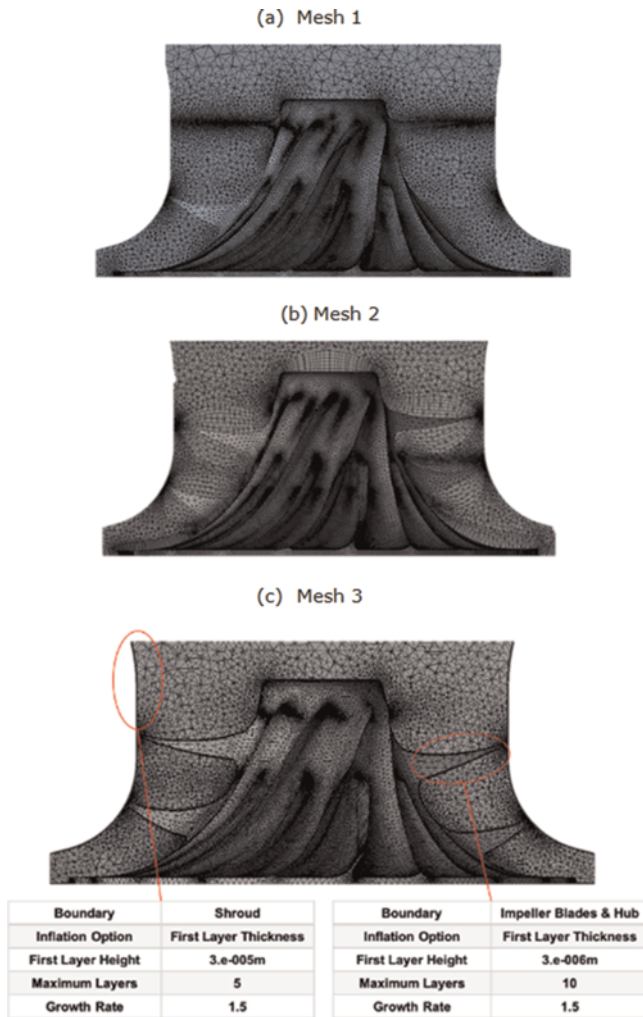
(a) Mesh 1

(b) Mesh 2

(c) Mesh 3

Boundary	Shroud	Boundary	Impeller Blades & Hub
Inflation Option	First Layer Thickness	Inflation Option	First Layer Thickness
First Layer Height	3.e-005m	First Layer Height	3.e-006m
Maximum Layers	5	Maximum Layers	10
Growth Rate	1.5	Growth Rate	1.5

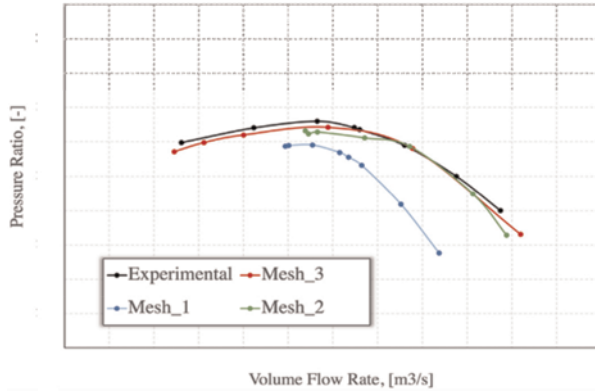**Figure 21. Comparison of different mesh densities.**

Figure 22. Pressure ratio comparison for three mesh densities and experimental results.

4.1 CFD analysis and flow-field assessment for blade Mach and original compressor – Comparison at near surge and peak efficiency conditions

Figure 23 shows the obtained pressure ratio from CFD results for the three simulated cases – Original no cavity (red), Blade Tip Cavity (green) and Blade Mach cavity (blue) cases. Figure 24 shows the efficiency results obtained by CFD analysis for the simulated cases. Performance results (pressure ratio) show the same trends as the ones obtained in the experimental campaign. Blade Mach cavity case is the best candidate for compressor surge enhancement followed by Blade Tip cavity case. Both cavity cases, Blade Tip (green) and Blade Mach (blue) present a surge margin improvement when compared to original (reference – red) case under steady condition.
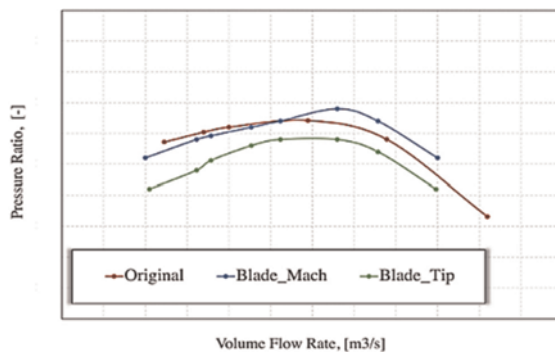

Figure 23. CFD performance results for original compressor, blade Mach and tip cases at 40krpm.
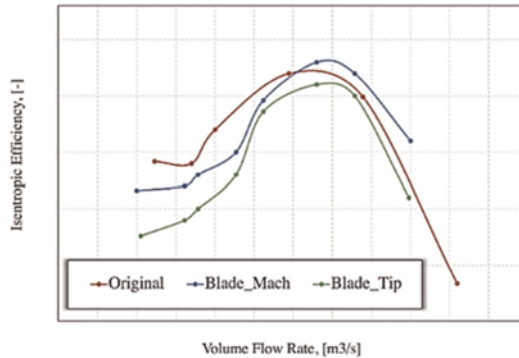
116

Figure 24. CFD efficiency results for original compressor, blade Mach and tip cases at 40krpm.

Looking at the peak pressure ratio point, one can observe that Blade Mach case shows better performance when compared to original (no cavity) case. Similar results were observed during experimental campaign. The performance improvement observed in the Blade Mach case can be explained by the reduction of the vortex created in each channel after the compressor blade tip.

Both graphs presented above follow the trend shown in the experimental results and demonstrate the potential of the Blade Mach case. It improves surge limit and efficiency (the latter, based on CFD results). To understand what effects this cavity has on the fluid field, a comparative study of the fluid field between the original case and the Blade Mach case was conducted. This analysis will mainly be conducted under two operating conditions where cavities potentially improve compressor performance. These conditions of analysis will be points close to surge and points in areas of maximum efficiency. Figures 25 and 26 show a mid-plane of the inlet and the impeller at a point near stall and peak efficiency point, respectively. In this evaluation, high values of static entropy indicate the areas of vortex formation that results in flow instability initiation or stall inception.

Looking at the static entropy results presented in Figure 25 (low mass flow rate), one can observe that the presence of a cavity near the leading edge of the blade has an influence on the resulting vortex formation. For the Blade Mach cavity case (right figure), the region affected by the vortex created at the impeller inlet extends further upstream than for the original case (left figure), as shown by the plotted streamlines. This larger vortex increases the entropy creation, which increases losses. These conclusions on the fluid field agree with the data obtained both experimentally and numerically, where, although the Blade Mach cavity model extends the surge limit, it does so with a compressor efficiency penalty. The isentropic efficiency at the impeller outlet was calculated for both geometries, with the Blade Mach case showing a deterioration of 0.5%. However, when analysing the operating point in the most efficient area, the scenario changes completely, see Figure 26. In both cases, the static entropy generated decreases substantially, which is a likely scenario in the high efficiency region of the compressor. Considering the differences shown between the two cases, it can be seen that Blade Mach reduces the vortex created behind the blade tip of the impeller at the leading edge to a greater extent. In fact, the cavity is able to move the vortex to its interior thus leaving more passage area to the fluid in each impeller channel. In this way, the impeller is able to be more loaded, which improves performance.
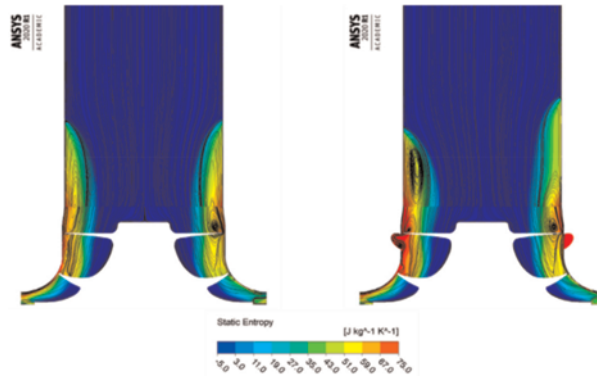
Figure 25. Inlet and impeller mid plane with static entropy and streamlines at point near stall.
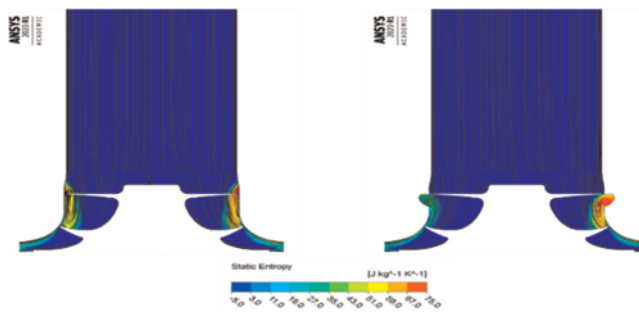

Figure 26. Inlet and impeller mid plane with static entropy and streamlines at peak efficiency point.

To gain a better understanding of the impact of the cavity on the impeller, a fluid field analysis for the Original and Blade Mach cases was conducted, Figure 27 shows the three inlet planes chosen for this analysis. The aim is to study the effect that the cavity has on the fluid at the inlet and the modifications that the change of geometry intro-duces in the fluid. Figure 28 shows planes along the impeller. These planes will give a view of how the fluid flows through the impeller channels.

Figure 27. Planes at the inlet of the impeller.

Figure 28. Planes along the impeller channels.

Figure 29 shows the static entropy in the planes introduced above, under low mass. Each of these planes are detailed separately in Figure 30 and Figure 31. Figure 30 shows the first three planes, corresponding to the impeller inlet, in the upper part of which the contours of the original casing can be seen, while the bottom part shows the Blade Mach case. In general, blade Mach has higher values of static entropy, which indicates that the intensity of the vortex created is greater, and with it the energy loss in the fluid. Both cases show a uniform distribution of entropy in a ring-shaped manner. Looking at plane 4, in Figure 30 it can be seen how the cavity increases the area of loss creation inside its volume. It can also be seen that from the cavity the downstream static pressure contour more closely resembles those presented for the original case.

A very different scenario is seen when the compressor operates at higher flows, in peak efficiency regions. In Figure 32 one can see the static entropy contours are for original (left) and Blade Mach (right) at peak efficiency point. In general, the static entropy generated is lower for all planes at peak efficiency point.

Figure 33 shows a considerable reduction of entropy for the Blade Mach case for the 3 planes under consideration. In fact, for plane 3, the closest to the impeller, the original case starts to develop secondary flows at the impeller tip, the red contour area. These vortices extend in an annular way covering the entire circumference of the tip clearance. For the same plane, the cavity can suppress this generation by accommodating and recirculating the fluid, as seen in plane 4.

This inlet cavity action improves the performance of each impeller channel, see contours 5–7 in Figure 34, and allows for greater impeller loading. This increase in load is translated into an increase in the efficiency of the component. It is relevant to observe how in plane 5 almost all the secondary flows have been accommodated by the cavity, which thanks to its shape has recirculated the flows and introducing them into the main flows of the impeller channel.
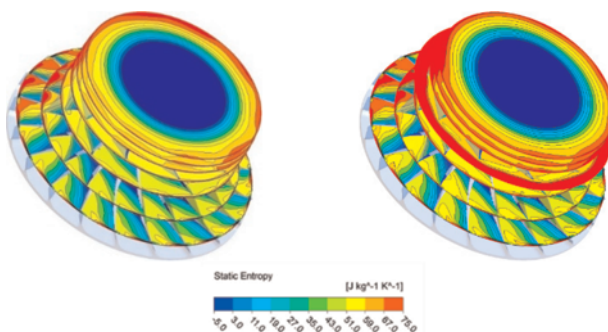

Figure 29. Static entropy contours for original (left) and Blade Mach (right) at low mass flow original (top) and Blade Mach (bottom).

Looking at the Mach number distribution in the cavity cases, one can observe that the low Mach number areas are located further away from the rotor tip when compared to the "no cavity" case. This retards the surge point by allowing a degree of impeller tip blockage and thus postponing stall inception. It seems that the presence of a cavity near blade tip relieves the Mach number and therefore allows more inflow at near surge point.

The Mach number study was conducted following the same structure as the one conducted previously for the static entropy. The simulated conditions represent low mass flows and the point of highest compressor efficiency., where planes 1–3 represent the fluid distribution at the impeller inlet and planes 4–7 display the impeller channels in Figure 35. Figure 36 and 37 show the Mach number and static entropy contours, respectively. The top of the figures represent values for the original case, and those in the bottom the Blade Cavity case. The blue areas represent regions where the fluid loses its normal velocity component, initiating vortices that block the normal passage of the fluid through the impeller channels (Figure 36). These regions are commonly referred to as low momentum areas in the fluid. The propagation of these vortices leads to the creation of instabilities in the impeller that leading to the trigger of surge.

As we have seen previously, the efficiency of the Blade Mach case is lower than the efficiency of the original case for near surge operating point. However, when looking at the Mach number, it seems to accommodate the fluid better. If we look at the entry planes 1–3, the low momentum regions of the fluid near the shroud are diminished by the cavity effect, which indicates that the intensity and size of the vortex is smaller. Looking at plane 5, it can be seen how the cavity recirculates part of the separated flow in the tip. This recirculation of the fluid restores the fluid structure and makes that for the rest of the downstream planes (5–7), both geometries behave in a very similar way.

Finally, it could be said that at low mass flows the cavity introduces losses in the compressor, since it increases the volume of the tip clearance. But as far as the impeller inlet zone is concerned, see planes 1–3 in Figure 35, the fluid structure delays the appearance of the annular vortex, a common effect of the inlet recirculation mechanism. This delay retards the onset of surge, and therefore both experimentally and numerically an improvement in the surge limit has been observed.
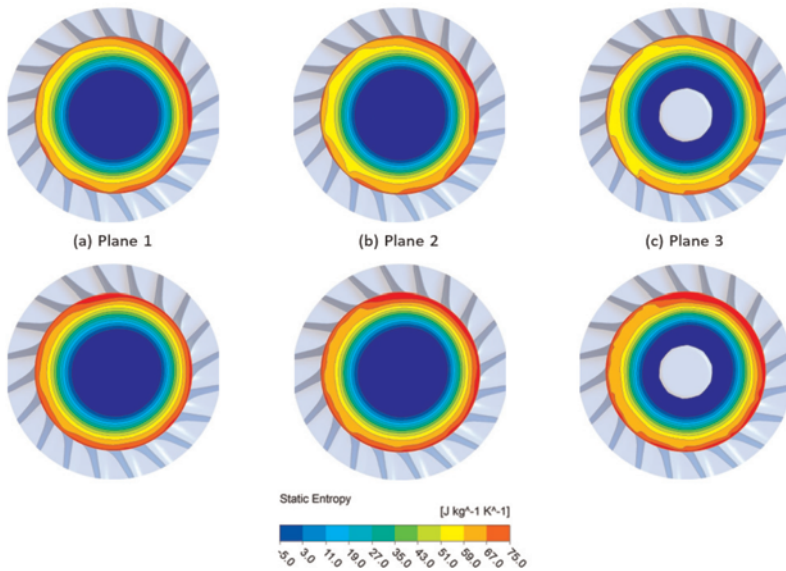

Figure 30. Static entropy at the impeller inlet (Planes 1, 2 and 3) at ṁ and Blade Mach (bottom) at near surge point.
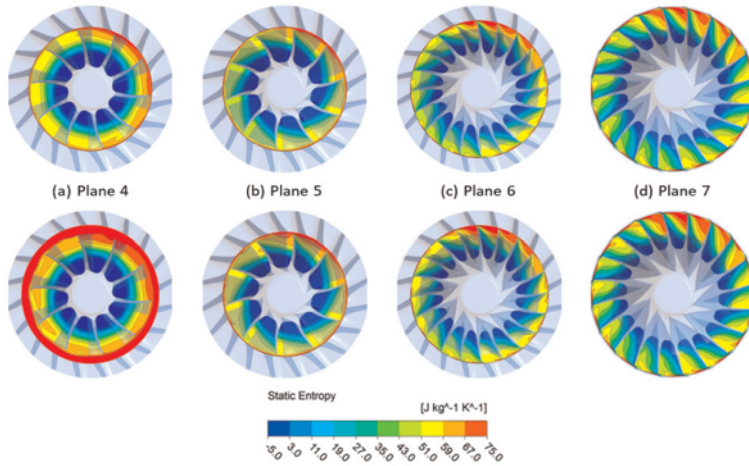
Figure 31. Static entropy at the impeller channels (Planes 4, 5, 6 and 7) at m˙ original (top) and Blade Mach (bottom) at near surge operating point.
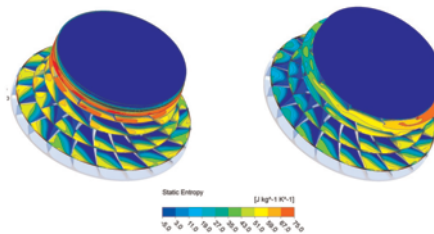

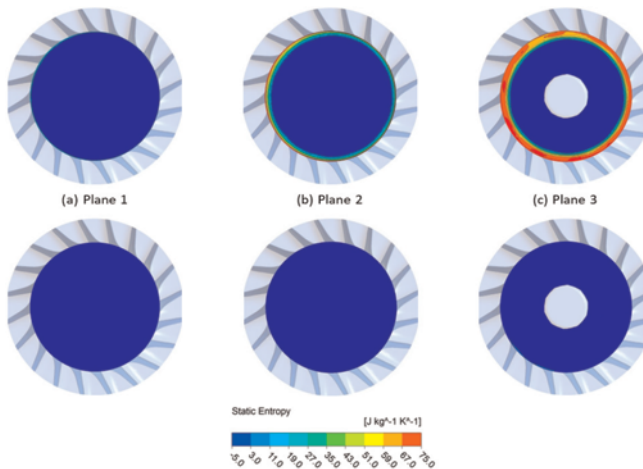**Figure 32. Static entropy contours for original (left) and Blade Mach (right) at peak efficiency point.**

Figure 33. Static entropy at the impeller inlet (Planes 1, 2 and 3) at m˙ and Blade Mach (bottom) at peak efficiency point.
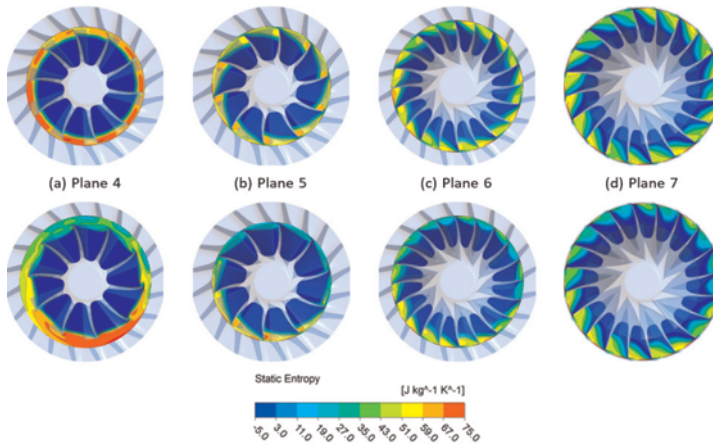
Figure 34. Static entropy at the impeller channels (Planes 4, 5, 6 and 7) at ṁ original (top) and Blade Mach (bottom).
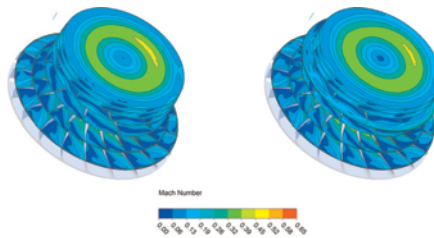

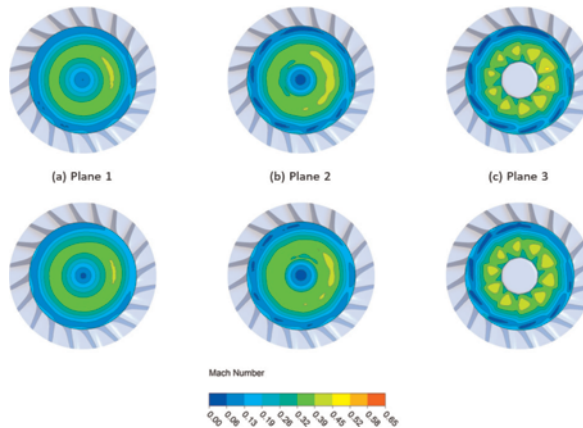**Figure 35. Mach number contours for original (left) and Blade Mach (right) at near surge point.**

Figure 36. Mach number at the impeller inlet (Planes 1, 2 and 3) at ṁ and Blade Mach (bottom) at near surge point.
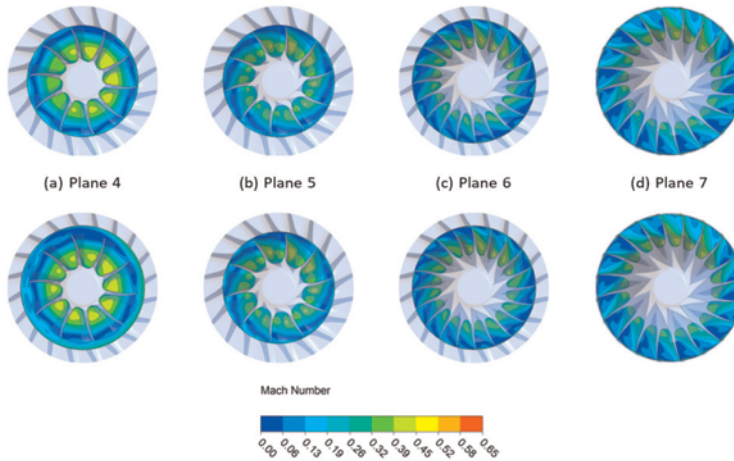
122

Figure 37. Static entropy at the impeller channels (Planes 4, 5, 6 and 7) at ṁ original (top) and Blade Mach (bottom) at near surge point.
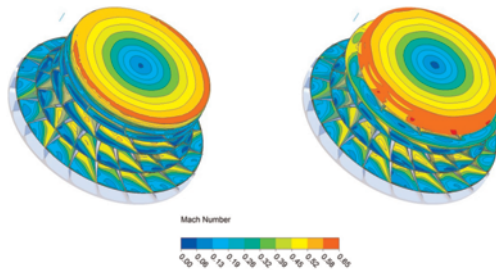

Figure 38. Mach number contours for original (left) and Blade Mach (right) at peak efficiency point.

When looking at the Mach number for the maximum efficiency operating point, the effects of the cavity become more evident. It is very interesting to study the evolution of the secondary flow creation for the original case as we approach the leading edge of the impeller, Figure 38. Observing the area near the shroud in plane 2 (top middle) the original casing starts to decrease in Mach Number values. And in plane 3 (top right) the whole ring is dominated by the vortex created in the tip. However, the Blade Mach case can maintain high velocities in the region close to the shroud wall. This forces the flow to maintain its axial component and not detach from the impeller tip in the form of a vortex.

Analysing the contours 4–7, Figure 40. it becomes very relevant to see how the cavity effectively removes the secondary flows in the tip clearance compared to the original geometry (see planes 4 and 5 in more detail). This improvement in turn has an impact on the fluid flow in the splitter area, where the occurrence of secondary flows in the tip clearance is also reduced (see planes 6 and 7 in Figure 40).
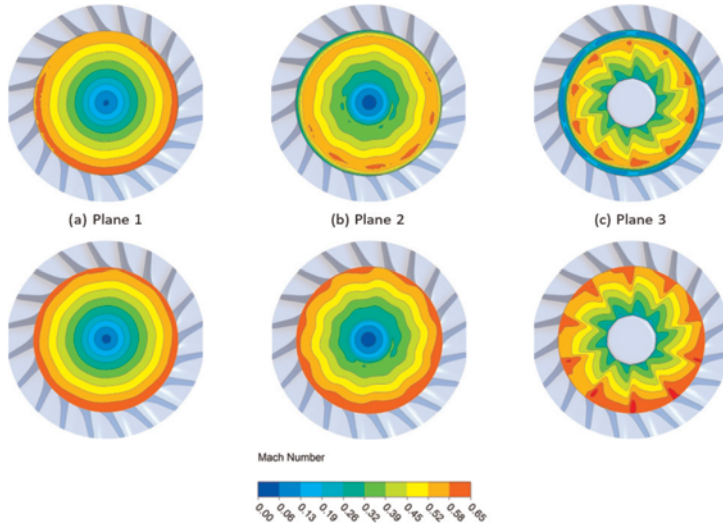
Figure 39. Mach number at the impeller inlet (Planes 1, 2 and 3) and Blade Mach (bottom) at peak efficiency point.

This CFD analysis has confirmed the data obtained experimentally. The blade Mach cavity case can delay the appearance of the surge phenomenon, albeit at a loss of efficiency, when compared to the original case. On the other hand, when analysing the peak efficiency, the Blade Mach case even improves the performance of the original case. The entropy generation results presented show a significant reduction in static entropy at the impeller channel for the blade Mach cavity case at peak efficiency point. This indicates that the blade Mach cavity concept performs more efficiently than the original compressor (no cavity) for the same operating conditions, which will have a direct impact of
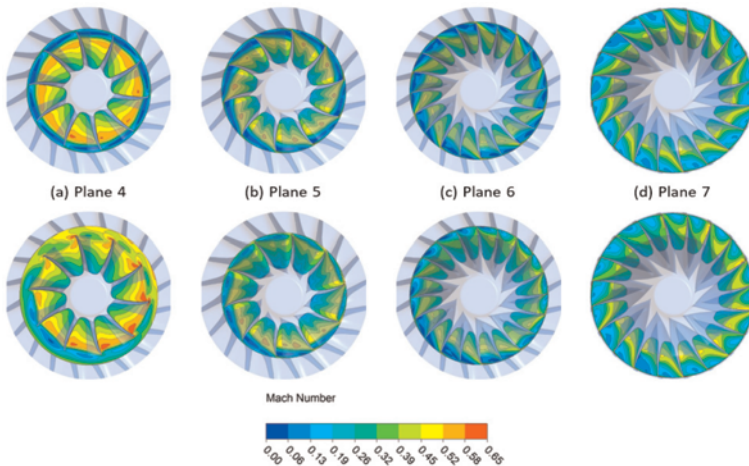

Figure 40. Mach number at the impeller channels (Planes 4, 5, 6 and 7) original (top) and Blade Mach (bottom) at peak efficiency point.

resulting compressor efficiency – the calculated efficiency based on experimental results also showed an efficiency improvement at "peak efficiency" operating point.

The decrease in efficiency in low mass flow regions has also been shown and justified. However, by analysing the fluid field using the Mach number, it has been shown that the cavity is able to improve the fluid structure for both simulated conditions, which influences the surge phenomena when the compressor operates at low mass flow rates.

5   SUMMARY

In this paper a novel idea was presented to delay the onset of surge and thus increase the operating range of the compressor at lower mass flow rates. To achieve this goal, four designs of annular cavities were created around the impeller shroud at four different locations. These locations are the blade tip, a region just below the blade tip, the splitter tip and, again, a region just below the splitter tip. It has been numerically and experimentally demonstrated that the presence of a cavity near the compressor blade improves the compressor overload margin for all simulated/tested cases, both in steady and unsteady conditions. By observing the Mach number distribution in the cavity cases, the low Mach number areas are reduced at the rotor inlet when compared to the original case. Therefore, the presence of a cavity near the impeller tip allows the compressor to operate more efficiently at higher flow rates because of a more effective Mach number distribution along the impeller span.

It can therefore be summarised that the Blade Mach cavity is the one that has shown the best performance, and that thanks to its location and shape it is able to improve the compressor at low mass flow conditions, with an acceptable loss of efficiency, thus demonstrating the hypothesis behind the design.

REFERENCES

[1]   Yano, T., "*Performance of Centrifugal Blower under Pulsating flow*," in Proceedings of the Japan Society of Mechanical Engineers, 1963.
[2]   Cumpsty, N. A. *Compressor Aerodynamics*, Essex, England: Longman Scientific & Technical, Ltd, 1989.
[3]   Fink, D. A., Cumpsty, N. A. and Greitzer, E. M., "Surge Dynamics in a Free-Spool Centrifugal Compressor System," *Journal of Turbomachinery*, vol. 114, pp. 321–332, 1992.
[4]   Arnulfi, G. L., Blanchini, F., Giannattasio, P., Micheli, D. and Pinamonti, P., "Extensive Study on the Control of Centrifugal Compressor Surge," *Journal of Power and Energy*, vol. 220, pp. 289–304, 2006.
[5]   Hansen, K. E., Jorgensen, P. and Larsen, P. S., "Experimental and Theoretical Study of Surge in a Small Centrifugal Compressor," *Journal of Fluids Engineering*, vol. 103, pp. 391–395, 1981.
[6]   Greitzer, E. M. "Surge and Rotating Stall in Axial Flow Compressors- Part I: Theoretical Compression System Model," *Journal of Engineering of Power*, pp. 190–197, 1976.
[7]   Greitzer, E. M. "Surge and Rotating Stall in Axial Flow Compressors – Part II: Experimental Results and Comparison With Theory," *Journal of Engineering for Power*, pp. 199–211, 1976.
[8]   Tamaki, H. "Effect of Piping System on Testing of Centrifugal Compressors for Turbochargers," in Turbocharging Seminar, Tianjin, China, 2015.
[9]   Maria Barrera-Medrano. *The Effect of Exit Pressure Pulsation on the Performance and Stability Limit of a Turbocharger Centrifugal Compressor*. PhD dissertation, Imperial College London, 2017.

[10] Taher Halawa, Mohamed S Gadala, Mohamed Alqaradawi, and Osama Badr. Influence of Changing Casing Groove Parameters on the Performance of Centrifugal Compressors Near Stall Condition. *Journal of Fluids Engineering*, 138 (2), 2016.

[11] Hiroshi Uchida, Akinobu Kashimoto, and Yuji Iwakiri. Development of Wide Flow Range Compressor with Variable Inlet Guide Vane. *R&D Review of Toyota Crdl*, 41 (3):9–14, 2006.

[12] Schobeiri, M. *Turbomachinery Flow Physics and Dynamic Performance*. Springer-Verlag, Berlin, Germany, 2012

[13] Hunziker, R., Dickmann, H. and Emmrich, R. Numerical and Experimental Investigation of a Centrifugal Compressor with an Inducer Casing Bleed System. *Proc. IMechE, Part A: J.Power and Energy*, 215, 2001.

Novel materials and challenges

Taylor & Francis
Taylor & Francis Group
http://taylorandfrancis.com

Development of low nickel austenitic stainless steel for high temperature gasoline turbochargers

C.S. Prashanth, Ragupathy Kannusamy, Philippe Renaud, Arthur Fischer

Garrett Advancing Motion

ABSTRACT

Conventional austenitic stainless steel (ASS) with nickel (Ni) content in the range of 20 to 40 Wt% are primarily used for the Turbine Housing component of turbochargers for gasoline applications. Due to the increase in cost of the nickel in the global commodity market, has become imperative to develop alternative cost-effective material solution. Therefore, few potential options were evaluated, and Nitrogen has been identified as one of the strong austenitic stabilizers, which can reduce Nickel content while simultaneously enhancing mechanical properties and crack resistance under severe Thermo-Mechanical Fatigue (TMF) loading conditions. The "Integrated Computational Materials Engineering" (ICME) methodology was developed to explore new options of material composition for low Ni steel. The optimum chemical composition of low Ni steel was down selected by performing a wide range of kinetics and thermodynamic studies under equilibrium & non-equilibrium conditions, and optimum nitrogen solubility limit. The impact of various undesirable phase formations during solidification was systematically addressed without compromising the manufacturability of the alloy. The sensitivity of various casting process parameters was systematically evaluated with the selected alloy composition. Large casting trials were conducted to minimize casting defects and achieve optimum microstructure features. The turbine housing component was tested up to 1050°C gas temperature under severe thermal shock loading conditions and compared with existing high Ni conventional steels. The overall development of this new material with a well-integrated development process, encompassing both computational and experimental techniques, proves it is a promising alternative solution providing both better performance and lower cost for high temperature turbocharger applications.

Keywords: Low Ni steel, ICME, TMF, Casting Process Parameters

1   INTRODUCTION

During operation, automotive turbocharger components are subjected to elevated operating temperatures, loading and vibrations. In addition, the Turbine housing must be able to contain the potential burst of a turbine wheel subjected to extremely high rotational speeds. These hostile operating conditions represent a significant challenge for the designer of turbocharger components to achieve the reliability targets that are today's standard in the automotive industry. Since high-speed performance improves with higher exhaust gas temperature (TIT) the tendency has been gradually raise the upper limits for both continuous operation and peaks. This has contributed to a significant increase of the thermal load on turbocharger components in direct contact with the exhaust gas, such as the exhaust manifold and the turbine housing.

Various failure modes have been encountered in conjunction with the rise of the exhaust gas temperature. The most relevant examples are the problems of thermally induced cracks and high-temperature corrosion. At temperatures above approximately

950°C and depending on the particular alloy employed, oxygen may begin to attack its metallic elements, causing them to oxidize and thus lose their beneficial physical and mechanical properties. Over repeated cycles of operation, high-temperature corrosion can eventually cause a part to fail entirely.

In order to overcome the challenges associated with higher operating temperatures, turbocharger applications have usually adopted stainless steel alloys of higher chromium and nickel content, such as commercially available high chromium and/or nickel stainless steel casting alloys. As used herein, the term "operating temperature" refers to the maximum temperature of exhaust gas (barring the occasional higher transient temperatures) designed to be experienced by the turbine housing and blade components of the turbocharger. These higher chromium and nickel stainless steels are primarily austenitic with a stable austenite phase that exists well above the operating temperature, as well as minimal to no delta ferrite phase, which promotes corrosion/oxidation.

Stainless steel alloys are well-known in the industry. Current conventional austenitic stainless steel materials for turbine housing applications between 1,000°C–1,020°C have a specification for chromium between 23% and 27% and nickel between 19% and 22% (all percentages by weight). While meeting the high temperature property requirements for turbocharger housings, stainless steel is quite expensive because of its high chromium and nickel contents. As the turbocharger housing is generally the most expensive component of the turbocharger, its choice of material greatly affects the overall cost of the machine.

Thus, materials that are less expensive, with less manufacturing issues and better resistance to thermo-mechanical loading and oxidation, would be a suitable alternative to the currently available options. These materials should have a stable austenite phase that exists above the operating temperature, as well as minimal to no delta ferrite phase. Accordingly, there is a strong need for stainless steel alloys useful in turbocharger applications that can withstand the higher operating temperatures produced by modern internal combustion engines, but that minimize the expensive nickel content.

2 NITROGEN ALLOYED STAINLESS STEEL

Nitrogen is an effective and most economical interstitial solid solution strengthener. The strengthening effect of nitrogen is due to the clusters of Cr-N, which result in increased elastic stress in the lattice. Nitrogen increases the creep life significantly due to precipitation strengthening from Cr-N clusters [3] by reducing the formation and growth of Cr-rich carbides and Nb-rich carbonitrides during creep. When Boron is added, the number density of M23C6 along the grain boundaries increases, thus increasing the creep rupture strength. The composition of this carbide varies depending on the composition of the steel. Except in fine intragranular form, the presence of M23C6 is not desirable for creep properties. The creep rupture life of steel can be improved by addition of Nb however the ductility is decreased. The decreased ductility is due to increased intragranular strength, thus concentrated failure at the grain boundaries. Addition of nitrogen increases the flow stress even at 950°C and reduce the resistance to ductile crack propagation and increases the tensile strength. The variation of fracture toughness with nitrogen is related to the size of the precipitates. It can act like carbon in stabilized steels by precipitating in the form of nitrides (Nb-N). Nitrogen remaining in the solid solution has much greater strengthening effect than carbon. M23C6 is the main carbide in austenitic stainless steels, formed in an un-stabilized stainless steel [5]. Manganese and chromium increase the solubility of nitrogen in steel [14].

The formation of NbN or Nb(C,N) is a function of the amount of nitrogen. Increase in nitrogen concentration shifts the phase stability from Nb(C,N) to NbN. Thus, nitrogen replaces carbon and releases carbon for formation of M23C6. If nitrogen is increased in the absence of Nb, it combines with Cr to form Cr2N[4]. At still higher N, Cr2N consumes the Cr, which results in austenite. Carbides of types M23C6, M6C, M7C3 reduce strength and toughness. Addition of nitrogen increases hardness and hardenability induced by nitrogen is higher than for carbon. Though nitrogen brings several benefits, it tends to increase hardness linearly with increasing nitrogen content, which increases the cost of machining process. Therefore, keeping optimum nitrogen level is extremely critical to maintain machining cost at an acceptable level when compared to conventional steel.

A new composition developed by addition of nitrogen enabled a significant reduction of nickel in the austenitic stainless steel, which is a potential replacement of conventional stainless steel of 25Cr20Ni category.

3   ICME APPROACH TO DESIGN A NEW MATERIAL COMPOSITION

Integrated Computational Materials Engineering (ICME) refers to the use of computer simulations that integrate mathematical models of complex metallurgical processes with computer models used in component and process design. Traditionally, ICME gives a sort of cradle to grave approach to accelerate materials development, among others through integration of computational materials engineering tools. In this approach the characteristics of the material and process are predicted at different scale. For instance, one should ideally be able to start with chemical composition and predict the following thermodynamic characteristics, microstructure, microstructure variation during solidification, thermal properties, mechanical properties, variation of properties in the casting due to segregation and performance of the component [8].

This integration demands that tools exist that can link the models from each length scale, such as thermodynamics to microstructure. The primary function of those tools is to communicate model A from first scale to model B in a different scale. This communication/integration is achieved by combined effort from model A and model B developers, who are typically commercial software producers. Such co-development will be hindered if the integration is not commercially beneficial to both parties. The interests and needs of these two parties must be independently discussed. A plug-and-play combination of tools in these workflows is a key feature for successful implementation of ICME.

Traditional material development from composition to casting at foundry takes years rather than months and requires an experiment intensive approach. The reason behind the long cycle time of material development is usually due to lack of optimization of the material composition and missing interaction with the manufacturing process in the foundry in the early stages of material development work. ICME approach helps to run design of experiments across all chemical elements and their ranges. Composition design using computational method is extensively used with software like Thermo-Calc® to run with all possible design variables of composition and evaluated parameters to the critical to quality. Figure 1 shows the representative process map of the material composition design where the chemical composition ranges were evaluated in a random composition space by combining with artificial intelligence (AI) approach. This random composition space will further down select the composition needed to evaluate its phase fraction analysis under equilibrium and non-equilibrium conditions using Thermo-Calc® software. Further stage of design optimization involves evaluating the required properties against composition to down select the potential composition that can be taken for manufacturing stages.

Nitrogen alloyed steel was evaluated to down select the potential chemical composition that fulfils required properties in terms of nitrogen solubility, phase stability, carbide and nitrides quantification, freezing range and others. Figure 2 shows the interaction between composition and casting process which leads to optimized microstructure and intended mechanical properties [13]. The design optimization on nitrogen steel was also evaluated to understand the nitrogen solubility limits with respect to each chemical element.

The optimized chemical composition exhibits equilibrium phase fraction as shown in Figure 3. The presence of stable austenitic phase can be seen in the diagram. Further Cr carbides and Nb carbides are present which help in improving the mechanical properties along with the complex Cr-N. Evolution of ferrite phase is inevitable and the study was conducted carefully to reduce the ferrite phase within the mushy zone and at lower temperatures. Further analysis also conducted to understand the difference in phase evolution during equilibrium and non-equilibrium condition as shown in Figure 4. The non-equilibrium phases arises at lower temperature than equilibrium conditions.
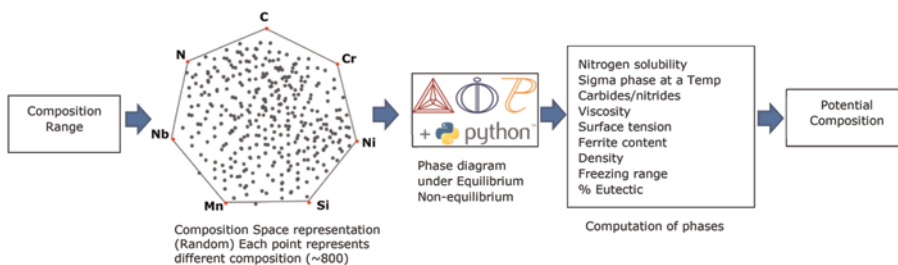

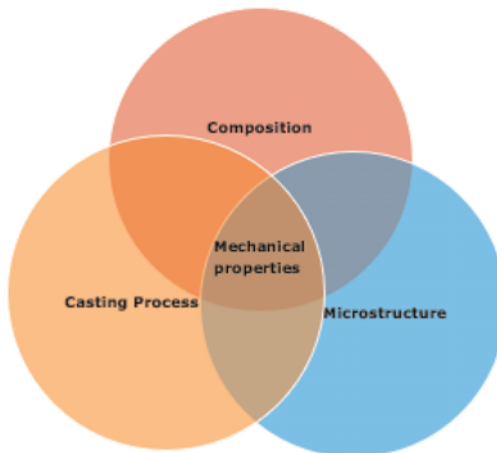**Figure 1. ICME approach of material composition design.**

Figure 2. Interaction of materials and process, Composition + Process = Microstructure + Mechanical Properties [13].
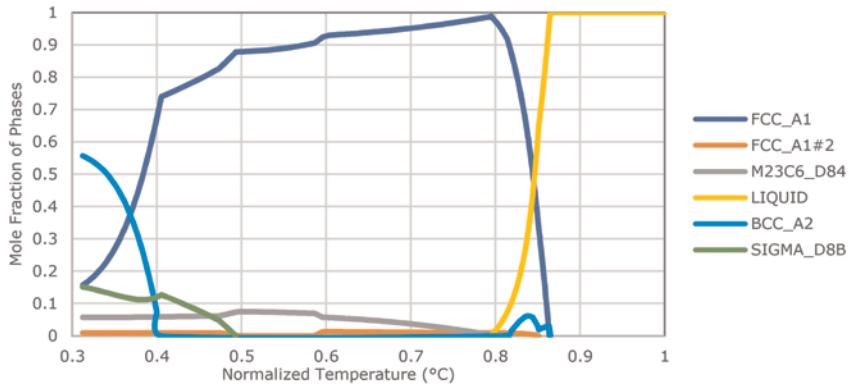
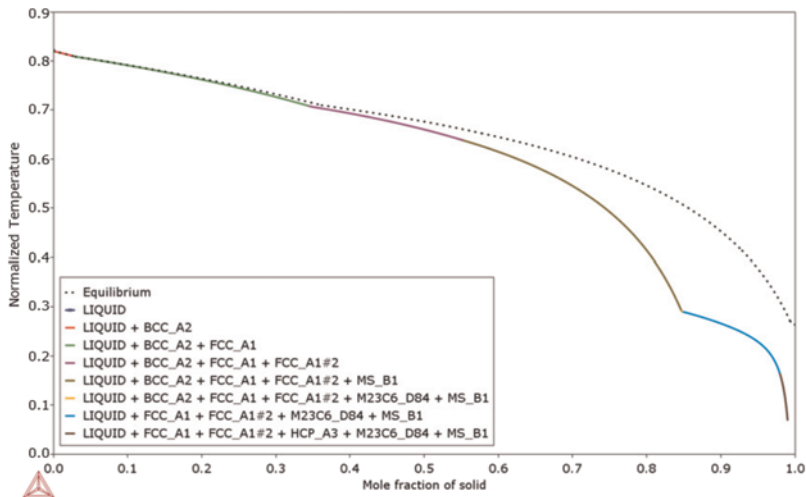**Figure 3. Equilibrium phase diagram of nitrogen steel.**

Figure 4. Phase evaluation of nitrogen steel under equilibrium and non-equilibrium condition.

Figure 5 shows the nitrogen solubility in terms of formation of gaseous nitrogen with respect to nitrogen content and temperature. The design of the new composition needs to fall within the safe region as shown in Figure 5. Figure 6 shows the random chemical design space varies with respect to individual elements and its influence on nitrogen solubility. Cr increases the nitrogen solubility whereas Si decreases nitrogen solubility in the melt. Other elements like Mn, Nb, Ni and C has marginal impact on increase or decrease of nitrogen solubility. Therefore, optimized element ranges were frozen without reaching unsafe region of nitrogen solubility. During casting process, the nitrogen emits a gaseous form and evaporates from the melt if falls into unsafe region. This optimum chemical ranges should also satisfy with the intended mechanical properties and manufacturing process.
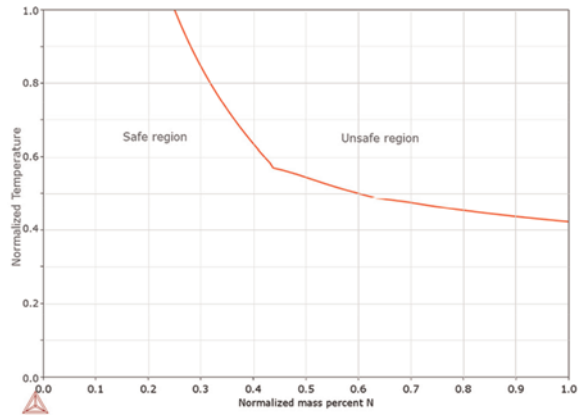
Figure 5. Typical solubility trend of nitrogen in austenitic stainless steel.
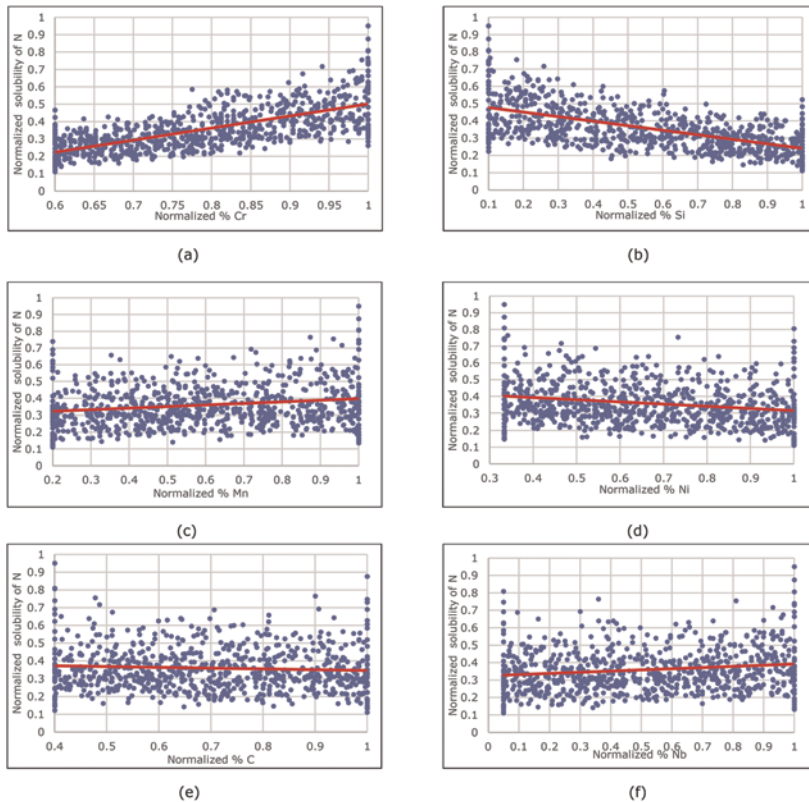

Figure 6. Nitrogen solubility for different chemical elements with random composition space. Trendline of nitrogen solubility with respect to increased elements (a) Cr (b) Si (c) Mn (d) Ni (e) C (f) Nb.

4   INFLUENCE OF MICROSTUCTURE FEATURES

The microstructure has a strong influence on the desired mechanical properties and the overall component level ability to maintain structural integrity. Figure 7 shows the component level microstructure after exposure to 150hrs of durability thermal shock test. Figure 7 (a) and (b) represent the conventional steel and (c) and (d) is nitrogen steel. Both materials have well retained dendritic arm spacing with the network of Cr and Nb carbides. In addition to that nitrogen steel shows presence of complex Cr and Nb nitrides. Secondary phases may be observed between Cr and Nb carbides which is typical behavior after exposure to high temperature. No presence of detrimental phases like TCP and Sigma phases was observed after durability test.

5   MATERIAL CHARACTERIZATION OF NITROGEN ALLOYED STEEL

Material characterization was systematically conducted on conventional and nitrogen alloyed steels using keel blocks casted from the same foundry process as component level casting. Strain controlled tensile tests were conducted using a 100kN hydraulic controlled universal testing machine at room temperature and elevated temperature. Creep tests were conducted using a 50kN creep test machine at 900°C and 1000°C temperatures where creep is dominant. Strain controlled isothermal fatigue test were conducted at 800°C and 1000°C. Thermo-mechanical fatigue tests, which is a non-isothermal loading in nature were conducted using a 100kN hydraulic controlled TMF test machine from 300°C–1000°C with a heating and cooling rate of 4°C/s using induction heating system which interfaced with mechanical loads [7].
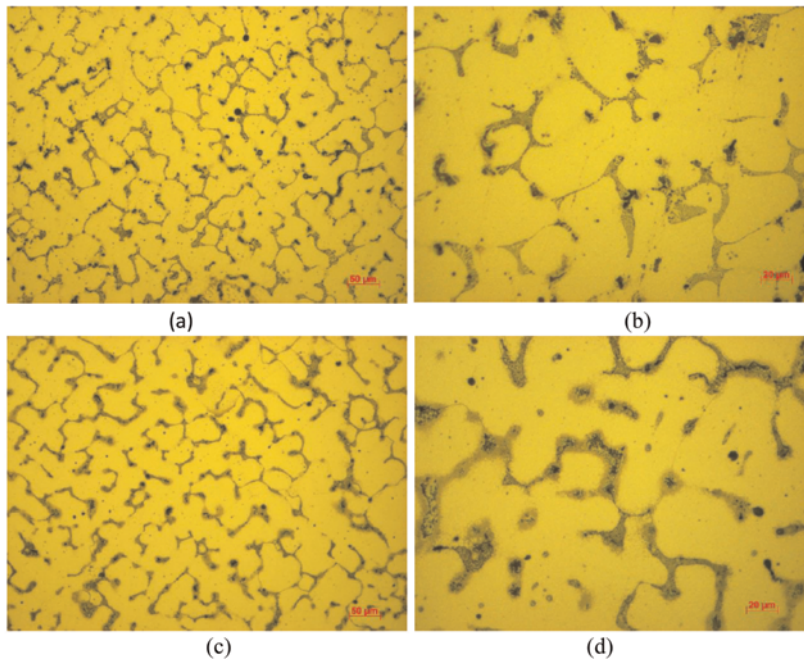

Figure 7. (a), (b): Microstructure of conventional steel containing network of Cr and Nb carbide. (c),(d): Microstructure of nitrogen steel containing network of Cr and Nb carbide along with nitrides.

Figure 8 shows the tensile results of two steels. The modulus of nitrogen alloyed steel is showing better results at all temperatures since the material has higher stiffness from interstitial solid solution of nitrogen element in the FCC crystal structure of austenitic phase. Yield and ultimate tensile stress show better results than conventional steel up to 900°C. Beyond 900°C the advantage of strength remains at the reduced level. The ductility of nitrogen alloyed steel shows a reduction at intermediate temperatures. The possible cause of reduction in ductility at intermediate temperature is due to ductile to brittle transition of nitrogen alloyed steel.

As the nitrogen element is positioned as interstitial solid solution within the FCC crystal structure of the austenitic phase, the creep properties at all temperature given in Figure 9 show better results than conventional steel. The creep strength increases due to precipitation strengthening from Cr-N clusters. The strengthening effect of nitrogen is due to the clusters of Cr-N, which result in increased elastic stress in the lattice. Therefore, the secondary creep rate for nitrogen alloyed steel is lower leading to longer creep life. Isothermal fatigue test reveals better fatigue life at 800°C and equivalent fatigue life at 1000°C for nitrogen alloyed steel as shown in Figure 10 (a) and (b). Thermo-mechanical fatigue properties undergo non-isothermal mechanical and thermal loading at a particular heating/cooling rate and strain rate. The life of nitrogen alloyed steel is marginally lower than conventional steel at higher strain ranges. However, this effect becomes insignificant when strain ranges start going down as shown in Figure 10 (c) and (d). In general, the alternate stress range induced in nitrogen alloyed steel is higher than in conventional steel during the TMF test. The resulting outcome is a lower TMF life. To achieve the same TMF life in nitrogen alloyed steel as compared to conventional steel, design optimization of the component using FEA is needed to reduce the mechanical strain at a given location in the component.
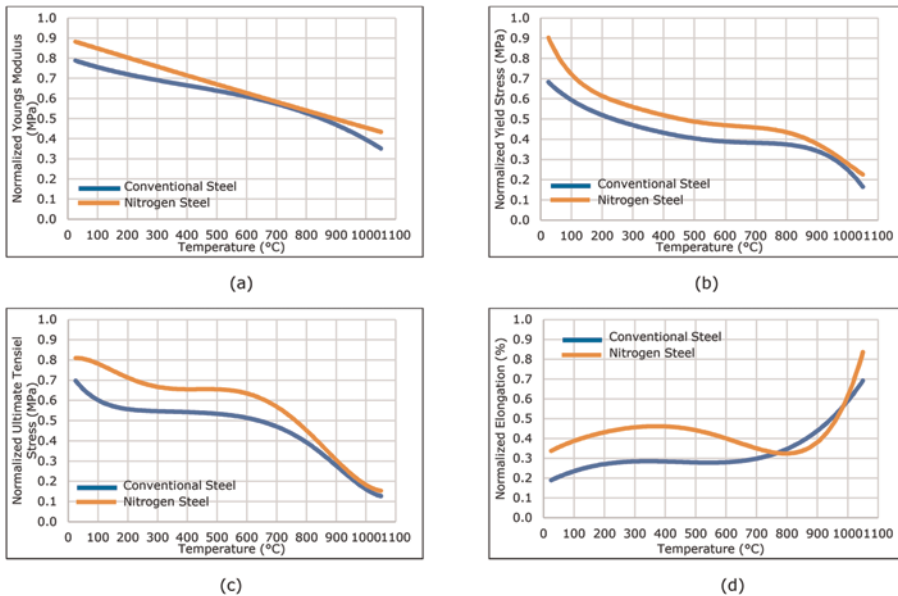

Figure 8. Tensile properties (a) Youngs Modulus (b) Yield stress (c) Ultimate Tensile Stress (d) Elongation.
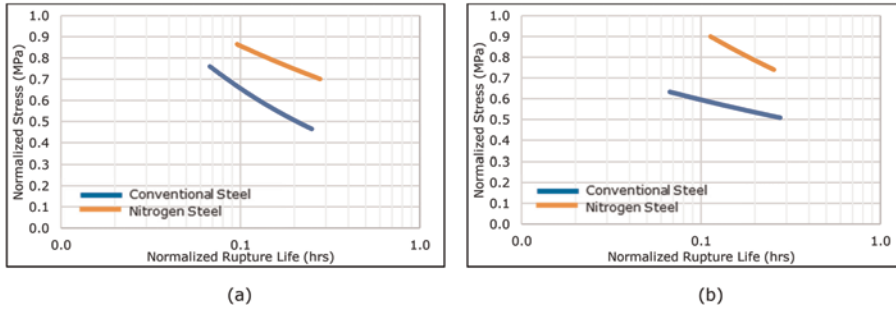
Figure 9. Creep properties results for convention and nitrogen alloyed steel (a) 900°C (d) 1000°C.
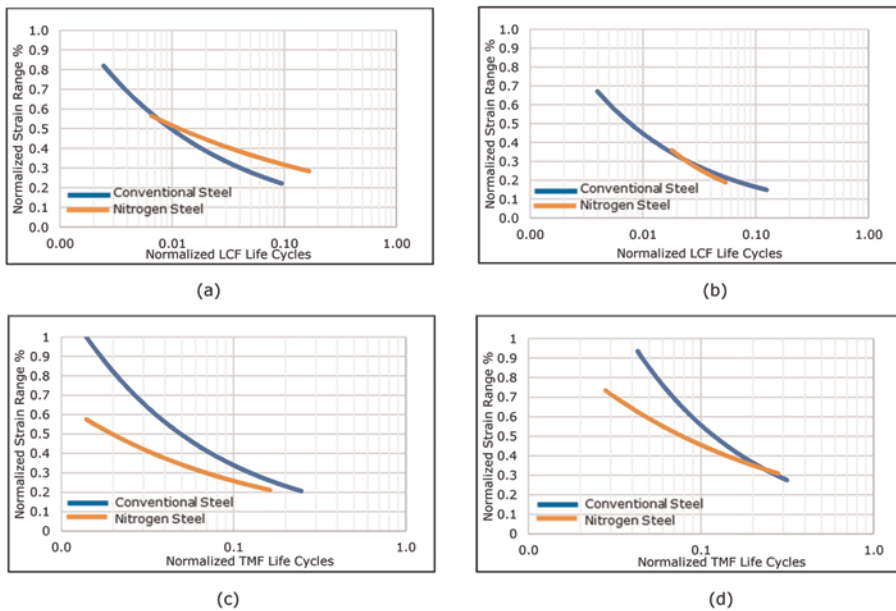
Figure 10. Isothermal fatigue test (a) 800°C (b) 1000°C; Thermo-mechanical fatigue test from 300–1000°C at 4°C/s rate (c) In phase (d) Out of phase.

6   OPTIMIZATION OF MANUFACTURING PROCESS PARAMETERS

The casting process is another prime important factor to achieve better cast component performed by ensuring optimum part quality. Nitrogen steel was initially cast using the same gating system and casting process parameters as conventional steel. A considerable number of process related issues occurred as the nitrogen steel melt behaved differently than conventional steel without nitrogen. Nitrogen alloyed steel exhibits multiple unacceptable surface defects. Metallurgical analysis later revealed that the defects shown in Figure 11(a) were caused predominantly by the reoxidation of molten metal reacting with the atmosphere within the mold cavity during pouring. The

137

reoxidation elements which are coming from material composition and a residual element leading to surface porosity in the inner surface. Another contributing factor was the reaction of the core material with the melt [9–11]. The gating system is optimized using casting simulation and validated with casting trials, which confirms the absence of reoxidation traces within the inner surface of the cast part as shown in Figure 11 (b).

A second type of casting issues occurred in locations corresponding to the areas of the mould that were the last ones to be filled, in the form of cavities with relatively smooth surface and rounded edges, indicating gas entrapment. It was observed that this failure only occurred on ladles with the lowest pouring temperature as shown in Figure 12 (a), and that by maintaining this pouring temperature above a minimum threshold the problem could be solved permanently. A third type of casting issues shown in Figure 12 (b) occurred in conjunction with the use of one of types of coating for internal cores. The reaction of the melt with the coating produced multiple gas bubbles, affecting the casting qualities where this type of coating was used. The switch to a different coating type eliminated this problem completely. Neither of these defects occurred on comparable parts cast with conventional steels and it is conjectured that the reduced surface tension of the Nitrogen steel is a contributor, underlining the necessity to define restricted limits and maintain a tight control on casting process parameters to ensure consistent and conforming production.

(a)   (b)

Figure 11. (a) Nitrogen steel with re-oxidation defect (b) Nitrogen steel without defect after optimizing the gating system.

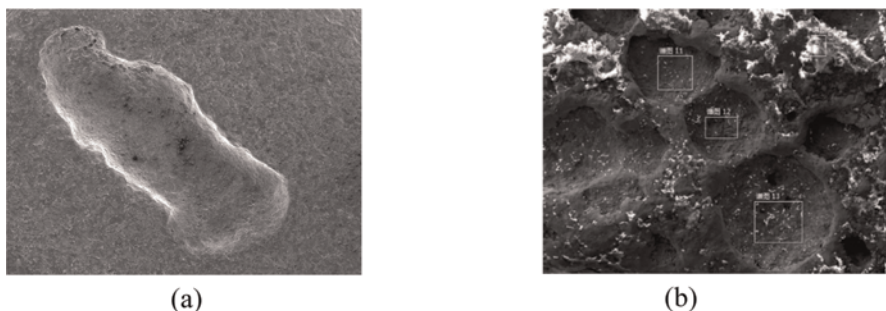(a)   (b)

Figure 12. (a) SEM image of gas hole in turbine housing inlet (b) SEM image of gas bubbles in turbine housing outlet.

The increased hardness of nitrogen steel vs conventional steel poses additional challenges for machining. During back to back trials with conventional steel parts, using identical tools and machining process parameters, cutter life was reduced. Therefore, it requires some amount of optimization of machining parameters to keep cost and machining tool life within acceptable limit. Though the machining cost of nitrogen alloyed steel is relatively on the higher side than conventional steel, the overall cost of the component level is significantly reduced.

7   HOUSING DESIGN AND VALIDATION

Turbine housing is a very critical component of a Turbocharger with complex design features, which requires a very robust design and simulation capabilities to meet a very severe thermal shock loading conditions. Turbine housing is optimised for a new composition using TMF simulation process comprises of unified visco-plastic material constititutive model and damage mechanism based life model, which captures a wide range of material deformation mechanisms as shown in Figure 13 (a) and (b).

Validation of Nitrogen steel against conventional steel was performed on a component level test rig to evalute the durability of the new material. Figure 14 shows the thermal cycle profile which the component was exposed. The thermal cycle comes with dwell time at highest and lowest temperatures.This test was conducted with the actual engine environment to assess the risk to the structural component. Both steel material components were exposed to very severe operating conditions for longer durations and both components were evaluted back to back for all critical locaitons. The locations in FEA are correlating well with actual durability test results as shown in Figure 15 in location 1.

Figures 16 and 17 further show the locations 2 & 3 features of the components between conventional and nitrogen steels. While visual observation shows the surface cracks for nitrogen steel to be marginally wider, propogation is in fact reduced compare to conventional steel. Overall it can be concluded that the nitrogen steel is equal or better in terms of crack resistance or severity at all inspected locations. There were no through cracks and no gas leaks to the external environment for both materials, indicating their suitability for the evaluated application and operating conditions.

(a)   (b)
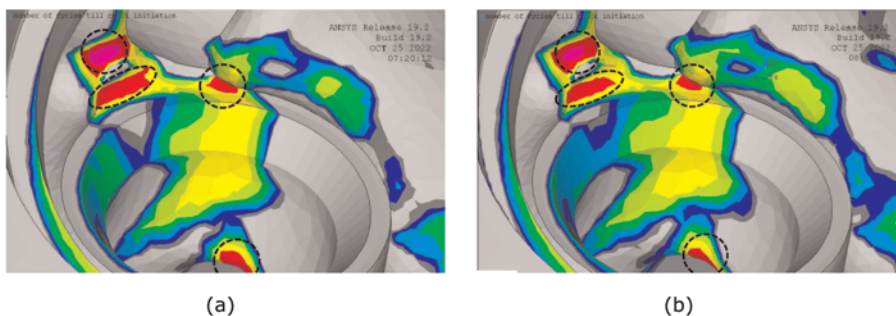
Figure 13. Localized plastic deformation from thermo-mechanical analysis [14] (a) Conventional steel (b) Nitrogen steel.

Figure 14. Thermal shock cycle profile at the component level test.

(a)   (b)

Figure 15. Component level durability test for 150hrs at location 1 (a) Conventional steel (b) Nitrogen steel.

(a)   (b)

Figure 16. Component level durability test for 150hrs at location 2 (a) Conventional steel (b) Nitrogen steel.

Figure 17. Component level durability test for 150hrs at location 3 (a) Conventional steel (b) Nitrogen steel.

8 CONCLUSION

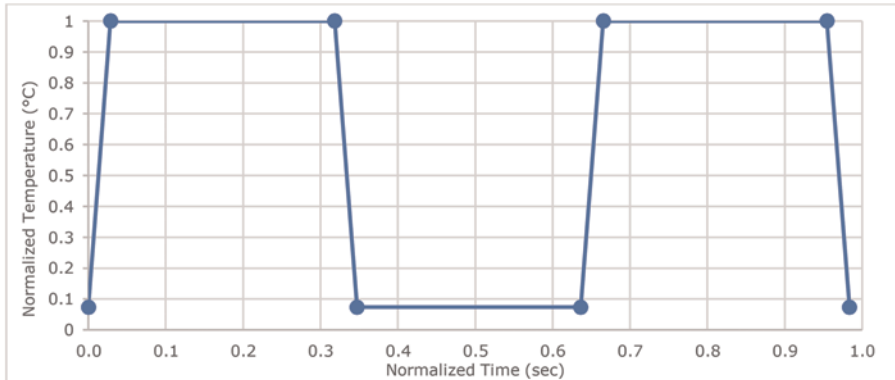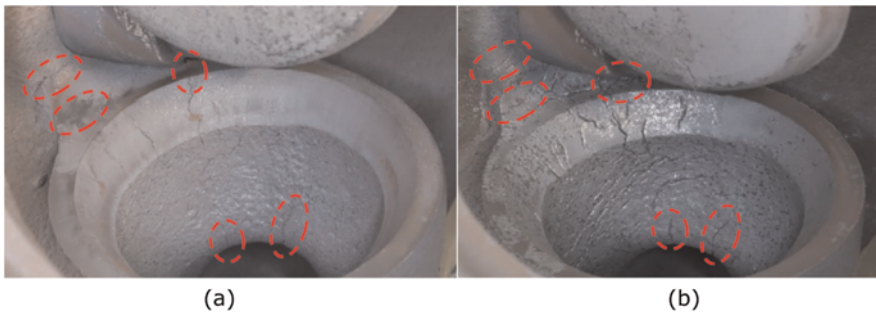Nitrogen is a very strong austenitic phase stabilizing element, which can be used to replace nickel to reduce cost while enabling better mechanical properties. Addition of nitrogen element also exhibits better creep resistance, higher fatigue life and fracture toughness, which is a significant advantage for severe thermal shock loading conditions. An in-house ICME approach was developed and used extensively for composition design which reduces the overall material development cycle time. An AI based Analytical model was developed to predict a wide range of compositions and the same was integrated into the ICME approach. Integration of computational and experimental techniques enabled to design a low nickel stainless steel material at lower cost and development cycle time. The new nitrogen alloyed stainless steel showing promising mechanical properties at coupon level. The same level of benefit is visible at the component level validation study under severe loading conditions. Nitrogen alloyed steel is sensitive with the conventional casting process. Therefore, optimization of casting process parameters using casting simulation method is critical to minimize the potential casting defects and reduce the variation of mechanical properties. The overall development and validation work reveal that the new material can be used for high temperature applications as an alternative to existing conventional stainless steels.

NOMENCLATURE

AI:	Artificial Intelligence
ASS:	Austenitic Stainless Steel
BCC:	Body-centered cubic
DTMF:	Damage mechanism based Thermo-Mechanical Fatigue
FCC:	Face-centered cubic
FEA:	Finite Element Analysis
ICME:	Integrated Computational Materials Engineering
IP:	In Phase

(*Continued*)

(*Continued*)

OP:	Out of Phase
SEM:	Scanning Electron Microscope
TCP:	Topologically Close-Packed
TIT:	Turbine Inlet Temperature
TMF:	Thermo-mechanical Fatigue
UTS:	Ultimate Tensile Strength
YS:	Yield Strength

REFERENCES

[1] V.G. Gavriljuk, H. Berns "High Nitrogen Steels: Structure, Properties, Manufacture, Applications".

[2] Oak Ridge National Laboratory and Honeywell International *"Cast CF8C-Plus Stainless Steel for Turbocharger Applications".*

[3] Kim, Yong Uk; Jung, Woo Sang; Chung, Young Hoon; Kwun, S.I. Effect of Nitrogen on Creep Properties of 22Cr-25Ni Austenitic Heat-resistant Steels, Key Engineering Materials, v 385–387, p 425–428, 2008.

[4] Tendo, Masayuki; Tadokoro, Yutaka; Suetsugu, Kazuhiro; Nakazawa, Takanori Effects of Nitrogen, Niobium and Molybdenum on Strengthening of Austenitic Stainless Steel Produced by Thermo-mechanical Control Process, ISIJ International, v 41, n 3, p 262–267, 2001.

[5] Park, I.; Masuyama, F.; Endo, T. Effect of Soluble Nitrogen on the Creep Strength of an Austenitic 25Cr-20Ni steel, Key Engineering Materials, v 171–174, p 445–452, 2000.

[6] Rawers, J.; Tylczak, J.; Blankenship, D.; Bullard, S. Characterizing Alloy Additions to High Nitrogen Steels Materials Science Forum, v 426–432, pt.2, 931–6, 2003.

[7] Rajkumar G, Ragupathy Kannusamy, Avadhoot Kulkarni, Amit Kumar, "Development of High Temperature Material Constitutive Model for Thermo-Mechanical Fatigue (TMF) Loadings in Turbochargers", Structures & Fatigue Center of Excellence, Honeywell Transportation System, 2018.

[8] Integrated Computational Materials Engineering, John E. Allison, Mei Li, and XuMing Su, *Ford Motor Company, ASM Handbook, Volume 22A: Fundamentals of Modeling for Metals Processing.*

[9] Mariusz Holtzer "Interfacial Reaction Between High-manganese Cast Steel and Silica Sand or Chromite Sand", AGH University of Science and Technology in KrakówFaculty of Foundry Engineering, 1990.

[10] Mariusz Holtzer, Artur Bobrowski, D. Drożyński, Jan Mocek *"Selection of Protective Coatings of Moulds for Castings of High-Manganese Cast Steel in Dependence of the Applied Moulding Sand Kind"*, 2013.

[11] John Campbell *"Complete Casting Handbook-Metal Casting Processes, Metallurgy, Techniques and Design"*, Second edition, 2015, p365–368

[12] *Porosity Defects in Iron Castings From Mold-Metal Interface Reactions*, R.L. Naro, ASI International, Inc. Cleveland, Ohio.

[13] Mike Ashby, Hugh Shercliff, David Cebon, "Materials: Engineering, Science, Processing and Design*"*, 3rd edition, 2014, Elsevier Ltd.

[14] M. V. Pridantsev and F. L. Levin, *"Effect Of Manganese On The Structure And Properties Of Nonmagnetic Stainless Steels"*, pp. 10–14. December. 1965.

[15] Ansys, www.ansys.com.

Design and optimisation of compressors

Taylor & Francis
Taylor & Francis Group
http://taylorandfrancis.com

Detailed experimental performance and efficiency assessment of a turbocharger centrifugal compressor under steady and pulsating conditions

A. Parikh, C. Noon, M.E. Barrera-Medrano, R. Martinez-Botas

Department of Mechanical Engineering, Imperial College London, London, England, UK

Y. Hayashi

Mitsubishi Heavy Industries, R&I Division

ABSTRACT

The performance of a turbocharger centrifugal compressor is affected by the opening and closing of the engine intake manifold and consequently experiences a pulsating back-pressure. This off-design pulsating environment results in internal losses and affects compressor performance. Previous research on the effect of exit pulsation has demonstrated a surge margin improvement at low end torque conditions, however the pulsating effect on instantaneous efficiency is yet unknown; this paper aims to address this lack of knowledge.

Experimental analysis is undertaken on an instrumented centrifugal compressor under compressor exit pulsating conditions. The instrumented compressor has been manufactured to include sensor ports for measurements of static pressure and temperature at internal locations at the impeller, diffuser and volute. The experiments have been conducted on steady flow conditions and pulsating outlet conditions at pulse frequencies of 30, 46.7 and 66Hz. These frequencies are critical engine frequencies that correspond to near surge, peak pressure, and peak efficiency operating points of the turbocharger compressor under study. Instantaneous static pressure amplitudes for operating points and the corresponding hysteresis behaviour have been studied for the volute, diffuser and impeller pulses.

The results show that the pressure amplitude is largest when the flow rate is high and reduces as the flow rate reduces. The efficiency in pulsating conditions starts to decrease as the flow rate increases and it is largest at high flow conditions. The volute is influenced by the pulse amplitude as well as the frequency of pulsation. Within the volute, the resulting large flow fluctuations have internal disturbances which effect the propagation of the pressure waves; near the tongue, instantaneous static pressure measurements show the pressure in that location distinctively does not follow the pressure wave at the outlet. The region near the volute tongue region has been shown to be particularly critical due to its vicinity to the outlet changing (pulsating) boundary condition and reduces the efficiency of the compressor. This initial assessment leads to interesting insights in the response of the compressor to an unsteady pulsating environment thus allowing a better understanding on the real turbo-engine system performance.

1   INTRODUCTION

The rise of greenhouse gases in the atmosphere is a globally important environmental concern as it leads to drastic changes in the ecosystem and the natural climate. One of

the ways in which greenhouse gases are minimised is through the reduction of harmful emissions from the transport industry as this sector is one of the largest emitters of greenhouse gases [1] Within the transport industry, in 2020 it was found that passenger cars and trucks share 63% of the worldwide CO_2 emissions [2], therefore, it is essential for transport manufacturers to reduce the emissions from their engines to curb the harmful effects of global warming. Turbochargers are commonplace in internal combustion engines as they enable a more efficient system.

The role of the turbocharger is to increase the density of the air reaching the engine by utilising wasted exhaust energy in the process. Turbochargers are made of two components; the turbine runs on the exhaust flow and a compressor that compresses the incoming air. The performance and efficiency of a turbocharger is affected by the opening and closing of the engine intake valve [3]. The focus of this paper is on the centrifugal compressor which experiences a pulsating backpressure under engine conditions. The compressor exit sees a backpressure of different amplitudes and frequencies corresponding to the engine operating conditions. This causes the compressor to operate in dynamic off-design conditions rather than the steady design conditions. The performance and efficiency of the compressor is consequently reduced in comparison to the steady operating conditions [4]. It is important for manufacturers and turbocharger designers to understand the deviation from steady conditions as knowledge of the operational behaviour improves the turbocharger matching process. This research aims to understand the deviation in performance and efficiency under pulsating flow in selected operating points, as these correspond to key operating points for the engine.

2   LITERATURE REVIEW

A number of experimental studies in recent literature have shown that the performance of an automotive turbocharger is affected by pressure pulsations due to the opening and closing of the engine intake manifold. Even though this effect is much more prominent and more extensively researched in turbines, recent studies have shown a reduction in performance of the compressor due to the fluctuating backpressure environment created by the opening and closing of the engine intake manifold. Majority of this research focusses on the surge regime, the lower limit of stable operation for the compressor, as the operating range of the compressor is a key parameter in defining the compressor range. Some of the initial findings by Yano and Nagata [5] and Bensen and Whitfield [4] show that unsteady environments affect the onset of compressor surge. Galindo et al. [6] found that at a pulsating flow of 40–67Hz, the surge margin increased by around 15\% and that increase in surge margin was dependant on the amplitude of the pulse. Furthering the work of Galindo, Marelli [3] [7] and Barrera-Medrano [8] [9] also show that that under pulsating backpressure conditions, the lower limit of stable operation moves further to the left, and the compressor can even instantaneously operate on the left of the surge line for a significant period of the pulse [7]. However the extent to which the stability of the system is affected is determined by a combination of factors, such as the system size [10] and the level of imposed unsteadiness.

Although pulsating conditions improve the surge margin and enable a stable operation at lower mass flow rates, there is a performance deficit due to the unsteady environment. This is due to the pressure wave created by the engine intake and it has corresponding effects on the mass flow and inertia of the system. Marelli, Capobianco \& Zamboni noted that the compressor was subjected to the filling and emptying wave action just as that of a turbine and evaluated the hysteresis loops under several pulsing conditions [7]. By comparing the instantaneous performance of the compressor to that of the steady performance, it was found that at the same mass

flow rate, the mean pressure ratio is less than that of steady operation. Shu et al. [11] investigated the performance of a centrifugal compressor experimentally and found that at the peak efficiency, the performance dropped by around 3–7%. At the different speeds, the peak efficiency decreased by 7%, 5% and 3% for 25, 30 and 35kRPM of the compressor. Other studies have also shown a deficit in the compressor performance. In the hysteresis behaviour of the compressor system at the Genoa facility, two loops are visible in the performance loop; the main loop is found to be dependent on the upstream pressure wave and the secondary loop is due to wave reflections in the exit [7].

The volute and tongue have a significant impact the overall compressor efficiency and loses [12]. Ayder et al. [13] show that the behaviour of the volute is dependent on key factors like volute cross section area and position of the tongue inlet. In a study conducted by Gulich [14], blockage around the inlet due to the presence of the tongue resulted in a deviation of the otherwise uniform pressure distribution at the volute inlet, leading to flow separation at the outer wall of the volute inlet near the tongue. Whereas for high flow rates, the flow separation occurs at the pressure side due to a more radial velocity of the flow. At the tongue, this deviation from design point is critical, as it affects the overall efficiency of the impeller. Further work is required to understand how the tongue, volute and impeller behave under off-design pulsating conditions.

The aforementioned studies show that pulsating conditions affect the performance and efficiency of the centrifugal compressor. Although there is a surge margin improvement, there is also a reduction in performance and efficiency at critical operating points such as peak efficiency, which reduce the effectiveness of the turbocharger compressor when placed in engine conditions. Therefore, it is important to explore the extent of efficiency reduction in the pulsating environment as it has an influence on the compressor design. Experimental internal flow measurements of a compressor under pulsating flow could provide further insight on where the efficiency deterioration takes place and how it consequently affects compressor performance. With this in mind, the purpose of this study is two-fold. Using an instrumented volute, the internal static pressure profile of the pulsating environment is to be studied experimentally. An assessment of efficiency reduction at specific operating points for the compressor is to be established and insights drawn on the internal flow behaviour at specific regimes. It is expected that this research provides baseline information for computational studies and also further helps understand the efficiency and performance reduction of centrifugal compressors in these conditions.

2.1 Experimental set up

The experimental set-up is shown in Figure 1. The compressor is driven by a 110kW motor and epicyclic gearbox with a 27:1 reduction ratio. A pulse generator is used to simulate the exit pulsating conditions. The pulse is generated by the rotating action of a disc which blocks the flow with every rotation. The position, amplitude and location of the pulse generator has been previously validated for producing pulses that have an engine likeness [15]. The mass flow rate of the system is calculated with a v-cone purpose built for this facility. A CTA probe, which acts as the instantaneous mass flow sensor is also placed at the compressor inlet.

The flow rate through the system is controlled by a butterfly valve at the exit of the pipework. The compressor is directly mounted on a bearing housing with a separate oil-feed and operates in an open system, drawing in ambient air from the atmosphere. In order to accurately measure compressor efficiency, the facility has been insulated between the inlet and outlet measurement planes such that the compressor system behaviour is close to adiabatic conditions. Minor modifications have also been made to the compressor piping to

move the inlet measurement plane further upstream from the compressor inlet. This has been important to ensure the instantaneous mass flow rate measurements close to surge are not affected by inlet recirculation.

The compressor is run at a constant speed of 40,000rpm. The tests are conducted with steady flow operating conditions and later with pulsating frequencies of 30Hz, 46.7Hz and 66Hz. The compressor has a large open type impeller with a tip clearance and an exit diameter of 136mm. These frequencies correspond to the operating conditions of the engine at near surge, peak pressure, and peak efficiency conditions for the compressor system of interest. The valve is fully open at the beginning of the test and the compressor is taken to surge to record a full speed line.
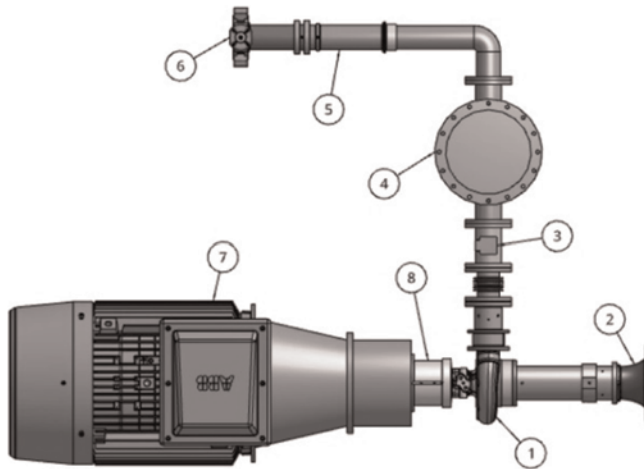

Figure 1. Experimental testing facility. 1 – volute, 2 – bellmouth, 3 – pulsating device, 4 – plenum, 5 – v-cone, 6 – butterfly valve, 7 – motor, 8 – adapter.

For this research, the compressor volute has been re-manufactured and modified for the detailed internal measurements as shown in Figure 2. This has enabled placement of static pressure transducers and thermocouples at different locations within the compressor where possible such as the impeller, diffuser, and volute. The positions of the sensors have been limited by the manufacturing constraints and sensor ports have been placed where possible. Instantaneous mass flow is recorded with a DANTEC 10 micron CTA probe. Temperature measurements are taken at the diffuser inlet and outlet with a k-type beaded thermocouple. Overall inlet and outlet pressure measurements are taken with Omega PX321B transducers. Internal unsteady pressure is taken with Kulite pressure transducers in the 10 locations shown in Figure 2. All data is recorded at a sampling rate of 12.5kHz.

Figure 2 shows the impeller inlet, middle of impeller and impeller exit, corresponding to positions P1, P2 and P3. The diffuser measurement is shown in position P4 and P5. The volute sensors are indicated using clock positions and placed in positions P6 to P11. Lastly, the static pressure at the exit of the compressor is measured at position 12.
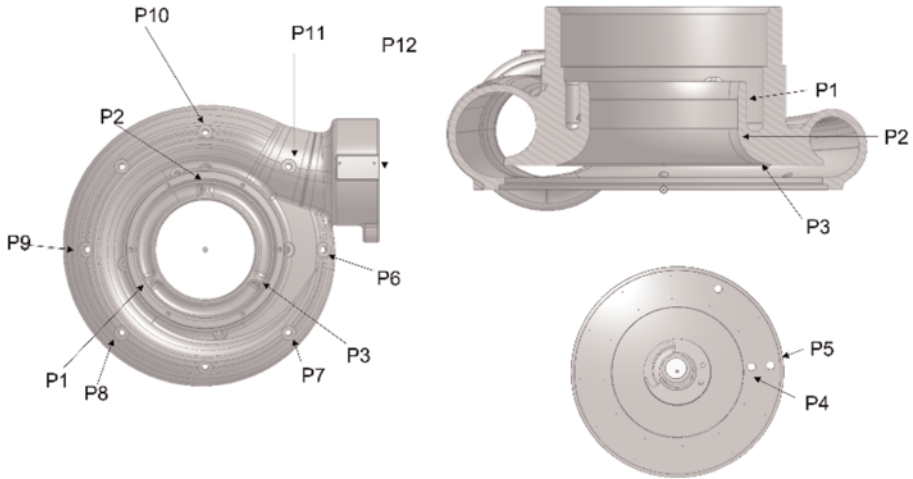
Figure 2. Location of different static pressure sensors. P1 – impeller inlet, P2 – impeller midspan, P3 – impeller outlet, P4 – diffuser inlet near tongue, P5 – diffuser outlet near tongue, P6 – volute at clockwise location 3:00, P7 – volute at clockwise location 4:30, P8 – volute at clockwise location 7:30, P9 – volute at clockwise location 9:00, P10 – volute at clockwise position 12:00, P11 – volute at clockwise position 1:30, P12 – compressor outlet.

3 RESULTS AND DISCUSSION

3.1 Cycle average pressure ratio and efficiency

Cycle-average results of pressure ratio and total efficiency have been obtained for the steady and exit pulsating conditions. It is worth noting that the cyclic average is the numerical average of the data points collected within the pulse. This numerical average operating point does not exist in reality but is a representative measure that is used here to position the performance of the compressor under pulsating flow conditions with respect to the steady flow conditions. Operating points with similar mass flow rates for the steady and pulsating flow conditions are compared, so that the difference in performance for the same swallowing capacity of the compressor system can be determined.

The pressure ratio of the compressor system, Π, is given by Equation (1), where P_{01} is the cycle-average total pressure at the compressor inlet and P_{02} is the cycle-average total pressure at the compressor outlet.

$$\Pi = \frac{P_{02}}{P_{01}} \qquad (1)$$

The total-to-total efficiency is calculated using Equation (2) where T_{01} is the cycle-average total temperature at the compressor inlet and T_{02} is the cycle-average total temperature at the compressor outlet.

$$\eta = \frac{C_p(T_{02s} - T_{01})}{C_p(T_{02} - T_{01})} \qquad (2)$$

Figure 3 shows the performance and efficiency of the compressor system for the reference steady flow conditions at three corresponding locations, labelled A-C, and the equivalent cycle-average pulsating flow operating points. Frequencies 30Hz, 46.7Hz and 66Hz correspond to circle, dot and cross indicators respectively. On the pressure ratio curve, it is clear to see that there is a drop in performance at operating point C for the three pulsating frequencies, with the largest drop in performance seen for the 30Hz frequency. At operating points A and B, the performance is similar or equivalent to the reference steady conditions. In Figure 3, it can be seen that there is a drop in the cycle-average efficiency for operating point C but this drop in efficiency is independent of the frequency, on average.

At point A, the cycle-average performance for the pulsating conditions is similar to the steady reference conditions however, the cycle-average efficiency drops with an increase in exit pulse frequency and it is worst for the 66Hz case. In state B, the difference in cycle average pulsating and steady flow performance and efficiency is smallest relative to points A and C. At operating point C, the performance deficit for pulsating exit conditions is most evident, with the largest drop in performance being the 30Hz frequency. What can be immediately inferred from Figure 3 is that there is a frequency effect on the performance and efficiency of the compressor system when compared to a given reference operating point, this is in line with the previous studies. Note that OP D has also been recorded in steady conditions, however, it was not possible to obtain this operating point in pulsating conditions as the throttling of the flow reduces the maximum swallowing capacity of the compressor system. OP D has been plotted on the Figure to show that OP C corresponds to the equivalent peak efficiency condition if the flow was steady.
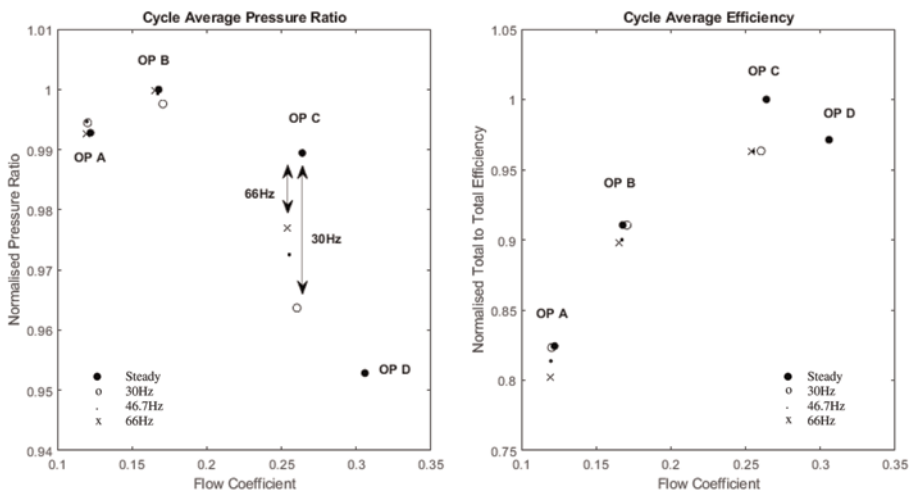

Figure 3. Pressure ratio and efficiency curve at operating points A, B and C which correspond to low flow, mid flow, and high flow conditions for the compressor system.
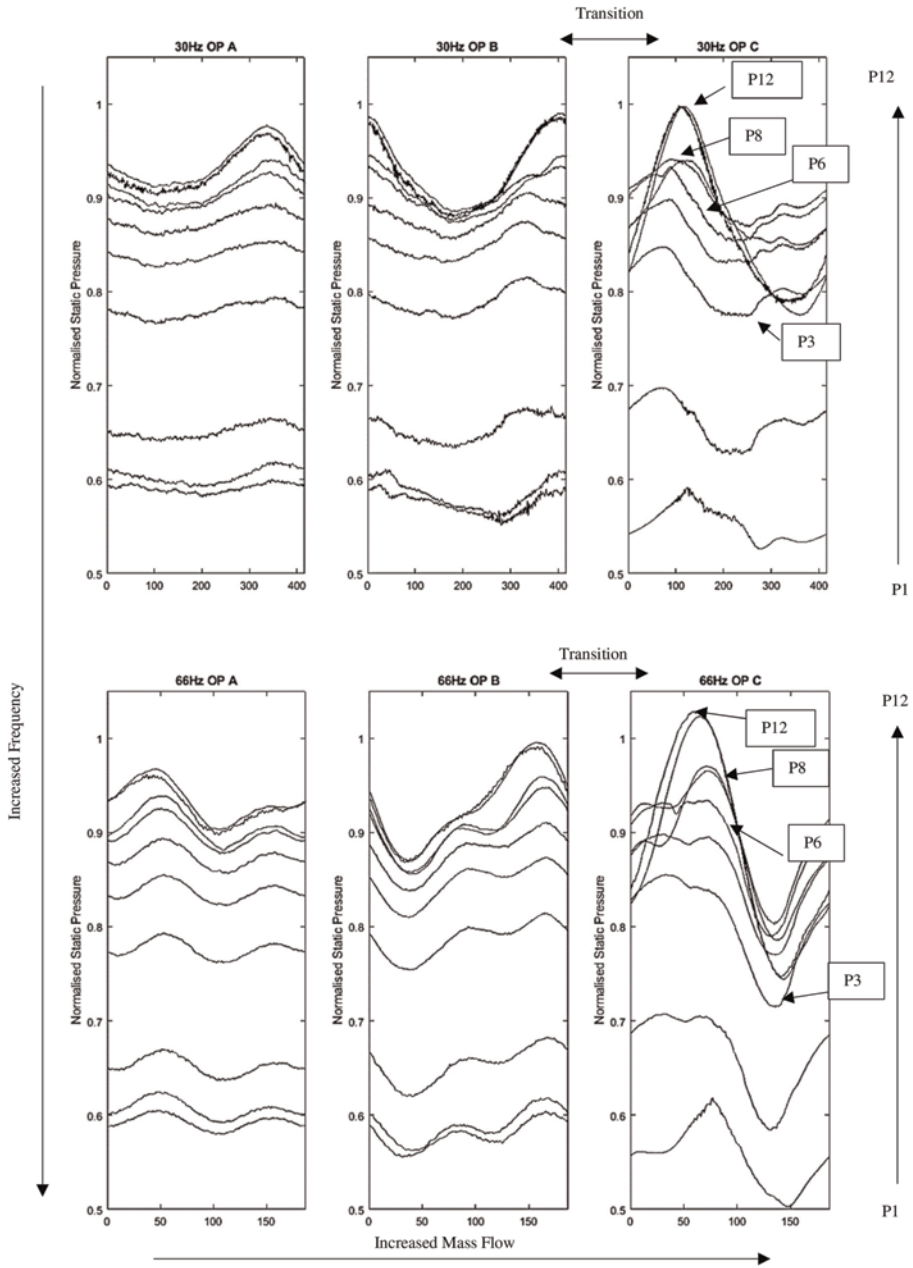
Figure 4. 30Hz (Top) and 66Hz (Bottom) Trace from selected static transducer locations 1 – 12. 1 – impeller inlet, 2 – impeller midspan, 3 – impeller outlet, 4 – diffuser inlet near tongue, 5 – diffuser outlet near tongue, 6 – volute at clockwise location 3:00, 7 – volute at clockwise location 4:30, 8 – volute at clockwise location 7:30, 9 – volute at clockwise location 9:00, 10 – volute at clockwise location 12:00, 11 – volute at clockwise location 1:30, 12 – compressor outlet.

151

3.2 Static pressure measurement for one pulse

The static pressure is measured at different positions shown in Figure 2 and visually represented in Figure 4 for 30Hz and 66Hz and operating points A, B and C. Figure 4 (top) is 30Hz whereas Figure 4 (bottom) shows 66Hz. The static pressure for all measurements (P1 – P12) have been mapped on one figure, volute measurements P9 and P10 have not been included for simplifying the figure; The first measurement, position 1, is at the impeller inlet and the measurement at position 12 is at the compressor outlet. From position 1 (P1) to position 12 (P12), the pressure measurements effectively track the static pressure rise through the compressor. Note, the figure shows one average pulse profile which is an average of all the pulses recorded during data acquisition.

First, it is possible to notice that at operating point C (large flow) for 30Hz and 66Hz the internal static pressure traces in the diffuser and volute section of the compressor (P4-P8) do not follow the imposed static pressure at the compressor exit (P12). Additionally, this variation from the imposed static pressure at the outlet is affected differently in the 30Hz case vs the 66Hz case.

Note that Figure 3 showed that at operating point C, for the same swallowing capacity or mass flow rate, the compressor system with exit pulsating conditions was unable to match the steady performance, and that the pressure ratio attained was lower for the imposed frequency of 30Hz compared to 66Hz. In contrast, at operating point A there was a similar performance for both pulsating frequencies and the pressure ratios were close to the reference steady conditions. This drop in performance can be immediately attributed to a few factors. First, the difference in pressure trace at OP A and OP C is that the pulse is of a higher amplitude in OP C compared to OP A; the pulse amplitude reduces as the operating point shifts towards lower mass flow rates for all frequencies (note, the 46.7Hz case is not shown for conciseness of this paper). This is because the amplitude of the backpressure wave is dependent on the amount of flow that is being periodically blocked by the valve; at high flow rates, as the mass flow rate is higher. When the valve closes, a large amount of mass is instantaneously stopped which creates a large localised static pressure; instantaneously a large deviation from mean pressure takes place resulting in a backpressure wave of high amplitude. At low flow rates, the backpressure wave does not have a high amplitude because there is less mass to create the backpressure and therefore there is less deviation from mean pressure. As the only controlled change has been the reduction of the flow capacity from valve closure, this pressure wave must be a function of the flow rate in the system.

It is also possible to see that between OP B and OP C there is a transition in the way the pressure wave propagates through the volute internally, see Figure 4. For and between OP A and OP B the pressure wave propagation at all positions within the compressor follows the imposed pressure profile closely and at OP A, there is a distinct pressure rise for both 30Hz and 66Hz case throughout the compressor. However, Figure 4 shows that between OP B and OP C, the static pressure within the volute does not uniformly rise. There appears to be a transition point after which static pressure measurements at P4-P8 are distinguishingly different from the static pressure measurement at P12, suggesting that the pressure wave propagation has been altered.

It is possible that the reduction of performance for 30Hz and 66Hz for operating point C is related to local variation or disturbance of pressure in the vicinity of the tongue. This local disturbance is worse in the 30Hz case compared to the 66Hz case as local pressure seems is out of phase with the compressor outlet for at least half the wave cycle. In the 66Hz case, only the maximum pressure signal appears stunted, when the backpressure drops, the pressure near the tongue locally also drops. In the 30Hs case, when the overall backpressure at the compressor outlet drops, the pressure in the tongue vicinity does not drop but stays high.

This local disturbance could be due to a reflection of pressure waves at the tongue gap, which is shown in Figure 5. For this compressor system, the behaviour is influenced by the outlet pressure pulse wave. The pressure pulse wave travels downstream through the collecting duct but also travels through the tongue gap. These two pressure waves propagate in different directions and can therefore interfere. It is possible that it is because of internal reflection of the pressure wave, that the local pressure is disturbed at different wave positions, the 66Hz case is most disturbed at the wave peak whereas the 30Hz is disturbed at the wave trough.
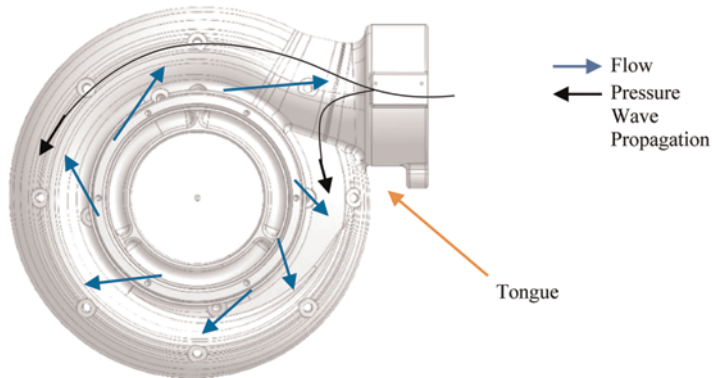

Figure 5. Schematic of pressure wave propagating through tongue gap and disturbing the main flow.

3.3 OP C 'filling and emptying' effect volute

The static pressure and mass flow instantaneous response can be seen in Figure 6 this is characterised by a hysteresis behaviour, well established in the literature, refer to Figure 2 for the location of the different pressures. It can be seen that there is a 'filling and emptying' effect of the volume where the volume accumulates and dissipates mass locally. The static pressure is normalised to the maximum static pressure obtained during the 30Hz pulse. The x axis shows the mass flow range that is swept instanta-neously during this operating point. There are four positions tracing back the static pressure from the outlet imposed static pressure. As mentioned before, a hysteresis behaviour is more 'rounded' if the inlet mass flow rate takes a longer time to respond to the imposed static pressure, otherwise known as a 'lagging' response of the system and indicative of more localised filling and emptying of the volume. It is interesting that Figure 6 shows a difference in the location of a more rounded hysteresis behaviour for the 30Hz and 66Hz case. In position 12 which is at compressor exit, 66Hz shows less lag or filling and emptying in that location; the mass flow rate drops and rises in response to the rising and falling of the static pressure at the outlet. However contrastingly position 12 for the 30Hz case shows that there is more lag in the mass flow response to the outlet static pressure. However, different positions within the pulse respond differently.

In contrast, at position 10 shown in Figure 6, the static pressure at 30Hz shows almost no lag to the inlet mass flow rate whereas the 66Hz case shows a more significant lag. At position 11, which is around 180 degrees away from the compressor outlet and the half-way point of the collecting duct, the hysteresis loop is bigger and rounder in 66Hz case compared to 30Hz case, showing that the inlet mass flow rate does not coincide with

the static pressure variation in this region. Interestingly, position 6, which is just before the compressor tongue, shows two distinct features for the 66Hz case. First, the static pressure trace for 66Hz shows less hysteresis behaviour than the 30Hz case. In this position the mass flow rate follows the static pressure variation as seen by the narrower hysteresis loop. However, there is a clear flat region of the pulse. This same flat region corresponds to the flat region shown in Figure 4 and is due to the pressure wave deviating at that location.

It is clear that filling and emptying of the flow is taking place within the volume, however, it appears that it is occurring at different positions within the volume. For the 30Hz case, it is occurring more near the compressor exit and around the tongue, whereas for the 66Hz case it is occurring more away from the compressor exit. Additionally, this is interesting because if the static pressure is different along the volute, different passages of the impeller also perform differently. The overall performance (based on the volute exit alone) reflects this difference in performance for the different frequencies.

Additional to the location of the 'filling and emptying', the 66Hz case may be performing better than the 30Hz case because the pulse acts for a shorter time. It is worth noting that since 30Hz is near half the frequency of 66Hz, it has double the time period. The time period can be thought of as the residence time of the pulse. As the mass in the system has flow inertia, if the pressure changes faster than the flow can respond to the changing pressure, then the flow is less affected by the changing pressure conditions. Therefore, the instantaneous pressure propagation could be a function of the flow inertial response. Since the 30Hz case shows localised 'filling and emptying', it is an indication of localised flow inertial response that could be a reason for the larger drop in performance for 30Hz case.
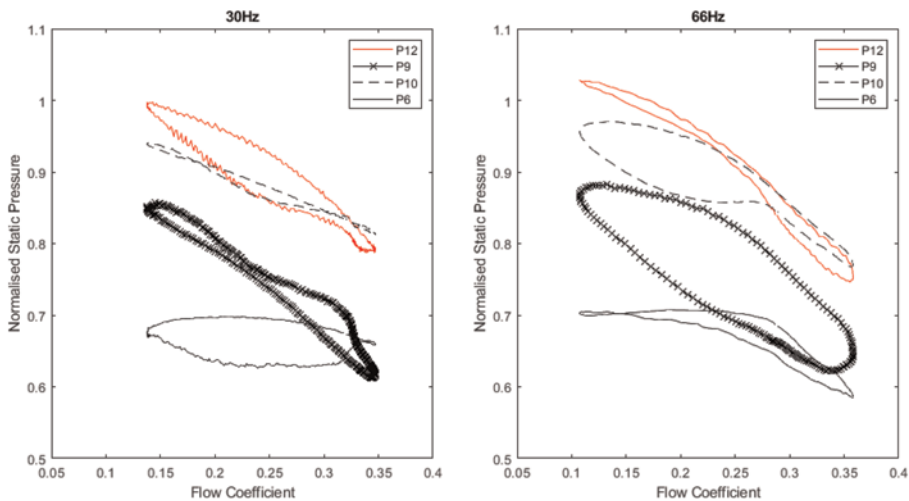

Figure 6. Static pressure hysteresis behaviour for OP C for volute locations P12 – compressor outlet, P9 – volute at clock position 9.00, P10 – volute at clock position 12.00, P6 – volute at clock position 3.00 for 30Hz and 66Hz case.

154

3.4 Quasi-steady vs unsteady OP A and OP C

As previous research has shown, the instantaneous performance under exit pulsating flow conditions for a centrifugal compressor is different to the steady performance. For a single operating point, instantaneously, the pressure drops and rises within a single pulse and the mass flow rate rises and falls accordingly. Depending on the physical size of the compressor system, there is a filling and emptying effect which affects the hysteresis behaviour. The inlet mass flow and outlet pressure are out of phase. For any given compressor system, the hysteresis behaviour differs depending on the frequency of pulsation, as the time to react to the imposed pressure reduces with increased frequency.

Figure 7 shows the instantaneous hysteresis of compressor performance, given by the instantaneous pressure ratio, at operating points A and C. Also indicated on the figure is the quasi steady (QS) approximation of the performance for the same operating point. The QS approximation is the performance of the system if the compressor was behaving under steady conditions. It is approximated using the data from the steady performance map and the instantaneous mass flow rate swept by the system. It can be seen that, for both operating points A and C the hysteresis behaviour in the 30Hz case differs from the 66Hz case. In the 66Hz case, the hysteresis behaviour is narrower than the 30Hz case; this indicates that the phase shift between the mass flow and the pressure is smaller in 66Hz than the 30Hz case This is much more evident at OP A than at OP C.

It can also be seen that at OP C, for both frequencies the instantaneous pressure ratio is much higher than QS pressure ratio. When the instantaneous mass flow rate drops to the low-mass flow rate region, the instantaneous pressure ratio is larger than expected compared to QS approximation, so instantaneously, it is possible for the compressor system to generate a pressure ratio that is higher than would be achieved if in steady. This high instantaneous pressure achieved under pulsating conditions is what leads to a higher cyclic average calculation of pressure ratio compared to the Q-S approximation. In contrast, in the low flow rate conditions at OP A, the 30Hz and 66Hz instantaneous behaviour spans a much smaller flow range instantaneously compared to OP C.
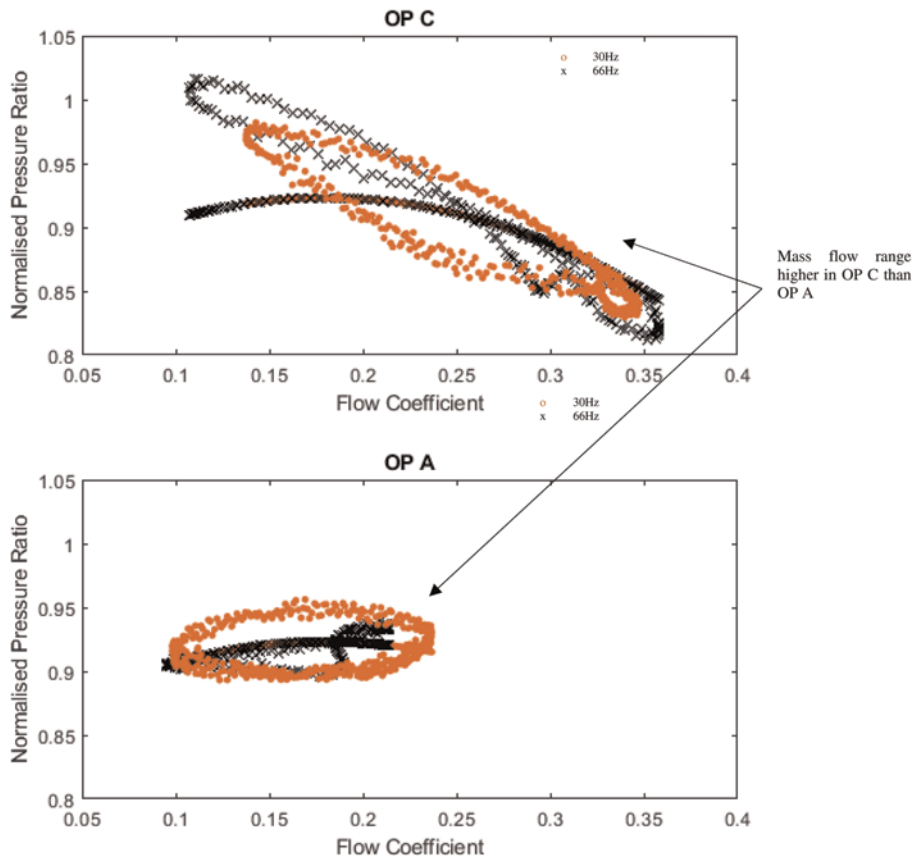
Figure 7. Instantaneous pressure ratio vs QS pressure ratio for Op A and C steady, quasi steady and unsteady cyclic average efficiencies.
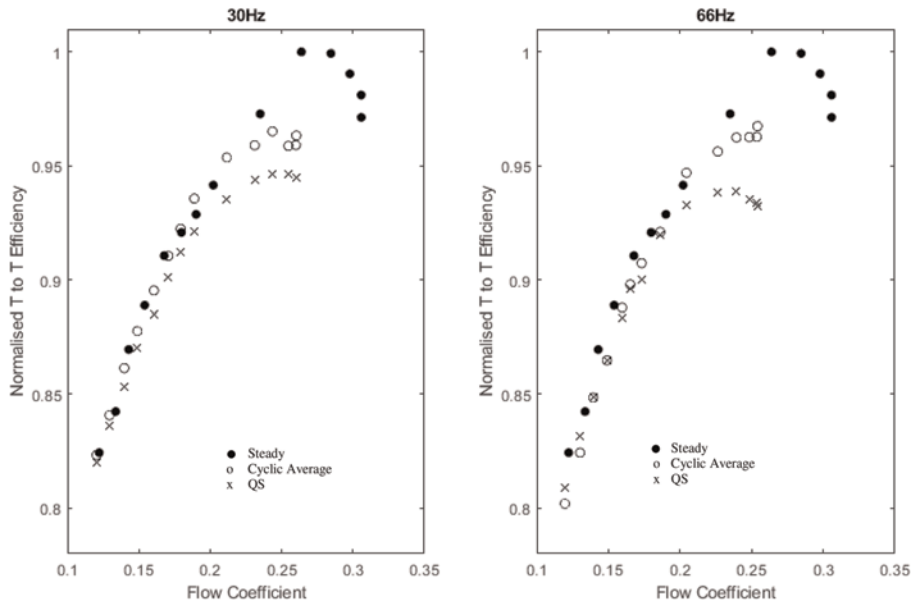
Figure 8. Steady, quasi steady and unsteady average efficiencies for 30Hz and 66Hz.

Figure 8 shows the steady, quasi steady and pulsating cyclic average efficiencies for the full speed line. As before, the cycle average is representative of the pulsating performance but does not exist in practice. First, it can be seen that, the steady flow efficiencies, shown by the filled black dots, are higher than the cycle average and quasi steady (QS) case for all operating points, as expected. At low mass flow rates, the efficiencies predicted by the QS approximation closely match the unsteady cycle average efficiency for both 30Hz and 66Hz case; indicating that the QS approximation can be applied when the flow rates are low. A deviation between the actual cycle average and the QS approximation begins to appear strongly after a flow coefficient of ∼0.2 for this system. Once this flow coefficient is surpassed, as the flow rate increases, the QS efficiency prediction no longer matches the actual unsteady cyclic average, and is in fact predicted to be much lower. However, the fact that the actual cycle average efficiency is greater than the QS prediction is due to the large discharge pressures that are attained instantaneously which pull the average up, as seen in Figure 7.

It is clear to see the benefit of pulsation with respect to the instantaneous effect on the pressure rise in the system. If behaving in the QS manner, as a result of the large amount of mass flow swept for each instantaneous operating point, the average performance would be much lower. However, in reality, the performance instantaneously is higher than quasi steady performance, pulling the average efficiency for high mass flow rate conditions. In low mass flow rate conditions, the behaviour of compressor system is close to quasi steady because the mass flow swept by the compressor system is much lower. The compressor feels the benefit of the pulsation without the efficiency being compromised. At high flow rates, the efficiency is compromised because the compressor is less capable of producing a work output in the pulsating state.

4   CONCLUSION

In this study, the performance and internal pressure distribution of the centrifugal compressor under pulsating conditions was studied using data gathered from an instrumented volute. The key findings from this paper are detailed below.

- As expected, both 30Hz and 66Hz pulses suffer from the drop in efficiency under pulsating flow as well as a drop in performance because the compressor is unable to produce the same amount of work. The performance drop is dependent on the frequency; it is largest when the frequency is the lowest.
- The drop in efficiency is much more significant as mass flow increases due to an increase in system flow inertia. When the compressor flow rate increases, the compressor system has more mass, as the valve closes, a larger amount of flow is halted resulting in an increase in localised pressure, which generates the backpressure wave. This pressure wave amplitude is much larger compared to lower efficiency.
- The cycle average performance shows a deviation from the quasi-steady (QS) predictions as the mass flow rate increases for the 30Hz and 66Hz cases. In both cases for high flow conditions, the cyclic average performance is higher than the QS predictions because instantaneously the pressure rise exceeds the steady performance, resulting in a higher average than predicted. At low mass flow rates, the cycle averaged behaviour closely matches quasi-steady approximations as the mass flow spans a smaller range and the cycle behaviour , if present, is uniformly distributed around the QS prediction.
- The filling and emptying effect of the flow within the volute occurs in different positions depending on the frequency of the pulse. For the 30Hz case, it is occurring more near the compressor exit and around the tongue, whereas for the 66Hz case it is occurring more away from the compressor exit. The filling and emptying for the 66Hz case may not be significant because the pulse acts for a shorter time than the 30Hz case, therefore the flow has less time to respond.
- The internal static measurements show that the static pressure trace within the compressor volute at high flow conditions deviate from the outlet imposed pulse and this deviation occurs in different positions for the 30Hz and 66Hz case. The reflection of the pressure wave affects the performance of the impeller in the vicinity of the tongue.

In summary, the average performance at 30Hz and 66Hz is different because of a few differences in the way the volute responds to the imposed pressure, and how it carries this information downstream. It is expected therefore that different passages of the impeller will perform differently and the overall performance (based on the volute exit alone) reflects this difference in performance for the different frequencies. At large flow (OP C) and 30Hz frequency, the stage has the worst performance compared to the other two frequencies due to more significant effects the tongue and the wave reflections that follow.

REFERENCES

[1] Edgar/JRC. Distribution of Global Carbon Dioxide (CO2) Emissions in 2020, by Sector. *Statistica*. [Online] 31 December 2021. [Cited: 12 December 2022] www.statistica.com

[2] IEA. Distribution of Carbon Dioxide Emissions Produced by the Transportation Sector Worldwide in 2020, by subsector [Graph]. Statistica. [Online] 25 May 2021. [Cited: 12 December 2022.] www.statistica.com

[3] Marelli, S. and Capobianco, M., *Experimental investigation under unsteady flow conditions on turbocharger compressors for automotive gasoline engines*.

Elsevier Ltd, 2012. 10th International Conference on Turbochargers and Turbocharging, London.

[4] Benson, R. S. and Whitfield, A, *An Experimental Investigation of the Non-Steady Flow Characteristics of a Centrifugal Compressor*. 1, s.l, Proceedings of the Institution of Mechanical Engineers, 1965, Vol. 180, pp. 641–672.

[5] Yano, T. and Nagata, B, *A Study on the Surging Phenomena in Diesal Engine Air Charging System*: Proceedings of the Japan Society of Mechanical Engineers, 1971.

[6] Galindo, J, *et al*, On the effect of Pulsating Flow on the Surge Margin of Small Centrifugal Compressors for Automotive Engines. *Experimental Thermnd Fluid Science*, 2009, pp. 1163–1171.

[7] Marelli, S., Capobianco, M. and Zamboni, G, Pulsating Flow Performance of a Turbocharger Compressor for Automotive Application,: *International Journal of Heat and Fluid Flow*, 2013.

[8] Barrera-Medrano, M. E., *et al*, Effect of Exit Pressure Pulsation on the Performance and Stability Limit of a Turbocharger Centrifugal Compressor: *Journal of Engineering for Gas Turbines and Power*, 2017, Vol. 139, pp. 052601-9.

[9] Barrera-Medrano, M. E., *et al*, On the Effect of Engine Pulsations on the Performance of a Turbocharger Centrifugal Compressor, *Journal of Engineering for Gas Turbines and Power*, Vol. 141.

[10] Greitzer, E. M., Surge and Rotating Stall in Axial Flow Compressors—Part I: Theoretical Compression System Model, *Journal of Engineering for Power*, Vol. 98, pp. 190–198.

[11] Shu, M., *et al.*, Unsteady Responses of the Impeller of a Centrifugal Compressor Exposed to Pulsating Backpressure. 2008, *Journal of Engineering for Gas Turbines and Power*, Vol. 141.

[12] Worster, R., *The Flow in Volutes and its Effect on Centrifugal Pump Performance*. 1963. Proceedings of the Institution of Mechanical Engineers.

[13] Ayder, E, den Braembussche, R. V. and Brasz, J., Experimental and Theoretical Analysis of the Flow in a centrifugal Compressor Volute. 1993, *Journal of turbo-machinery*, Vol. 115, pp. 582–589.

[14] Gulich, J. F, *Centrifugal Pumps*.: Springer, 2010, Vol. 2.

[15] Barrera-Medrano, M. E. *The Effect of Exit Pressure Pulsation on the performance and stability limit of a turbocharger centrifugal compressor*. 2017.

Design and optimization of compressor for a fuel cell system on a commercial truck under real driving conditions

L. Zhang

Advanced design Technology Ltd, UK

T.J. Wanat, P. Mireault

Gamma Technologies LLC, US

M. Zangeneh

University College London, UK

ABSTRACT

Decarbonisation of heavy-duty vehicles has an important impact on reducing emissions. More specifically, in the United States, medium and heavy-duty trucks are responsible for 23% of total CO2 emissions at present. Furthermore, the annual road freight traffic is expected to grow by 54% by 2050. The recent growth in lithium-ion battery use in Light Duty Vehicles (LDV) has resulted in reductions in battery costs. However, for Medium and Heavy Duty (MDV and HDV) applications, fuel cells offer important advantages in terms of energy density and refuelling time, which makes this technology more attractive for these classes of vehicles. Recent US DOE targets for Class 8 long haul trucks highlight the importance of even longer driving ranges and increased efficiency demands for fuel cell systems. To this end, it important to design and optimize the components of a fuel cell system, such as the compressor, not in isolation, but as part of the integrated system under real-driving conditions, thus capturing the strong co-dependencies among subsystems and the intricacies of real-life operation.

This paper presents a novel methodology, that uses a system-level simulation platform to create a complete vehicle model and simulate the performance of a fuel cell powered truck in order to obtain the key fuel cell compressor operating points together with the resulting residence time spent on each point based on real driving condition. The key compressor operating points are then fed into a meanline compressor design optimization code which uses a map prediction model for a range of compressor speeds, impeller diameters, hub diameters and axial length ratios to find the optimum settings that meet the same weighting factor obtained from real driving conditions. This initial flow path and design conditions obtained from the meanline design optimization are then used by a 3D Inverse design method to generate an initial 3D impeller geometry. Automatic optimization is then used to optimize the impeller geometry. The casing is also designed by using a unique inverse design method and the performance of the resulting stage is computed by using a 3D CFD simulation package. Furthermore, the structural integrity of the compressor is analysed with a 3D structural analysis software package. The resulting full stage compressor map is then fed into the system-level model and the impact of the new design on the energy consumption over the actual real-life driving scenario is assessed and analysed. The methodology highlights the importance of rigorous simulation as a means for improving component performance and system efficiency, while reducing time-to-market and thus development costs.

1 INTRODUCTION

In the past ten years there have been increasingly ambitious reduction targets on CO_2 emission and on pollutants such as NOx and PM. The powertrain market sees a trend to go from diesel or gasoline engines towards battery electric and hydrogen fuel cells. Both battery electric and hydrogen fuel cell powertrains have the potential for zero-emission operation. However, battery electric vehicles have limits on driving range due to battery capacity [1]. Recharging is required and battery temperature control is critical. For heavy-duty vehicles fuel cells has the advantages in terms of energy density and refuelling time. It is under active research and development in the recent years and will be a more practical option in the foresee future. The fuel cell is pressurized by an air compressor, which is electrically driven. The air compression system is important to the overall performance. Compared to the previous turbocharger air compressors there are some differences in the compressor operating requirements. The pressure ratio required is generally lower than a turbocharger compressor. But the operating range requirement is high. The electric motor also functions at lower RPMs. On the other hand, the fuel cell exhaust temperature is much lower than that of an ICE, so there is not enough energy to recover through a turbine to drive the compressor. Additional power input from electric machine is needed. This makes the compressor efficiency very important for power consumption. The air compression system needs to be redesigned or optimized based on these changes [2].

In this paper, a novel design methodology is presented. The system-level simulations (based on complete vehicle model) are used to provide real driving conditions for a fuel cell powered truck. The compressor operating conditions are obtained from the simulations. The residence time spent on different operating conditions is taken into consideration when the compressor design is carried out. A multi-points design is carried out first in the meanline analysis. Based on the initial sizing and design condition selected a 3D impeller design is then generated in 3D inverse design method. The volute is also created in an inverse design approach. They are used as the baseline compressor design. Further impeller optimization is carried out in an automated workflow that couples the inverse design solver with an optimizer. The volute can also be optimized to reduce the size by using over-hang cross sectional shape. Finally, the performance of the optimized compressor design can be fed back to the system-level analysis. The impact of the optimized design on the energy consumption overall the real driving scenario can be evaluated. The methodology is relatively fast, which is important to the reduction of development time and cost. It also demonstrates the importance of rigorous simulation when designing for a new powertrain system.

2 SYSTEM-LEVEL SIMULATION IN REAL DRIVING CONDITIONS

To establish realistic boundary conditions for the compressor design under real world conditions, an example model of a heavy goods vehicle (HGV) with a fuel cell powertrain from the simulation package GT-SUITE [3] was selected and a real-world drive cycle was developed. The vehicle is a 6×2 tractor trailer with a total weight of 30,000 kg including cargo. The drivetrain is powered by a single electric motor providing a peak torque of 2800 Nm.

A drive cycle was created by imagining a typical journey of such an HGV from a shipping port to a warehouse in the UK. For this study, the journey starts at the Port of Felixstowe on the eastern coast of England (Oysterbed Rd, Felixstowe IP11 4SH) and ends at a warehouse in Westhoughton, Bolton (BL5 3XU), northwest of Manchester, refer to Figure 1. This 423 km journey takes slightly over 5 hours to complete and represents typical traffic conditions that would be encountered if the vehicle departed on Wednesday morning at 09:00. To generate the route, the start and end locations were

entered into GT-RealDrive, a virtual route generation app in GT-SUITE. In addition, the dimensions and weight of the truck were also input to ensure that the route is compliant with any physical or legal restrictions. The route information contains road elevation data along with traffic light locations to make it as realistic as possible.

Other routes were considered before making this selection, such as standard drive cycles used for determining fuel consumption and emissions ratings, because they could produce a wider range of driving conditions. However, due to emphasis on real driving cycles during the past decade, it was decided that a realistic driving cycle should provide the realism expected in modern times. Of course, it is possible that alternative cycles could produce different average operating points. This could be a goal of a future study.

Figure 1. Image of map coming from here in GT-RealDrive.

This route was used as an input to the model. The model has a simulated driver, which targets the mean traffic velocity along the route as a function of vehicle distance and stops were necessary (e.g. at traffic lights). The resulting vehicle velocity profile that the driver produces while traveling along this route is shown in Figure 2, along with the required power of the fuel cell compressor, which will be discussed as well.
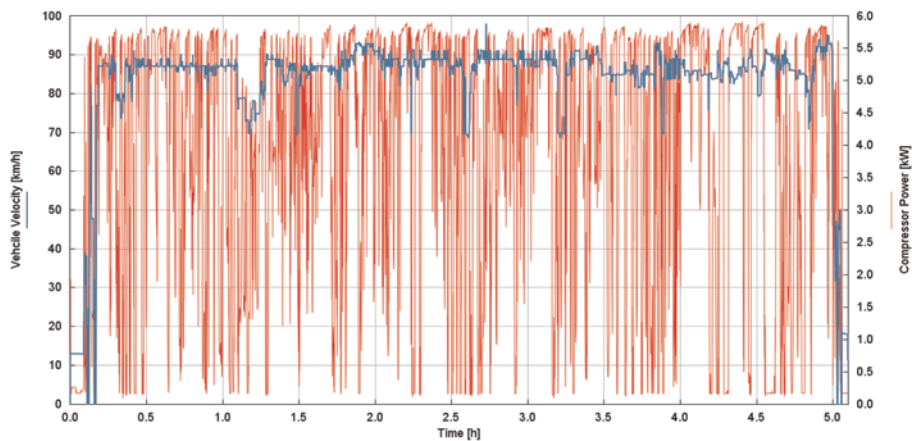
Figure 2. Vehicle velocity profile and compressor power.

The velocity target is converted into torque and power demands on the e-motor and ultimately the fuel cell. A high voltage battery in the system acts as a buffer to handle the large increases in torque demand during vehicle accelerations and hill climbs as well as store energy during regenerative braking events. Losses in between each component in the system are accounted for.

The powertrain is a pair of fuel cell systems, which are both designed for a maximum output of 110 kW. For each fuel cell, the open circuit voltage is 700 V and the current at maximum power is 216A. The compressor maps in the model that force air through the fuel cell stacks and system were generated using a methodology developed by Casey and Robinson [4]. This methodology allows one to provide a wheel diameter and 4 dimensionless parameters common to radial compressor design to generate a full map. Gamma Technologies has added an option to enter the speed, pressure ratio, mass flow rate and isentropic efficiency of the design point from which the dimensionless coefficients are calculated. In this case the wheel diameter is 40 mm and at the design point the speed is 200,000 RPM, the pressure ratio is 2.0, the mass flow rate is 80 g/s and the isentropic efficiency is 73%. The resulting coefficients at the design point are a tip speed Mach number of 1.21, a work input coefficient of 0.503, a flow coefficient of 0.102 and a polytropic efficiency of 0.76. A visualization of the map with speed lines plotted over the efficiency contours is shown in Figure 3 (left).

After the simulation was run, the residence time of the flow rates and pressure ratios of the compressor was analysed to determine the points at which the compressor operates most often. This data was used to develop a lug-line that could be used to design a compressor with higher efficiency for these points with the goal to reduce the fuel consumption. The compressor map with operating points averaged over 1 second interval is displayed in Figure 3 (right) to show the range over which the operation took place over this long cycle. In addition, the compressor power has been plotted on the second vertical axis of Figure 2, to illustrate the demand on the compressor during the drive cycle.

The ranges of operation for both the flow rate and pressure ratio were divided into 25 bins in both the flow rate and pressure ratio axes and the time fraction of operation calculated by a macro in the post processing tool that comes with GT-SUITE, GT-POST. The display was adjusted to show the compressor map with the coloured display of the analysed bins. The small collections of coloured lines near pressure ratio of ~1.2 and mass flow rate of ~0.015 kg/s stretching up to pressure ratio of ~1.65 and mass flow rate of 0.085 constitute the collection of operating points that resulted from the drive cycle simulation with fuel cell system, including the compressor. The red lines represent regions in which the operating point resided over 7.5% of the total duration of the cycle. The region near pressure ratio of 1.65 and mass flow rate of 0.085 kg/s was above the limits of display, with over 27% of the residence time spent in the white region inside the dark red semi-circle.
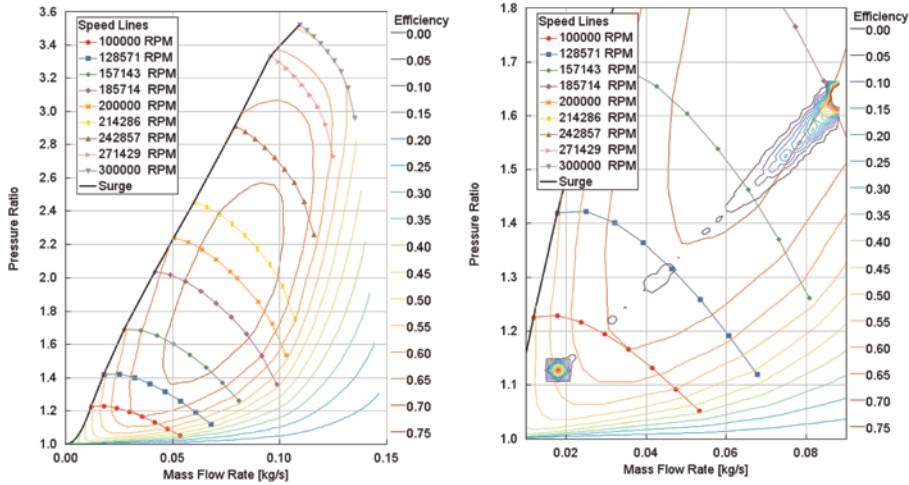
Figure 3. Left: initial compressor map; right: compressor map with analysed bins (close-up).

It can be observed that the compressor does spend a lot of time at a high operating point, at maximum power of the fuel cell. This is due to the large percentage of time that the vehicle is driving at maximum speed in the cycle, 100 kph. The other most significant amount of time is at the low speed, essentially idling at a stop. As a result of this analysis, a set of 3 operating points were selected to provide the targets for optimal design of the compressor.

3   COMPRESSOR MEANLINE DESIGN OPTIMIZATION

After the compressor operating conditions are obtained from the real driving simulation, the meanline design of the compressor can be carried out. In order to have overall good performance, the various operating conditions have to be considered in the meanline design stage. This was done using TURBOdesign Pre [5], which is a meanline solver used for the sizing and design of turbomachinery components. From the basic design specification (flow rate, rpm and pressure ratio) the solver uses a number of loss models in the meanline calculation. The meridional shape and key dimensions of the compressor will be provided after the calculation. Meanwhile, a performance map (pressure ratio, efficiency, power and work coefficient versus massflow rate) prediction is also produced based on one-dimensional models, experimental and CFD data. For designs with consideration on various operating conditions, 'multiple design points' can be specified. Then a Design of Experiments (DoE) will be carried out using the meanline solver. The mass flow rate, total pressure ratio and weighting factor are specified for each design point. The design is generated by finding a speedline for each design point, see Figure 4. The overall weighted efficiency is optimized then to get the final design. In this case three operating points were selected from the system simulation (Figure 3, right). Table 1 listed the design points and their weighting factor.

164

Table 1. Selected operating points for compressor design.

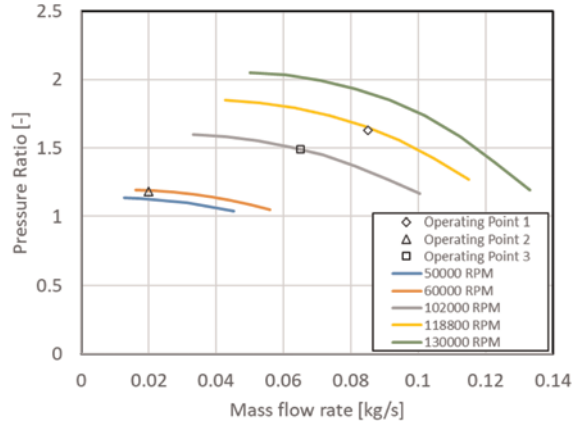|	Massflow [kg/s]	Pressure Ratio [-]	Weighting Factor [-]
Operating Point 1	0.085	1.63	0.334
Operating Point 2	0.02	1.18	0.332
Operating Point 3	0.065	1.49	0.334

Figure 4. Compressor map prediction from meanline analysis to cover the three operating points.

A full factorial method is adopted in producing the seeds for DoE. For each design variable, a number of levels and the range of variation need to be specified. The seeds are linearly spaced in this range. The DoE has four input variables. The range and number of levels are listed in Table 2. The solver then sizes the machine based on all possible combinations of parameters seeded. Since each candidate calculation takes only a few seconds the DoE results could be obtained within a few minutes.

Table 2. Meanline DoE study range of variation.

Variable	Level	Minimum	Maximum
RPM	50	60000	120000
Axial Length Ratio (L/D2)	5	0.275	0.325
Inlet Hub Diameter	5	10	16
Outlet Tip Diameter	10	45	55

4   COMPRESSOR COMPONENTS DESIGN

4.1   Impeller design

From the meanline design an initial compressor sizing was obtained. Figure 5 shows the meridional shape of the impeller and vaneless diffuser. The design condition and key dimensions are listed in Table 3.

Table 3. Compressor key dimensions.

Blade number	7 full blade + 7 split-ter blade
Design RPM	96,000 rev/min
Design flowrate	0.065 kg/s
Hub diameter	10 mm
Shroud diameter	30.8 mm
Tip diameter	54 mm
Impeller outlet width	3.6 mm
Blade thickness	1 mm (hub)/0.5 mm (shroud)
Tip clearance	0.25 mm
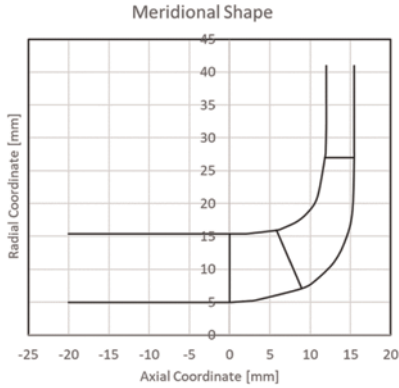
Figure 5. Compressor meridional shape.

Then the detailed impeller design was carried out with 3D inverse design method TURBOdesign1 (TD1). The method was developed and demonstrated in the previous work [6] in 1990s. Since then, it has been used in compressor design and optimization work extensively, especially in the turbocharger compressor design applications. Both the full blade and full blade with splitter design can be generated with TD1 [7,8]. Unlike in the conventional design where the impeller geometries are created by geometrical parameters, the inverse design method produces blade geometries subject to certain blade loading description. The circumferentially averaged bound circulation is used as input to specify the impeller work. It is defined as:

$$r\bar{V}_\theta = \frac{N}{2\pi} \int_0^{2\pi/N} r \cdot V_\theta d\theta \tag{1}$$

The work coefficient is imposed by specifying the spanwise $r\bar{V}_\theta$ distribution at the leading edge and trailing edge of the impeller. $r\bar{V}_\theta$ is normalized by the impeller outlet tip radius and speed in TURBOdesign1. The normalized value $r\bar{V}_\theta^*$ is used specifying the loading.

For the splitter design the $r\bar{V}_\theta ratio$ also needs to be specified. It is defined as the specific work of the splitter blade divided by the total specific work of the impeller:

$$r\bar{V}_\theta ratio = (\Delta r\bar{V}_\theta)^{splitter} / (\Delta r\bar{V}_\theta)^{total} \tag{2}$$

166

$r\bar{V}_\theta ratio$ is normally based on the ratio of the meridional length of the splitter over the overall meridional length, so the full blade and the splitter have similar level of maximum loading. But it can also be varied during design optimization for better performance.

For compressible flow the meridional derivative of $r\bar{V}_\theta$ is related to the enthalpy difference between the blade pressure surface and suction surface:

$$h^+ - h^- = \frac{2\pi}{N} W_{mbl} \frac{\partial(r\bar{V}_\theta)}{\partial m} \tag{3}$$

If in the boundary layer local compressibility is ignored:

$$\Delta h \cong \frac{\Delta p}{\rho}$$

By prescribing the meridional derivative $\frac{\partial(r\bar{V}_\theta)}{\partial m}$ the pressure jump across the blade can be controlled. The blade geometry is then computed by the inverse design procedure (inviscid potential flow solver), which converges within a few seconds. In this way the aerodynamic inputs (blade loading) can be used to generate blade designs, which gives better control on the flow field. The blade loading on the full and splitter blades are shown in Figure 6 (left). At the hub the blade is aft-loaded. At the shroud the blade is mildly aft-loaded to have a good stall margin, as the required compressor operating range is big for fuel cell applications. Four parameters (NC, ND, SLOPE and DRVT$_{LE}$) are needed to define a main blade loading curve. For the splitter blade, two parameters (NC, DRVT$_{LE}$) are needed to define the splitter loading near LE. The rest of the loading will follow the profile of the main blade loading.
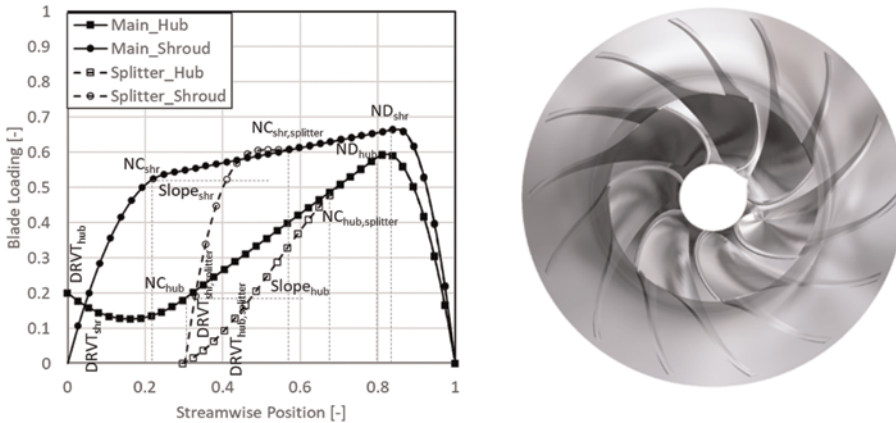
Figure 6. Left: baseline design loading; right: baseline design geometry.

Another input specification is the stacking condition. The wrap angle variation along the span can be specified at a chordwise location (impeller TE in this case). It can introduce blade lean and add additional control of the spanwise pressure field. Therefore, it is possible to use only 13 parameters to define a complex 3D impeller (with splitter) shape. For the baseline design the wrap angle at the hub and shroud is the same at the impeller TE. The generated impeller is shown in Figure 6 (right).

There are three major advantages of the inverse design method compared to the conventional design based on blade angle description. Firstly, the design inputs are aerodynamic parameters, which imposes good control of fluid physics. For example, the specific work is directly controlled by $r\bar{V}_\theta$ and the blade surface pressure is controlled by the loading parameters. Secondly, apart from obtaining a 3D geometry the flow field information is also available after the solver converges. The designer can use the flow field information to guide the design iterations before running the more time consuming CFD analysis. The key aerodynamic parameters such as diffusion ratio can be used to rule out poor design candidates. It can also be coupled to optimizer directly since the inverse design solver is fast. Finally, the inverse design method can define a complex 3D blade geometry with less parameters comparing to the methods that parameterize the camber line geometries with control points etc. This makes it efficient when used in optimization process, as it can explore a large design space with less degree of freedom.

4.2   Volute design

The volute design was carried out using TURBOdesign Volute, which is a 2D inverse design tool for the design of volutes. The inputs are volute inlet pressure, temperature and velocity components, which can be extracted from the flow field upstream of the volute. The cross-sectional area distribution is then calculated based on the mass and momentum conservation equations [9]. This results in a good match between the upstream component and the volute. Various cross-section shapes can be generated in TURBOdesign Volute. For the baseline design an asymmetric circular cross section was used. The tongue radius is also an input. The solver automatically generates the 3D geometry with a smooth tongue. Figure 7 shows the volute generated for the baseline design. Table 4 shows the key dimensions of the volute.
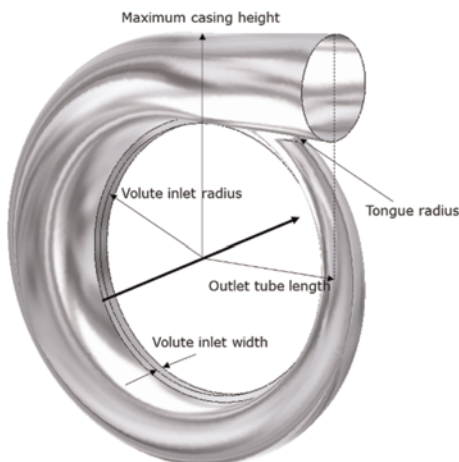

Figure 7. Baseline compressor volute.

Table 4. Baseline volute key dimensions.

Volute inlet radius	43 mm
Volute inlet width	3.47 mm
Tongue radius	2.5 mm
Maximum casing height	70 mm
Outlet tube length	55 mm

4.3   Steady CFD analysis

The baseline compressor stage performance was then evaluated in steady CFD simulation. The computational domain and mesh are shown in Figure 8. The impeller and vaneless diffuser mesh is structured mesh generated using TurboGrid. The volute mesh

is unstructured and generated using ANSYS Meshing. Average Yplus of the mesh is 1.37 and the total number of elements is around 3.3 million. Total pressure, total temperature and flow direction are specified at the domain inlet. Massflow rate is specified at the volute outlet. The impeller domain is rotating. The inlet domain, diffuser and volute are stationary. Frozen rotor is specified at the interface between the inlet block and impeller. It is also used at the interface between the impeller and vaneless diffuser. The Stage (mixing plane method) interface is used between the vaneless diffuser and the volute. ANSYS CFX (2020 R2) is used in all the CFD simulations in this work. It uses an element-based finite volume method and a pressure-based coupled solver approach. The solution variables and fluid properties are stored at the nodes (mesh vertices). A tri-linear element shape function is employed to interpolate the diffusion term and a linear-linear interpolation shape function is used for the pressure gradient terms. A high-resolution advection (2nd order accuracy) is used with the SST turbulence model. The same numerical setup has been used in centrifugal compressor simulations extensively. Previous validation with test data was discussed in [10], where good agreement was obtained for both subsonic compressor and transonic compressor cases.
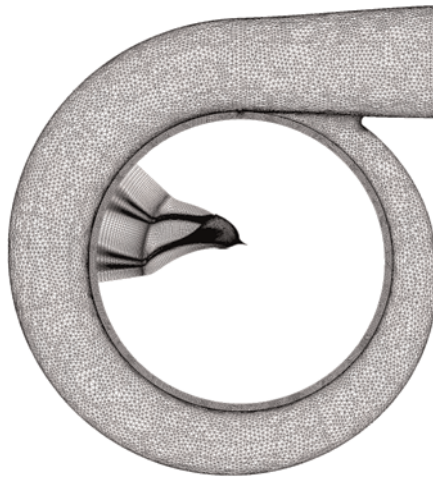
Figure 8. Compressor mesh detail.

The baseline compressor stage performance was shown in Figure 9. It can be seen that the baseline design has achieved the pressure ratio at all three key operating conditions. Meanwhile the efficiency of the overall compressor stage is reasonably good, which means it can be used to set up the optimization workflow. With Casey and Robinson methodology [4], the compressor efficiency is an input and the performance map is produced from algebraic equations calibrated to match the test data. The previous turbocharger compressors tend to have relatively high specific speed in order to reduce the wheel size (and inertia) for transient response requirement. The compressors were quite often not designed at the optimum aerodynamic design space. The fuel cell compressors do not have the requirement of low inertia. The aerodynamic performance can be potentially improved with the proper design space selection. The efficiency level therefore can be higher than the Casey and Robinson methodology's assumption and prediction (as shown in Figure 9), which was largely based on turbocharger database.
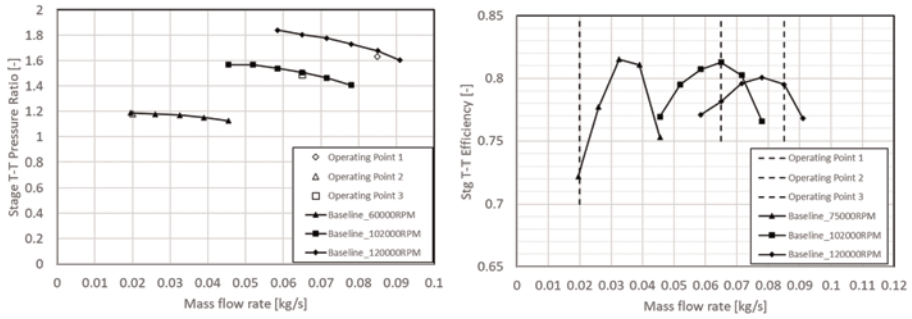
Figure 9. Baseline compressor performance.

5 COMPRESSOR COMPONENTS OPTIMIZATION

5.1 Impeller optimization

Apart from the compressor performance, the overall size is also an important factor for fuel cell applications. To further improve the performance and to reduce the compressor size, an optimization was carried out on both the impeller and the volute. The impeller optimization was done within TURBOdesign Suite [11] using its embedded genetic optimizer (TDOptima). A direct multi-objective genetic algorithm optimization was conducted. Figure 10 shows the parameters used to describe the meridional profile. 5 parameters (normalized by the impeller radius) are used to allow the shroud, hub and LE shape to vary. The range of the 5 parameters is shown in Table 5. The LEangle is defined as the angle between the chord of LE contour (connecting shroud and hub) and the vertical direction. The splitter position is also allowed to vary. The pink lines show the smallest blade area and the blue lines show the largest blade area. The variation of the meridional shape covers a large range. The impeller outlet diameter and width are kept constant during the optimization work. The inlet shroud radius is also fixed.
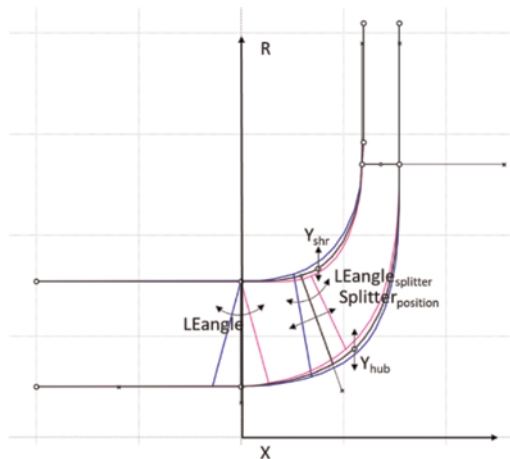
Figure 10. Meridional profile variation during optimization.

170

Table 5. Optimization variables range, constraints and objectives.

Optimization Input Variables				Optimization Constraints	
Blade Loading		**Meridional Profile**		Main blade throat	+5%
NChub	0.25–0.45	Y_{shr}	0.6–0.64	Splitter blade throat	+6%
ND_{hub}	0.75–0.85	Y_{hub}	0.3–0.35	Main blade LE lean	<20 [deg]
$Slope_{hub}$	0.7–1.0	LEangle	−15–15 [deg]	LE bow ratio	< 25%
$DRVT_{hub}$	−0.25–0.4	$Splitter_{position}$	0.275–0.35	Splitter blade LE lean	<20 [deg]
NC_{shr}	0.25–0.45	$LEangle_{splitter}$	10–25 [deg]	Blade angle change near LE at hub	<18 [deg]
ND_{shr}	0.75–0.85			Main blade diffusion ratio	1.6–1.89
$Slope_{shr}$	0.3–0.6			Splitter blade diffusion ratio	1.6–1.89
$DRVT_{shr}$	−0.25–0.2			Blade surface maximum Mach number	<0.7
$NC_{hub,splitter}$	0.3–0.6			Blade surface minimum Mach number	0.18–0.26
$DRVT_{hub, splitter}$	−0.25–0.25			Main blade leakage loss	<130
$NC_{shr,splitter}$	0.3–0.6			Splitter blade leakage loss	<90
$DRVT_{shr,splitter}$	−0.25–0.25			**Optimization Objectives**	
Stacking	−4-4 [deg]			Main blade secondary flow factor	Minimize
RVT_{mean}	0.645–0.655			Splitter blade secondary flow factor	Minimize
RVT_{shr}	0.635–0.665			Total profile loss	Minimize
$RVTRatio_{mean, splitter}$	0.4–0.43				
$RVTRatio_{shr, splitter}$	0.4–0.43				

As shown in Figure 6 (left), 12 loading parameters are needed to define a 3D blade geometry. The stacking condition is defined with 1 parameter. 4 more parameter is used to vary the spanwise distribution of $r\bar{V}_\theta$ and $r\bar{V}_\theta ratio$. Linear distribution is used with the mean value and shroud side value allowed to vary. The ranges of these parameters are listed in Table 5. A few constraints are also used to rule out invalid designs. The throat of the main and splitter blade is constrained so that the choke margin is not smaller. The LE lean and bow ratio are used to control the stress level near the blade LE. The blade angle change near the LE at the hub is constrained to avoid sudden turning near the LE. For the aerodynamic performance, the diffusion ratio (maximum relative velocity on the blade surface divided by the relative velocity at the trailing edge) is constrained to avoid flow separation. The maximum and minimum Mach number on the blade surface are constrained to avoid high Mach number or low velocity. The leakage loss (related to the blade surface velocities near the tip) is limited to avoid high tip clearance loss. The objectives are set to minimize the blade profile loss and the secondary flow factor. The profile loss factor is computed from the integration of the cube of the blade surface velocity predicted by the inverse design code. The secondary flow factor is character-ized by the loading difference between the hub and shroud. It is related to the hub-to-shroud motion of fluid [12]. It is calculated in the inverse design code by using the

velocity difference (downstream of 50% streamwise location) between the hub and the shroud of the blade.

Figure 11 shows all the feasible inverse design solutions (the ones that don't satisfy the constraints are ruled out). In total, 679 feasible inverse design solutions have been generated. A Pareto front is obtained between the two contrasting objectives. The size of the bubbles represents the splitter blade secondary flow factor. A final 'optimized design' is selected from the Pareto front.
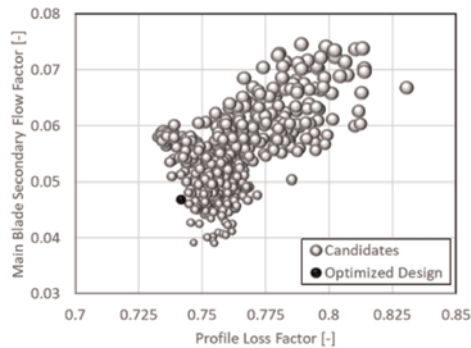

Figure 11. Feasible solution from optimization.

Figure 12 (left) shows the meridional shape of the optimized design. It can be observed that the optimized design has LE cut-back and the splitter LE is moved downstream. The blade loading of the optimized design is shown in Figure 12 (right). The $DRVT_{LE}$ has been adjusted for both the full blade and the splitter.
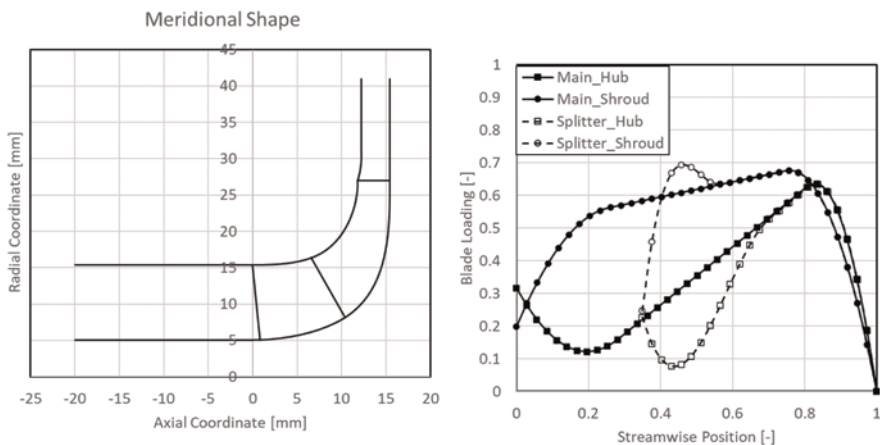
Figure 12. Left: meridional shape of optimized compressor; right: optimized design loading.

5.2 Volute optimization

To control the overall housing dimension the volute casing height is important. Since the cross-sectional area is critical to the volute performance, reducing the cross-sectional area will have a big penalty on the compressor performance. On the other hand, small changes in cross sectional shape have less impact on the volute performance. In TURBOdesign Volute an 'over-hang' volute is therefore used, as shown in Figure 13. The flow ratio is used to specify how much volume flow is going through the upper region of the cross-section. In this case 0.95 is used. This leaves 5% of the volume flow to go through the lower region. The volute W/H ratio is kept as 1.0 to be close to circular. The cylindrical wall has a width t of 2 mm. Figure 13 (right) shows the comparison of the over-hang volute compared to the baseline volute. It can be seen that the casing height has been reduced.
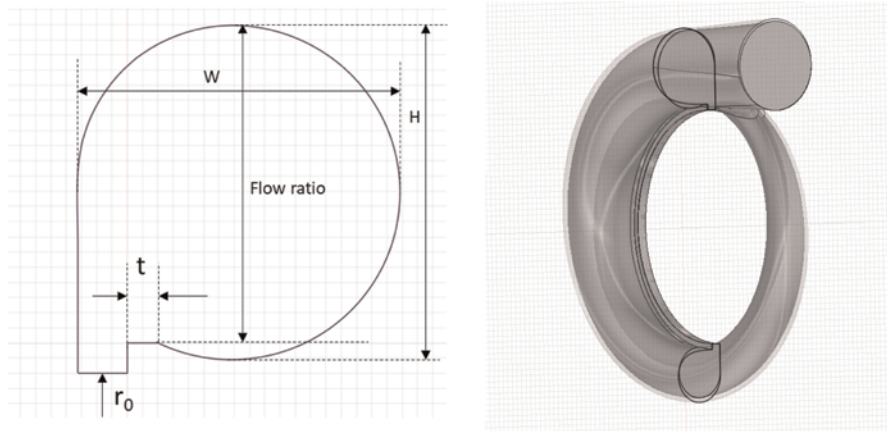
Figure 13. Left: overhang volute cross section; right: overhang volute compared to baseline.

5.3 Steady CFD analysis of optimized compressor stage

The performance of the optimized compressor stage (with optimized impeller and over-hang volute) was verified in the same CFD setup. The speedline performance is shown in Figure 14. The results show that the optimized compressor stage has similar total to
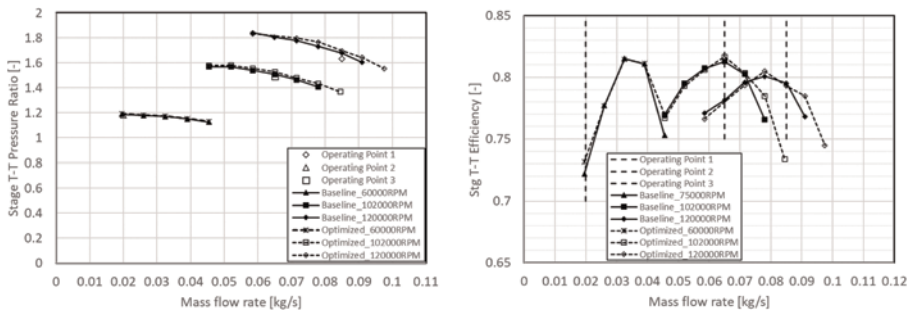
Figure 14. Optimized compressor performance.

total pressure ratio as the baseline stage. Meanwhile the operating points' efficiency is improved and the high flow rate performance is generally better. The stall margin is the same as the baseline design. The optimized design managed to reduce the overall compressor dimension without degrading the performance.

5.4 Static structural analysis

To evaluate the stress of the impeller, static structural analysis was carried out on a single sector impeller with back plate. Fixed radius (0.75 mm) fillet was generated between the blade root and the hub surface. This reduces the stress concentration. 3 mm thickness was applied to the back plate. The mesh is generated by using ANSYS Meshing and the total number of unstructured elements is around 589,000 as shown in Figure 15 (left). The mesh in the blade tip, hub fillet and the blade trailing edge is refined further to better resolve the local stress level. Cylindrical support is specified at the hub from the shaft. Fixed support is provided from the back plate. The material used in the calculation is Aluminium 2014-T651, with a Young's modulus of 72 GPa and a Poisson's Ratio of 0.33. The tensile yield strength is about 414 MPa at 25°C and 393 MPa at 100°C. The rotational speed was 144,000 to leave some margin for overspeed.
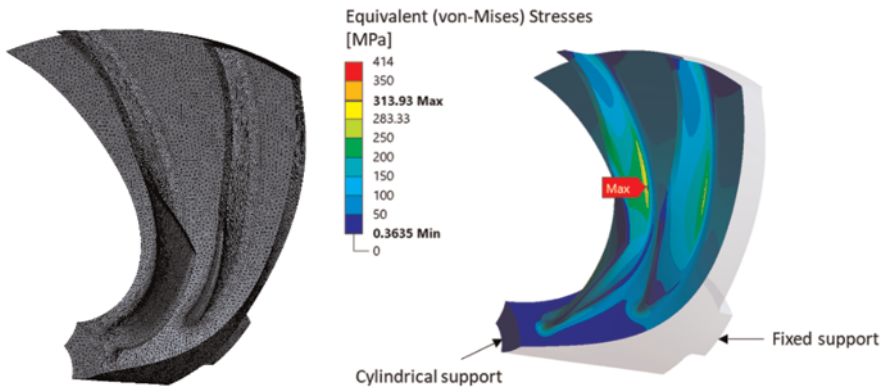
Figure 15. Left: impeller model mesh detail; right: blade surface stress contour.

The stress contours of the optimized designs are shown in Figure 15 (right). The maximum stress on the blade is at the pressure surface near the hub. It is around 314 MPa, which is below the material limit.

6   FINAL PERFORMANCE EVALUATION IN SYSTEM MODEL

Upon completion of the optimized compressor design, the resulting map was entered into a copy of the original system model and the simulation was run again. Like the initial analysis, the residence times of the operating points were plotted over the compressor map as a function of the fraction of the total time of the simulation to evaluate how well the new design performed in the system.
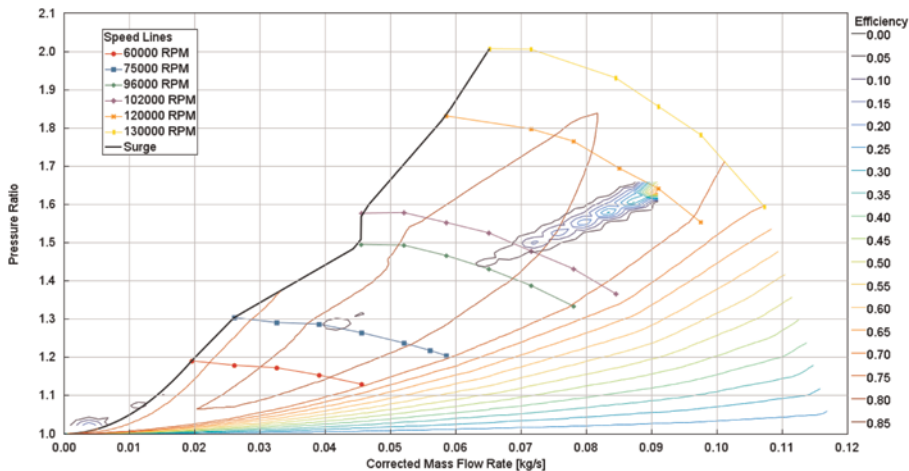
Figure 16. Compressor map including fraction of time spent at each operating point.

As shown in Figure 16, the operation of the fuel cell in this cycle straddles the maximum efficiency of the compressor. The compressor operates at the region near 0.09 kg/s and pressure ratio of 1.63 when the vehicle is driving at or near 100 km/hr. The compressor operates at the region in the lower left of the map near pressure ratio of 1.02 during many slower portions of the driving cycle, in roundabouts and so on. The compressor speed is limited by a controller not to fall below 20,000 RPM, to ensure that there is always some flow through the stack even at idling conditions. The fact that the maximum efficiency of the compressor is higher in this design provides an improved fuel consumption of the vehicle in this cycle at 2.18% due to reduced power demand on the electrically driven compressor, as shown in Table 6.

Table 6. Fuel consumption comparison.

Vehicle Model	Compressor Peak Efficiency	Fuel Usage (kg)	Fuel Consumption (kg/100 km)
Initial Compressor	73%	25.763	7.709
Optimized Compressor	81.5%	25.202	7.541

7   CONCLUSIONS

The methodology of coupling the system-level simulation with compressor design/optimization has been demonstrated on a fuel cell application. A real-world drive cycle was analysed and the operating conditions were used in compressor design/optimization. Through system level analysis and state-of-the-art compressor design techniques, it has been shown that there is potential to obtain fuel economy improvements for fuel

cell powered vehicles. This design and optimization approach is efficient and effective. It shows the importance of coupling the component design with system simulation during the development of a new fuel cell powertrain.

NOMENCLATURE

Roman symbols	
D2	impeller diameter
DRVT	$\partial(r\bar{V}_\theta)/\partial m$
h	enthalpy
H	volute cross section width
L	impeller axial length
m	percentage meridional distance
N	number of blades
p	pressure
RPM	revolutions per minute
r, R	radius
$r\bar{V}_\theta$	circumferentially averaged bound circulation
$r\bar{V}_\theta^*$	non-dimensionalized $r\bar{V}_\theta$
t	volute cylindrical wall width
V	velocity
W	meridional velocity
W	volute cross section width
X	axial direction
Greek symbols	
θ	circumferential direction
π	$\approx 3.1415926\ldots$
ρ	density
Superscript	
$\pm$	blade pressure/suction surface
Subscript	
LE	blade leading edge
mbl	meridional component on blade surface
mer	meridional direction
TE	blade trailing edge

REFERENCES

[1] Thomas, C. E. (2009) Fuel Cell and Battery Electric Vehicles Compared. *International Journal of Hydrogen Energy.* Volume 34, Issue 15, August 2009, Pages 6005–6020. https://doi.org/10.1016/j.ijhydene.2009.06.003

[2] Baines, N.C., Krivitzky, E.M., Bai, J., Zhang, X. (2020) *Trends in Passenger Car Powertrains and Their Impact on Turbocharger Developments.* 14th International Conference on Turbochargers and Turbocharging. DOI: 10.1201/9781003132172-25

[3] *GT-SUITE, Version 2023.0*, 2022, Gamma Technologies LLC, Westmont, IL, USA.

[4] Casey, M., and Robinson, C.J., (2013) A Method to Estimate the Performance Map of a Centrifugal Compressor Stage, *ASME Journal of Turbomachinery*, March 2013; Volume 135(2): 021034-1–021034-10. doi: 10.1115/1.4006590.

[5] TURBOdesign Pre, Version 2022.1, 2022, Advanced Design Technology Ltd. London, UK.

[6] Zangeneh, M. (1991) A compressible three-dimensional design method for radial and mixed flow turbomachinery blades. *International Journal for Numerical Methods in Fluids*, 13 (5) 599–624, 1991. https://doi.org/10.1002/fld.1650130505

[7] Zangeneh, M. (1998) *On 3D Inverse Design of Centrifugal Compressor Impellers with Splitter Blades,* ASME Paper 98-GT-507.

[8] Zangeneh, M., Nikpour, B., Watanabe, H. (2010) *Development of a High Performance Centrifugal Compressor Using a 3D Inverse Design Technique.* DOI: 10.1243/17547164C0012010010

[9] Qi, D., Pomfret, M., Lam, K., (1996) A New Approach to The Design of Fan Volute Profiles. *Engineering Proceedings of the Institution of Mechanical Engineers, Part C: Journal of Mechanical Engineering Science.* https://doi.org/10.1243/PIME_PROC_1996_210_198_0

[10] Zhang L.Y., Kritioti L., Wang P., Zhang J.N., Zangeneh M. (2022) A Detailed Loss Analysis Methodology for Centrifugal Compressors. *J. Turbomach*. May 2022, 144 (5): 051013 (14 pages). https://doi.org/10.1115/1.4054065

[11] *TURBOdesign Suite, Version 2022.1*, 2022, Advanced Design Technology Ltd. London, UK.

[12] Zangeneh, M., Goto, A. and Harada, H., (1998) On the Design Criteria for Suppression of Secondary Flows in Centrifugal and Mixed Flow Impellers, *Journal of Turbomachinery*, 120(4), 723–735.

Turbine design considerations

Performance improvement of turbine in regulated two-stage turbocharger via bypass flow control

Zhanming Ding[1]*, Shilue Zhou[2], Zecheng Zou[2], Yan Zhang[1], Mingyang Yang[2]

[1]Science and Technology on Diesel Engine Turbocharging Laboratory, China North Engine Research Institute, Tianjin, China
[2]Shanghai Jiao Tong University, Shanghai, China

ABSTRACT

The sequentially connected configuration of two stage turbine in a regulated two-stage turbocharger introduces a coupling effect of flow field between the high-pressure turbine (HPT) and low-pressure turbine (LPT), thus the performance of these two turbines will inevitably be affected by each other. However, most of current design methods of turbines assume they as isolated devices. In this study, a new method which is based on the control of flow-interaction between two stages is developed via experimentally validated three-dimensional numerical method. The influence of different positions of the bypass branch on the inter-stage coupling effects is investigated. Results manifest that different positions of the bypass branch significantly change the performance of low-pressure turbine and the flow interactions within the inter-stage. The detailed flow field analysis of the inter-stage pipe, volute and rotor is conducted to reveal the flow mechanism behind the inter-stage interactions.

Keywords: Turbocharger, two-stage turbocharging, Bypass, passive flow control, flow field coupling

1   INTRODUCTION

The increasingly stringent regulations and legislation trends of emission are continually keeping up the pressure on internal combustion engine (ICE) manufactures. In order to actively alleviate the environmental crisis, ICE technology has been promoted towards low-carbon and clean development in recent decades. As one of the most vital technologies to achieve the high performance of ICE, turbochargers have been widely used in vehicle industry at an unprecedented rate [1].

The performance of the two-stage regulated turbocharging system is the key factor to maximally exploit the potential of the ICE [6]. Therefore, an extensive number of investigations have been studied on two-stage turbocharging, mainly concerning about its matching methods and regulation strategies. In a regulated two-stage turbine system, two turbines are the most crucial components that affect the optimum load distribution and regulation strategies [7]. With current design and optimization techniques, it is feasible to demand turbines for the specific swallowing capacity and efficiency at the design point. In the study of Zhang et al., it has been proven that the control strategies of the bypass valve should be customized according to the swallowing capacity and the efficiency of the two turbines. Particularly, the improvement of the

---

*Corresponding Author: dingl25172@163.com

turbine efficiency can enhance the regulation capability [8]. In high altitude environments, the investigation of Yang et al. has confirmed that the swallowing capacity and efficiency of the two turbines are still the most crucial factors to the altitude adaptability of the engine with a regulated two-stage turbocharger system. A load division principle of the two stage turbines was proposed to improve the altitude adaptability of the engine [9]. The swallowing capacity and efficiency of each stage are the keys to the design and optimization of two-stage turbocharging.

The turbine performance maps currently used to determine the matching method for two-stage turbocharging are obtained through experiments or numerical simulations of each stage turbine under independent operational conditions. In performance measurements, the turbine is connected with straight pipes. However, due to the constraint of the compactness of the engine, these two turbines have to be connected by exhaust pipes with sharply steered junctions and elbows. The complicated and compact pipes would deviate the realistic on-engine performance of the two-stage turbocharger from the initial design point and may exacerbate engine performance.

Therefore, the research on the coupling effect of the regulated two-stage turbocharging system is attracting increasing attentions. In the study of Zhao at al., it has been confirmed that the interaction between two sequentially connected turbines has a strong impact on the efficiency of the downstream axial turbine. As the inter-stage coupling effect is considered, the method of axial turbine counter-rotating is proposed to mitigate the negative influence of swirling flow and improve the power efficiency by 3.8% [10]. His research illustrates that swirling is a concrete manifestation of the inter-stage coupling effect. And it is widely acknowledged that the swirls are almost inevitable in ICE exhaust manifolds and inter-stage elbows in the two-stage turbocharger. Ding et al. focused on the swirls which came from the upstream high-pressure turbine (HPT) and propagated along the elbow [11,12]. As the outcome generated by the HPT, this swirl has a simple vortex core. It preserves this feature to reach the LPT and distorts inlet flow. The effect of intensity and rotation direction of this swirl on the LPT has been studied. It was found that the swirling intensity correlates with the efficiency reduction. The opposite rotation direction introduces the different movements and deformation of the vortex which mainly influences LPT performance. Although the flow mechanism behind the two-stage turbocharging system still needs to be further unveiled, it provides an effective idea that the swirling flow can be constructed for the LPT demand to improve performance.

The turbine performance research with bypass branch involved has not been investigated intensively, despite the main function of the two-stage turbocharging system is achieved by its regulation. In the reported study, only Yang has investigated the influence of stage-interaction on turbine performance when the bypass valve is open. In his research, with the bypass flow injected into the exhaust manifold, the two streams of swirling flow encounter at the junction of the inter-stage pipe and bypass branch. They will entangle each other, and a new swirling flow will emerge downstream of the junction. This new swirling flow plays a decisive role in the performance of LPT [13]. The swirling flow is deeply influenced by the bypass flow in such a case, thus the bypass flows with different injected locations are expected to diversely influence the turbine performance. Therefore, it would be more valuable to obtain control principles of bypass branch location for providing favorable swirling flow to low-pressure turbine.

2 NUMERICAL METHOD

In this paper, the regulated two-stage turbine employed in a heavy-duty diesel engine is studied, as shown in Figure 1. The two turbocharger turbines are connected via an

inter-stage pipe, which has an elbow near the HPT. A bypass branch connects the pipe upstream and downstream the HPT, with an electrical bypass valve installed on it.
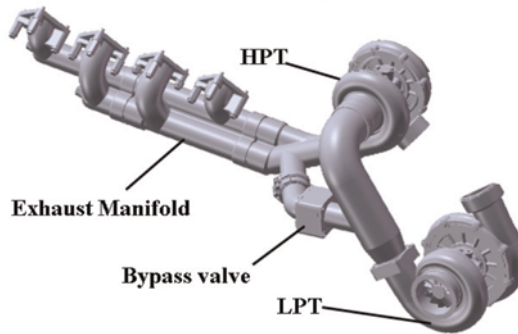

Figure 1. The investigated two-stage turbocharger system.

It is not convenient to investigate the flow control method experimentally, hence the three-dimensional numerical simulation is adopted to investigate the influence of the position of the bypass branch on the swirling flows and performance of LPT. The fluid domain corresponding to the regulated two-stage turbine system is shown in Figure 2. Commercial software ANSYS CFX is adopted to perform the computational fluid dynamics (CFD) calculation. In the computational domains of pipes and two volutes, the hybrid mesh method is used to achieve spatial discretization. As a representative of final meshes, the mesh of LPT volute is shown in Figure 3 (a). There are 1.05 million nodes in the HPT volute, 1.34 million nodes in the LPT volute, and 1.5 million nodes in the rest of the domains of the pipes, respectively. As the key components of the turbocharging system, the computational domains of the two turbine rotors are meshed by the structured mesh. According to the grid independence study of the rotors, the optimal first layer thickness is 2×10^{-6} m to guarantee reasonable y^+. And the mesh of the turbine rotor is shown in Figure 3 (b). There are 4.65 million and 4.43 million nodes in HPT rotor and LPT rotor, respectively.
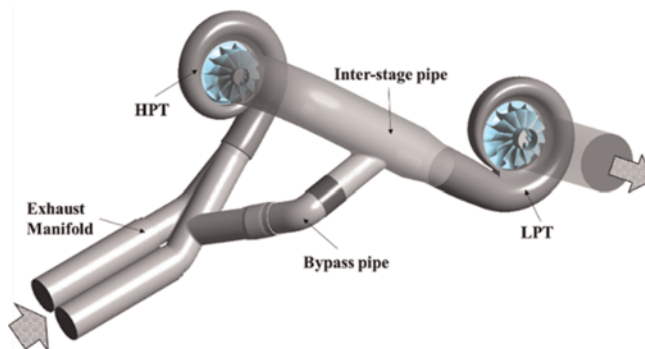
Figure 2. Computational domain of the two-stage turbocharger.
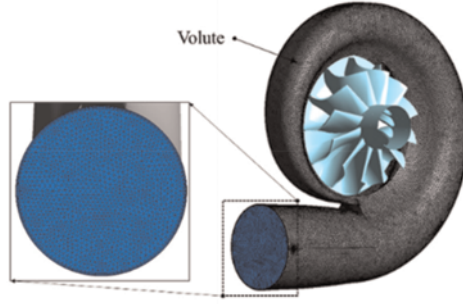
(a) The mesh of volutes
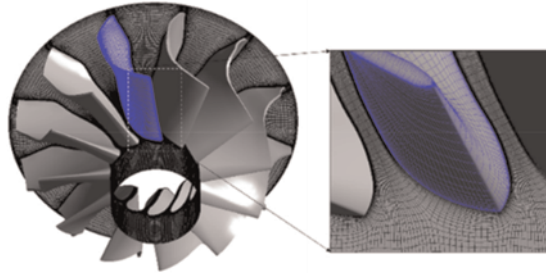
(b) The mesh of turbines

Figure 3. Mesh in the study.

Total temperature and total pressure experimentally are applied as the inlet boundary condition. The outlet static pressure is set as the ambient pressure in all cases. All the solid walls are assumed as non-slipping and adiabatic. The Shear Stress Transport (SST) model is chosen to model the turbulence. To account for the non-uniformity of azimuthal flow in volute and rotor, the frozen rotor method is employed to model the interface between the volute and rotor.

To verify the credibility of numerical results, the computed turbine performance at different pressure ratios is validated against the experimental measurements. It is worth mentioning that the experimental measurements of HPT and LPT are carried out on the standard test rig separately. The numerical predictions of HPT and LPT are obtained under the same boundary conditions. The turbine performance is generally characterized in Equations (1) ~ (3):

$$PR = \frac{P_{t-in}}{P_{s-out}} \tag{1}$$

$$MFP = \frac{m \cdot \sqrt{T_{t-in}}}{P_{t-in}} \tag{2}$$

$$\eta = \frac{1 - \dfrac{T_{t-out}}{T_{t-in}}}{1 - \left(\dfrac{P_{s-out}}{P_{t-in}}\right)^{\frac{\gamma-1}{\gamma}}} \tag{3}$$

The validation results of swallowing capacity and efficiency are shown in Figure 4. The numerical predictions of the two turbines shows good agreement with the experimental results. The average deviation of calculated MFP all over the testing condition is about 1.6% for LPT and 2.3% for HPT. The average deviation of calculated efficiency is about 3.1% for LPT and 3.6% for HPT. In particularly, the discrepancy is more evident at low pressure ratio conditions. Several factors can result in the discrepancies, among which the uncertainty of temperature at turbine exit especially at low load conditions, the heat transfer and geometrical differences (i.e. scallops of rotor) are considered to be the key contributors. The numerical method is considered to be reliable and will be used in the following study.
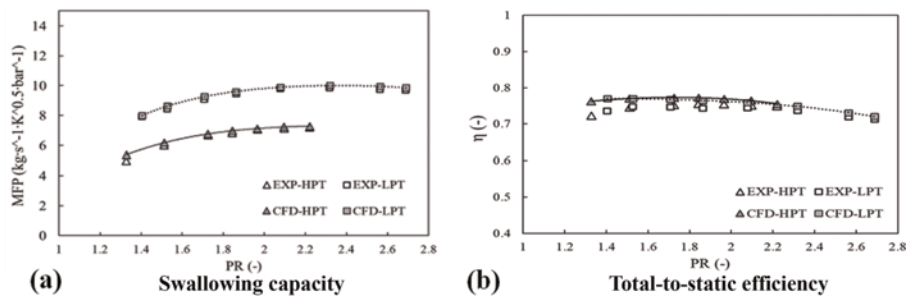
Figure 4. Validations of CFD against experiments.

To reduce calculation costs, only the LPT and its upstream and downstream pipe are considered for the further numerical calculations. It is worth mentioning that the part of the inter-stage pipe from the HPT outlet to the elbow is too short. If the boundary condition is set at the inlet of the short end of the inter-stage pipe, the boundary will forcibly change the inherent influence of the elbow geometry on the flow. Therefore, this section of pipe needs to be extended to eliminate this effect. The simplified computational domain is shown in Figure 5.
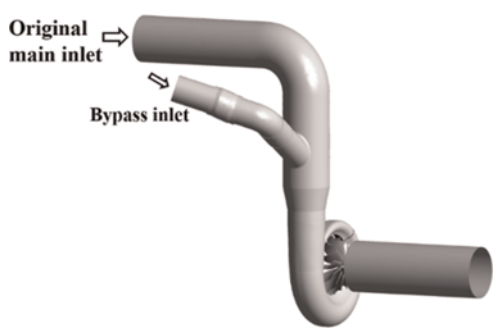
Figure 5. Simplified computational domain of LPT.

In order to reflect the role of HPT and the exhaust manifold in the two-stage turbocharger, the velocity profiles and mass-average total temperature at the HPT outlet and the exhaust manifold outlet connected to the bypass branch are extracted from the complete two-stage numerical simulation results. Then the two velocity profiles and

total temperature are imposed at the inlets of the main pipe and bypass branch of the new computational domain respectively as the boundary condition. The swirls and the corresponding axial velocity distribution are shown in Figure 6.
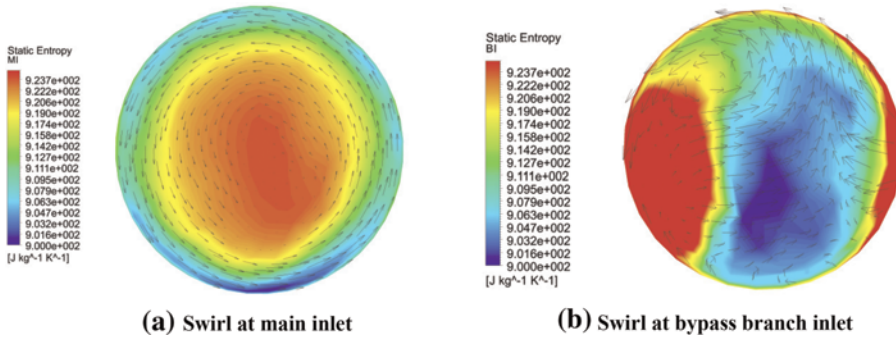

(a) Swirl at main inlet   (b) Swirl at bypass branch inlet

Figure 6. Swirls at two inlets.

The prediction results of the simplified model and the whole two-stage turbocharger model are compared. It can be seen from Table 1 that the swallowing capacity and efficiency have small discrepancies between the two methods. So that the simplified model is proven to be reliable for the prediction of turbine performance as well as flow field.

Table 1. Comparison of LPT performance predictions of the simplified model and the whole two-stage turbocharger model.

	Pressure Ratio	LPT/ RPM	Swallowing capacity	Efficiency
LPT in two-stage domain	1.7	52100	9.1722	73.49
LPT in simplified domain	1.7	52100	9.1063	73.34

Three different locations of bypass branches are investigated, as shown in Figure 7. With the main pipe fixed, the intersection of the main pipe and the bypass branch changes with the horizontal direction of the bypass branch. The bypass branch locates 20mm to the left in Case I, while it stays in the middle as original and locates 20mm to the right respectively in Case II and III. The coordinates of the velocity profile at the bypass branch inlet shift with the corresponding bypass branch while keeping the values of the velocity profile the same.

To focus on the impact of the bypass flow positions, the rotational speed and pressure ratio of the LPT are set the same in three cases, which are 52100 rpm and 1.7 respectively, corresponding to the working condition when the engine speed is 2200 RPM and the bypass valve fully opened.
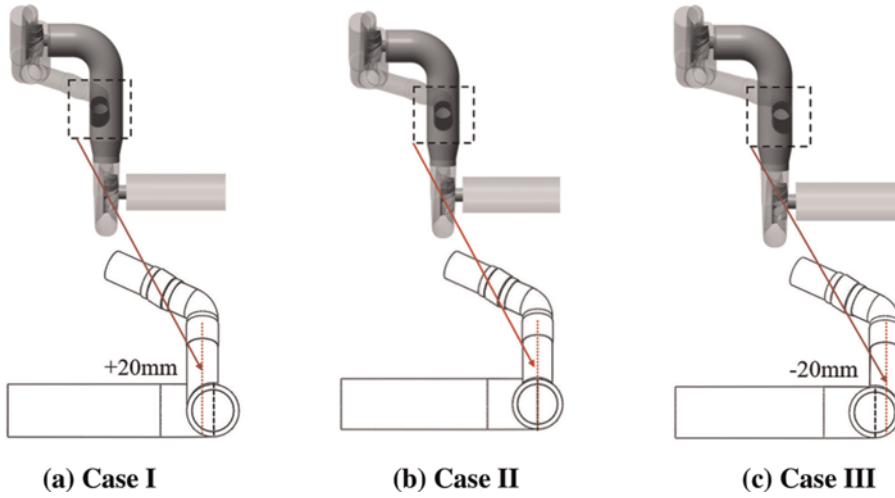
Figure 7. Different positions of bypass branches.

3   ANALYSIS OF INFLUENCE OF BYPASS FLOW ON TURBINE PERFORMANCE

Figure 8 shows the performance of LPT for the cases with different configurations. As shown in subfigure (a), it is seen that the swallowing capacity can be altered notably by the different placing of the bypass branch. Specifically, compared with the location in the middle (case II), MFP can be reduced by placing the branch on the right side (case III), while it be increased by placing the branch on the left (case I).

Subfigure (b) compares the efficiency among three configurations. The bypass flow on the left and right has opposite effects on turbine efficiency. In particular, when the bypass flow is on the left, it inserts a negative influence on efficiency and results in an efficiency reduction of 0.8%~1.6%. When the bypass flow is on the right, it improves the efficiency by about 1.1%~4.3%. And the efficiency discrepancy is more obvious at three cases when the load is low. Therefore, it is a solid proof that the performance of LPT can be notably improved by changing the position of the bypass branch.
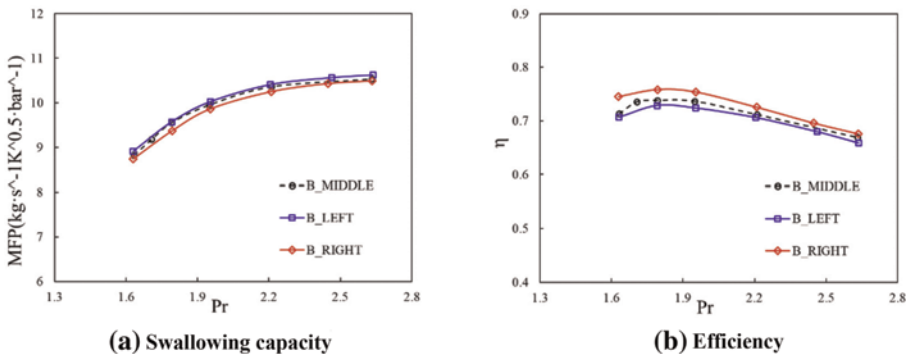
Figure 8. Performance of LPT in cases of different bypass branches.

In order to address the reason for the influence of bypass branch on turbine performance, more detailed flow information is discussed in following contents.

The reaction of a turbine illustrates the division of expansion between the rotor and the stator. In this study, the reaction degree (Λ) of the turbine is defined in Equation (4).

$$\Lambda = \frac{T_2 - T_3}{T_1 - T_3} \tag{4}$$

As shown in Figure 9, the reaction degrees are all higher than 0.5 in three cases, illustrating the acceleration of the fluid in the rotor is higher than that in the volute. The reaction degree of the turbine gradually decreases with the position of bypass flow moving from left to right, implying slighter influence on the rotor.
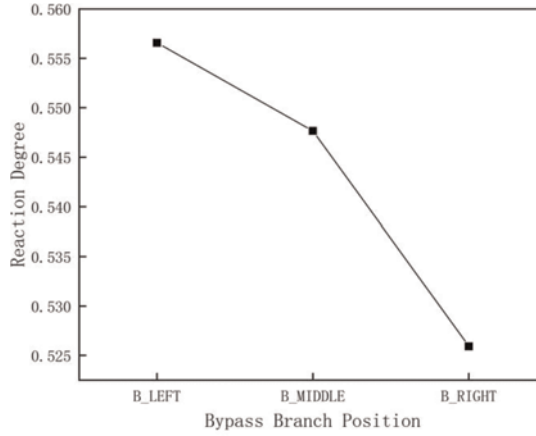
Figure 9. Comparison of the reaction degree of the LPT in three cases.

To further investigate the effects of the inter-stage coupling on the volute and rotor with the change of bypass branch position, the method used in Ref. [17] is adopted. The lost efficiency in the volute and rotor is defined as the ratio of work difference between the inlet and outlet of each component and the total work obtained by the turbine, as shown in Equations (6) and (7) respectively.

$$LE_{\text{volute}} = \frac{W_{\text{ideal, volute inlet}} - W_{\text{ideal, rotor inlet}}}{W_{\text{ideal, 1}}} \tag{6}$$

$$LE_{\text{rotor}} = \frac{W_{\text{ideal, rotor inlet}} - W_{\text{real}}}{W_{\text{ideal, volute inlet}}} \tag{7}$$

In which

$$W_{\text{ideal}} = mc_p T \left[1 - \left(\frac{P_{\text{in}}}{P_{\text{out}}} \right)^{\frac{\gamma-1}{\gamma}} \right] \tag{8}$$

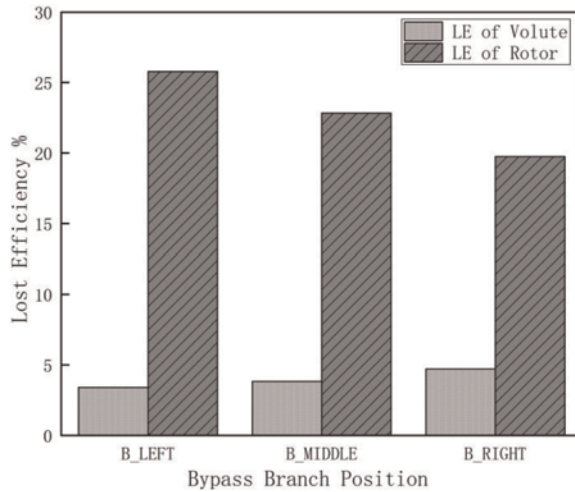$$W_{\text{real}} = \text{Tor} \cdot \omega \tag{9}$$

188

Figure 10. Comparison of the lost efficiency of three cases.

The comparison of the lost efficiency of the three cases is shown in Figure 10. As the bypass branch moves from left to right, the lost efficiency in the volute slightly increases and that in the rotor significantly decreases. Although the interval between the left and middle bypass branches is the same as that between the right and middle, moving the bypass position to the right has twice the impact on the LE_{volute} as moving the bypass position to the left. But in terms of the lost efficiency in the rotor, these two movement effects are similar, and both reduce the lost efficiency by about 3%. In comparison with the performance of the volute, the performance of the rotor is more significantly affected by the position of the bypass branch. Moving the bypass branch to the right could notably alleviates the loss in the rotor and improves its efficiency.

The difference in LPT performance within the three cases results from the aerodynamic reason. Strong aerodynamic interactions are happening in LPT. The mechanism of aerodynamics will be discussed in detail in the following section.

4 INFLUENCE OF BYPASS FLOW ON FLOW INTERACTIONS

In order to further investigate the effects of the bypass flow, a detailed analysis of the flow field inside the LPT system was carried out. The loss mechanisms in the inter-stage pipe, volute and rotor are compared in three cases with different bypass branch positions.

4.1 Flow field analysis of the inter-stage pipe

As shown in Figure 11, there is a particular interaction between the main swirling flow and the bypass flow within the inter-stage pipe. With the comparison of three cases, it is obviously seen that the different injection positions of bypass flow led to a large change in the flow field structure and the interaction effects. In the upstream of the confluence, the flow fields are similar in three cases, which indicates that the upstream region is rarely affected by the interaction. The interaction effects in these three cases play an important role at downstream of the junction, which results in completely different flow field.
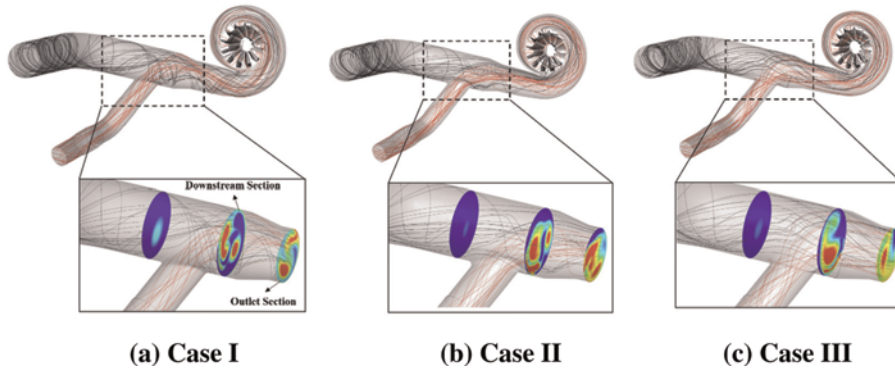
189

(a) Case I   (b) Case II   (c) Case III

Figure 11. Inter-stage pipe flow field in three cases.

The flow coming from HPT rotor is highly swirling and approaches towards the elbow with rapid evolvement. The most interesting thing is that there are three kinds of flow interactions when the swirling flow encounters the high-momentum bypass flow injected from different positions.

In Case I, the bypass flow enters the main pipe in the circumferential direction of the main pipe. Since the bypass flow is fed to the main flow offset the central line, additional tangential component of velocity is added to the main flow. This tangential flow is in the same direction of the main flow and hence further enhances the strength of the swirling of the main flow. Consequently, the enhanced swirling flow with a single vortex core keeps developing and propagates to the LPT inlet, as shown in Figure 12 (a).

(a) Case I   (b) Case II   (c) Case III
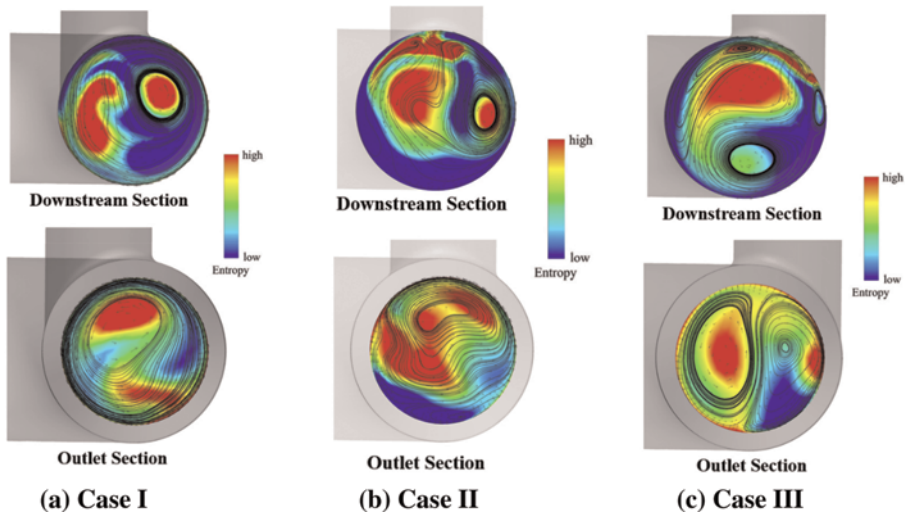
Figure 12. Entropy generation and velocity of flow interactions in three cases.

As the branch pipe moves to the middle of the main pipe (case II), a large portion of the main flow is pushed towards the other side of the main pipe by the injected bypass flow. The bypass flow impinges with the main flow directly and the inner wall of the main pipe, which forms a strong secondary flow structure including a strong vortex in the same swirling direction as the main flow and a weak vortex in the opposite swirling direction. Figure 12 (b) also proves that the secondary structure introduces more entropy generation. At the LPT inlet, the strong vortex dominants this region, and the weak vortex locates at a small corner of inner wall and nearly vanishes.

When the bypass flow injects into the main pipe from the right side (case III), the bypass flow is fed in the opposite direction of the main swirling flow, and hence weakens the vortex of the main flow. A swirling flow in the opposite direction of the main flow is generated at the position where the weak vortex lies in the case of middle bypass flow. For the intense interaction between the bypass flow and main flow, there is no doubt that the entropy generation is significantly enhanced at the downstream location of main pipe. This phenomenon is also shown in Figure 12 (c). At the LPT inlet, a secondary structure within shape of Dean vortex is formed. Each of them occupies half of the inlet region and tends to conflict with each other.

4.2 Flow field analysis of the volute

It has been confirmed previously that the swirling flow at the LPT inlet is different in three cases. The evolution of different swirling flows in the volute is analyzed. The λ_2-criterion, as proposed in the reference [14], is used to identify the vortex core region in this study. λ_2 is defined as the second eigenvalue of the symmetry square of the velocity gradient tensor. The vortex core regions of all cases are visualized using this criterion, as shown in Figure 13.
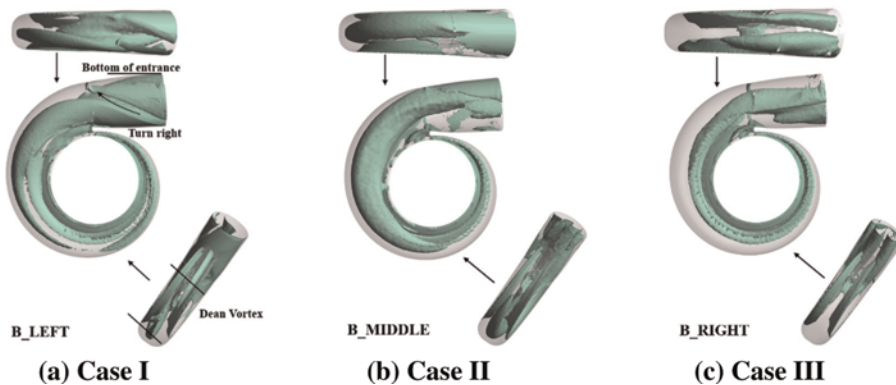

Figure 13. Visualization of the vortex region by λ_2.

In Case I, there is only one vortex core staying at the bottom of volute inlet. This vortex core first turns right along the bottom of entrance section, then turns left to the rotor shroud side in the volute, as demonstrated in the subfigure (a). The movement is accompanied by the appearance of Dean Vortices and enlargement of vortex core. This vortex core approaches rotor inlet after passing the volute tongue, which forces the vortex to enter the rotor earlier. This behavior is the main reason why the lost efficiency within volute is smallest in Case I. In comparison, in Case II two vortices exist at the volute inlet. The location of the weak vortex raises the strong vortex, then the weak one

dissipates in the entrance section, which makes the strong vortex core is far from the rotor inlet. The strong vortex has to travel within the volute until it enters to rotor, thus the lost efficiency within volute discussed above is higher than that of left bypass branch. As for Case III, the pair of opposite vortices continue to conflict with each other and move to the front left in the volute. This pair quickly dissipates in the volute, which explains the highest lost efficiency within volute among three cases.

As discussed previously, drastically different kinds of secondary flow exist in the volute under the three cases. The specific patterns of secondary flow and entropy generation rate are demonstrated in Figure 14. It can be seen that the region with high entropy generation approximately accompanies the large vortex or distortion flow in general. This further verifies the conclusion that the loss is produced by or linked to this secondary flow structure. However, these three cases have different preferences for the distribution of entropy generation.

(a) Case I   (b) Case II   (c) Case III
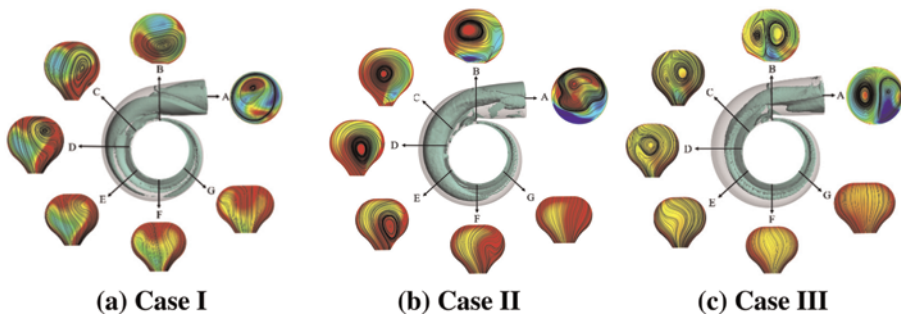
Figure 14. Evolution of secondary flow in the volute.

In Case I, the entropy generation occupies the region near the shroud side. And the strong inlet vortex manifests similar properties to a forced vortex. When the vortex propagates azimuthally, a boundary layer separation on the inner-wall side is induced by this strong vortex. The flow movement is against a downward pressure gradient, and eventually results in an opposite-rotating vortex, as shown in Section C. Moreover, the strong vortex is always near the volute outlet until it decays, causing a serious blocking effect. Therefore, the rotor performance is expected to be poor.

With a middle bypass branch, the region of high entropy propagates from up-left to down-right, maintaining the same movement as the vortex core. Compared with the case of left bypass, the swirling strength is smaller and the location of vortex core is more central so that it does not cause boundary layer separation before decay. But the vortex also moves near the volute outlet, which will result in poor performance of the rotor.

As for Case III, this pair of vortices quickly decays through conflict with each other. Due to the interaction of the pair of vortices, there is always a certain distance between the vortex core and the rotor inlet, which greatly improves the inlet flow of the rotor. Moreover, the vortex no longer exists in the volute from Section E. Therefore, the performance of rotor will significantly improve under inlet conditions.

4.3   Flow field analysis of the rotor

The entropy distribution of the rotor at two blade heights (50% and 90%) is shown in Figures 15 and 16 respectively. The volute tongue is located near passage 7. It can be
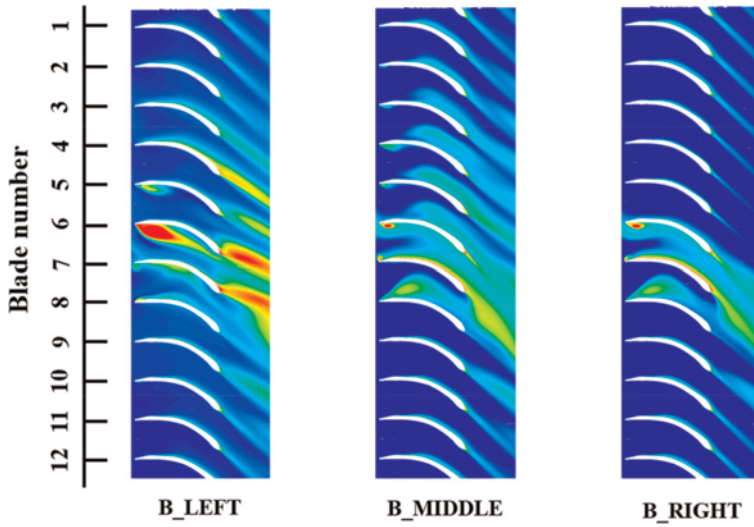
Figure 15. Blade-to-blade view of the entropy distribution in the rotor at mid span.
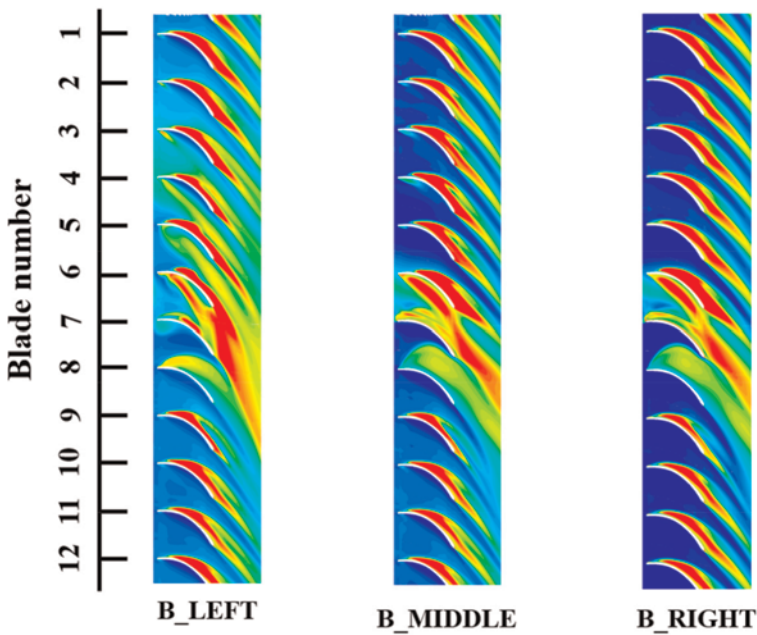

Figure 16. Blade-to-blade view of the entropy distribution in the rotor at 90% span.

seen that the entropy distribution in rotor passages is strongly dependent on the secondary flow structures in the volute. High entropy is produced by the disturbance of the volute tongue. At the mid span, a large flow separation occurs at the inlet of blades 5, 6 and 7 on the pressure surface in Case I. The same happens at blades 3, 4, 5 and 6 in the case of middle bypass flow, although the separation on pressure surface involves more blades, the degree of separation is much smaller than the former. In Case III, the separation on the pressure surface only occurs at blade 6, where is a slight separation.

At the 90% span, it can be seen that stronger pressure side separation occurs in all cases. The main reason is the influence of the tip leakage vortex. But there are still many different behaviors among them. In Case I, the large entropy generation happens at blades 3, 4, 5 and 6. In Case II and III, the entropy generation also occurs at blades 6 and 7. Case III shows the lowest entropy generation. As the above discussion, it is clearly manifested that the bypass flow fed on the right side is capable of depression the generation of tongue-induce entropy significantly than other two cases, and thus the performance of LPT is notably benefited from this effect.

5 CONCLUSIONS

In this study, a new method based on the control of the bypass flow is proposed to improve the performance of the regulated two-stage turbocharger. Under the premise of the same injected angle and level, the eccentricity of the bypass branch to the main pipe on the aerodynamic stage interaction and its influence on the performance of the LPT were studied. Three cases of left, middle and right bypass branches are investigated in three-dimensional numerical calculation. The main conclusions are as followings:

1. The aerodynamic performance of the LPT is significantly influenced by changing the position of the bypass branch. The swallowing capacity of the LPT in the case of middle bypass flow is higher than that in the case of left and right. The efficiency of the LPT is the highest in the case of right bypass.
2. The loss distributions of the LPT are analyzed by the reaction degree and lost efficiency methods. The performance influence by the flow control is a balance between the enhance of loss in the volute and reduction of loss in the rotor. As the bypass branch moves from left to right, the reduction in efficiency loss within the rotor exceeds the increase in loss efficiency within the volute, which improves the efficiency of LPT.
3. Through the analysis of the flow field of the interstage pipe, the effects of the bypass flow at different positions on the main swirling flow are revealed. Specifically, the left bypass flow enhances the main swirling flow. The right bypass flow depresses the main swirling flow. They eventually generate different swirling structures at the LPT inlet.
4. This proposed flow control method is proved to be an effective measure to improve the performance of the regulated two-stage turbocharger. Different arrangement of the bypass branch brings about different inter-stage coupling effects, which can be regarded as a tool to carve the main swirling flow coming from HPT and create a favorable flow field to LPT.

REFERENCES

[1] Zifei Y, Anup B. Light-Duty Vehicle Greenhouse Gas and Fuel Economy Standards. 2017.
[2] Ricardo M-B, Apostolos P, Mingyang Y. Overview of Boosting Options for Future Downsized Engines. *Sci China Technol Sci* 2011.

[3] Yuncheng G, Zetai M, Sipeng Z, Mingyang Y, Kangyao D. A Methodology to Extend the Altitude Adaptability of a Turbocharged Heavy-duty Diesel Engine. *International Journal of Automotive Technology volume*, 2021.

[4] Hualei L, Guozheng Z, Huiyan Z. Equivalent Matching Model of A Regulated Two-Stage Turbocharging System for the Plateau Adaptability. *Proceedings of the Institution of Mechanical Engineers, Part D: Journal of Automobile Engineering.*

[5] Ruilin L, Zhongjie Z, Surong D, Guangmeng Z. High-altitude Matching Characteristic of Regulated Two-stage Turbocharger with Diesel Engine. *Journal of Engineering for Gas Turbines and Power*, 2017.

[6] A. Chasse, P. Moulin, P. Gautier, A. Albrecht, L. Fontvieille, A. Guinois and L. Doléac. Double Stage Turbocharger Control Strategies Development. *SAE International Journal of Engines*, 2009.

[7] Jinsuk K, Jaeyeon L, Hyun-soo S. *Enhancing Power Density with Two-Stage Turbochargers*. SAE 2012 World Congress & Exhibition, 2012. A common turbo-charger stage matching method is to employ a bypass valve in the exhaust manifold to made load distribution between the two turbine stages appropriate, of which the two turbines work as the crucial components to affect the optimum load distribution and regulation strategies [7].

[8] Qingning Z, Chris B, Sam A, Richard B. *Simulation Study of the Series Sequential Turbocharging for Engine Downsizing and Fuel Efficiency*. SAE 2013 World Congress & Exhibition – Detroit, 2013.

[9] Mingyang Y, Yuncheng G, Kangyao D. Influence of Altitude on Two-Stage Turbocharging System in a Heavy-Duty Diesel Engine Based on Analysis of Available Flow Energy. *Applied Thermal Engineering*, 2018.

[10] Rongchao Z, Weilin Zm Xinqian Z. Design of Counter-Rotating Turbine to Improve the Off-Design Performance Of Turbo-Compounding Systems. *ASME Turbo Expo 2013: Turbine Technical Conference and Exposition*, 2013.

[11] Zhanming D, Weilin Z, Yangjun Z. Assessment of Turbine Performance Under Swirling Inflow Conditions. *Energy*, 2019.

[12] Zhanming D, Weilin Z, Yangjun Z. *Investigation on Pulsating Flow Effect of a Turbocharger Turbine*. ASME 2017 Fluids Engineering Division Summer Meeting, 2017.

[13] Lee SP, Jupp M, Nickson A. The Influence of Secondary Flow Structures in a Turbocharger Turbine Housing in Steady State and Pulsating Flow Conditions. Mechanical and Aerospace Engineering (ICMAE). In: *2016 7th international conference on. IEEE*; 2016.

[14] Jeong J, Hussain F. On the Identification of a Vortex. *Journal of Fluid Mechanics*, 285, 2006.

A 3D inverse design based rapid multi-disciplinary optimization strategy for radial-inflow turbines

J. Zhang, L. Zhang

Advanced Design Technology Ltd, UK

M. Zangeneh

Department of Mechanical Engineering, University College London, UK

ABSTRACT

The radial-inflow turbines have been widely used in the turbocharger applications and the most common challenges for designing turbocharger turbines are to obtain good efficiencies for design point and off-design points, meeting the maximum mass flow requirement, having low moment of inertia and maintaining a good stress level which is quite difficult due to the very high tip speed and high turbine inlet temperature. The conventional way of tackling this multidisciplinary problem is to perform CFD/FEA analysis for a large number of designs (DOE) and build an RSM/surrogate model based on the design matrix then use optimiser to find the optimal solution. Inverse design method which is a 3D inviscid design method for turbomachinery blades has been used in the same way with some post modification/treatment on the blade geometry called radial-filament modification. In this paper, we proposed to use some aerodynamic and mechanical performance parameters from inverse design solution and a direct optimisation approach to perform the multidisciplinary optimisation. The final optimised design shows similar aerodynamic and mechanical performance as the baseline design (optimized through DOE) with significantly reduced number of CFD/FEA simulations.

1   INTRODUCTION

Typical radial turbine losses include incidence loss, tip leakage loss, secondary flow loss, windage loss and exit kinetic energy loss [1]. For radial-inflow turbines, the blade designed using conventional method is always radial-fibred or radial-filament which means the blade is stacked along the radial direction and the blade is always supported by the blade element beneath it which minimises the centrifugal bending stress. However, this type of blading severely restricts the designer's choices when defining blade shapes. Barr et al. [2,3] and Jason et al. [4] have used non-radial blading near LE (back swept) to improve turbine's off-design performance (low U/C) by reducing the incidence loss.

Inverse design method, also known as Circulation method, has been widely used in the design and optimisation of different types of turbomachinery blades including compressors, turbines, pumps and fans etc [5–8]. The radial-inflow turbine blades designed using the inverse deign method is three-dimensional (3D), which can provide a higher aerodynamic performance but can result in high stress concentration on the blade surface which may exceed the material strength especially for the turbocharger cases where the turbine inlet temperature is extremely high. A number of different approaches have been applied to tackle this problem including modifying the blade thickness

[5] and carrying out post-adjustment on the blade wrap angle distribution for the 3D blades to get fully radial-fibred or partially radial-fibred blades [6,9–11]. Multidisciplinary optimisation of radial-inflow turbines using conventional design methods usually involves a large number of CFD/FEA simulations [12–14].

In this paper, a direct optimisation methodology coupling the inverse design method with Genetic Algorithm (GA) will be used to optimise the aerodynamic and mechanical performance of a radial-inflow turbine blade without any CFD/FEA simulations. Instead of using radial filament the geometry is controlled through geometry parameters extracted from the inverse design solver.

2   OPTIMISATION METHODOLOGY

The baseline design used in this paper is an optimised design through DOE (design of experiments consists of hundreds of CFD/FEA simulations), RSM (response surface model) and MOGA (multi-objective genetic algorithm) [15]. This optimized baseline design was able to improve the efficiency of a conventionally design baseline stage subject to stress and modal frequency constraints. The objective of this paper is to propose a new optimisation methodology which is numerically much more efficient compared to the conventional DOE based method. The flowchart of the optimisation methodology used in this paper is shown in Figure 1.

Baseline CFD and FEA analysis will be performed first and its CFD and FEA performance parameters will be used as the reference. Some parameters will be defined based on the inviscid flow field information from the inverse design method and geometrical parameters of the blade which will be used in the optimisation later to control the aerodynamic and mechanical performance of the design. A direct optimisation based on the inverse design method and MOGA will be used for the given constraints and objectives while varying the design parameters within the specified range. As a result, the optimal design will then be selected from the Pareto front and its performance is validated through CFD/FEA simulation against the baseline design.
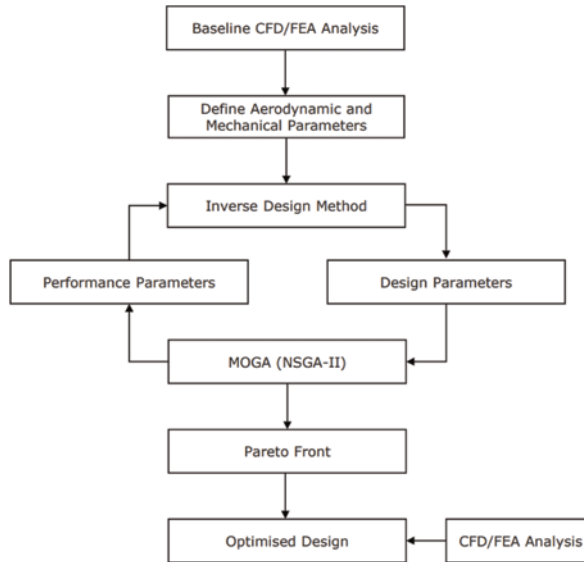
Figure 1. Flowchart of the optimisation methodology.

3   BASELINE CFD AND FEA ANALYSIS

The meridional geometry of the baseline design is shown in Figure 2 and all the main dimensions and geometrical parameters are summarised in Table 1.

The nozzle blade (14 blades) and rotor blade (11 blades) are meshed using ANSYS Meshing (unstructured mesh) and ANSYS TurboGrid (structured mesh) as shown in Figure 3. The near-wall element size is 0.01 mm and there are 20 layers in the 0.5 mm tip clearance region to resolve the tip gap flow. The total number of elements is around 1 million. ANSYS CFX is used for the steady-stage RANS simulations. As shown in the Figure 4, the nozzle domain is stationary and the rotor domain is rotating. The stage interface (mixing-plane) is used between the stationary and rotational domain. Inlet boundary condition is set as total pressure (2.2 bar) and total temperature (403.2 K). The inlet flow angle is set as 40° from the tangential direction. The outlet static pressure is set as 1.0 bar. The RPM will be varying from 50,000 to 90,000 rev/min. k-e turbulence model is used for the turbulence modelling. The resulting turbine mass flow rate and efficiency are shown in Figure 5. The CFD model and setup have been validated against test data by Zhang [11].
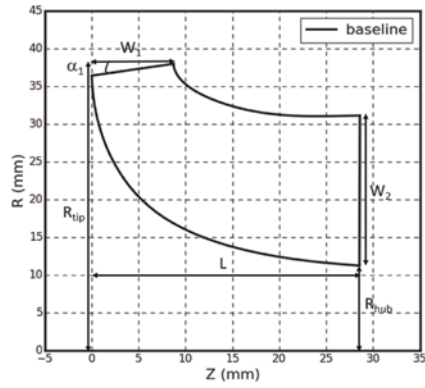
Figure 2. Meridional geometry of the baseline design.

Table 1. Meridional geometry parameters of the baseline design.

Meridional parameter	Value	Unit
R_{tip}	38	mm
R_{hub}	11.25	mm
W_1	8.7	mm
W_2	19.9	mm
L	28.55	mm
α_1	10.2°	–
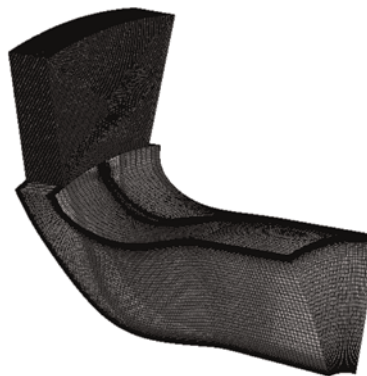
Figure 3. Computational mesh for turbine nozzle + rotor.
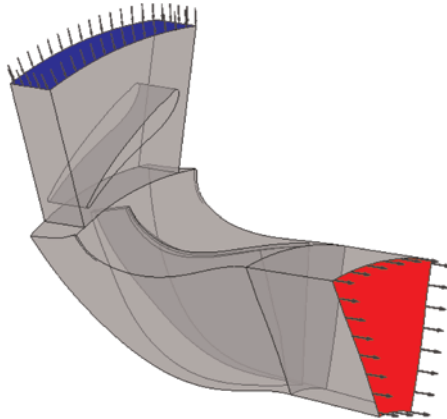
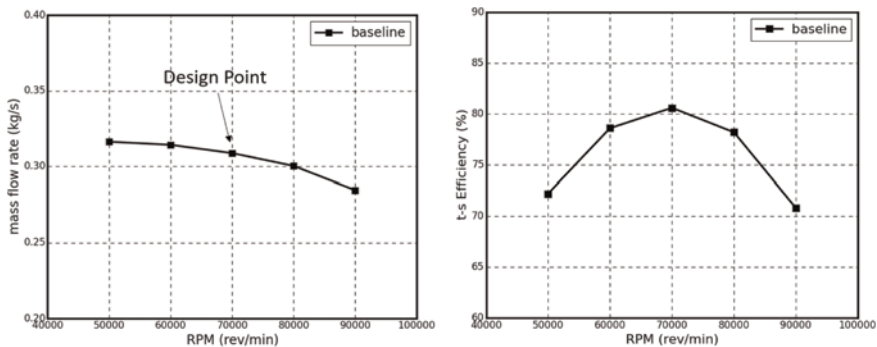**Figure 4. Computational domain for turbine nozzle + rotor.**

Figure 5. Baseline mass flow rate and t-s Efficiency for different RPM.

The static structural analysis and modal analysis are also performed using the blade-only model in ANSYS Mechanical. The mesh used is shown in Figure 6 (around 100,000 elements). A fix support is applied at the blade hub and the blade is rotating with maximum speed of 120,000 rev/min. The von-Mises stress contour on the blade surface is shown in Figure 7. It is noted that the stress values are normalised by the material yield strength and all the values above 1.0 are shown in red. Since the blade is completely radial-filament, the stress level on the blade is well below the material strength. The stress concentration occurs near the LE and TE hub locations which is mainly caused by the lack of modelling the fillet. The blade vibration mode shape is shown in Figure 8 which is a typical exducer flex with natural frequency of 10,529 Hz.
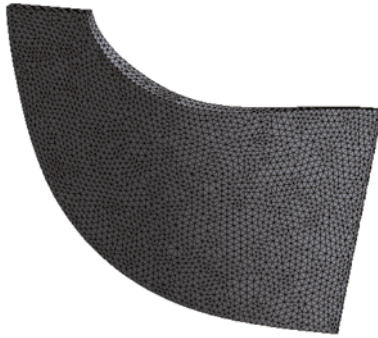
Figure 6. Baseline mesh for FEA analysis.

Figure 7. Baseline normalised von-mises stress contour (left – suction side and right – pressure side).

Figure 8. Baseline vibration mode shape.

4 INVERSE DESIGN BASED AERODYNAMIC AND MECHANICAL PERFORMANCE PARAMETERS

A detailed derivation and formulations of the inverse design method can be found in [16].

The main inputs are meridional geometry, blade thickness distribution, LE/TE rV_θ^* and streamwise blade loading distribution ($\frac{\partial rV_\theta}{\partial m}$). rV_θ^* is a circumferentially averaged

circulation term where r is the radius and V_θ is the tangential velocity. rV_θ^* is normalised by R_{tip} and U_{tip} in Equation (1). For radial-inflow turbines, the LE rV_θ^* is equivalent to the work/loading coefficient and has a typical value between 0.7–0.9. The TE rV_θ^* is ideally to be minimised to have zero swirl at the turbine exit. The static enthalpy jump across the blade surfaces is defined in Equation (2), where '+' and '−' means the pressure and suction side, B is the number of blades, W_{mbl} is the relative meridional blade surface velocity and $\frac{\partial rV_\theta}{\partial m}$ is the derivative of rV_θ along the meridional direction (m). In the inverse design method, we use $\frac{\partial rV_\theta}{\partial m}$ to control the blade loading distribution and the blade loading is defined by a three-segment method [17]. 4 parameters are used to define a unique loading shape including LE $\frac{\partial rV_\theta}{\partial m}$, NC, ND (meridional coordinates whose values are between 0 and 1) and SLOPE which is the slope of the middle straight line.

$$rV_\theta^* = \frac{rV_\theta}{R_{tip}U_{tip}} \tag{1}$$

$$h^+ - h^- = \frac{2\pi}{B} W_{mbl} \frac{\partial rV_\theta}{\partial m} \tag{2}$$

The 3D velocity field is divided into two parts including a circumferentially averaged velocity and a periodic velocity. The mean tangential velocity has been given as an input through rV_θ^* and $\frac{\partial rV_\theta}{\partial m}$. Mean radial and axial velocities are solved through Stokes-stream function. The periodic velocity field is solved using discrete Fourier transform in the frequency domain. Once the full velocity field is resolved, the blade camber (wrap angle) can be obtained through the boundary condition assuming that the blade surface velocity is parallel to the blade surface with some initial camber values along a quasi-orthogonal streamline (stacking condition). The pressure and temperature field are then solved based on the ideal gas equation and conservation of rothalpy.

As a result, the output of the inverse design method will be the blade geometry (camber distribution) and pressure/velocity field. The surface static pressure from the 3D inverse design method generally matches well with CFD calculation of the same blade geometry, see [18]. The following parameters can then be defined based on the inverse design method output.

   (I)   The Diffusion Ratio is the ratio of the maximum relative velocity on the blade surface and the relative velocity at the blade trailing edge.

  (II)   The Profile Loss is computed from the integration of the cube of the blade surface velocity predicted by the inverse design code. Previous work [19] shows that the entropy generation on the blade surface is largely proportional to this value.

 (III)   UD_work is calculated by the volume flow averaged rV_θ variation between LE and TE which is related to the turbine power through Euler's turbomachinery equation.

 (IV)   UD_LeavingKE is the area averaged leaving kinetic energy at the rotor exit.

  (V)   UD_RMSE calculates the root mean square error of all the wrap angle difference between shroud and hub, between shroud and mid span, between midspan and hub, and between 15% span and hub near TE as shown in Figure 9. For a perfectly radial-fibred blade, all the wrap angle difference along the vertical direction will be zero which leads to UD_RMSE = 0.

 (VI)   UD_MaxDeviation is the maximum value of all the wrap angle differences used in the calculation of UD_RMSE.

(VII)   UD_Wrap0.15HubTE is the wrap angle difference between 15% span and hub at blade TE.

(VIII)   UD_0.9_MaximumBow calculates the maximum deviation from the linear span at 90% of streamwise location (near TE). It is the normalised by the linear span length as shown in Figure 10. For a perfectly radial-filament blade, this value will be zero.
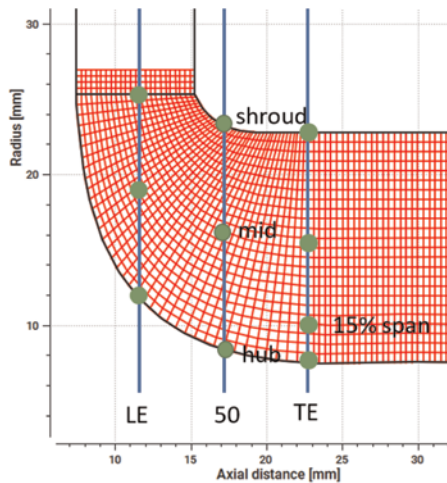

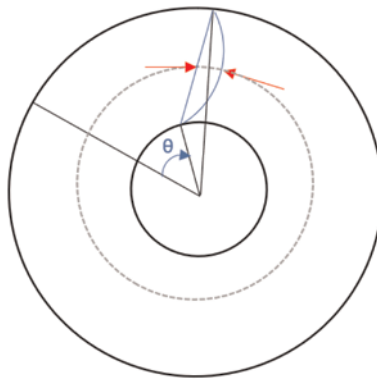**Figure 9. Wrap angle difference between different spanwise and axial locations.**

Figure 10. Illustration of UD_0.9_MaximumBow.

5   DIRECT OPTIMISATION AND RESULTS

A direct optimisation is carried out using the inverse design method and MOGA (NSGA-II algorithm [20]). The range of design parameters are shown in Table 2. The constraints and objectives are summarised in Table 3. The profile loss and the leaving kinetic energy are closely linked to aerodynamic performance. They are set to be minimized. The external loss (scallop, back disk flows, mixing loss etc) can be evaluated in more detailed CFD model or test rig. Since the solution is at design point, the optimization aims at improving design point efficiency. However, the off-design condition performance can

also be controlled through proper loading prescription in the inverse design method and key parameters such as throat and diffusion ratio can be monitored to help control the overall performance characteristics. This optimization does not rule out any potential improvements from refining the smaller details of the machine. These measures can be applied on top of an optimized rotor blade design, which may bring more benefit to the turbine performance. 40 (population size) x 40 (number of generations) designs will be generated during the optimisation to search the optimal design for the given range of design parameters and specified constraints/objectives. All the performance parameters are calculated for the design point using the inverse design method.

Table 2. Range of design parameters.

	Min	**Max**
rV_θ^* Hub TE	−0.05	0.1
rV_θ^* Mid TE	−0.05	0.1
rV_θ^* Shroud TE	−0.05	0.1
LE $\frac{\partial rV_\theta}{\partial m}$ Hub	−1	0.5
NC Hub	0.05	0.4
ND Hub	0.45	0.85
SLOPE Hub	1	2.5
LE $\frac{\partial rV_\theta}{\partial m}$ Shroud	−1	0.5
NC Shroud	0.05	0.4
ND Shroud	0.45	0.85
SLOPE Shroud	−8	0

Table 3. Constraints and objectives.

Diffusion Ratio	<= 1.8
UD_Wrap0.15HubTE	<= 6.125
UD_RMSE	<= 10
UD_work	>= 8.74
Profile Loss	minimise
UD_MaxDeviation	minimise
UD_0.9_MaximumBow	minimise
UD_LeavingKE	minimise

The resulting Pareto front of the optimisation is shown in Figure 11. Design 543 is selected as the optimal design for further CFD/FEA validation since it has the lowest UD_MaxDeviation value and highest UD_work value (9.04 versus 8.74 for the base-line). It has been found that the maximum blade stress increases significantly once the UD_0.9_MaximumBow is greater than 12.0 or the UD_MaxDeviation is greater than 5.0.
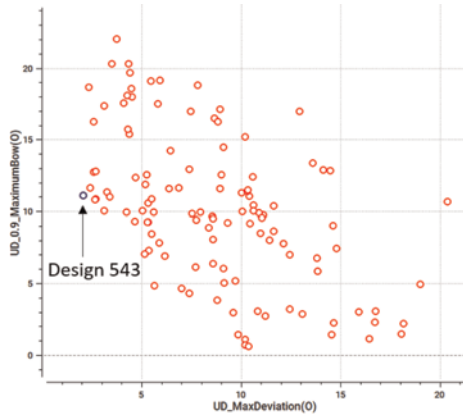
Figure 11. Pareto front and selected optimal design.

From Figure 12 it can be clearly seen that baseline design is purely radial-filament due to the post modification on the 3D geometry while Design 543 is close to radial-filament near the exducer region.
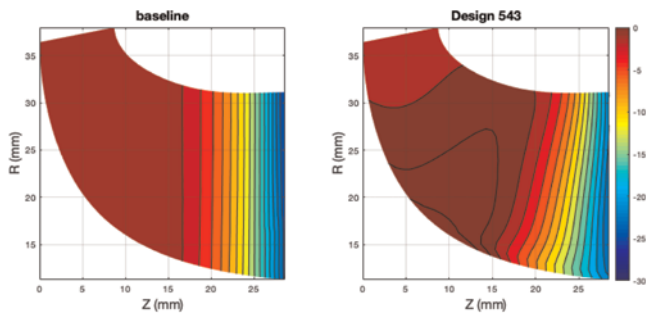

Figure 12. Comparison of wrap angle contour between baseline and Design 543.

The comparison of mass flow rate and t-s efficiency obtained from CFD simulations are shown in Figure 13. The mass flow rate of Design 543 is almost identical to the baseline value at the design point condition while slightly lower (2–3%) than the baseline at high RPM region. Design 543 has the same efficiency value as the bassline at the BEP and the whole efficiency curve is shifted to the high RPM slightly.
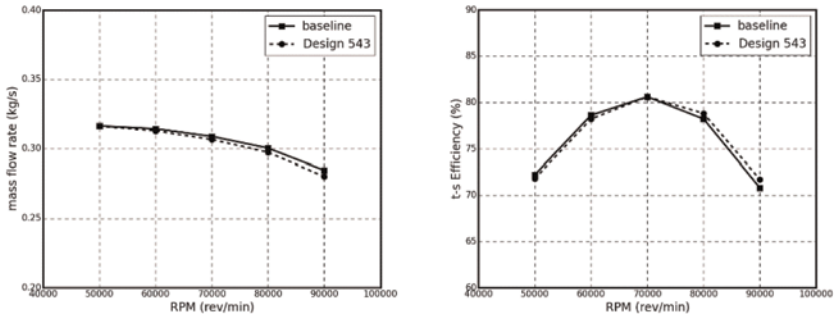
Figure 13. Comparison of mass flow rate and t-s efficiency of baseline and Design 543.

Von-Mises stress contour of Design 543 is shown in Figure 14 and it is very similar to the baseline distribution where the maximum stress occurs near LE and TE of blade hub. On the blade surface of Design 543, stress levels are quite low and only near the suction side of the exducer hub region the stress is a bit higher but still less than the material strength.

The modal shape of the Design 543 is same as baseline and its modal frequency is 11,999 Hz which is 14% higher than the baseline. The comparison of the blading of the baseline and Design 543 at section A-A is shown in Figure 15. The blade tangential thickness distribution does not change much due to the fact that the blade normal thickness has been kept the same and the blade camber along the meridional direction does not change much. As it can be seen that the main reason for the increased blade stiffness is the non-radial blading above the 30% of the spanwise location while the baseline (blue) has a completely radial blading.
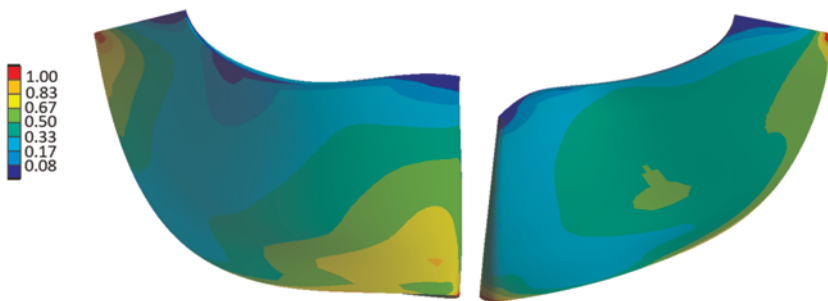
Figure 14. Design 543 normalised von-mises stress contour (left – suction side and right – pressure side).
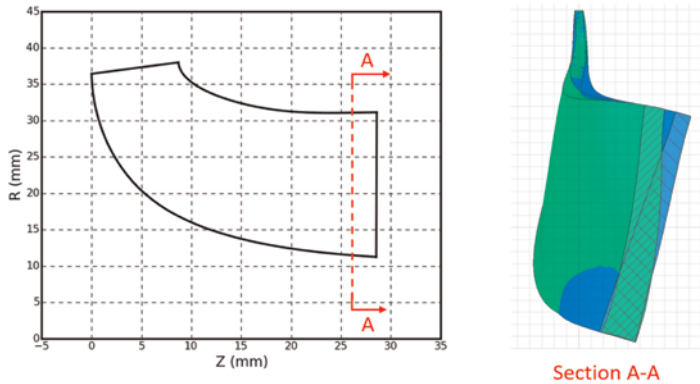
Figure 15. Comparison of blade geometries at Section A-A view (blue-baseline, green-Design 543).

6   CONCLUSIONS

In this paper an optimisation methodology using inverse design method and direct optimisation is presented. It shows that it is possible to obtained less 3D blade (not completely radial-filament) which has reasonable maximum stress values using inverse design method and direct optimisation. This newly proposed methodology can be used to design turbine blades which have similar aerodynamic and mechanical performance to that obtained through DOE based surrogate model approach with much less computational resources (10 CFD and 2 FEA cases versus around 280 CFD and 80 FEA cases [15]).

NOMENCLATURE

3D	three-dimensional
CFD	computational fluid dynamics
DOE	design of experiments
FEA	finite element analysis
GA	genetic algorithm
LE	leading edge
MOGA	multi-objective genetic algorithm
NC	normalised streamwise location
ND	normalised streamwise location
NSGA-II	non-dominated sorting genetic algorithm-II
RSM	response surface model
TE	trailing edge
α_1	blade LE angle
B	blade number

(*Continued*)

(*Continued*)

h^+	static enthalpy on the blade pressure side
h^-	static enthalpy on the blade suction side
L	blade axial length
m	meridional coordinate
R_{tip}	blade tip radius
R_{hub}	blade TE hub radius
rV_θ	radius x tangential velocity
rV_θ^*	normalised rV_θ
$\frac{\partial rV_\theta}{\partial m}$	steamwise blade loading parameter
U_{tip}	blade tip speed
W_1	blade inlet width
W_2	blade exducer width
W_{mbl}	relative meridional blade surface velocity

ACKNOWLEDGEMENTS

REFERENCES

[1] Suhrmann, J., Peitsch, D., Gugau, M., Heuer, T. & Tomm, U. 2010. *Validation and Development of Loss Models For Small Size Radial Turbines*.

[2] Barr, L., Spence, S. & Eynon, P. 2008. *Design and Analysis of a Radial Turbine with Back Swept Blading*. The 4th International Symposium on Fluid Machinery and Fluid Engineering.

[3] Barr, L., Spence, S. & Eynon, P. 2008. *Improved Performance of a Radial Turbine Through the implementation of Back Swept Blading*. ASME Turbo Expo 2008, GT2008-50064.

[4] Walkingshaw, J., Spence, S., Ehrhard, J. & Thornhill, D. 2011. *An Investigation Into Improving Off-design Performance In A Turbocharger Turbine Utilizing Non-Radial Blading*. ASME Turbo Expo 2011, GT2011-45717.

[5] Bonaiuti, D. & Zangeneh, M. 2009. On the Coupling of Inverse Design and Optimization Techniques for the Multi-objective, Multipoint Design of Turbomachinery Blades. *Journal of Turbomachinery*, 131(2): 021014.

[6] Zangeneh-Kazemi, M. 1989. *Three-dimensional Design of Radial-inflow Turbines*. Doctoral thesis, Cambridge University, Engineering Department.

[7] Yang, W. & Xiao, R. 2014. Multi-objective Optimization Design of a Pump-Turbine Impeller Based on an Inverse Design Using a Combination Optimization Strategy. *Journal of Fluids Engineering*, 136(1): 014501.

[8] Lee, K-Y, Choi, Y-S, Kim, Y-L & Yun, J-H. 2008. Design of axial fan using inverse design method. *Journal of Mechanical Science and Technology*, 22(10): 1883–1888.

[9] Zhang, J., Zangeneh, M. & Eynon, P. 2014. *A 3D Inverse Design based Multidisciplinary Optimization on the Radial and Mixed-inflow Turbines for Turbochargers*. IMechE 11th International Conference on Turbochargers and Turbocharging, pages 399–410.

[10] Zhang, J. & Zangeneh, M. 2015. *Increasing Pulse Energy Recovery of Radial Turbocharger Turbine by 3D Inverse Design Method*. ASME Turbo Expo 2015, GT2015-43579.

[11] Zhang, J. 2017. *Multidisciplinary Optimisation of Radial and Mixed-inflow Turbines for Turbochargers. Doctoral thesis*, University College London.

[12] Deng, Q., Shao, S., Fu L., Luan, H. & Feng, Z. 2018. An Integrated Design and Optimization Approach for Radial Inflow Turbines – Part II: *Multidisciplinary Optimization Design*. *Applied Sciences*, 8(11): 2030.

[13] Barsi, D., Perrone, A., Ratto, L., Simoni, D. & Zunino, P. 2015. *Radial Inflow Turbine Design Through Multidisciplinary Optimisation Technique*. ASME Turbo Expo 2015, GT2015-42702.

[14] Odabaee, M., Sauret, E. & Hooman, K. 2016. *Multi-objective Aerodynamic Optimisation of A Real Gas Radial-inflow Turbine*. ASME Turbo Expo 2016. GT2016-58132.

[15] Zhang, J. & Zangeneh, M. 2020. *Multidisciplinary and Multi-Point Optimisation of Radial and Mixed-Inflow Turbines for Turbochargers Using 3d Inverse Design Method*. IMechE 14th International Conference on Turbochargers and Turbocharging, pages 263–277.

[16] Zangeneh, M. 1991. A Compressible Three-Dimensional Design Method for Radial and Mixed Flow Turbomachinery Blades. *International Journal of Numerical Methods in Fluids*, Vol 13, 599–624.

[17] Zangeneh, M., Goto, A. & Takemura, T. 1996. Suppression of Secondary Flows in A Mixed-flow Pump Impeller by Application of Three-dimensional Inverse Design Method: Part I – Design and Numerical Validation. *Journal of Turbomachinery*, 118:536–543.

[18] Zhang, J., Gomes, P., Zangeneh, M. & Choo, B. 2017. *Design of a Centrifugal Compressors Stage and a Radial-Inflow Turbine Stage for a Supercritical Co2 Recompression Brayton Cycle By Using 3d Inverse Design Method*. ASME Turbo Expo 2017, GT2017-64631.

[19] Denton, J. D., 1993. Loss Mechanisms in Turbomachines. 1993 IGTI Scholar Lecture. *Journal of Turbomachinery*, 115(4), 621–656.

[20] Deb, K., Agrawak, S., Pratap, A. & Meyarivan, T. 2000. A Fast Elitist Non-Dominated Sorting Genetic Algorithm for Multi-objective Optimization: NAGA-II. *Proceedings of the Parallel Problem Solving from Nature VI Conference*, pages 849–858.

Taylor & Francis
Taylor & Francis Group
http://taylorandfrancis.com

Experimental investigations

Taylor & Francis
Taylor & Francis Group
http://taylorandfrancis.com

Design, optimisation and analysis of non-radial fibre turbines for electric turbocompounding applications

E. Alvarez-Regueiro, B. Yang, M.E. Barrera-Medrano

Imperial College London, UK

S. Rajoo

Universiti Teknologi Malaysia, Malaysia

R. Martinez-Botas

Imperial College London, UK

ABSTRACT

This paper presents the analysis and results of the implementation non-radial fibre blading radial turbines for waste heat recovery (WHR). WHR technologies, such as turbo-compounding, have to operate at low pressure ratios and low speed conditions, leading to lower centrifugal stress compared to traditional turbocharger turbines. Removing this constraint introduces a new degree of freedom and allows more flexibility in the blade design.

The design methodologies presented in this paper consist of a 3D parametric model coupled with Computational Fluid Dynamic (CFD). The 3D parametric model generated a sampling of about a hundred geometries and predicted the efficiency using single blade passage simulations. The sensitivity analysis showed the effect of each design parameter on efficiency. A radial fibre turbine geometry was optimised for maximum efficiency. The optimum radial fibre geometry was set as the baseline for further non-radial blading optimisation, based on a parametric-CFD approach. The efficiency improvement between the optimum non-radial fibred design and the optimum radial fibre design was found to be +2.0pp experimentally at the Imperial College turbocharger facility.

1   INTRODUCTION

Industrial processes, low-grade waste heat represents 50% of the total heat generated [1]. Traditionally, low-grade heat is released into the environment due to the lack of cost-effective and efficient technologies. With the growing environmental concern about greenhouse gas emissions, research and development has focused on the recovery of waste heat to reduce the fuel consumed and mitigate the environmental footprint.

This situation is significant in the offshore oil and gas industry. Offshore facilities are often isolated from the mainland power grid. These types of platforms have physical space and weight limitations, requiring compact and simple solutions. Maintenance is a complicated and costly task due to the difficulty of reaching offshore platforms, thus, robustness and reliability are essential characteristics of the machinery installed in the facilities. The literature on waste heat recovery literature on offshore oil and gas platforms is limited, however, some authors assessed their potential [2] and studied the implementation of WHR technologies, particularly organic Rankine cycle systems [3–7].

Waste heat from engine exhaust can be recovered by turbocompounding systems that transform it into mechanical or electrical energy. WHR technology has being applied to heavy-duty and passenger vehicles [8]. No electric turbocompounding (ETC) implemented in oil and gas applications has been found in the literature. However, the potential for energy recovery on offshore platforms is significant, harnessing waste heat streams which would otherwise be released into the atmosphere. Flare is another important waste heat stream to consider for ETC. Flare is particularly intermittent, ETC is a flexible technology with good unsteady response and performance as it originates from automotive applications.

Traditional radial turbines are designed for turbocharger applications, which have higher pressure ratios and rotational speeds than ETC applications. Therefore, when using conventional high-speed turbines in ETC conditions (low pressure, PR = 1.1-1.3) the performance is poor [9]. Radial turbines blades are commonly designed as radial fibred [10]. This means that the blade fibres are aligned in the direction perpendicular to the axis of rotation. As a result, the bending stress at the root and leading edge of the blade are kept low, this is particularly important when the rotational speed and temperature is high, which lead to high centrifugal forces and thermal stress. However, as the ETC occurs at low speed and low temperature conditions, a departure from the radial fibre constraint is possible. The design space can be widened using new camberline distributions and different blade angles. The literature available on non-radial blading is focused on turbocharger applications [11–13]. These applications are characterised by high pressure, temperature and high rotational speed.

This paper investigates the effect of non-radial fibre blading with an automated approach, at non-conventional low pressure and low speed turbine operating conditions, compared to a standard radial turbine.

2 PARAMETRIC MODEL AND OPTIMISATION

A 3D parametric model consisting of the nozzle and the rotor was created and coupled with a CFD commercial solver (CFX). The parametric-CFD based approach can assess the impact of 3D geometric features, such as non-radial fibre blading, on the resulting aerodynamic efficiency. This comes at a higher computational cost compared to 1D design approaches such as meanline modelling. The next sections describe in more detail the methodology and relevant parameters followed by the approach.

The 3D geometry of the nozzle vanes and rotor blades are based on the parametrisation of the meridional profile, camberline and blade thickness distribution. Some parameters defining the geometry are also modelled by the meanline methodology, while others have exclusively a 3D effect and cannot be modelled in meanline or other low fidelity approaches. The number of rotor blades and nozzle vanes was made based on the flow field analysis from CFD, ensuring enough guidance to prevent separation while minimising friction losses. The number of nozzle vanes and rotor blades was fixed to 19 and 11 respectively.

2.1 Nozzle parametrisation
The nozzle meridional geometry was set in the radial direction and constant blade height, matching the rotor inlet blade height, b_4, as shown in Figure 1(a). Two lines were set as hub and shroud contours defined by the blade height and nozzle inlet and outlet radius. The nozzle metal angle, α_{nozzle} was used for vane camberline definition, which was set to be the same at nozzle inlet and outlet, $\alpha_{nozzle,2} = \alpha_{nozzle,3}$, see Figure 1(b).

2.2 Radial fibre rotor parametrisation
The rotor meridional curves are quadratic Bezier polynomials defined at the hub and shroud. Figure 1(a) shows the meridional contour definition with the relevant
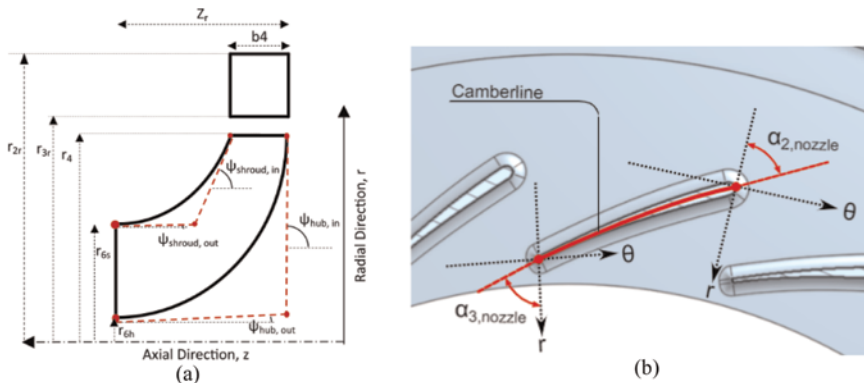
Figure 1. 3D parametrisation: (a) meridional profile and (b) nozzle camberline.

parameters. Their definition consists of the two end points based on inlet and outlet radii and axial position. The third point of the polynomial was set by the cone angles, ψ of the hub and shroud curves at the two ends.

The cone angle is defined as the angle between the hub, shroud or any streamline projected onto the meridional plane, and the z-axis at any point [10], as shown in Eq. (1). In this study the cone angle is a parameter exclusively used in 3D geometry and its effect on the performance of the turbine is not considered in the meanline prediction method. For the same radii and blade height, different meridional profiles can be created by varying the cone angle. The effect of this variation in efficiency can only be measured using CFD.

$$\cos \psi = \frac{dz}{\sqrt{dr^2 + dz^2}} \tag{1}$$

The design of the rotor blades for the ETC baseline was set to radial fibre. Figure 2 shows the section of a radial fibre rotor at different axial locations.

(a) $z = 3\ mm$ (b) $z = 13\ mm$ (c) $z = 23\ mm$ (d) $z = 33\ mm$
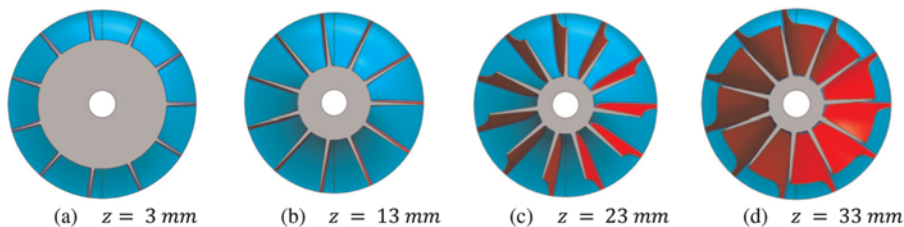
Figure 2. Cross section views of a rotor wheel showing the radial blade fibres.

The rotor camberline is defined by the wrap angle, θ, at a reference radius and the axial position. Since the rotor is radial fibre, a single camberline defines the blade shape entirely. The curve consists of a quadratic Bezier polynomial, the two ends are defined

215

by the leading edge and trailing edge wrap angle, θ, while the inner point is set by tangential angles at both edges, as shown in Figure 3.
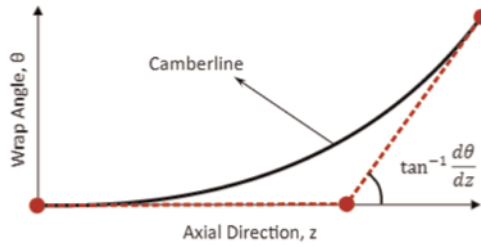
Figure 3. 3D parametrisation of the camberline of the radial fibre rotor.

The relation of the blade angle, β_{blade}, the camber angle, φ and the cone angle, ψ at any point of the blade is shown in Eq. (2) (10). The tangent of the camber angle is defined as the derivative of the camberline, $d\theta/dz$.

$$\tan\beta_{blade} = \tan\varphi \cos\psi = \frac{r}{r_{ref}}\frac{d\theta}{dz}\cos\psi \tag{2}$$

Therefore, the blade angle at the inlet was set to zero, $\beta_{blade,4} = 0°$, since the camber angle was set to zero too, $\varphi_4 = 0°$. The blade angle at the trailing edge, $\beta_{blade,6}$, was determined by the cone and camber angles. In case of a cone angle equal to zero at the trailing edge of the blade, $\varphi_6 = 0°$, the blade angle and the camber angle are assumed equivalent, as indicated in Eq. (3):

$$\tan\beta_{blade,6} = \tan\varphi_6 = \frac{r}{r_{ref}}\frac{d\theta}{dz}_6 \tag{3}$$

The rotor blade was built by taking the radial fibre at each axial location turning them the corresponding wrap angle, θ, indicated by the camberline. Figure 4 shows a different view of the axial sections of the rotor indicating the radial fibre and the wrap angle.

(a) $z = 3\ mm$ (b) $z = 33\ mm$
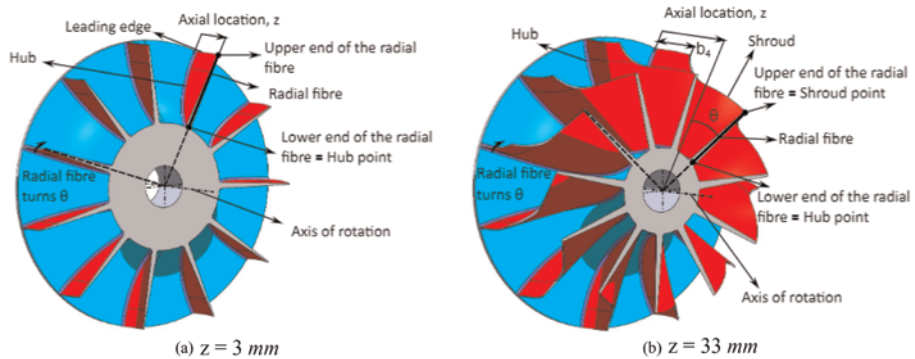
Figure 4. Radial fibre and wrap angle of the rotor at two axial locations.

In the rotor section at low z shown in Figure 4(a), the radial fibre can be identified very clearly as the thick black line. The fibre, which is aligned with the axis of rotation, has an upper end, which lays on the leading edge of the blade and a lower end, which corresponds to the hub point. When the axial location, z, increases beyond the blade height, b_4, the upper end of the radial fibre shown in Figure 4(b) corresponds to the shroud point. The blade of radial fibre designs was built based on the fibres at each axial location, from $z = 0$ to $z = Z_r$. For the parametrisation of non-radial fibre blades, extra parameters have to be introduced to define the blade geometry. Non-radial fibre parametrisation is explained in the next section.

2.3 Non-radial fibre rotor parametrisation

The design flexibility allowed by the non-radial fibre design introduces more variables in the parametrisation of the blade geometry. Figure 5 shows the overlapping sections of a radial rotor the non-radial fibre modification at the same axial location. The non-radial fibre rotor is built from the radial fibre rotor. The parametrisation of the non-radial fibre is also shown in the figure and consisted of 3 steps, highlighted in black, blue and red in Figure 5. Each of the parametrisation steps is described as follows:

1. A radial fibre (black) was built according to the wrap angle, θ, distribution for that axial location, z.
2. The radial fibre was transformed by changing its angular position according to the lean angle, v, with the hub location of the radial fibre as centre of the transformation. This leaned, straight fibre (blue) is non-radially arranged, therefore the lower end of the fibre is not coincident with the axis of rotation of the turbine anymore. When $v = 0°$ the leaned fibre is coincident with the radial fibre.
3. The non-radial fibre (red) was built as a quadratic Bezier polynomial with the upper end and the lower end of the leaned straight fibre as outer nodes. The inner node was set by the tangential angles at the ends of the b-spline, named as γ_{lower} and γ_{upper}. These two angles were defined as the angle between the tangential line (dotted red) and the leaned straight fibre (blue). This means non-radial fibre with tangential angles set to zero, $\gamma_{lower} = \gamma_{upper} = 0°$ corresponds to the leaned straight fibre itself.
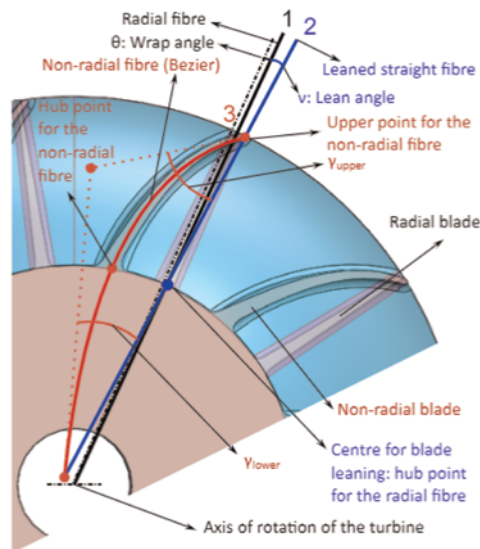

Figure 5. Non-radial fibre blading parametrisation showing the radial fibre (black), the leaned straight fibre (blue) and the non-radial fibre (red) on top of overlapping sections of the radial and non-radial rotors.

The number of parameters required to build the non-radial fibre of the blade located at a certain axial position, z is four: wrap angle, θ, lean angle, ν, and two tangential angles of the non-radial fibre, γ_{lower} and γ_{upper}. Consequently, the distribution of each of the four parameters with the axial location, z, needs to be defined to build the full blade, which constitutes all the fibres from $z = 0$ to $z = Z_r$.

Any distribution could be used to define non-radial blades to different levels of complexity, but, for simplicity the following distributions were applied. The wrap angle distribution with the axial position is defined by the camberline, as shown in Figure 3. A quadratic distribution was specified for ν, where the lean angle at the leading edge was set to zero, $\nu_{LE} = 0$, and ν_{TE} was set as a variable, as shown in Figure 6(a). A linear distribution was specified for γ_{lower}, which both $\gamma_{lower,LE}$ and $\gamma_{lower,TE}$ set as variables, as shown in Figure 6(b). The distribution of, γ_{upper} was parametrised as a horizontal line when $z < b_4$ (effectively keeping the value of γ_{upper} constant at the first part of the rotor) and as a straight line when $> b_4$, shown in Figure 6(c).

Figure 6. Distribution of (a) lean angle, ν, (b) tangential angle of the non-radial fibre at the lower end, γ_{lower} and (c) tangential angle of the non-radial fibre at the upper end with the leaned straight fibre, γ_{upper}, which can be expressed as function of the inlet blade angle, $\beta_{blade,4}$ when $z < b_4$.

The reason of setting a constant $\gamma_{upper,LE}$ is that the upper end of the blade fibre (radial or non-radial) corresponds to the leading edge when the axial location is lower than the blade height, $z < b_4$, as shown above in Figure 4(a). The blade angle at the leading edge, $\beta_{blade,4}$, is the angle between the tangential direction of the blade at the leading edge (upper point of fibre when $z < b_4$) and the radial direction at the same point. In the radial fibre configuration, the blade angle at the leading edge, $\beta_{blade,4}$ is set to zero, the leading edge of the blade is aligned with the radial direction. However, the non-radial fibre is allowed to have a non-zero $\beta_{blade,4}$. At the leading edge of the non-radial fibre, $\nu \approx 0$ when $z < b_4$, as shown in Figure 6(a). This means that the radial fibre and the leaned fibre are almost coincident, therefore the upper point of the non-radial fibre is aligned with the radial direction. As a result, the blade angle at the leading edge, $\beta_{blade,4}$ is equal to γ_{upper} at the leading edge.

As a result of the application of the presented parametrisation method, a non-radial fibre rotor is built. Figure 7 shows the section of the non-radial fibre blades at different

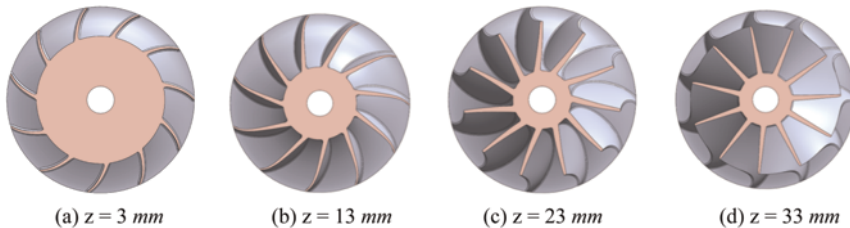(a) $z = 3$ mm   (b) $z = 13$ mm   (c) $z = 23$ mm   (d) $z = 33$ mm

Figure 7. Cross section views of a rotor wheel showing the non-radial blade fibres.

axial planes. When comparing to the radial fibre rotor in Figure 2, these blades are clearly non-radial, particularly at the low z, as shown in Figure 7(a) and (b). Then the blade becomes straight, but leaned, (c), and finally recovers the radial alignment at the trailing edge, shown in (d). This also reflects on the camberlines at different span locations (hub, midspan and shroud), as shown in Figure 8.
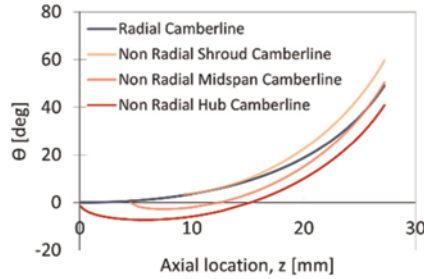

Figure 8. Camberline comparison for the radial and non-radial fibre optimised geometries at different span locations.

2.4 Other 3D parametrisation

Nozzle and rotor blade thicknesses were defined by polynomials at leading edge, middle section and trailing edge thicknesses. The thickness distribution for both the nozzle and the rotor was kept constant in every design. The rotor tip clearance was set to $\varepsilon = 0.5mm$ for all ETC geometries. In this way the 3D geometry of the nozzle vane and rotor blade is completely defined. Flow domains were then created from the geometries and exported to external software for CFD simulation.

The parametrisation explained in this section is used for the generation of the nozzle and rotor full 3D geometries. A detailed evaluation of the performance of the geometries was carried out using numerical simulations. The next section presents the specifics of the CFD evaluation.

2.5 Numerical set up

Single passage nozzle and rotor simulations were set to run the geometry optimisation coupled with the parametric model. The full stage simulation with the volute domain was set up for validation and comparison with experimental results. ANSYS CFX 19.4v was the CFD software used for meshing, solver and data post processing, integrated in CAESES platform [14].

The flow domain for the nozzle and rotor consisted of extended hub and shroud contours (2 times the wheel diameter for the exit pipe) and single blade passage, as shown in Figure 9(a). The curves and contours were imported to TurboGrid to build the structured mesh.

The CFD simulations were set to steady state and the turbulence model used was $k - \varepsilon$. The change of frame of reference between the nozzle-rotor and rotor-outlet interfaces was set to mixing plane, based on the circumferential averaging of the flow field for the single passage simulations and frozen rotor for the full stage simulations. While this coupling approach based on single passage has some limitations regarding local flow interactions, it is representative of a nozzled turbine, which provides a highly uniform flow at the nozzle outlet.
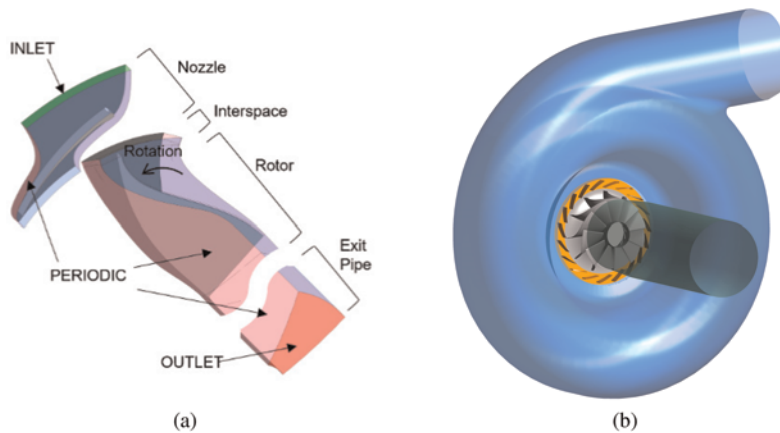
Figure 9. CFD domain: (a) single passage simulations and (b) full stage simulations.

Total temperature and pressure were imposed at the nozzle inlet and static pressure was set at the outlet boundary of the exit pipe, placed at 2-wheel diameter length of the rotor trailing edge to ensure fully developed flow. Periodic interfaces were set at lateral boundaries of the nozzle, rotor and exit pipe domains. Figure 9 shows a picture of the CFD domain highlighting the components and main boundaries.

Static Structural package from ANSYS was used for the structural calculations of the rotor for ETC applications to ensure that non-radial fibre blade was structurally safe. The FEA model consists of the full rotor with some holes on the front face of the rotor that simulate the rigid attachment of the rotor to the shaft. The material chosen was Al7075 T76, also selected for manufacturing. The most extreme conditions that could be achieved experimentally were chosen as boundary conditions in order to ensure the structural integrity of the designs during operation, the rotational speed was set to 50,000 rpm and the body temperature was set to 40 C.

2.6 Platform integration and optimisation algorithm

The parametric optimisation described in this study involves CFD calculations, which implies high computational cost compared to other methods. Therefore, a global optimisation on a response surface was chosen as optimisation strategy for the CFD-parametric model. The operating conditions used for the optimisation are set from the exhaust of the engine ($T_{01} = 743K$, $P_{outlet} = 1.0atm$, $PR = 1.2$, $\dot{m} = 0.13kgs^{-1}$). The system is expected to operate at steady state conditions, therefore a single operating point is considered in during the design process.

A response surface is a statistical model built based on the relationship between the variables and the objective function [15]. In this method, a genetic algorithm is conducted on a response surface that is iteratively build-up. For the initial response surface, the LHS carried out for the meanline calibration can be used. The best designs of each generation are evaluated and added to the response surface. This updates and improves the response surface in each iteration. With this approach, the algorithm aims to reduce the number of computationally costly evaluations.

The total-to-static efficiency was the objective function for:

- Optimisation of the meridional profile, nozzle and rotor blade angles and rotational speed.
- Optimisation of the non-radial fibre blade defined by the non-radial fibre parameters from the best meridional configuration in the optimisation above.

The area at the nozzle outlet throat was set constant. This effectively constrained the mass flow to keep it close to the applications conditions. That means that the blade height, b_4, was an output, as indicated in Eq. (4):

$$b_4 = b_3 = A_{nozzle,throat}/2\,\pi r_3 \cos \alpha_{nozzle,3} \tag{4}$$

The set up for numerical simulations explained above allows for an accurate prediction of the performance of turbine designs and provides detailed information of the flow field. This helps understanding the impact of geometry modifications in the performance of the turbine and the physics behind.

3 RESULTS AND DISCUSSION

This section introduces the sensitivity analysis and optimisations of the radial fibre and non-radial fibre geometries following the methodology outlined above. In addition, the experimental results obtained on the optimised geometries which further validate the CFD analysis of the losses and flow structures.

3.1 Sensitivity analysis and optimised radial fibre geometry

The sensitivity study based on the sampling to create the response surface for optimisation shows interesting results. The range set for each parameter in the sampling was decided based on the physical constraints of the test rig, as well as manufacturing considerations. Figure 10 summarises the effect of each design parameter on efficiency, Figure 10(a) shows a clear correlation of increasing efficiency with increasing r_4. Other parameters determining the geometry of the rotor outlet, r_{6s}/r_4 and r_{6h}/r_4, have only a small effect on efficiency, as shown in Figure 10(b) and (c), leading to slightly higher performance for high values of r_{6s}/r_4.

Figure 10(d) shows the effect of $\alpha_{nozzle,3}$ on efficiency, a better performance results with lower values of $\alpha_{nozzle,3}$. The correlation of $\beta_{blade,6}$ with efficiency is not so strong, as shown in Figure 10(e), since high efficiency designs are achieved with a wide range of blade angles at the trailing edge, from $-70°$ to $-50°$. Finally, Figure 10(f) shows an optimum region of N_{rpm} for high efficiency, around $30{,}000 rpm$.

The global optimisation carried out from the response surface resulted in the geometry summarised in Table 1. This geometry is set as the radial fibre baseline design from which the non-radial fibre blading investigation is carried out.

The maximum equivalent stress registered in the radial fibre design was found to be 89.2 MPa at the blade root close to the trailing edge. This value was well below the yield strength of the material, 480MPa and sets a baseline to compare the stress of the non-radial fibre design.
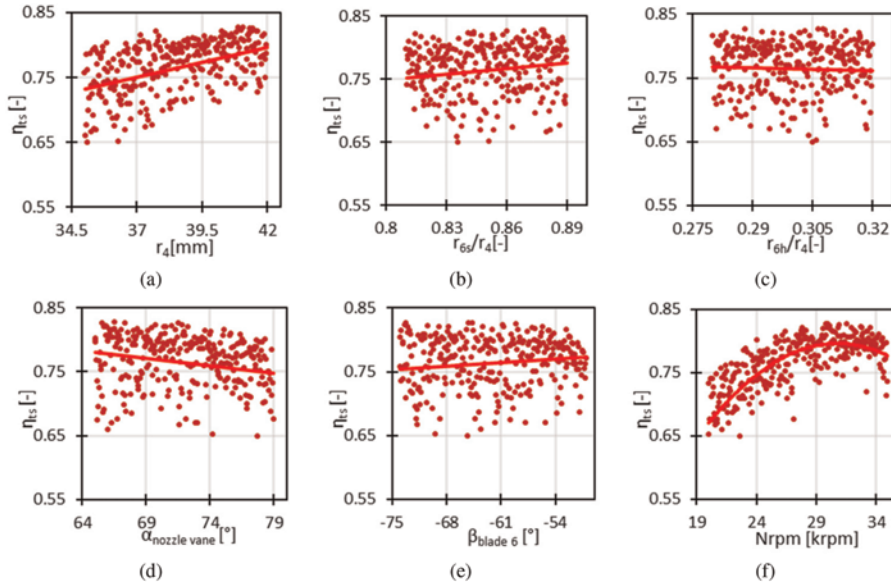
Figure 10. Sensitivity analysis of η_{ts} as function of (a) rotor wheel radius, r_4, (b) rotor shroud radius to wheel radius ratio r_{6s}/r_4, (c) rotor hub radius to wheel radius ratio, r_{6h}/r_4 (d) nozzle vane metal angle nozzle vane, $\alpha_{nozzle,4}$, (e) rotor blade metal angle at trailing edge, $\beta_{blade,6}$ and (f) rotational speed N_{rpm} and fitting curves (solid line) for CFD-based sampling.

Table 1. Radial fibre optimised geometry.

| Parameter | Geometry Variables | | | | | | | | Results |
	r_4 (mm)	r_{6s}/r_4 ($-$)	r_{6h}/r_4 ($-$)	$\alpha_{nozzle,4}$ ($°$)	$\beta_{blade,6}$ ($°$)	N_{rpm} (rpm)	b_4 (mm)	η_{ts} (%)	MFP (kg s^{-1} $K^{0.5}$ Pa^{-1})
Value	40.83	0.88	0.31	65.9	-66.98	30798	7.39	82.9	1.93e-5

3.2 Sensitivity analysis and optimised non-radial fibre geometry

After the radial fibre geometry was optimised, the blade is modified to investigate the effect of non-radial fibre parameters. The radii and rotational speed are kept constant to limit the number of variables for optimisation. A sensitivity study was carried out as part of the surface response for the optimisation of the non-radial fibre parameters, with which the impact of each parameter on efficiency can be assessed.

The results of this analysis are summarised in Figure 11. An optimum $\alpha_{nozzle,3}$ around $68°$ can be guessed from the correlation of the parameter with efficiency, as shown in Figure 11(a). This trend is possibly due to the effect of $\alpha_{nozzle,3}$ on the incidence angle. The incidence angle, i, is the difference between the flow angle into the rotor in the relative frame of reference, $\beta_{flow,4}$ and the blade angle at the leading edge, $\beta_{blade,4}$. Optimum incidence, around -20 to $-40°$ as reported in the literature [10], leads to low leading edge
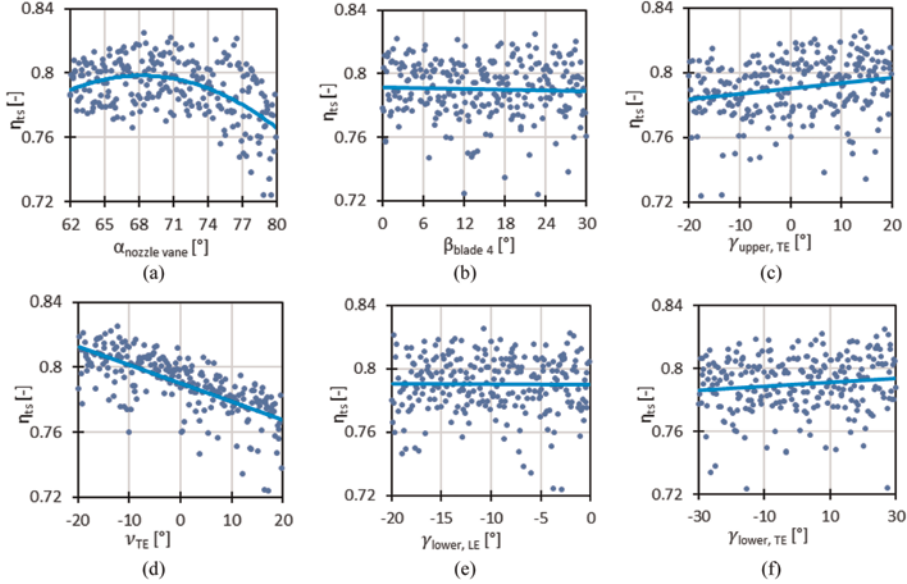
Figure 11. Sensitivity analysis of η_{ts} as function of (a) nozzle vane metal angle nozzle vane, $\alpha_{nozzle,4}$, (b) rotor blade metal angle at leading edge, $\beta_{blade,4}$, (c) tangential angle of the non-radial fibre at the upper end with the leaned straight fibre at trailing edge, $\gamma_{upper,TE}$, (d) lean angle at the trailing edge, ν_{TE} and tangential angle of the non-radial fibre at the lower end with the leaned straight fibre at (e) the leading edge, $\gamma_{lower,LE}$, and (f) the trailing edge, $\gamma_{lower,TE}$ and fitting curves (solid line) for CFD-based sampling.

losses and high efficiency. Assuming there is no deviation and the free vortex effect in the interspace is negligible, $\alpha_{nozzle,3}$ is equal to the flow direction into the rotor in the absolute frame of reference, $\alpha_{flow,4}$. This way, incidence angle can be expressed using velocity triangles [10], as indicated in Eq. (5). A combination of $\alpha_{nozzle,3}$ and $\beta_{blade,4}$ that gives an optimum incidence angle leads to high efficiency designs. Contrarily to $\alpha_{nozzle,3}$, $\beta_{blade,4}$ seems to have small correlation with efficiency (Figure 11(b)).

$$i = \beta_{flow,4} - \beta_{blade,4} = \tan^{-1}\left(\frac{C_4 \sin \alpha_{flow,4} - U_4}{C_4 \cos \alpha_{flow,4}}\right) - \beta_{blade,4} = \tan^{-1}\left(\frac{C_4 \sin \alpha_{nozzle,3} - U_4}{C_4 \cos \alpha_{nozzle,3}}\right) \quad (5)$$

The tangential angle at the upper end of the non-radial fibre with the leaned straight fibre at the trailing edge $\gamma_{upper,\ TE}$ and the lean angle at the trailing edge ν_{TE}, have a strong correlation with efficiency as shown in Figure 11(c) and (d), respectively. However, the effect is quite the opposite. Low, negative ν_{TE} and high, positive $\gamma_{upper,\ TE}$ lead to high performance. Minimum impact of the γ_{lower} on efficiency was found, as the fitting curves are flat for the leading edge and trailing edge shown in Figure 11(e) and (f).

The results of the sensitivity analysis were used for the optimisation, Table 2 summarises the values of the non-radial fibre parameters and the resultant efficiency and *MFP* of the optimised geometry. The radii and rotational speed were the same as the radial fibre optimised geometry presented in the previous section and summarised in Table 1. The achieved η_{ts} of the non-radial fibre design was +0.3 pp higher than the

Table 2. Non-radial fibre optimised geometry.

Parameter	Non-radial Fibre Geometry Variables						Results	
	$\alpha_{nozzle,3}$ (°)	$\beta_{blade,4}$ (°)	$\gamma_{upper,TE}$ (°)	ν_{TE} (°)	$\gamma_{lower,LE}$ (°)	$\gamma_{lower,TE}$ (°)	η_{ts} (%)	MFP (kg s^{-1} K$^{0.5}$ Pa^{-1})
Value	70.23	24.02	0.29	−9.66	14.05	19.47	83.2	2.03e-5

radial fibre design performance. The MFP also increased by 5.18%. In order to understand and validate the small performance improvement of the non-radial fibre blading design compared to the radial fibre baseline, experimental tests were carried out, as outlined in the next section.

The non-radial fibre design showed a maximum equivalent stress of 139.9 MPa, an increase of 44% compared to the radial fibre design. However, the value remained also below the yield strength of the material (480 MPa), leading to a safety factor of 3.4, concluding the non-radial fibre design is structurally safe like the radial fibre design at these operating conditions.

3.3 Experimental results

The experimental data of this study was obtained with the turbine test facility at Imperial College London, Figure 12(a). A detailed description of this experimental facility can be found in the literature [16].

Total-to-static efficiency is calculated as the ratio between the actual power and the isentropic power, as shown in Eq. (6). The actual power of the turbine is derived from the torque, τ, and rotational speed in revolutions per second, n_s. The isentropic power is calculated from the mass flow, $\dot{m}$, inlet temperature, T_{01}, pressure ratio, PR and specific heat at constant pressure, C_p:

$$\eta_{ts} = \frac{\dot{W}_{act}}{\dot{W}_{isen}} = \frac{\tau n_s}{\dot{m} \quad C_p T_{01} \left(1 - PR^{\frac{n-1}{n}}\right)} \tag{6}$$

In order to limit the manufacturing cost a new stator assembly was designed consisting of a single volute and two nozzle inserts, one for the radial fibre rotor and another one for the non-radial fibre rotor, as shown in Figure 12(b). The volute, which has no area
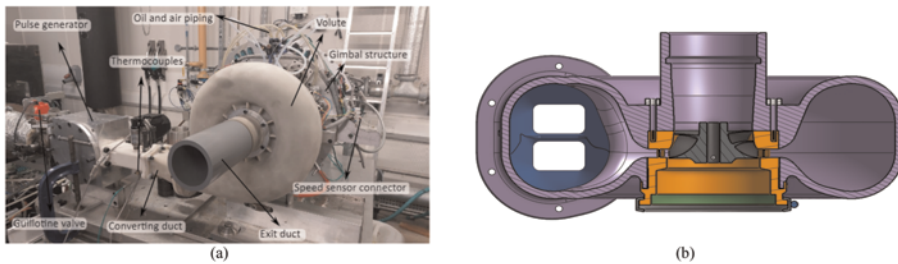
Figure 12. Experimental set up (a) Turbine rig and (b) Section view of the full assembly consisting of common volute (purple), nozzle insert for radial and non-radial fibre designs (orange) and radial and non-radial fibre rotor wheels (grey).

reduction, distributes the flow around the nozzle inlet and was printed using laser sintering in glass fibre nylon polyamide 12. The nozzle inserts are secured to the volute by 6 bolts and were metal printed in aluminium.

The rotor wheels of the radial and non-radial fibre designs were manufactured by CNC machining of Al7075, an aluminium alloy with zinc. Figure 13(a) and (c) show front and top views of the radial fibre rotor, while (b) and (d) show the non-radial fibre rotor after manufacturing.
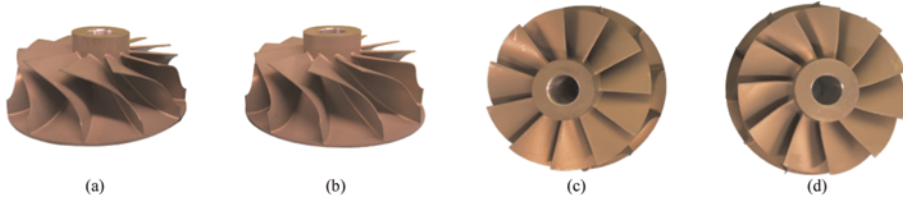

Figure 13. Manufactured rotor wheels: (a) front view and (c) top view of the radial fibre rotor, (b) front view and (d) top view of the non-radial fibre rotor.

The experimental tests of both designs were carried out at steady state conditions at three different rotational speeds, 20,000, 28,000 and 38,000 *rpm* and at a range of static pressure ratios, *PR*, varying from 1.06 to 2.4. Figure 14 shows the experimental results of the two designs compared to the CFD results for one speedline, 28,000 *rpm*. Good agreement was found in efficiency and mass flow parameter between CFD and experiments (around 2.5 - 2.8 pp - percentage points - average deviation). At low velocity ratios, 0.3 to 0.65 the non-radial fibre design shows a consistent improvement in efficiency of 3.3 pp compared to the radial fibre design. Around the peak efficiency point, velocity ratio around 0.7, the non-radial fibre design show 2.0 pp higher efficiency than the radial fibre design in experiments. CFD results show smaller difference in performance between the two designs at peak efficiency, only 0.9 pp. However, at high velocity ratio, above 0.7, the radial fibre design performs better than the non-radial fibre design. A greater performance improvement between non-radial fibre rotors and equivalent radial fibre rotors at low velocity ratios compared to design point and high velocity ratios has also been observed by previous studies [11,17]. This effect can be explained by the lower incidence angle of the non-radial fibre design, which is closer to the optimum incidence angle at low velocity ratios than the incidence of the radial fibre design. However, at high velocity ratios the incidence angle of the non-radial fibre design is too low, penalising the total-to-static efficiency more than in the radial fibre design.
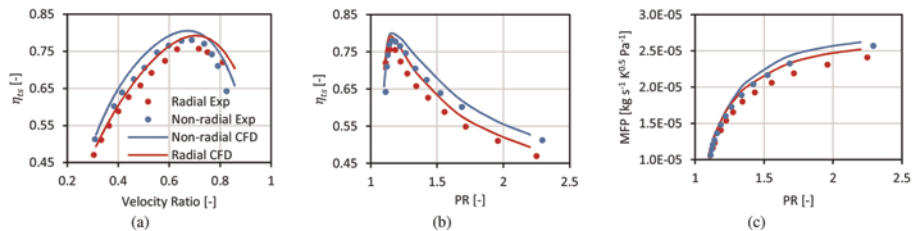
Figure 14. Experimental (circle marker) and CFD (solid line) performance results for the radial fibre design (red) and non-radial fibre design (blue) for the design speedline, 28,000 *rpm*: (a) η_{ts} as function of the velocity ratio, (b) η_{ts} as function of the *PR* and (c) *MFP* as function of the *PR*.

Figure 14(c) also shows an increase in the swallowing of the non-radial fibre design, especially at high pressure ratios (equivalent to low velocity ratio) to a maximum of 3.9% increase in MFP at the highest PR.

These experimental results also validate the CFD simulations used for performance prediction in the parametric model calculations. Although the CFD results shown in Figure 14 take into account the full assembly of the turbine (volute, nozzle, rotor and outlet pipe), the performance and trend of the single passage simulations for the radial and non-radial fibre designs are in agreement with the full stage simulations and the experiments. This can be seen in Table 3, which compares the efficiency at design point predicted by different CFD set up and the experiments. Discrepancy between experimental and CFD simulations mainly come at the fact that back disk losses and leakage are not accounted for in the numerical simulations. In addition, heat losses, although small, have an impact in experimental efficiency and are not calculated in CFD. Average uncertainty of the experimental results was found to be 1.3pp for the efficiency and 1.7% for the mass flow measurements.

Table 3. Predicted efficiency by different CFD set up and experiments for the two optimised geometries, the radial fibre and the non-radial fibre designs.

Design/ Predicted η_{ts}	Single passage	Full stage	Full stage with volute	Experiments
Radial fibre [%]	82.9	82.6	79.2	76.1
Non-radial fibre [%]	83.2	83.1	80.2	78.1

3.4 Losses and CFD analysis

In order to further analyse and explain the difference in performance between the two designs, the entropy generation across the different components was calculated, as an indication of energy losses [18]. Furthermore, the rotor domain was divided in several regions and the entropy generation across each of them was assigned to a different loss mechanism, the regions are highlighted in Figure 15(a). The loss breakdown, as entropy generated per unit mass flow, across the rotor and the other components is shown in Figure 15(b).
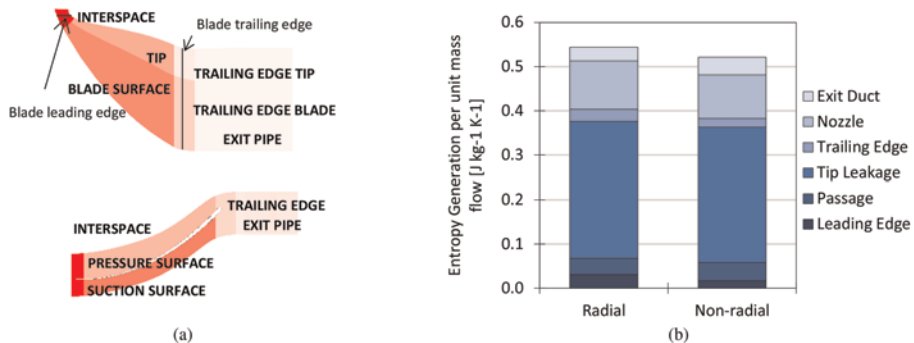
Figure 15. Entropy generation for loss breakdown: (a) rotor domain division (b) results for the radial fibre and non-radial fibre designs.

Overall, the entropy generation across the whole turbine was lower for the non-radial fibre design, Figure 15(b), in agreement with the higher efficiency found. When comparing the non-radial fibre design to the radial fibre design, exit duct and passage losses increased 22% and 11%. Tip leakage losses remain the same in both designs. Nozzle losses decreased only by 11% in the non-radial fibre design, but trailing edge and leading edge losses were 39% and 80% lower in the non-radial fibre design.

The decrease in the leading edge losses is due to a better alignment of the flow with the blade leading edge. Figure 16 provides more understanding in this matter showing the incidence angle at the rotor inlet. As discussed in Eq. (5), incidence depends on the relative angle of the flow when approaching the leading edge and the blade angle at the leading edge. Figure 16(b) shows a lower (more negative) incidence angle for the non-radial fibre design compared to the radial fibre design shown in Figure 16(a). The averaged incidence for the radial fibre design was $i_{radialf} = -20.45°$ and the non-radial fibre design had an average incidence of $i_{non-radialf} = -46.73°$. Lower incidence reduces the entropy generation at the rotor leading edge and reduce the flow separation in this region.
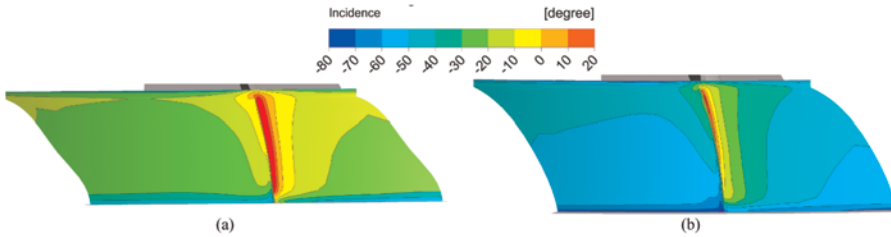
Figure 16. Incidence angle at the leading edge of the (a) radial fibre and (b) non-radial fibre designs.

Entropy generation can also be linked to total-to-total efficiency across the rotor, $\eta_{tt-ROTOR}$, according to Eq.(7), where the total-to-total efficiency is a function of the total-to-total pressure ratio across the rotor, P_{04}/P_{06}, and the specific entropy change across the turbine, Δs, which corresponds to the entropy generation per unit mass for adiabatic processes discussed in Figure 15(b). Comparing the total-to-total efficiency of the two designs, the non-radial fibre rotor achieved a $\eta_{tt-ROTOR} = 90.1\%$, 0.3pp higher than the radial fibre rotor. Since the pressure ratio across the rotor remained constant for the two geometries, the reduction in entropy generation was the only factor explaining the increase in $\eta_{tt-ROTOR}$.

$$\eta_{tt-ROTOR} = \frac{\dot{W}_{act}}{\dot{W}_{iso,total-ROTOR}} = 1 - \frac{\Delta h_{ROTOR}}{c_p T_{04}\left(1 - \frac{P_{04}}{P_{06}}^{-\frac{n-1}{n}}\right)} = \frac{\frac{P_{04}}{P_{06}}^{\frac{n-1}{n}} - e^{\frac{\Delta s_{ROTOR}}{R}\frac{n-1}{n}}}{\frac{P_{04}}{P_{06}}^{\frac{n-1}{n}} - 1} \qquad (7)$$

Reduction in entropy generation implies reduction in losses and therefore, higher in actual power recovered in the rotor. The increase in actual power in the non-radial fibre design can also be observed when comparing the blade loading as shown in Figure 17. The blade loading of the non-radial fibre improves at the midspan and tip, as indicated by the arrows in Figure 17(b) and (c). The blade loading increase occurs at the leading edge and at the middle of the passage. Higher loading means higher power recovered which increases the efficiency of the turbine.
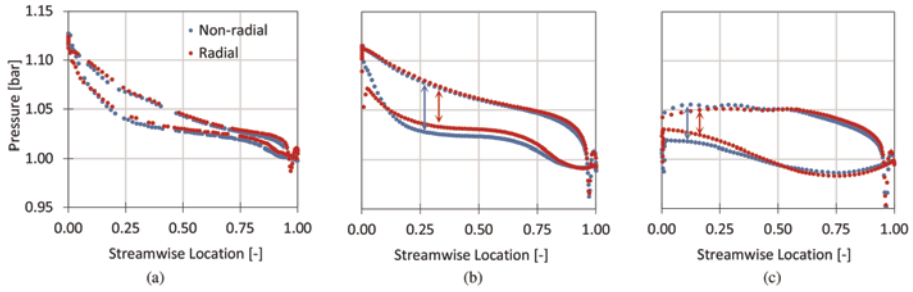
Figure 17. Blade loading of the radial and non-radial fibre design along the streamwise direction at different span location: (a) hub, (b) midspan and (c) blade tip.

4   CONCLUSIONS

A systematic study of the influence of traditional design parameters, but also 3D blading parameters on efficiency of radial turbomachinery for electric turbocompounding (ETC) applications was carried out in this paper. A 3D parametric model coupled with CFD was developed to evaluate the effect of each parameter by performing a sensitivity study, but also to optimise a radial fibre and a non-radial fibre designs.

The two optimised geometries were tested experimentally showing increased efficiency of the non-radial fibre geometry compared to the radial fibre baseline geometry, of 2.0pp at the design operating point. The experimental results also validated the CFD simulations which explained the improved performance. Non-radial fibre blading made the second design more efficient than the radial fibre baseline by reducing the entropy generation, especially at the leading edge and improving the blade loading.

Although more exhaustive research is needed to add more flexibility to the 3D blade parametrisation, including mixed flow blade design and using the incidence angle as design parameter, this research shows that non-radial fibre blades can achieve higher performance than the radial fibre baseline.

NOMENCLATURE

b	Blade height (mm)	**Greek Letters**		
C	Absolute velocity (m s^{-1})	α_{nozzle}	Nozzle vane angle (°)
C_p	Heat capacity at constant pressure (J kg^{-1} K^{-1})	β_{blade}	Rotor blade angle (°)
CFD	Computational fluid dynamics	γ_{upper}	Upper angle for non-radial blading definition (°)
ETC	Electric turbocompounding	γ_{lower}	Lower angle for non-radial blading definition (°)
i	Incidence angle (°)	φ	Camber angle (°)
$\dot{m}$	Mass flow rate (kg s^{-1})	ψ	Cone angle (°)

(Continued)

(*Continued*)

MFP	Mass Flow Parameter	θ	Circumferential angle (°)
n	Adiabatic coefficient (-)	ε	Tip clearance (mm)
n_s	Rotational speed (rps)	τ	Torque (N)
N_{rpm}	Rotational speed (rpm)	ν	Lean angle (°)
P	Pressure (Pa)	**Subscripts**	
PR	Pressure ratio (-)	1	Volute inlet
r	Radius (mm)	2	Nozzle inlet
T	Temperature (K)	3	Nozzle outlet
$\dot{W}$	Power (W)	4	Rotor inlet
WHR	Waste heat recovery	6	Rotor outlet
x_{upper}	Non-radial fibre upper point x-coordinate	act	Actual
y_{upper}	Non-radial fibre upper point y-coordinate	isen	Isentropic
z	Axial position (mm)	LE	Leading edge
Z_r	Rotor length (mm)	TE	Trailing edge

ACKNOWLEDGEMENTS

REFERENCES

[1] Hung TC, Shai TY, Wang SK. A Review of Organic Rankine Cycles (ORCs) for the Recovery of Low-grade Waste Heat. *Energy*. 1997 Jul 1;22(7):661–7.

[2] Nguyen T van, Fülöp TG, Breuhaus P, Elmegaard B. Life Performance of Oil and Gas Platforms: Site Integration and Thermodynamic Evaluation. *Energy*. 2014 Aug 14;73:282–301.

[3] Barrera JE, Bazzo E, Kami E. Exergy Analysis and Energy Improvement of a Brazilian Floating Oil Platform Using Organic Rankine Cycles. *Energy*. 2015 Aug 1;88:67–79.

[4] Bhargava RK, Bianchi M, Branchini L, de Pascale A, Orlandini V. Organic Rankine Cycle System for Effective Energy Recovery in Offshore Applications: A Parametric Investigation With Different Power Rating Gas Turbines. In: Volume 3: Coal, Biomass and Alternative Fuels; Cycle Innovations; Electric Power; Industrial and Cogeneration. *American Society of Mechanical Engineers*; 2015.

[5] Gotelip Correa Veloso T, Sotomonte CAR, Coronado CJR, Nascimento MAR. Multi-objective Optimization and Exergetic Analysis of a Low-grade Waste Heat Recovery ORC Application on a Brazilian FPSO. *Energy Convers Manag*. 2018 Oct 15;174:537–51.

[6] Pierobon L, Benato A, Scolari E, Haglind F, Stoppato A. Waste Heat Recovery Technologies for Offshore Platforms. *Appl Energy*. 2014 Dec 31;136:228–41.

[7] Pierobon L, Nguyen T van, Larsen U, Haglind F, Elmegaard B. Multi-objective Optimization of ORGANIC RANKINE CYCLES for Waste Heat Recovery: Application in an Offshore Platform. *Energy*. 2013 Sep 1;58:538–49.

[8] Legros A, Guillaume L, Diny M, Zaïdi H, Lemort V. Comparison and Impact of Waste Heat Recovery Technologies on Passenger Car Fuel Consumption in a Normalized Driving Cycle. *Energies (Basel)*. 2014 Aug 14;7(8):5273–90.

[9] Aman Mohd, Ihsan Bin. *Design and Development of a High Performance LPT for Electric Turbocompounding Energy Recovery Unit in a Heavily Downsized Engine [PhD Thesis]*. [London]: Imperial College London; 2012.

[10] Arnold Whitfield, Nicholas C Baines. *Design of radial turbomachines*. New York, NY: John Wiley and Sons Inc.; 1990.

[11] Barr L, Spence SWT, Eynon P. Improved Performance of a Radial Turbine Through the Implementation of Back Swept Blading. In: Volume 6: Turbomachinery, Parts A, B, and C. *ASMEDC*; 2008. p. 1459–68.

[12] Walkingshaw J, Spence S, Ehrhard J, Thornhill D. An Investigation Into Improving Off-Design Performance in a Turbocharger Turbine Utilizing Non-Radial Blading. In: Volume 7: Turbomachinery, Parts A, B, and C. *ASMEDC*; 2011. p. 2023–32.

[13] Mulloy JM, Weber HG. A Radial Inflow Turbine Impeller for Improved Off-Design Performance. In: Volume 1: Turbomachinery. *American Society of Mechanical Engineers*; 1982.

[14] *Computer Aided Engineering System Empowering Simulation by Friendship Systems*. Caeses v.4.4.2. Germany: https://www.caeses.com;

[15] Box GEP. The Exploration and Exploitation of Response Surfaces: Some General Considerations and Examples. Biometrics. 1954 Mar;10(1):16.

[16] Shinri Szymko. *The Development of an Eddy Current Dynanometer for Evaluation of Steady and Pulsating Turbocharger Turbine Performance [PhD Thesis]*. [London]: Imperial College London; 2016.

[17] Alvarez-Regueiro E, Barrera-Medrano E, Martinez-Botas R, Rajoo S. Numerical Analysis of Non-Radial Blading in a Low Speed and Low Pressure Turbine for Electric Turbocompounding Applications. In: Volume 2D: Turbomachinery — Multidisciplinary Design Approaches, Optimization, and Uncertainty Quantification; Radial Turbomachinery Aerodynamics; Unsteady Flows in Turbomachinery. *American Society of Mechanical Engineers*; 2021.

[18] Herwig H, Kock F. Direct and Indirect Methods of Calculating Entropy Generation Rates in Turbulent Convective Heat Transfer Problems. *Heat and Mass Transfer*. 2006 Nov 6;43(3):207–15.

Comparative analysis of the inverted Joule cycle, closed Joule cycle, and various approximate Ericsson cycles for waste heat recovery from exhaust gases with the working fluid as a variable

K.Y. Kenkoh[1]*, S.R. Gubba[2], J.W.G. Turner[1]

[1]Mechanical Engineering, KAUST Clean Combustion Research Center, King Abdullah University of Science and Technology, Saudi Arabia
[2]KAUST Clean Combustion Research Center, King Abdullah University of Science and Technology, Saudi Arabia

ABSTRACT

Decarbonization for a net-zero future has gained momentum in recent years due to the impact of greenhouse gases on our environment. Various governments and industries have announced their strategies to achieve low-carbon or net-zero carbon strategies, which will require the use of renewable energy resources and alternative fuels. Achieving a net-zero carbon future may take anywhere between 20–50 years. In the interim, it is apparent that there is a need to make the current energy-producing devices such as internal combustion engines and gas turbines more efficient, helping to bridge the gap. One such concept is waste heat recovery (WHR) from hot exhaust gases.

In this paper, Aspen Plus software is used to model and analyze WHR systems, based on different variations of the Joule Cycle: Inverted Joule Cycle, Closed Joule Cycle (CJC), CJC with heat recuperation, two-stage Ericsson Cycle (approximated as a CJC with two stages of compression with intercooling between the compression stages, two stages of expansion with reheating between the expansion stages, and heat recuperation), three-stage Ericsson Cycle (approximated as a CJC with three stages of compression with intercooling between the compression stages, three stages of expansion with reheating between the expansion stages, and heat recuperation), CJC with two stages of expansion, reheating and heat recuperation, and CJC with two stages of compression, intercooling and heat recuperation. In multistage compression, the temperature of the inlet stream into all the compressors was kept constant using intercoolers, and equally, in multistage expansion, the temperature of the inlet stream into all the turbines was also kept constant through reheaters. Air, argon, and carbon dioxide are separately investigated as working fluids. Sensitivity studies of the exhaust gas temperature and the system pressure ratio and their impact on the cycle thermodynamic efficiency and specific net work output were carried out for the considered working fluids and a comparative analysis of the different system models was also performed. The results show that for an exhaust gas temperature of 600°C, theoretical cycle thermodynamic efficiencies up to about 40%, and specific net work output values up to about 160 kW/kg of exhaust gas can be obtained, with the two-stage Ericsson cycle and the CJC with heat recuperation and intercooling striking a pragmatic balance between

---
*Corresponding Author: kesty.kenkoh@kaust.edu.sa

system efficiency and system complexity. Also, the results show that argon is the most effective working fluid at low-pressure ratios while carbon dioxide is most suitable for high-pressure ratio applications.

1   INTRODUCTION

Increasing fuel prices, energy crises, and global warming are some key challenges the current generation faces. Waste heat recovery (WHR) is a step toward resolving these issues by making sure less fuel is burned to produce the same amount of work, generating less CO_2 in the process.

Waste heat is rejected in a thermodynamic process and is usually rejected into the surrounding. From the Kelvin-Planck statement of the second law of thermodynamics, no heat engine can have a thermal efficiency of 100%, so some of the heat from the source must always be thrown away into the surrounding [1]. By the year 2030, 49.3–51.5% of the energy consumed globally is expected to end up as waste heat, with the transport sector accounting for 43% of the recoverable waste heat [2]. Therefore, recovering waste heat from existing internal combustion engines such as marine engines, and heavy-duty truck engines is a need of the hour.

The temperature of the exhaust gas is an important criterion in choosing the appropriate WHR system [4] and WHR cycles are classified as high-temperature exhaust gas ($>$ 400°C), medium-temperature exhaust gas (100–400°C), and low-temperature WHR ($<$ 100°C) [4]. The work presented in this investigation mainly focuses on high- and medium-temperature WHR systems based on variations of the Joule and the Ericsson cycles.

The Joule cycle was first fully described by the English physicist James Prescott Joule (together with William Thomson, later Lord Kelvin) in 1852 [5]. It is composed of four internally-reversible processes, isentropic compression, isobaric heat addition, isentropic expansion, and isobaric heat rejection. It is sometimes termed the Brayton cycle because American engineer George Brayton developed the first practical engine to successfully operate on it, patenting his "Ready Motor" in 1872: however, Brayton received his patent 20 years after Joule's original full analysis. Both Joule and Brayton envisaged or used positive-displacement piston machinery to achieve the compression and expansion in their engines; today the cycle is more usually associated with continuous-flow devices (these not being available at the time of the original cycle description by Joule). It is interesting to note that while one can make a case for naming the cycle after either man, it was initially imagined and patented by another Englishman, John Barber, in 1791, although he could not perform an accurate analysis of the cycle as Joule could do 60 years later. The Joule cycle is normally considered as an open cycle, breathing from and rejecting heat to the atmosphere, but a closed version of the cycle can be achieved by replacing the combustor with a high-temperature heat exchanger for heat addition and recirculating the stream after expansion through a low-temperature heat exchanger for constant pressure heat rejection; as such, combustion takes place externally.

The Ericsson cycle was proposed by Swedish American engineer John Ericsson in 1853. It is also made up of four processes: isothermal compression, constant pressure heat addition, isothermal expansion, and constant pressure heat rejection. In this paper, approximate Ericsson cycles are designed by modifying the CJC. Multi-stage compression and expansion are used while cooling the working fluid between stages of compression to a temperature equivalent to that before compression and reheating the working fluid between expansion stages to its initial temperature before expansion. Theoretically, an Ericsson cycle can be obtained from a Joule cycle by introducing an infinite number of stages of compression with intercooling between each of these

stages and an infinite number of expansion stages with reheating taking place between each of these stages. This is illustrated in Figure 1.
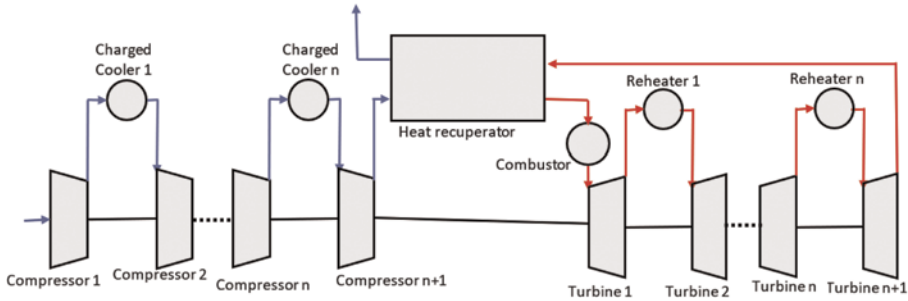

Figure 1. Ericsson cycle with n + 1 compressors, n + 1 turbines, n intercoolers, and n reheaters.

The working fluid in the cycle illustrated in Figure 1, behaves like a perfect gas. Compression and expansion follow the isentropic process, and combustors, charge coolers, and heat exchangers follow the isobaric process. Intercooling and reheating are carried out to the initial temperature before compression and expansion respectively. If we assume that the pressure ratios between adjacent stages of compression and expansion are the same and denoted r, the working fluid has an adiabatic index of γ, the effectiveness of the heat exchanger is ε, and the number of extra stages of compression is equal to the number of extra stages of expansion, it can be shown that the efficiency of the cycle η is:

$$\eta = \frac{(n+1)t\left(1 - r^{-\frac{\gamma-1}{(n+1)\gamma}}\right) - (n+1)\left(r^{\frac{\gamma-1}{(n+1)\gamma}} - 1\right)}{t\left(1 - \varepsilon r^{-\frac{\gamma-1}{(n+1)\gamma}}\right) + (\varepsilon - 1)r^{\frac{\gamma-1}{(n+1)\gamma}} + tn\left(1 - r^{-\frac{\gamma-1}{(n+1)\gamma}}\right)}$$

$$\text{where, } t = \frac{Temperature\ of\ stream\ after\ the\ combustor}{Temperature\ of\ the\ stream\ before\ the\ combustor}$$

$$\lim_{n \to \infty}\left(\frac{(n+1)t\left(1 - r^{-\frac{\gamma-1}{(n+1)\gamma}}\right) - (n+1)\left(r^{\frac{\gamma-1}{(n+1)\gamma}} - 1\right)}{t\left(1 - \varepsilon r^{-\frac{\gamma-1}{(n+1)\gamma}}\right) + (\varepsilon - 1)r^{\frac{\gamma-1}{(n+1)\gamma}} + tn\left(1 - r^{-\frac{\gamma-1}{(n+1)\gamma}}\right)}\right) = 1 - \frac{1}{t}$$

This is equivalent to the Ericsson cycle efficiency, and it can be influenced by varying the number of compression and expansion stages and the working fluid. In the current investigation, argon (a monoatomic gas), air (78% of its composition being nitrogen and 21% oxygen, both diatomic gases) and carbon dioxide (a triatomic gas) are considered to study the effect on the system efficiency and specific work output.

Galindo et al. [6] explored the possibility of WHR from the exhaust gas of a family car with an IC engine following a Joule cycle composed mainly of a heat exchanger and an alternating piston serving as a compressor and an expander. The exhaust gas flow rate, in this case, was low with varying temperatures. Therefore, the WHR system had to be sufficiently small and lightweight. They reported that the system mainly experienced

losses due to pressure pumping, friction, and heat transfer, which together accounted for almost all of the power that could be generated from the cycle. However, positive results would have been obtained if there existed a hotter and more stable flow along with more mechanically efficient equipment and more effective heat exchangers.

Sharma et al. [7] studied a supercritical CO_2 regenerative recompression Joule cycle coupled with a marine gas turbine for shipboard WHR. They reported that the overall system efficiency increased by 10% and the power of the system increased by 25%. They also found that the cycle was most sensitive to the pressure ratio such that even a small departure from the optimum pressure ratio could cause a significant reduction in cycle performance.

Chen et al. [8] analyzed the performance of a regenerative Joule cycle with internal irreversibility and concluded that the power output of the system increased with increasing regenerator effectiveness for a given pressure ratio.

Liu et al. [9] optimized the parameters of a closed Joule cycle to minimize the mass of space power systems using the non-dominated Sorting Genetic Algorithm (NSGA-II) method. They found out that a 4% change in the turbine inlet temperature from 1150K led to a 6% change in the mass of the system. Also, increasing the regenerator effectiveness led to an increase in the cycle efficiency, but led to a drastic increase in the mass of the system. The optimal range of cycle efficiency was between 16% to 28% and the optimal pressure ratio ranged from 1.9 to 3.

Finally, Turner and Togawa [10] investigated a complex open Joule cycle and then proposed closing it in order to change the working fluid to argon. Their analysis, while simple, suggested that significant gains could be made when the working fluid is changed, and was the original motivation behind the work described here.

The above researchers have analyzed Closed Joule Cycle WHR systems with a single working fluid. In this paper, various modifications have been made to the cycles to understand their effectiveness in recovering waste heat and specific work output. Simulations have been carried out at each stage with working fluids considered as a variable, with the objective to obtain the most practical and efficient WHR cycle for marine and heavy truck engine applications.

2   MODELLING OF WHR CYCLES

The WHR cycles considered particularly suitable for marine and heavy-truck engine applications are explored and modelled using MS-Excel and Aspen Plus. The cycles explored are briefly described below.

2.1   WHR cycles explored
2.1.1 *Inverted Joule cycle (IJC)*
This cycle has been proposed for use in waste heat recovery by other authors [16]. The exhaust gas is passed directly through the turbine where it expands to sub-atmospheric temperatures, with the turbine generating useful work. The stream is then cooled in a heat exchanger and compressed in a compressor to raise its pressure allowing it to be released into the ambient. This method however produces a remarkable back pressure and damages the blades of the turbine as the exhaust gas holds by-products of combustion. Also, the low pressure in the cycle means that the components of the WHR system need to be significantly large unlike in closed Joule cycles where high pressures can be attained, thus allowing for smaller components. In closed Joule cycles, different working fluids with better heat exchanger properties can also be tested. The major disadvantage of the closed cycles is the need to use extra heat exchangers which increase the size of the WHR system.

2.1.2 *Simple closed Joule cycle (CJC)*

The simple closed Joule cycle is a regular Joule cycle in which the working fluid is recycled. Heating is carried out in a heat exchanger, where the working fluid is heated by the hot exhaust gas. The expanded working fluid is cooled before it enters the compressor to reduce compression work. Recycling allows for the usage of other working fluids which are not readily available like argon and carbon dioxide.

2.1.3 *Closed Joule cycle with heat recuperation*

As the name of the cycle suggests, this cycle is an extension of the CJC. The expanded working fluid from the turbine is used to preheat the compressed stream in a heat exchanger before it is heated by the exhaust gas. This aims at recovering some of the heat energy not used to supply useful work in the turbine.

2.1.4 *Two-stage Ericsson cycle*

As shown in Figure 2, a two-stage Ericsson cycle is a CJC with heat recuperation, an extra stage of compression and an extra stage of expansion. The working fluid is cooled after the first stage of compression to reduce the compression work of the second compressor. Reheating of the working fluid is carried out after the expansion in the first turbine in a bid to improve turbine performance.
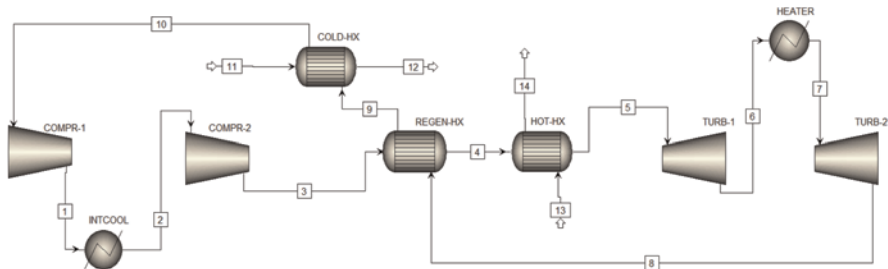
Figure 2. Two-stage ericsson cycle.

The two-stage Ericsson cycle could be oversized for certain small-scale applications, also, reheating is either done using a portion of the exhaust gas stream or by an external heat source which significantly complicates the cycle, hence the motivation to study a modification of this cycle: the CJC with intercooling, heat recuperation, and two stages of compression.

2.1.5 *Three-stage Ericsson cycle*

The cycle is approximated as a CJC with three stages of compression with intercooling between stages, three stages of expansion with reheating between stages, and heat recuperation. This WHR cycle is a modification of the two-stage Ericsson cycle and is expected to have higher thermodynamic efficiency.

2.2 **Modelling of WHR cycles**

2.2.1 *MS-Excel*

Initial modelling was carried out using MS-Excel to understand the cycles and supply data to verify and validate the basic models designed in Aspen Plus. A basic Joule cycle was chosen for comparisons with cycles designed in Aspen Plus as more complicated cycles require a more vigorous variation of parameters and more complex formulae to

characterize state properties in Excel. To further simplify the models, the working fluid was assumed to be a perfect gas.

2.2.2 *Aspen Plus*

Aspen Plus is one of the leading process simulators in chemical engineering. A few of the developed models were calibrated against the MS-Excel model and data presented in the literature [16] before proceeding to more complex cycles.

Aspen Plus V12 was used to simulate all the thermodynamic cycles presented in the subsequent sections. Calculations were performed using the Peng-Robinson equation of state. The working fluids considered in the closed cycle were argon, air, and carbon dioxide. The coolant in the cooling heat exchanger was water and the composition of the exhaust gas was obtained from Pacific Green Technologies as detailed in the second half of Table 1.

Table 1. Details of parameters and exhaust gas composition considered in this analysis.

Parameter	Value
Exhaust gas temperature	600°C
Exhaust gas pressure	1.1 bar
Exhaust gas mass flow rate	5 kg/s
Working fluid temperature after the cold heat exchanger	20°C
Working fluid pressure in closed cycles after the cold heat exchanger	1 bar
Working fluid pressure in closed cycles after the last turbine	1 bar
Working fluid pressure in the IJC after the compressor	1 bar
Working fluid mass flow rate	5 kg/s
Turbine isentropic efficiency	0.9
Compressor isentropic efficiency	0.85
Heat exchanger effectiveness (for all heat exchangers)	0.9
Exhaust gas composition (dry basis)	
O_2 in exhaust	13.84%
CO_2 in exhaust	5.54%
N_2 in exhaust	80.31%
SO_2 in exhaust	0.072%
NO in exhaust	0.237%
HCl in exhaust	0.0004%

3   RESULTS AND DISCUSSION

Models developed using Excel and Aspen Plus have been tested and compared to verify the accuracy of the mathematical equations shown in the earlier sections. Data from the

current simulations have been validated against the literature data found in reference [16]. For brevity, these results are shown in Appendix A.

The first set of simulations was aimed at obtaining a better understanding of the closed cycles by fixing the exhaust gas temperature at 873 K while varying the pressure ratio between 1 to 8. The parameters detailed in Table 1 were used in all the cases described unless otherwise specified. The thermodynamic efficiency (η) and specific net work output for each cycle were calculated and plotted against the pressure ratio. For instance, the efficiency of the two-stage Ericsson cycle, η is given by.

$$\eta = \frac{\text{net work output}}{\text{heat input}} = \frac{(h_7 - h_8) + (h_5 - h_6) - ((h_1 - h_{10}) + (h_3 - h_2))}{(h_5 - h_4) + (h_7 - h_6)}$$

where h_i is the enthalpy of the working fluid at position i in the cycle (Figure 4).

$$\text{Pressure ratio, } r = \frac{P_3}{P_{10}}$$

In the second set of simulations, the most promising cycles from the first set were studied in detail and compared to the inverted Joule cycle by observing the specific net work output generated by each WHR cycle. For the closed cycles, the compression ratio and the exhaust gas temperature were both varied and in the IJC, the expansion ratio and exhaust temperature were varied. The resulting specific net work output in each closed cycle case was plotted on a contour curve against the exhaust gas temperature and pressure ratio, and for the IJC, against the exhaust gas temperature and the expansion ratio. The specific net work output for the two-stage Ericsson cycle (Figure 2) is given by:

$$w = \frac{(h_7 - h_8) + (h_5 - h_6) - ((h_1 - h_{10}) + (h_3 - h_2))}{\textit{mass flow rate of the exhaust gas}}$$

Simulations were also carried out to understand the impact of the isentropic efficiencies of the compressors and turbines, the effectiveness of the heat exchanger and the pressure loss in the heat exchanger on the overall cycle efficiency and specific net work output. It was noted as expected that increasing the effectiveness of the heat exchanger or the isentropic efficiencies of either the compressors or turbines led to an overall increase in cycle performance while an increase in the pressure drop across the heat exchanger led to poorer cycle performance. These parameters were kept fixed in further simulations (Table 1) based on data from existing literature [8,12–14] and deductions from the simulations.

The mass flow rate of the working fluids was chosen to maintain a fixed change in temperature for all the different gasses used. This means that Argon for example would have the highest mass flow rate since it has the lowest specific heat capacity of the three gases being studied, and the temperature gain in the heat exchanger depends only on the effectiveness of the heat exchanger and the temperature of the exhaust gas. Considering the mass flow rate m, specific heat capacity c, and temperature T, the heat exchanger effectiveness ε has the following expression:

$$\varepsilon = \frac{(mc\Delta T)_{\textit{working fluid}}}{(-mc\Delta T)_{\textit{exhaust gas}}} = \frac{(\Delta T)_{\textit{working fluid}}}{(-\Delta T)_{\textit{exhaust gas}}}$$

3.1 Thermodynamic efficiency of the closed WHR cycles

Figure 3 depicts the fraction of the heat absorbed by the hot heat exchanger transformed into useful work by the various closed cycles. It can be deduced from
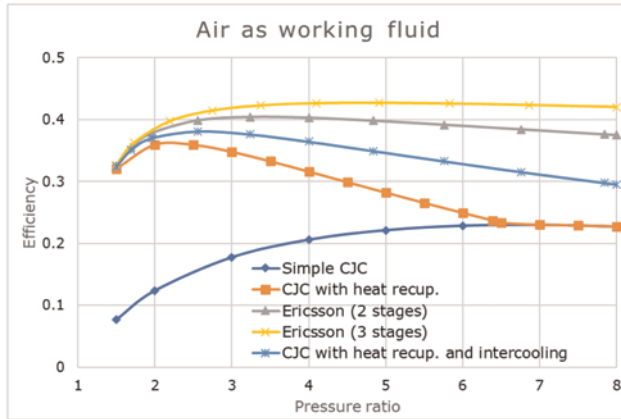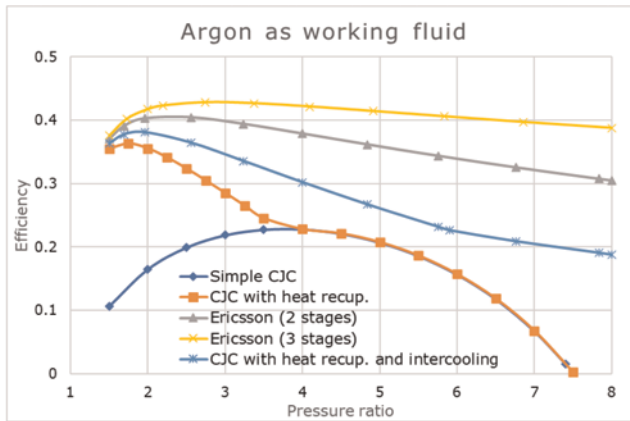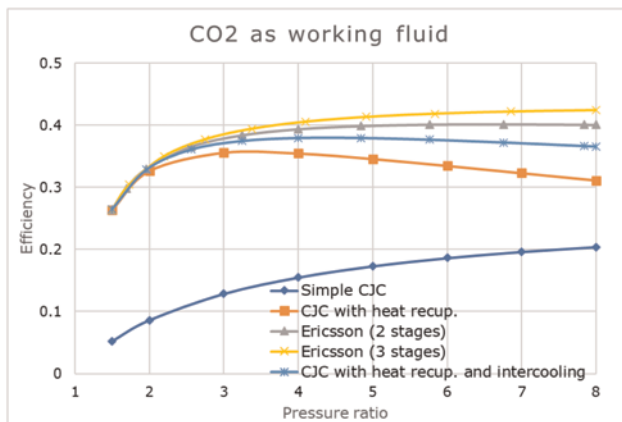
Figure 3. Thermodynamic efficiency of closed WHR cycles with (a) air, (b) argon, and (c) CO$_2$ as the working fluid.

Figures 3(a), 3(b) and 3(c) that the highest thermodynamic efficiency is observed in the three-stage Ericsson cycle, followed by the two-stage Ericsson cycle. The CJC with heat recuperation and intercooling exhibits a lower efficiency than those experienced in the Ericsson cycles. The simple CJC exhibited the lowest efficiency values. It can also be observed that the efficiency of the CJC with heat recuperation reduces to simple CJC at a pressure ratio of about 4 when argon is used as the working fluid; this is because at this present condition the temperature of the stream after expansion is as hot as the compressed stream and hence the heat recuperator is bypassed. Similar trends are observed when air and carbon dioxide are used as the working fluids, except in the CJC with heat recuperation and air reduces to a simple CJC at a pressure ratio close to 6.4 and occurs at much higher pressure ratios when CO_2 is used. This indicates how fast the temperature of each of these gases increases when compressed, fastest in argon and slowest in carbon dioxide. This is explained by the difference in the specific heat capacities of the gases.

Overall, the argon cycles peak at lower pressure ratios, followed by the air cycles. Although the highest thermodynamic efficiency recorded for all three cases is around 43% in the three-stage Ericsson cycle, it is not analyzed further as it is relatively complex. Adding more stages of compression and expansion would make the cycle more efficient and significantly increase its complexity. The simple CJC will not be analyzed further either as it yields the lowest efficiency. Thermodynamic cycle efficiency plots show the fraction of the heat transferred in the heat exchanger that is transformed into useful work. To gain a better understanding of the WHR cycles, the net work output generated per kilogram flow rate of exhaust gas (specific net work output) was also calculated and plotted.

3.2 Specific net work output of WHR cycles

In this section, the cycles determined in the previous section were considered and compared to the open inverted Joule cycle. In the case of the open cycle, the working fluid is simply the exhaust gas, whereas, in the case of the closed cycle, it is a choice of air, argon, or CO_2. Figure 4 depicts the specific net work output of various closed WHR Joule cycles and the open Joule cycle. It was noted that the two-stage Ericsson cycle yielded the highest net work output values compared to all the other cycles when air and argon are the working fluid. On the other hand, when CO_2 is the working fluid, the two-stage Ericsson cycle produces lower specific net work output values compared to the IJC under pressure ratios of 4.

Also, it is noticeable that the CJC with heat regeneration and intercooling has a significant gain compared to the IJC. Although the two-stage Ericsson cycle has higher efficiency and specific net work output values, techno-economical and mechanical complexities due to reheating make the CJC with heat regeneration and intercooling more desirable.

From the simulations, the IJC yields lower thermodynamic efficiencies (less than 13%) compared to the closed cycles (more than 30% in the CJC with heat regeneration and intercooling) but produces comparably large amounts of work. This is because in the IJC, the exhaust gas serves directly as the working fluid unlike in the closed cycles where the heat must be transferred via a heat exchanger. This implies that the resulting exhaust gas after WHR is much hotter in closed cycles than in the IJC, and as such, it might be reusable in other heating processes. A good example is shown in Table 2, where the air CJC with heat recuperation and intercooling and the IJC both yield near equal amounts of net work but the IJC exhaust stream after WHR is 160K colder. This is particularly useful in ships with enough space and mass allowance to install both WHR systems to recover some of the waste heat through the turbine shaft and some of it for heating purposes.
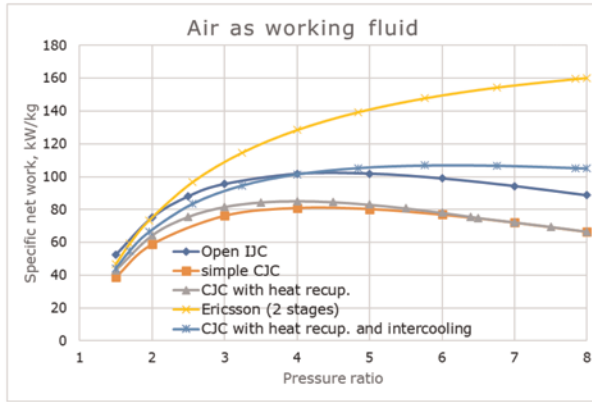
(a)
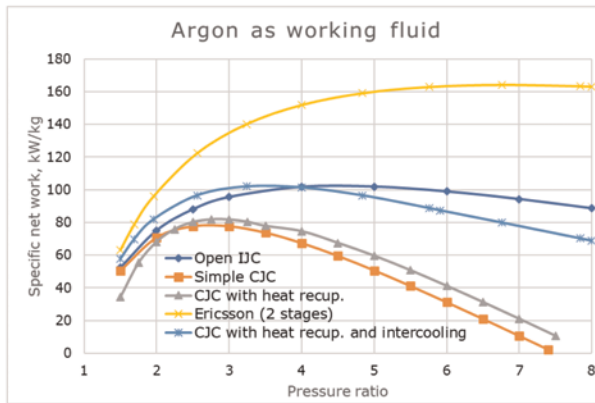
(b)
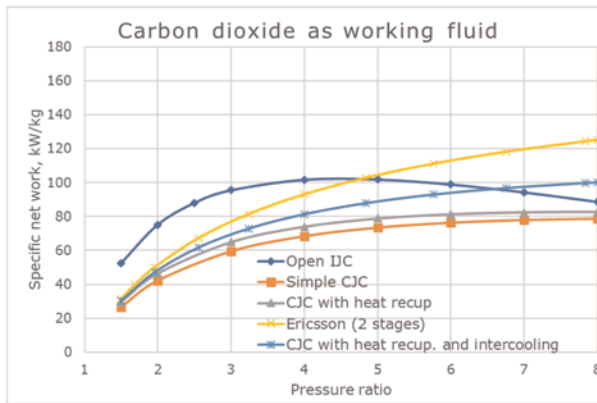
(c)

Figure 4. Specific net work output per kg of exhaust gas flow of WHR cycles with (a) air, (b) argon, and (c) CO_2 as the working fluid.

Table 2. WHR cycle results for an exhaust gas temperature of 600°C and pressure ratio of 4 and air as working fluid.

WHR cycle	Cycle thermo-dynamic efficiency, %	Specific net work output, kW/kg	Exhaust gas temperature after WHR, K
IJC	16.6	101.8	460
simple CJC	20.5	80.3	512
CJC with heat recuperation	31.6	85.2	629
CJC with heat recuperation and intercooling	36.4	101.5	620
2-stage Ericsson cycle	40.3	171.1	713

For a pressure ratio of 4 and air as the working fluid, the values of the thermodynamic efficiency, the specific net work output, and the exhaust gas temperature after WHR for the IJC, the simple CJC, the CJC with heat recuperation, the CJC with heat recuperation and intercooling and the 2-stage Ericsson cycle are shown in Table 2.

3.2.1 *Impact of exhaust gas temperatures on specific net work output*
Not all marine or truck engines have exhaust gases at 873K. Therefore, it is important to understand the impact of exhaust gas temperatures on the WHR cycles. This is achieved in this work by varying the exhaust gas temperature between 500 and 1000K for different compression and expansion ratios as illustrated in Figure 5 using air as the

(a)
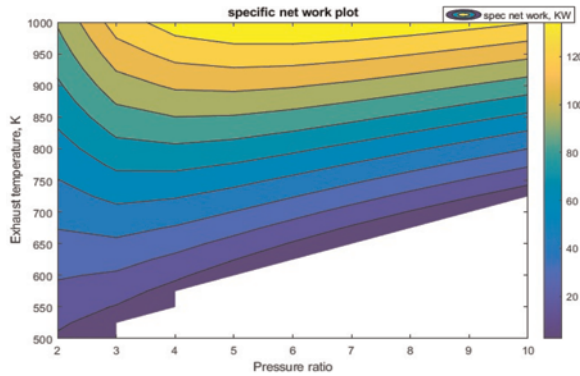
Figure 5. Specific net work output of WHR cycles using air as the working fluid with varying exhaust gas stream temperature and overall pressure ratio for the (a) Inverted Joule Cycle, (b) Closed Joule Cycle with heat recuperation, (c) 2-stage Ericsson cycle, and (d) Closed Joule Cycle with heat recuperation and intercooling.
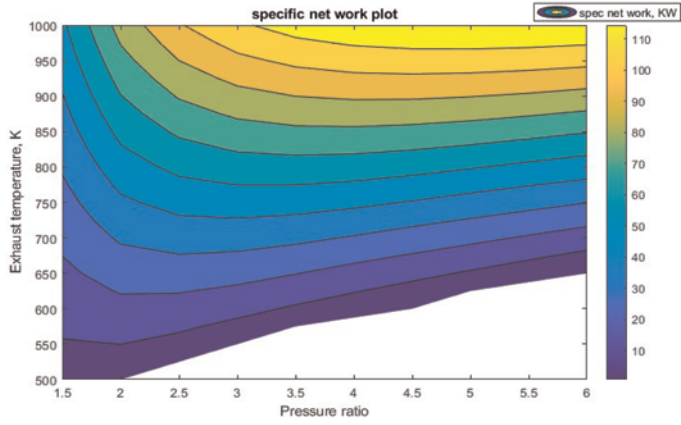
(b)
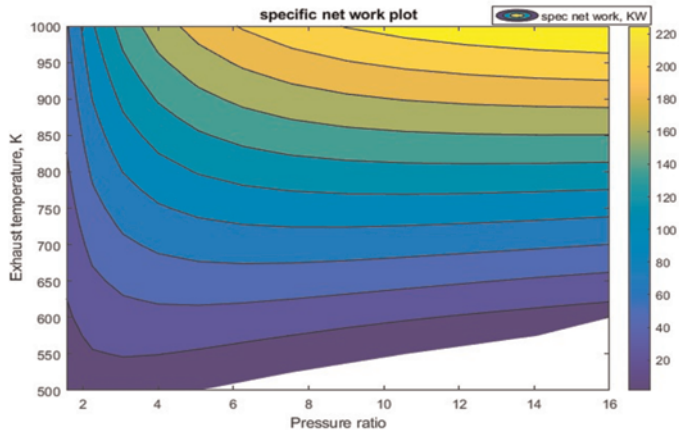
(c)
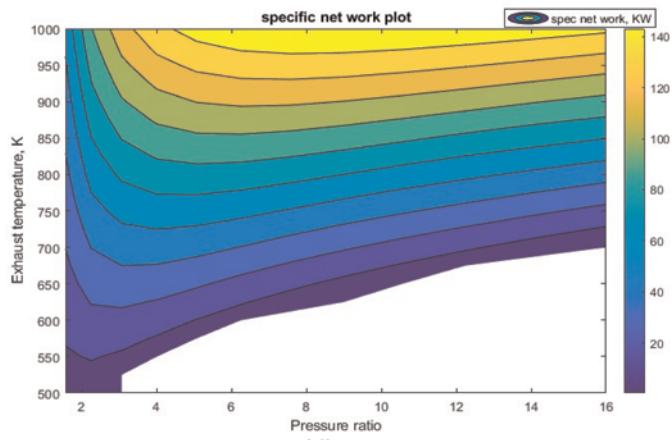
(d)

Figure 5.   (Continued)

working fluid (Figures showing the impact of the exhaust gas temperature when using argon or carbon dioxide as the working fluid are shown in Appendix B). At low-temperature regions such as 500–550K, for all WHR cycles considered, the net work output is small or negative in most cases, especially with increasing pressure ratios as relatively more work is required to compress the working fluid than can be recovered during its expansion. For such low exhaust gas temperatures per kilogram of exhaust gas flow, about 21 kW net work output is obtained in the IJC and 24 kW in the 2-stage Ericsson cycle (with air as the working fluid).

3.2.2 *Impact of working fluid on specific net work output in CJC*

Figure 6 depicts the impact of working fluid type on specific net work output in a closed Joule cycle with heat regeneration and intercooling for varying exhaust gas temperature and pressure ratio. At any given exhaust gas temperature, CO_2 shows to have the highest pressure ratio operating regime and argon, the lowest operating regime. Using argon allows for the best WHR at lower pressure ratios, with a maximum net work

(a)

(b)
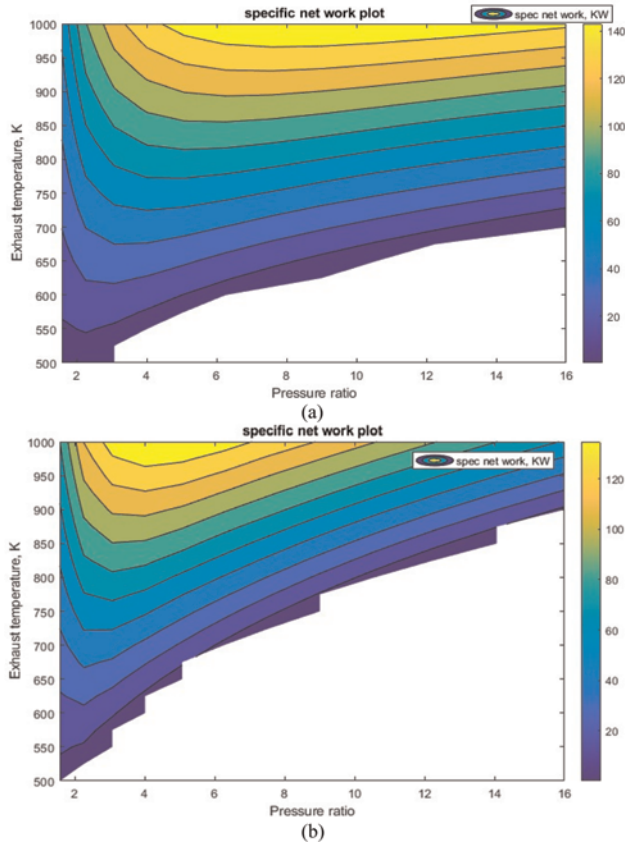
Figure 6. Specific net work output of the CJC with heat recuperation and intercooling with varying exhaust gas stream temperatures and pressure ratios using various working fluids: (a) air, (b) argon, and (c) CO_2.

243
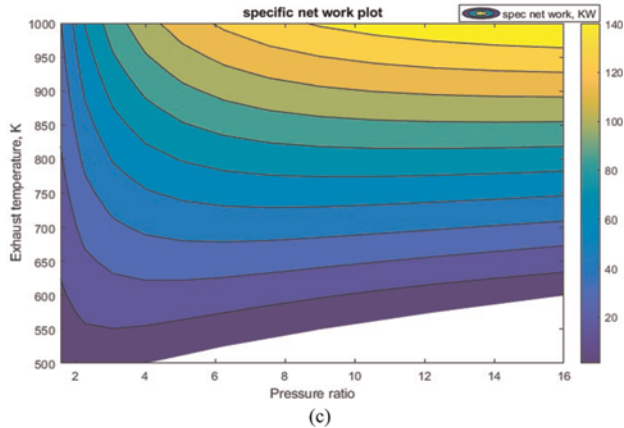
Figure 6.   (Continued)

output being experienced at a pressure ratio of 4, while carbon dioxide allows for higher pressure ratios to be used.

For an exhaust gas temperature of 600K, the approximate maximum possible specific net work output values that can be obtained and the corresponding pressure ratios for the various working fluids in a CJC with heat recuperation and intercooling are shown in Table 3.

Table 3. CJC with heat recuperation and intercooling: results for an exhaust gas with a temperature of 600K.

Working fluid	Pressure ratio	Specific net work output, kW/kg
Monoatomic	2.25	24.3
Diatomic	3	25.0
Triatomic	4	24.3

4   CONCLUSIONS

In this paper, approximated Joule cycle WHR systems operating with air, argon and carbon dioxide separately as working fluids were modelled and analyzed. The results obtained show that:

1. For a fixed exhaust gas temperature of 873K, the highest cycle thermodynamic efficiencies were obtained with the three-stage Ericsson cycle (up to 43%), followed by the two-stage Ericsson cycle (up to 40%), and then the CJC with heat recuperation and intercooling (up to 38%). The IJC exhibited the lowest thermodynamic efficiencies (below 16%) and higher efficiencies were experienced with the simple closed Joule cycle (up to 22%). Although the three-stage Ericsson cycle has the highest thermodynamic efficiency and specific net work output values, the two-stage Ericsson cycle and the CJC with heat regeneration and intercooling are more

244

desirable because they would likely be smaller in size and show fewer techno-economic and mechanical complexities due to their having fewer stages of compression and expansion. In the closed cycles, air, argon, and carbon dioxide cycles had similar thermodynamic efficiency peaks, with argon being most suitable for low-pressure ratio applications and carbon dioxide for high-pressure ratio applications.

2. Except for the three-stage Ericsson cycle, the two-stage Ericsson WHR cycle yields the highest amount of specific net work output (up to 160kW/kg for exhaust gas with temperature 873K and pressure ratio less than 8). Unlike the trend seen with the cycle thermodynamic efficiencies, the IJC and the CJC with heat regeneration and intercooling both have similar net work output values. This is because in the IJC the exhaust gas serves directly as the working fluid unlike in the closed cycles where the heat must be transferred via a heat exchanger. This implies that the resulting exhaust gas after WHR is much hotter in the closed cycles than in the IJC, and as such, it could be reusable in other heating processes. For example, the exhaust stream after WHR is 160°C hotter in the CJC with heat recuperation and intercooling with air as the working fluid than in the IJC for an exhaust gas temperature of 873K and pressure ratio of 4. The CJC with heat recuperation showed slightly higher values of specific net work output values compared to the simple CJC.

3. All the WHR cycles analyzed in this work became more efficient with increasing exhaust gas temperature, being able to recover larger fractions of the exhaust gas energy. For a 600K exhaust gas stream, 24–25kW/kg net work was recovered using the CJC with heat recuperation and intercooling irrespective of the working fluid used, however, the argon WHR cycle achieved this value at the lowest pressure while the carbon dioxide cycle achieved the value at almost twice as high a pressure ratio than the argon cycle.

REFERENCES

[1] Y. A. Çengel, M. A. Boles, *"Thermodynamics: An Engineering Approach"*, 5th ed, McGraw-Hill, 2006.

[2] A. Firth, B. Zhang, A. Yang "Quantification of Global Waste Heat and its Environmental Effects", *Applied Energy*, ISSN: 0306-2619, Vol: 235, Pages: 1314–1334, 2019.

[3] U. Jouhara, N. Khordehgah, S. Almahmoud, B. Delpech, A. Chauhan, S. A. Tassou, "Waste Heat Recovery Technologies and Applications", *Thermal Science and Engineering Progress*, ISSN: 2451-9049, Vol: 6, Page: 268–289, 2018.

[4] S. Bruckner, S. Liu, M. Laia, M. Radspieler, L. F. Cabeza and L. Eberhard, "Industrial Waste Heat Recovery Technologies: An Economic Analysis of Heat Transformation Technologies", *Applied Energy*, Vol. 151, no. 1, Pages. 157–167, 2015.

[5] Joule, J.P. and Thomson, W., "On the Air-Engine," *Phil. Trans. R. Soc.* Vol. 142, pp. 65–82, 1st January 1852, available at: https://royalsocietypublishing.org/doi/10.1098/rstl.1852.0006, last accessed 29th January 2023.

[6] J. Galindo, J. Serrano, V. Dolz, P. Kleut, "Brayton Cycle for Internal Combustion Engine Exhaust Gas Waste Heat Recovery", *Advances in Mechanical Engineering*, 7(6). 2015, doi:10.1177/1687814015590314

[7]   O.P. Sharma, S.C. Kaushik, K. Manjunath, "Thermodynamic analysis and Optimization of a Supercritical CO2 Regenerative Recompression Brayton cycle coupled with a marine gas turbine for shipboard waste heat recovery", *Thermal Science and Engineering Progress*, ISSN: 2451-9049, Vol 3, Pages: 62–74, 2017.

[8]   L. Chen, F. Sun, C. Wu, R.L. Kiang, "Theoretical Analysis of the Performance of a Regenerative Closed Brayton Cycle with Internal Irreversibilities", *Energy Conversion and Management*, ISSN: 0196-8904, Vol 38, Issue 9, Pages: 871–877, 1997.

[9]   H. Liu, Z. Chi, S. Zang, "Optimization of a Closed Brayton Cycle for Space Power", *Applied Thermal Engineering Systems*, ISSN: 1359-4311, Vol 179, Page:115611, 2020.

[10]   Turner, J.W.G. and Togawa, K., "*Analysis of a Supercharged Gas Turbine Engine Concept and Preliminary Investigation of a Version Using Argon as the Working Fluid*", SAE technical paper 2022-01-0595, SAE 2022 World Congress, Detroit, Michigan, USA, 5th-7th April, 2022, doi: 10.4271/2022-01-0595.

[11]   Internet website, https://www.geaerospace.com/propulsion/marine/lm2500 regarding specifications of shipboard aero-derivative marine gas turbine engine (Last accessed on 16/12/2022).

[12]   K. Kosowski, M. Piwowarski, "Design Analysis of Micro Gas Turbines in Closed Cycles", *Energies*, Vol 13(21), 2020.

[13]   S. Zhu, K. Zhang, K. Deng, "A review of waste heat recovery from the marine engine with highly efficient bottoming power cycles", *Renewable and Sustainable Energy Reviews*, ISSN: 1364-0321, Vol 120, Page: 109611, 2020.

[14]   Colin D Copeland, Zhihang Chen, *"The Benefits of an Inverted Brayton Bottoming Cycle as an Alternative to Turbo-Compounding"*, ASME Turbo Expo 2015, GT2015-42623

[15]   I. Kennedy, Z. Chen, B. Ceen, S. Jones, C. D. Copeland, "Experimental Investigation of an Inverted Brayton Cycle for Exhaust Gas Energy Recovery", *ASME. J. Eng. Gas Turbines Power*. 141(3): 032301, 2019. https://doi.org/10.1115/1.4041109

[16]   J. Tarlecki, N. Lior, N. Zhang, *"Evaluation of Some Thermal Power Cycles for Use in Space. Departmental Papers"* (MEAM), 2006.

APPENDIX A: TOOL VALIDATION

1. Aspen Plus vs Excel models for an open simple Joule cycle
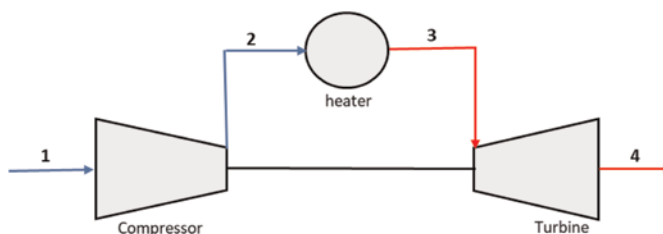
Figure A1. Simple open Joule cycle.

Table A1. Data from Excel and Aspen Plus models.

Pressure ratio, r	Efficiency in Excel	Efficiency in Aspen plus	Error	Error, %
2	0.240875	0.242140	0.001266	0.522643
3	0.353898	0.355603	0.001706	0.479648
4	0.423729	0.425648	0.001919	0.450868
5	0.472653	0.474692	0.002038	0.429400
6	0.509528	0.511638	0.002110	0.412421
7	0.538685	0.540840	0.002155	0.398390
8	0.562538	0.564721	0.002183	0.386610
9	0.582552	0.584752	0.002200	0.376182
10	0.599678	0.601889	0.002211	0.367314
11	0.614564	0.616781	0.002217	0.359407
12	0.62767	0.629889	0.002219	0.352290
13	0.639333	0.641551	0.002219	0.345831
14	0.649805	0.652021	0.002216	0.339928
15	0.65928	0.661493	0.002213	0.334499
16	0.667912	0.670120	0.002208	0.329479
17	0.675821	0.678023	0.002202	0.324816
18	0.683105	0.685301	0.002196	0.320465
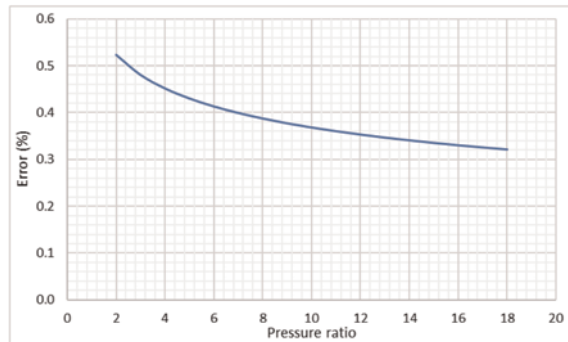
Figure A2. Error plot characterizing the difference between results obtained in Aspen Plus and Excel.

There is a small error which is thought to exist because of the Excel models assume the working fluid to be a perfect gas while in Aspen plus, the Peng-Robinson equation of state is used.

2. Validation of simulations against results obtained in [16]
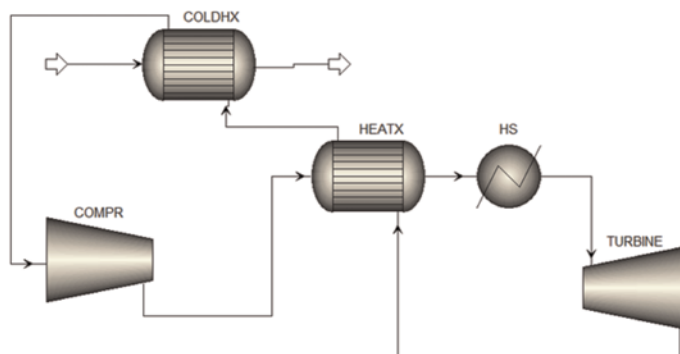
(a)
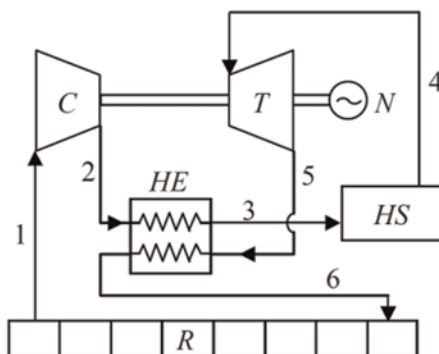
(b)

Figure A3. Closed Joule cycle with heat regeneration (a) from Aspen plus model, (b) from literature (16).

Table A2. Data from the simulated Aspen Plus model compared to results from literature (16).

Gas used	Results from Aspen Plus simulations				Results from literature	Error, %
	Compressor work, kW	Turbine work, kW	Heat added, kW	Efficiency	Efficiency	
N_2	19.2628	63.5606	69.8807	0.6339	0.6339	0
Ar	15.4168	38.5954	39.7841	0.5826	0.5826	0
He	154.3748	385.12	396.6399	0.5818	0.5818	0
H_2	270.5676	865.3963	940.8748	0.6322	0.6322	0

(a)

(b)

(c)
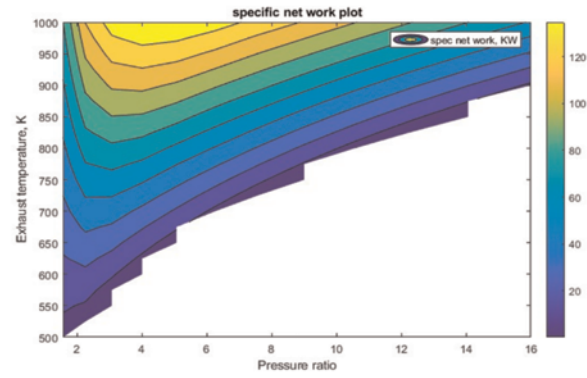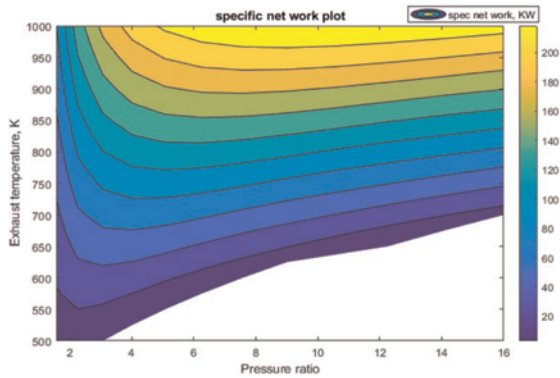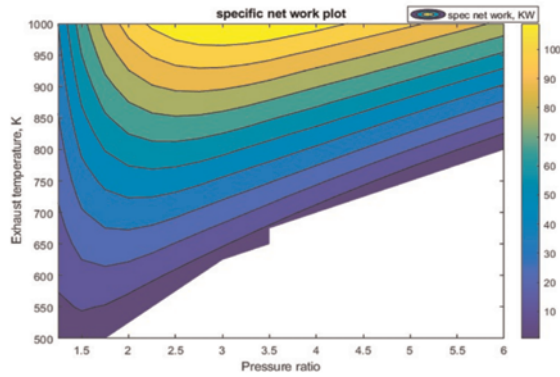
Figure B1. Specific net work output of WHR cycles using argon as the working fluid with varying exhaust gas stream temperature and overall pressure ratio for the (a) Closed Joule Cycle with heat recuperation, (b) 2-stage Ericsson cycle, and (c) Closed Joule Cycle with heat recuperation and intercooling.
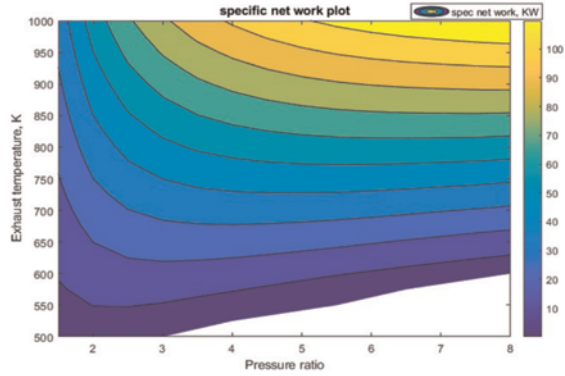
(a)
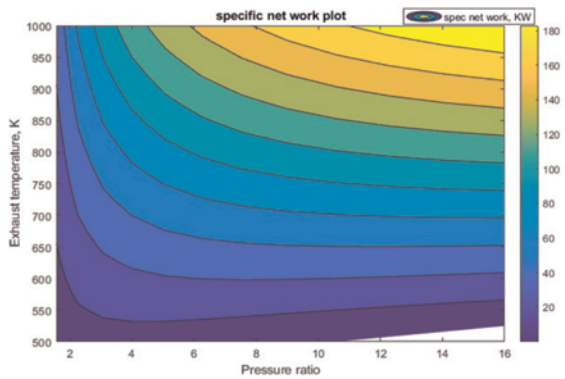
(b)
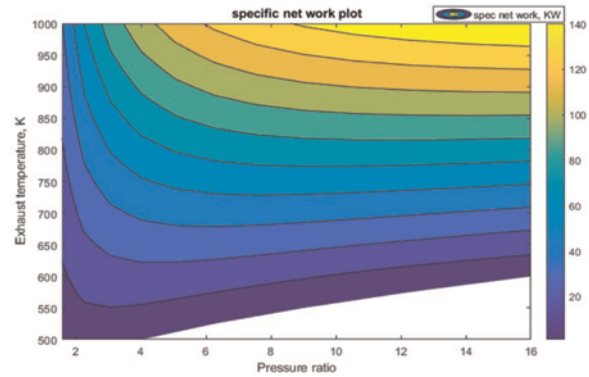
(c)

Figure B2. Specific net work output of WHR cycles using carbon dioxide as the working fluid with varying exhaust gas stream temperature and overall pressure ratio for the (a) Closed Joule Cycle with heat recuperation, (b) 2-stage Ericsson cycle, and (c) Closed Joule Cycle with heat recuperation and intercooling.

Blade vibration visualization of dual volute turbine with vaned nozzle by using high speed Digital Image Correlation

T. Otobe[1], A. Iwakami[2], D. Filsinger[3]

[1]Honda Racing Corporation, Japan
[2]IHI Corporation, Japan
[3]IHI Charging System International GmbH, Germany

ABSTRACT

In recent years, the performance of turbochargers has been improved by adopting complex blade shapes, multi entry turbines and optimized bearing systems. The combination of multi entry turbines and sophisticated blade shapes requires special focus on blade vibration behaviour. It is challenging to identify the blade vibration response mode and measure the stress using conventional measurement techniques. In this research, turbine blade vibrations under rotation at high temperature and speed are visualized with Digital Image Correlation (DIC) technology using high-speed cameras. By analyzing the resonance frequency and blade displacement, it is possible to determine the response mode and the dynamic blade loading.

1   INTRODUCTION

In recent years, the aerodynamic performance of turbocharger impellers has been improved by adopting three dimensional aero-design techniques. On the other hand, complex three-dimensional blades do not allow to avoid resonance modes within the operating range. Research of countermeasure methodology and analysis techniques is progressing to cope with this challenge [1–6]. Additionally, in attempt to reduce exhaust interference and maximize its pulsation effect, twin scroll and dual volute turbine housing designs are increasingly popular in multi-cylinder engine applications [7,8]. However, impellers of Dual Volute turbines are in risk to be damaged due to blade vibrations at resonance speed. The aerodynamic excitation forces are caused by alternating exhaust pulsations [4,9].

To solve these durability and reliability issues, conventional technology is to attach strain gauges to the blade and transfer the strain signals via slip rings or telemetry from the rotating component. Similarly, a measurement technology based on the Blade Tip Timing (BTT) method can also be applied. However, each method has its technical challenges [10]. In this research, blade vibrations of an impeller of a Dual Volute turbine stage with vaned nozzle was visualized with Digital Image Correlation (DIC) technology using high-speed cameras. This method is new and helps to analyze blade vibrations of turbine wheels, rotating at high temperature and speed. By analyzing the resonance frequency and blade displacement, the blade mode of the response can be reliably determined.

2   AERODYNAMIC EXCITATION MODE OF DUAL VOLUTE TURBINE

Adopting a Dual Volute turbine minimizes the cross flow in a V6 engine- the exhaust pulsations of the right and the left bank are nearly separated. Pulsating waves of

exhaust gas flow into the turbine with a typical V-angle phase difference. Under these conditions, momentarily the left and right bank exhaust pressures differ greatly as can be seen from the time resolved pressure traces in Figure 1.
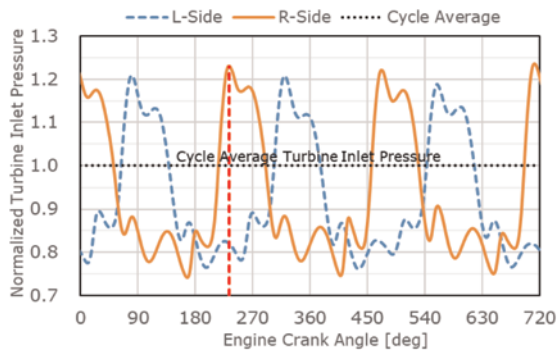

Figure 1. Turbine inlet pressure pulsation.

Figure 2 shows the momentary spatial total pressure distribution in the turbine housing under such conditions. During operation, the turbine impeller receives pressure fluctuations of the inflowing gas along the circumference as shown in Figure 3. This leads to strong unsteady aerodynamic forces on the turbine blades.
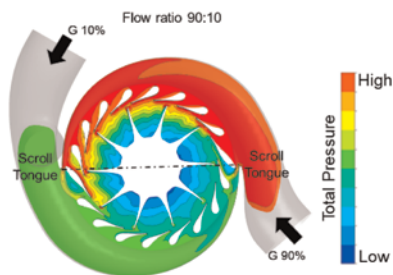
Figure 2: Momentary total pressure distribution.
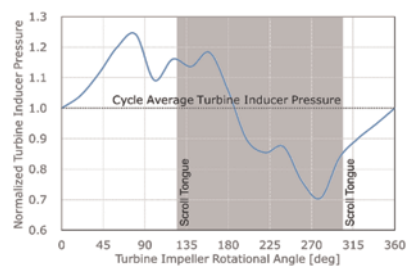
Figure 3: Total pressure fluctuations at turbine impeller inducer.

As a result, low order blade excitation with frequencies that equal multiples of the rotational speed N are present. Due to the specifics of Dual Volutes higher 2N, 3N and 4N excitation has to be expected [4]. High blade vibrations can occur when the resonance blade frequency especially of the low mode f1 and the excitation frequency of the second (2N) or third order (3N) of the rotation match.

3 RESONANCE MODE ANALYSIS AT TURBINE BLADE DESIGN STAGE

The test turbine investigated in the article at hand was designed as a prototype during the development process with the main purpose of improving aerodynamic performance. Table 1 shows its specifications.

Table 1. Prototype turbine specifications.

Inlet diameter (Tip)	116.2 mm
Inlet diameter (Hub)	112.4 mm
Outlet diameter	88.2 mm
Number of blades	10
Number of nozzle vanes	18

Generally, turbocharger turbines for series production are designed with natural frequency f1 above 4N or 5N. The reason for this is the general decay of the excitation with increasing excitation order [4]. Since the main purpose for the design at hand was to improve aerodynamic performance, it was compromised in terms of blade stiffness. Structural analysis confirmed that the resonance frequency f1 matches the frequency of the 3rd order of rotation (3N). The resonance is in the allowed rotation speed range. In addition, it can be seen from the Campbell diagram in Figure 4, that for this prototype turbine, the resonance excitation caused by the number of vaned nozzles exist at a similar rotational speed, but for a higher blade mode shape.
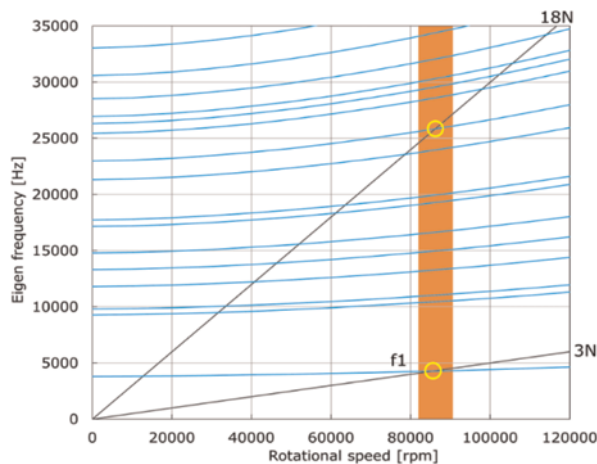
Figure 4. Campbell diagram of test turbine.

Figure 5 shows contours of the f1 blade displacement and stress, estimated by forced response Finite Element Analysis (FEA) considering the relevant excitation. In this snapshot the amplitudes of the single blades are different since the calculation considers also the wheel vibration. The relation between single blade vibration and wheel vibration characterized by nodal diameters is explained in [1]. From such FEA for each
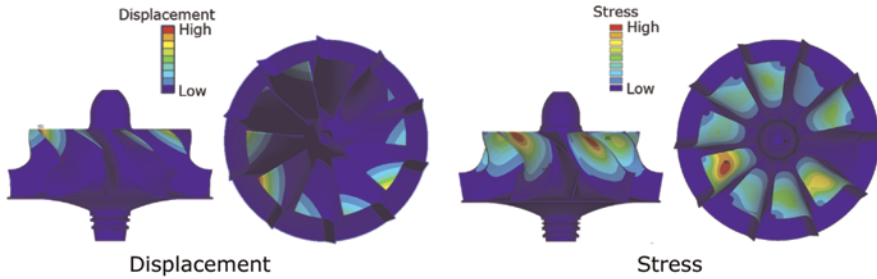
Figure 5. Blade displacement and stress estimation in resonance mode f1.

blade vibration mode, the correlation between local blade displacement and dynamic stress distribution can be derived. From measurement of the displacement of the blade tip or the displacement at any other blade location one can conclude the dynamic stress level in the blades. Mistuning of real structures introduces some uncertainty, that can be estimated [11]. Important is the ability to experimentally identify the blade mode shape for being able to correlate displacement and stress correctly.

4   BLADE VIBRATION ANALYSIS RESULT FROM HOOD TEST

The Optical Blade Vibration Monitoring System of HOOD (USA) is established as a blade vibration analysis technology [12–14].

The prototype turbine was operated on a hot gas test bench as shown in Figure 6.

In order to match the flow ratio of the hot gas flowing into each entry of the Dual Volute turbine to the conditions under pulsation in the actual engine, the flow path was branched at the exit of the burner, and an orifice was provided on one side to adjust the flow ratio. The turbine inlet temperature was set to 620°C to respect the heat resistance limit of the measurement probe. By measuring the passing timing of the tip of the blade with the HOOD test equipment, the displacement caused by blade vibration is determined (Figure 7).
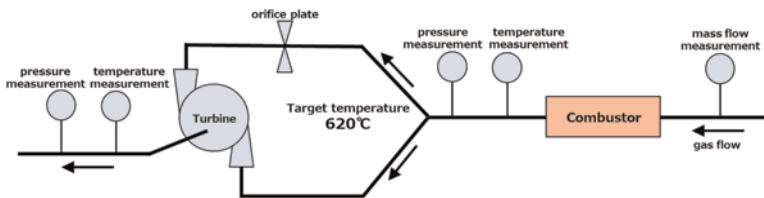
Figure 6. Schematic diagram of the hot gas test bench installation.

With equal admission turbine inflow, no significant blade vibration was detected (Figure 8-a). However, when an orifice was installed on one side of the Dual Volute turbine inlets and the left and right expansion ratios were operated under the conditions shown in Figure 2, large blade vibrations were detected, as shown in Figure 8-b. The resonance frequency matches with the numerical results from calculation, but also shows that the real structure is not ideal as it was expected. Mistuning is present and widens the resonance range and also modulates the singe blade amplitudes.

(a) Total view of the turbine   (b) Installed tip timing probes
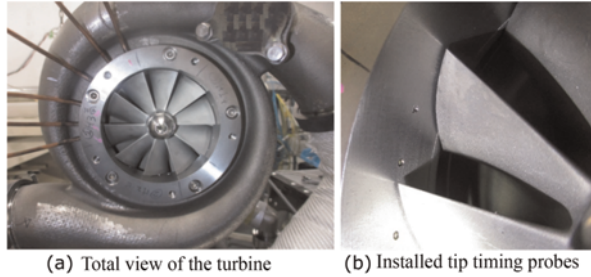
Figure 7. Prototype turbine with HOOD probe installed.

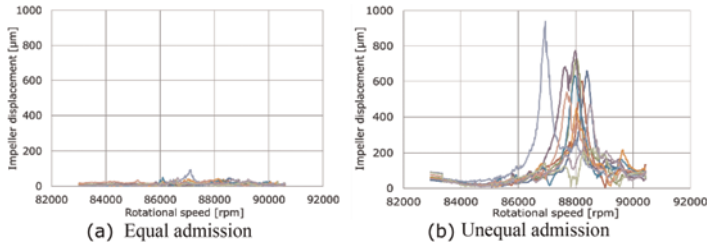(a) Equal admission   (b) Unequal admission

Figure 8. Impeller tip displacement from testing with the HOOD system.

From the blade displacements shown in Figure 8 the generated stress can be determined utilizing the simulation results from Figure 5 since these describe the correlation between blade deformation and dynamic stress. Following this procedure, Figure 9 exhibits normalized maximum stress for equal admission (without orifice-plate) and unequal admission (with orifice-plate). As expected, the much higher blade loading for the unequal admission can be seen. The assumption is here, that the blade mode f1 is excited. This assumption is supported by analysis of a failed turbine wheel, that is shown in Figure 10, since the origin of the fatigue failure matches with the calculated position of the peak stress in the blade for mode shape f1.
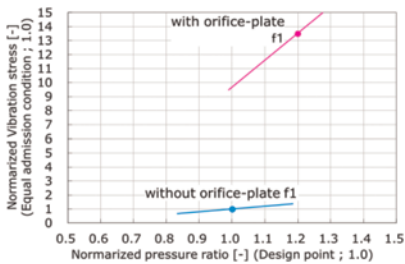
Figure 9. Blade stress comparison

Figure 10: Damaged turbine blade.

In the HOOD test, from the Campbell diagram, it is not possible to differentiate between different blade mode shapes. From displacement measurements one cannot distinguish

255

between the third order and the higher order nozzle count resonance shown in Figure 4 in the Campbell plot. In the evaluation in Figure 9, it was assumed that the vibration stress was caused by the mode one f1 resonance in a third order 3N excitation. Indications that underline this assumption are the slight difference in frequency of the mode shapes and also the location of the origin of the fatigue failure shown in Figure 10. Still, there was some uncertainty, that can only be eliminated utilizing a measurement technology that delivers spatial resolved blade displacements.

5   VISUALIZATION OF TURBINE BLADE VIBRATION USING DIC

Examples of strain measurement with DIC using high-speed cameras have been reported for fixed objects and propellers of wind turbines for wind power generation [15,16].

In this study, DIC using high-speed cameras with the target of visualizing low-order blade vibrations was applied for the first time to a turbine rotating at high temperature and high speed. In order to paint and fix the required random speckle pattern on the turbine blades, it is necessary to apply a heat-resistant paint to the turbine impeller. The paint is firmly applied after one hour in an oven with a temperature of 200°C. Figure 11 shows the turbine impeller after preparation.
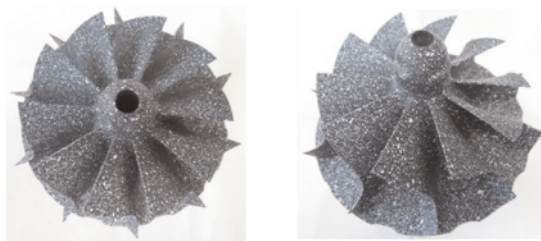
Figure 11. Random speckle pattern painted on the turbine impeller.

To allow access of the high-speed camera to the rotating turbine impeller at high temperature, the turbine outlet piping was arranged as shown in Figure 12.The images were taken with two high-speed cameras through a quartz glass. Table 2 shows the specifications of the high-speed camera used in this test.
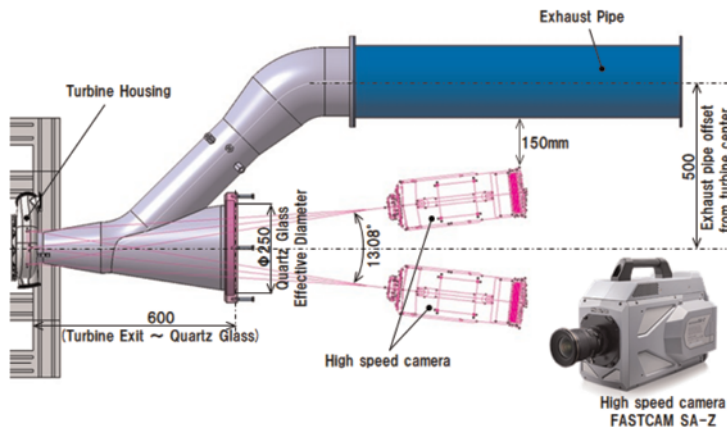
Figure 12. Setup for the DIC test with high-speed cameras.

Table 2. High speed camera, DIC software and light source specifications.

High Speed Camera	
Camera	FASTCAM SA-Z (Photron: Japan)
Frame Rate	100,000 FPS(Hz)
Exposure Time	1/2,880,000s (350nsec)
Resolution	384(H) x 408(V) pixel
Lens	F-mount 105mm
DIC Software	
VIC-3D HS FFT System (Correlated Solutions: USA)	
Light Source	
Model	LA-HLF100 (HAYASHI-REPIC: Japan)
Lamp	Laser-Pumped White Light Source

Since the resonance speed and frequency of the test turbine have already been confirmed by the HOOD test, the DIC test conditions were set as shown in Table 3 in consideration of the influence of the turbine inlet temperature.

Table 3. Hot gas bench DIC test conditions.

Turbocharger speed	90,000 rpm[*1]
Turbine inlet temperature	830°C
Left side volute inlet pressure	75% cycle average inlet pressure
Right side volute inlet pressure	125% cycle average inlet pressure

[*1]Differences in measurement methods and individual differences in test parts resulted in a difference of 2000rpm resonance speed.

The procedure to visualize the turbine blade vibration with DIC using a high-speed camera is shown below. Images of the rotating turbine impeller are captured by two high-speed cameras, and the results are analyzed by Fast Fourier Transformation (FFT) to extract the frequencies where the blade displacement is large. Figure 13, top, shows the spatial displacement at the selected frequency which is indicated with a red line in the FFT spectrum of the maximum blade displacement amplitudes (Figure 13, bottom).
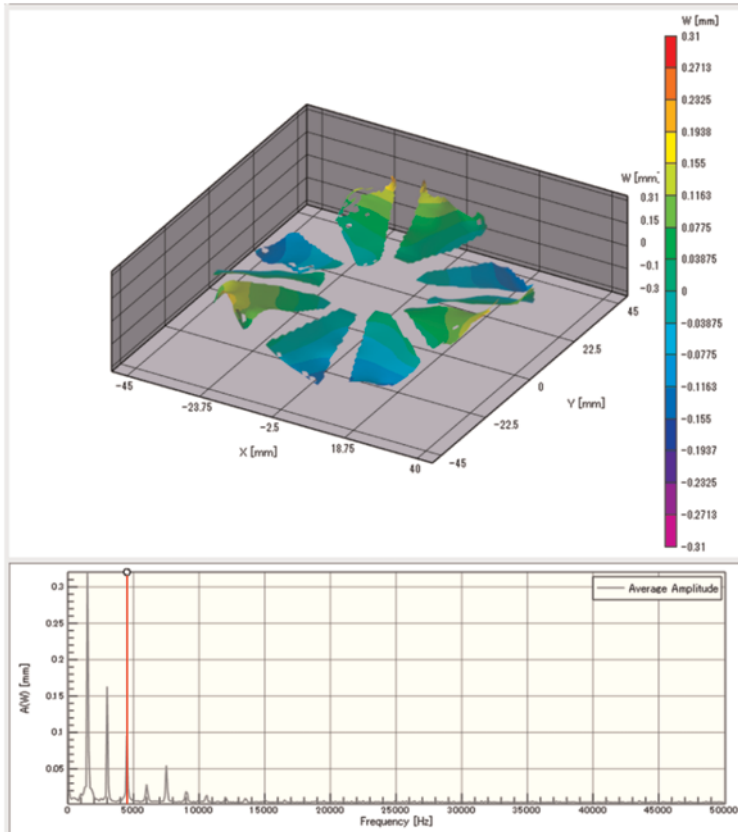
Figure 13. Spatial FFT analysis result of the DIC visualized data.

In a next step, all blade displacements at the extracted frequencies are visualized. Furthermore, the blade with the largest displacement is selected and the hub area is fixed in its position to accurately visualize the local vibration of this blade. By comparison with results from FEA, the blade vibration mode can be determined.

Figure 14(a) shows the visualization results of the displacement of the test turbine blades, including the deformation of the entire impeller. These DIC results show a maximum blade tip displacement of about 0.6 mm (peak to peak). By extracting a single blade from this result and fixing the displacement at the hub, the resonance mode shape can be visualized as can be seen in Figure 14(b). It shows a good agreement with the calculation of the blade vibration at the design stage shown in Figure 5. The mode 1 bending mode f_1 is clearly visible. The result also shows good correlation with the displacement from the tip timing measurements shown in Figure 8-b.
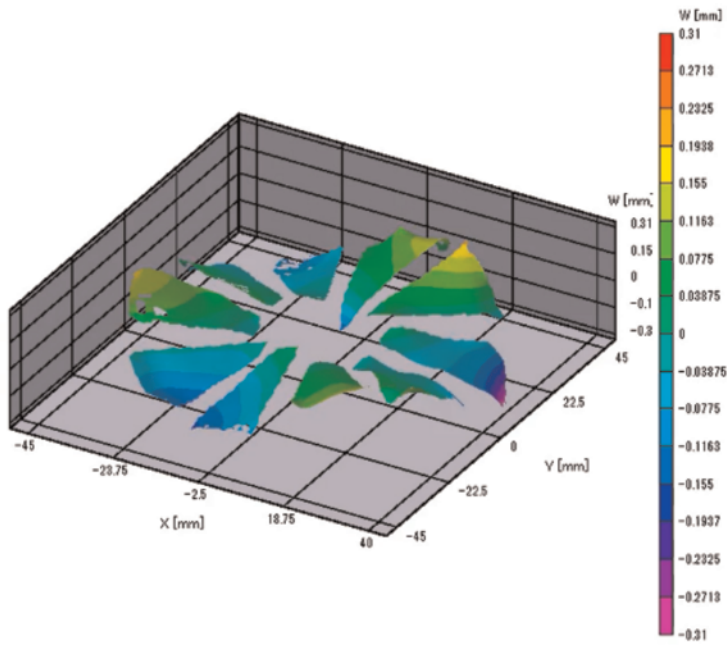
(a) DIC visualization result of all blades and rotor
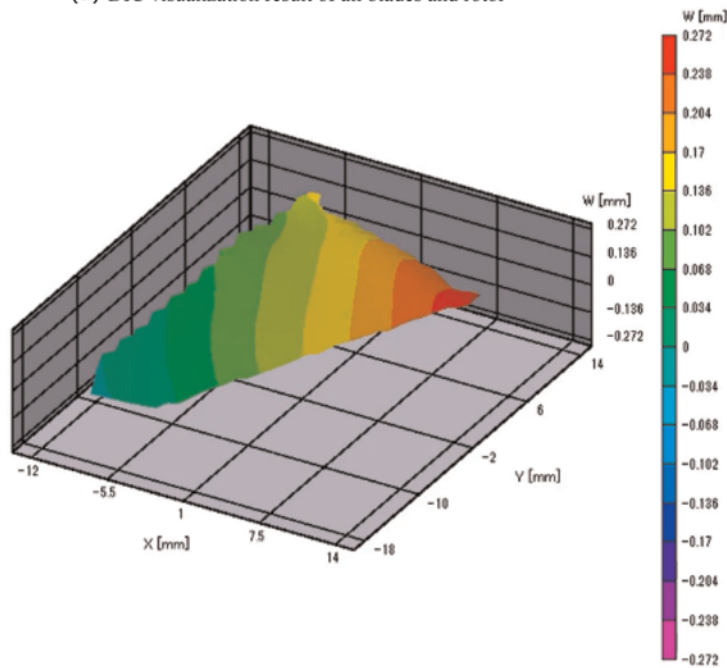
(b) DIC visualization result of the maximum single blade vibration

Figure 14. DIC visualization of the f1 displacements after FFT.

Following listed items need consideration for employing the current DIC method:

1. It must be distinguished between the displacement of the rotor by shaft motion from unbalance and the single blade vibrations. This can be done in a post processing as described above.
2. Related to the currently realized optical access it is difficult to visualize the displacement at the tip of the blade. Also blade vibrations on the inducer side of turbines and the exducer side of compressors cannot be visualized by the DIC.
3. The random speckle pattern coating gradually peels off from the outer periphery when driving at high temperature and high speed. The duration for measurements needs to be limited. As a countermeasure, application of random speckle pattern through laser marking can be considered.
   For this issue, data extrapolation and interpolation can help to determine the blade displacements also in areas where the speckle patterns are lost (Figure 15).
4. As shown in Table 2, maximum frame rate is currently 100kHz. A camera capable of higher speed imaging with higher resolution is required for high-order blade vibration measurement at high rotation speed.
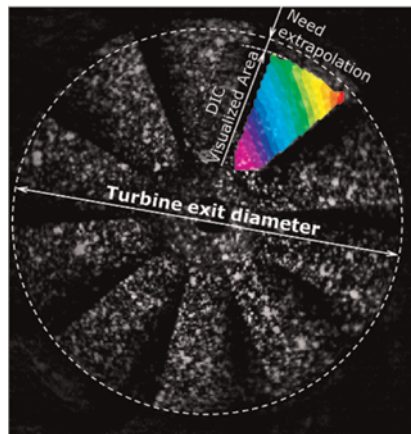
Figure 15. DIC Turbine blade displacement visualized area

6   CONCLUSIONS

Until now, blade vibration measurement during rotation has been performed by direct measurement using strain gauges and slip rings, telemetry, or by the Blade Tip Timing (BTT) method. DIC using high-speed cameras is effective for the measurement of low-order blade vibration stress by spatial displacement analysis and the identification of mode shapes of turbocharger turbine impellers. DIC enables measurement under high temperature conditions, which is challenging with the Blade Tip Timing (BTT) method. By visualizing the spatial vibration of turbine blades using DIC, it is possible to identify resonance modes, ascertain blade displacement and vibration frequency, and generated stress to ensure reliable designs.

REFERENCES

[1] T. Kreuz-Ihli, D. Filsinger, A. Schulz, S. Wittig, 2000: "Numerical and Experimental Study of Unsteady Flow Field and Vibration in Radial Inflow Turbines", *Journal of Turbomachinery*, Vol. 122, No. 2, pp. 247–254.

[2] D. Filsinger, O. Schäfer, 2003, "Numerical Calculation of Low Order Blade Excitation of Pulse Charged Axial Turbocharger Turbines and its Experimental Assessment", *ASME Turbo Expo*, GT2003–38182.

[3] A. Kulkari, G. LaRue, 2008. "Vibratory Response Characterization of a Radial Turbine Wheel for Automotive Turbocharger Application", *ASME Turbo Expo*, GT2008–51355.

[4] D. Hemberger, R. DeSantis, D. Filsinger, 2018, "Double Scroll Turbine for Automotive Applications: Engine Operating Point Versus Dynamic Blade Stress from Forced Response Vibration", *ASME Turbo Expo*, GT2018–76590.

[5] S. Netzhammer, S. Kraetschmer, J. Leweux, A. Koengeter, D.M. Vogt, 2017, "Aerodynamic Excitation Analysis of Radial Turbine Blades due to Unsteady Flow from Vaneless Turbine Housings", *ASME Turbo Expo*, GT2017–64468.

[6] J. Wallaschek, J. Seume, 2020, *"Mistuning with Aerodynamic Coupling II"*, FVV Spring Conference 2020, Report No 1269.

[7] J. Walkingshaw, G. Iosifidis, T. Scheuermann, D. Filsinger, N. Ikeya, 2015, "A Comparison of a Mono, Twin and Double Scroll Turbine for Automotive Applications", *ASME Turbo Expo*, GT2015–43240.

[8] T. Suzuki, G. Iosifidis, J. Starzmann, W. Sato, D. Filsinger, T. Bamba, 2020, *"1D Gas Exchange Modelling of Double Scroll Turbines: Experimental Validation and Improved Modelling"*, IMechE, 14th International Conference on Turbochargers and Turbocharging, London.

[9] M. Gugau, F. Winkler, S. Weiske, T. Heuer, R. Sauerstein, 2016, "The next Generation of Pulse Optimized Multi-Scroll Turbines for Automotive Applications– dual Volute and Twin Scroll", IMechE, 12th International Conference on Turbochargers and Turbocharging, London.

[10] G. Janicki, A. Pezouvanis, B. Mason, M.K. Ebrahimi, 2014, "Turbine Blade Vibration Measurement Methods for Turbocharges", *American Journal of Sensor Technology* 2014 Vol.2 No.2 P.13–19.

[11] D. Hemberger, D. Filsinger, H.-J. Bauer, 2013, "Mistuning Modelling and its Validation for Small Turbine Wheels", *ASME Turbo Expo*, GT2013–94019.

[12] S. Heath, M. Imregun, 1997, "A Review of analysis Techniques for Blade Tip-timing Measurements", *ASME Turbo Expo*, 97-GT–213.

[13] S. Heath, 1999, "A New Technique for Identifying Synchronous Resonances Using Tip-timing", *ASME Turbo Expo*, 99-GT–402.

[14] Y. Matsuda, T. Mitsutake, K. Ohashi, 2000, "Non-contact Vibration Measurement of Centrifugal Compressor Impeller", *GTSJ Autumn Conference*.

[15] T.C. Chu, W.F. Ranson, M.A. Sutton, W.H. Peters, 1985, "Applications of Digital-Image-Correlation Techniques to Experimental Mechanics", *Experimental Mechanics*, pp. 232–244.

[16] S. Lehnhoff, A.G. Gonzalez, J.R. Seume, 2020, "Full Scale Deformation Measurements of a Wind Turbine Rotor in Comparison with Aeroelastic Simulations", *European Academy of Wind Energy, Wind Energy Science*, https://doi.org/10.5194/wes-2020-28.

Internal flow investigation in a radial turbine non-axisymmetric diffuser using particle image velocimetry

Toshimitsu Tanaka[1], Koki Ito[1], Toyotaka Yoshida[2], Nobuhito Oka[2], Toru Hoshi[1]

[1]Mitsubishi Heavy Industries, Ltd., Research & Innovation Center, Japan
[2]Mitsubishi Heavy Industries Engine & Turbocharger, Ltd. Japan

ABSTRACT

Highly efficient turbine at high expansion ratio is required with the expanded application of the Miller cycle to automotive engines. At high expansion ratio, turbine diffuser plays an important role in turbine efficiency because of the increased leaving loss. In addition, since the turbine operates under engine exhaust pulsation, the diffuser's performance is required to be robust over a wide operating range of velocity ratio. Therefore, internal flow in a turbine diffuser is experimentally investigated under several velocity ratio conditions.

1   INTRODUCTION

As part of global warning countermeasures, regulations on automotive engine emissions have been tightened around the world. The application of turbocharger is expanding as a technology that contributes to the improvement of performance and reduction of fuel consumption of the internal combustion engines, and the development for the improvement of turbocharger performance has been carried out every year.

In recent years, the application of the Miller cycle has increased for automotive engines, and turbochargers with high pressure ratio and high efficiency are required to maintain engine power. In order to achieve higher turbine efficiency under such conditions, the aerodynamic performance of the diffuser should be improved because of the increased leaving loss at high pressure ratio. There are several investigations on diffuser performance parameters of annular diffusers [1, 2]. Singh et al. experimentally studied the effect of inlet swirl on diffuser performance and reported that the pressure recovery coefficient under inlet swirling conditions is higher than under non-swirling conditions [1].

However, the radial turbine of the automotive turbocharger investigated in this study is constrained by the size on the engine. To fit to their interface, diffusers tend to be shorter than ideal length, and non-axisymmetric shapes may be designed. It has not been clarified whether the knowledge of simple shape diffusers can be applied to automotive turbochargers. Several researchers have tried to investigate flow phenomenon in radial turbine diffusers. Yeo et al. measured velocity and flow angle at a wheel exit, or diffuser inlet by laser-2-focus velocimeter [3]. Osako et al. measured not only the turbine wheel outlet but also the internal flow with a laser Doppler velocimeter and analysed the flow vectors and loss distribution [4].

Nakamura et al. measured velocity distributions in the turbine diffuser under pulsating flow conditions by Particle Image Velocimetry (PIV) and concluded that transient losses are affected by Strouhal number [5]. Kawabata also tried to visualize flow in the turbine diffuser by using the 5-holes pitot tube, the oil flow, and the tuft grid methods [6]. In addition, Hasler reported visualization results of velocity and pressure distributions in the turbine diffuser with two different types of wastegate valves [7]. Turbocharger turbine designers have an interest in the influence on diffuser internal flow by velocity

ratio (U/C_0) conditions because they have influence on the turbine performance and are fluctuated during engine driven modes. However, little is known about it by these previous studies which have not focused on U/C_0 conditions. Therefore, PIV and wall static pressure measurements were conducted under several U/C_0 conditions and influence on diffuser internal flow by them are discussed.

2   MEASUREMENT DETAILS

2.1   PIV experimental equipment

A diagram of the experimental setup is shown in Figure 1. First, compressed air is supplied to a temperature controller via a compressor. A temperature controller then uses an electric heater to regulate the temperature. In a turbine inlet piping, the air flow and another one with tracer particles mixed each. The atomizer pressurizes enough air to pump out the tracer particles.

As shown in Figure 2, the turbine investigated in this study is designed for four-cylinder engine and has four intake ports [8], so the turbine inlet piping is branched into four lines. Six tracer particle injectors connected to the atomizer are inserted into the turbine inlet pipe. Two of them are inserted into the upstream section and the others into the branch downstream. The tracer particle injectors have 1mm diameter holes spaced 5mm apart.

The tracer particles are produced from DEHS (diethyl-hexyl-sebacate) liquid using the atomizer. The particle size ranges from 0.2 to 1.0 microns and the total production rate is 10^8 particles/cm^3. The particle size is theoretically determined by considering the effect of frequency response, particle sedimentation rate, and centrifugal force [9].

The PIV measurement section is shown in Figure 3. To enable laser irradiation of the turbine outlet, the outlet pipe is made of acrylic and connected to the turbine housing with silicone sealant. Two high-speed cameras are installed outside the measurement section to capture images of passing tracers and obtain velocity information. Table 1 shows the direct distance between the PIV camera and the origin of the measurement planes. As discussed later, four measurement planes (N1 to N4) are set in the measurement section. The specification of the optical devices is shown in Table 2.
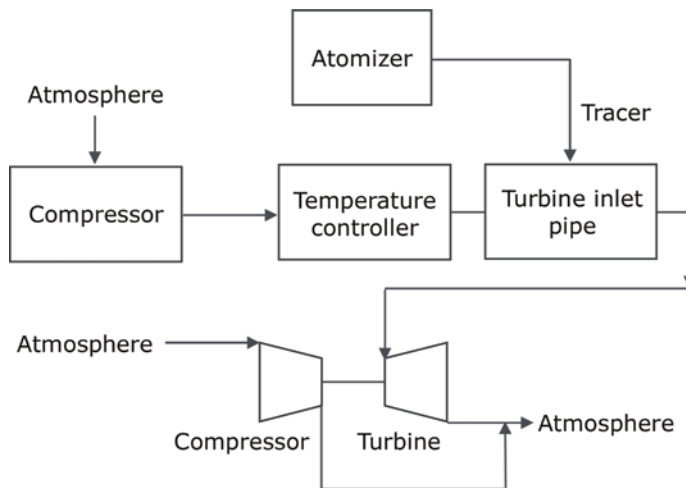

Figure 1. System diagram of PIV measurement.
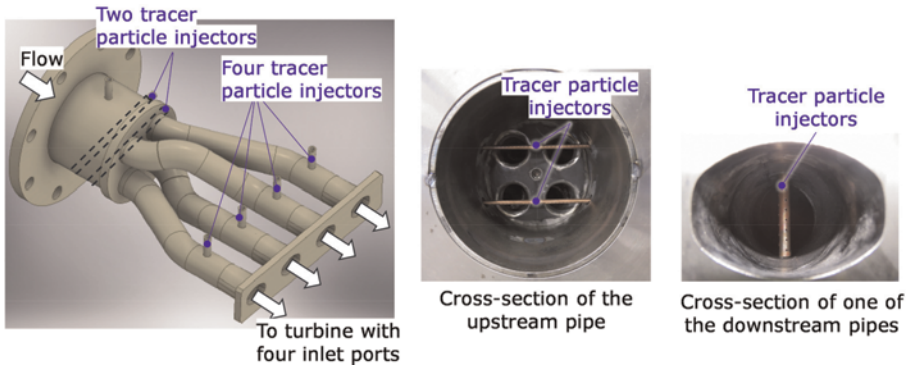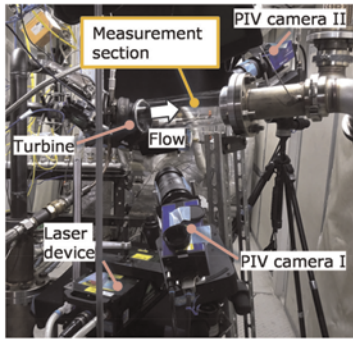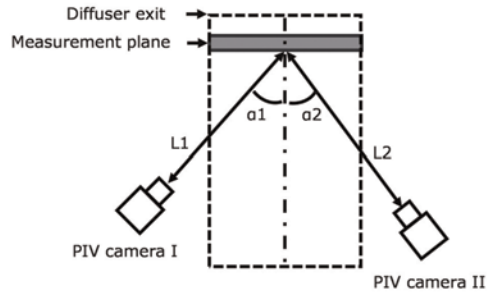
Figure 2. Structure of the turbine inlet pipe.

(a) The measurement section and equipment   (b) Illustration of the measurement section viewed from top

Figure 3. Configuration of the measurement section.

Table 1. Direct distance and stereo angle between PIV cameras and measurement planes.

Measurement Plane	L1[mm]	L2[mm]	$\alpha 1$[deg.]	$\alpha 2$[deg.]
N1 and N2	345	384	46	77
N3	730	590	21	58
N4	880	326	64	30

Table 2. Specification of measurement devices.

PIV camera	Sensor	Progressive scan CCD
	Pixel number	2048 x 2048 px
	Pixel size	7.4μm
	Dynamic range	1:10000
	Frame range	14fps
Laser	Output	200mJ/pulse
	Maximum frequency	15Hz
	Wavelength	532nm
	Beam diameter	<6.35mm

2.2 Turbine specification

The geometry of the turbine is shown in Figure 4. It consists of twin scroll, turbine wheel, and non-axisymmetric diffuser. The PIV measurement section is set downstream of the diffuser. The twin scroll is formed by a spiral flow path, which is divided into two axially by a separation wall. There are four inlet ports and working fluid is supplied to all in full admission condition, whereas to two in partial admission condition. Although the partial admission conditions are more important for turbine performance [8], to investigate the basic diffuser characteristics all measurements are conducted under the full admission condition. This is because velocity non-uniformity at the wheel exit can be strengthen by velocity distortion at the wheel inlet under the partial admission conditions [10].

The Turbine wheel is 45mm in diameter and has 11 blades. It rotates clockwise as seen from the outlet. Non-axisymmetric diffuse with a wastegate valve is equipped downstream of the turbine wheel. Figure 5 shows a cross-section inside the diffuser. "Plane A" is nearly axisymmetric, but downstream the flow path is non-axisymmetric due to constraints on the arrangement of wastegate valve. The wastegate valve connects flow path between the scroll and diffuser and controls the flow rate to the turbine wheel by bypassing a portion of the scroll flow.
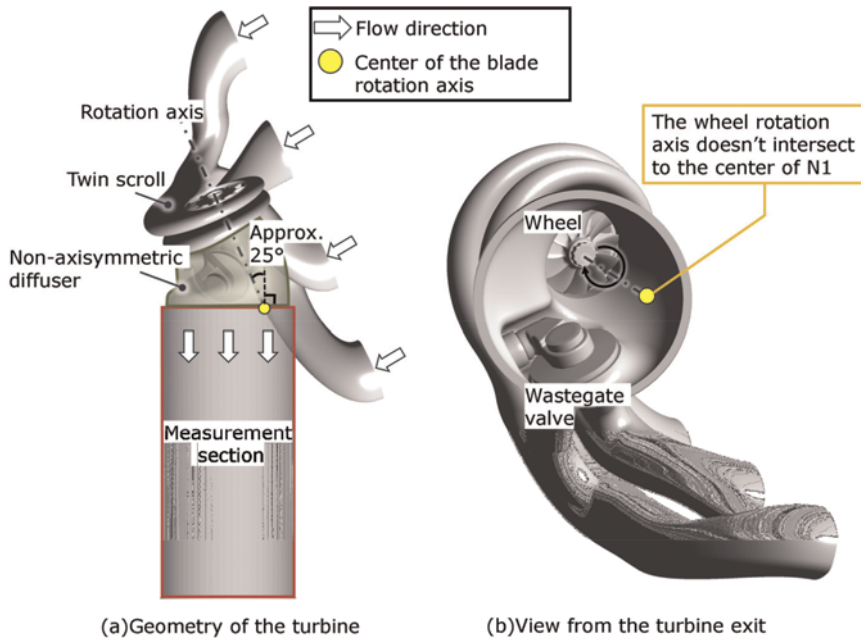
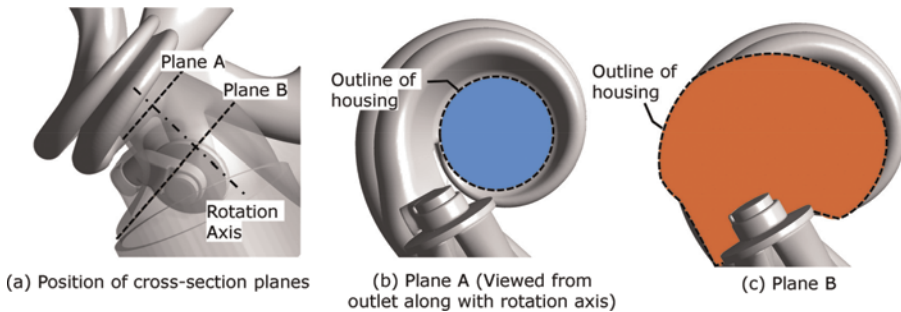Figure 4. Geometry of the twin-scroll turbine and the measurement section.

(a) Geometry of the turbine   (b) View from the turbine exit

(a) Position of cross-section planes   (b) Plane A (Viewed from outlet along with rotation axis)   (c) Plane B

Figure 5. Cross-section planes in the diffuser.

2.3   Turbine performance test

Figure 6 shows the results of a turbine performance test using air as working fluid, showing that the velocity ratio of turbine peak efficiency is about 0.65. The test equipment is the same as in Figure 1 except for the atomizer which is disconnected during the performance test. The performance test is conducted under full admission condition, with a pressure ratio of 2.5 and the inlet temperature of 80 degrees C to evaluate the aerodynamic performance with the effects of heat dissipation eliminated as much as possible, and the pressure ratio and velocity ratio are matched with the engine operating conditions. In addition to installing a drain separator at upstream of the turbine, the turbine outlet temperature is monitored to ensure that it does not fall below room temperature to minimize the risk of condensation.
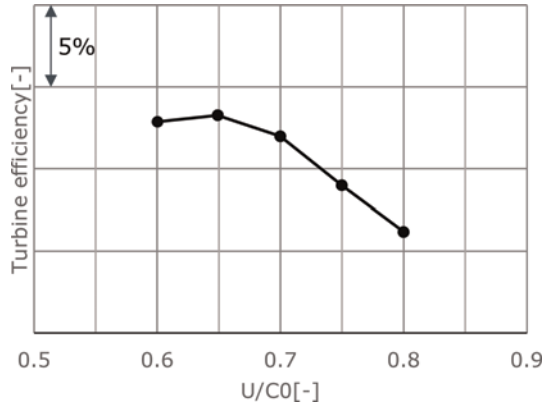
Figure 6. Results of the turbine performance test (Π_{ts} = 2.5).

2.4 PIV measurement planes

The measurement planes are shown in Figure 7. In this study, four planes are defined to analyse downstream of the diffuser outlet as well as the diffuser outlet. The distance from the diffuser exit is 8mm for N1 and 18mm for N2. The distance from the turbine wheel exit to the origin of N1 is $1.7 \times D_4$. The rectangular planes of N3 and N4 are set perpendicular to the diffuser outlet and perpendicular to each other. The measurements of N1 to N4 are conducted separately. Approximately 500 instantaneous velocity images are obtained for each measurement, and ensemble averaging method is applied to evaluate the velocity distribution. The resulting velocity data are organized by velocity components (V_x, V_y and V_z) defined as shown in Figure 7.

(a)Geometry of the turbine (b)View from the turbine exit
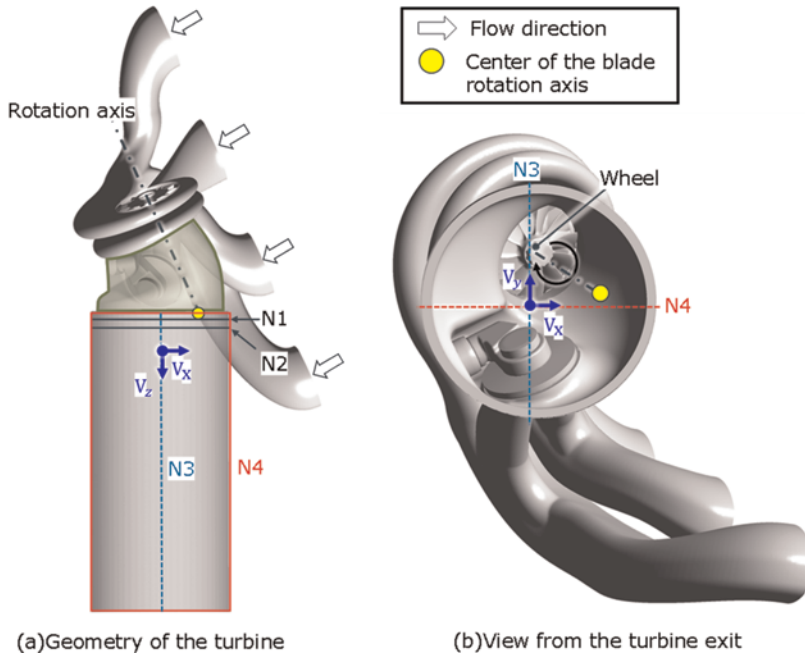
Figure 7. Measurement sections and definition of velocity components.

2.5 Wall static pressure measurement points

The locations of the wall static pressure measurement points are shown in Figure 8. A Total of eight static pressure holes are provided in the diffuser. They are grouped into "Group1" and "Group2", and their positions are defined by L_{diff}. The origin of L_{diff} is the beginning of the diffuser taper. The L_{diff} values for each measurement points are listed in Table 3. The area expansion ratio at No.4 is almost twice the turbine wheel exit area.
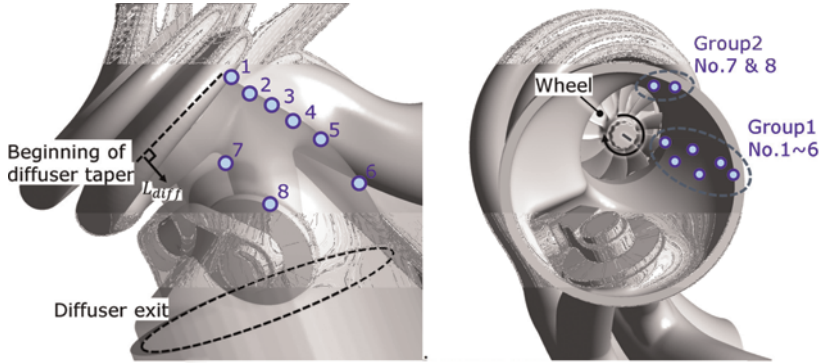

Figure 8. Locations of wall static pressure measurement points.

Table 3. L_{diff} values for wall static pressure measurement points.

Measurement point		L_{diff}[mm]
Group1	No.1	1.0
	No.2	9.0
	No.3	17.0
	No.4	25.0
	No.5	37.0
	No.6	57.0
Group2	No.7	19.5
	No.8	39.8

2.6 Measurement conditions

The measurement conditions are shown in Table 4. Due to the limitations of the experimental setup, the pressure ratio is set as 2.0, and the measurements are conducted with U/C_0 of 0.55, 0.60, and 0.65 to analyse the effect of swirling flow at the turbine wheel outlet on the diffuser performance. U/C_0 is defined by the below equation.

$$U/C_0 = \frac{\pi D_3 \frac{N}{60}}{\sqrt{2C_p \cdot T_{tin}\left(1 - \frac{1}{\Pi_{ts}}\right)^{\frac{\kappa-1}{\kappa}}}}$$

Table 4. Measurement conditions.

Working fluid	Air
$\Pi_{ts}[-]$	2.0
T_{tin} [deg. C]	65
$U/C_0[-]$	0.55/0.60/0.65

3   RESULTS AND DISCUSSIONS

3.1   PIV measurement results at N1

The V_z contours of the N1 plane are shown in Figure 9, and the V_z distributions along X and Y axes are shown in Figure 10. In Figure 9, black vectors represent the tangential flow and purple circles represent the measurement failure sections. The measurement failure sections are determined by observing the reflection of the turbine and halation. As a result, it is shown that the high velocity region is distributed around X = −20mm to X = 20mm at any U/C_0 conditions. Because the turbine has a non-axisymmetric diffuser, the extension of the turbine wheel rotation axis crosses at about X = 20mm. Therefore, these results indicate the flow from the turbine wheel generally passes along the axis and reaches the diffuser outlet. Focusing on the flow patterns under U/C_0 conditions, it is shown that the lower the U/C_0, the wider the low velocity region around the center of the turbine wheel's rotation axis. Because the static pressure recovery coefficient (C_{pr}) depends on an effective flow area, diffuser performance may be degraded in the low velocity region.

Illustrations of the turbine wheel outlet velocity triangle are shown in Figure 11. As shown in Figure 6, the peak efficiency of the turbine is around $U/C_0 = 0.65$, so the counter-clockwise circumferential velocity component may be stronger under low U/C_0 conditions. Since high velocity at the turbine wheel outlet under low U/C_0 conditions are prone to flow separation in the diffuser, the transport of flow separation along the extension of the turbine wheel's rotation axis may result in the low velocity region surrounded by the bow-shaped region.
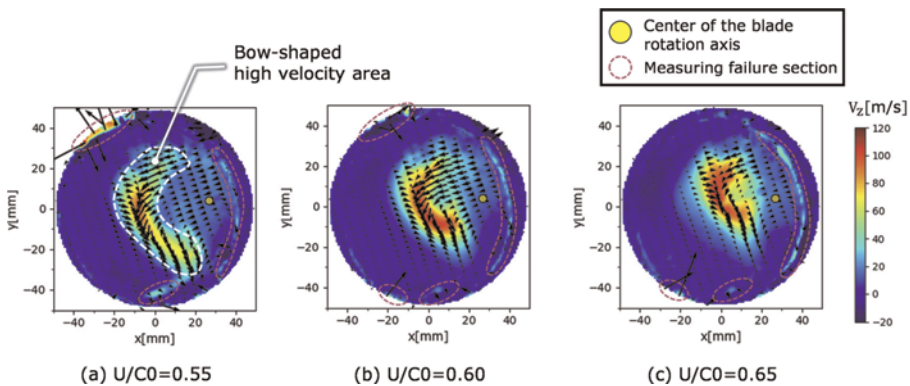

(a) U/C0=0.55   (b) U/C0=0.60   (c) U/C0=0.65

Figure 9. V_z contour and tangential vectors at N1.
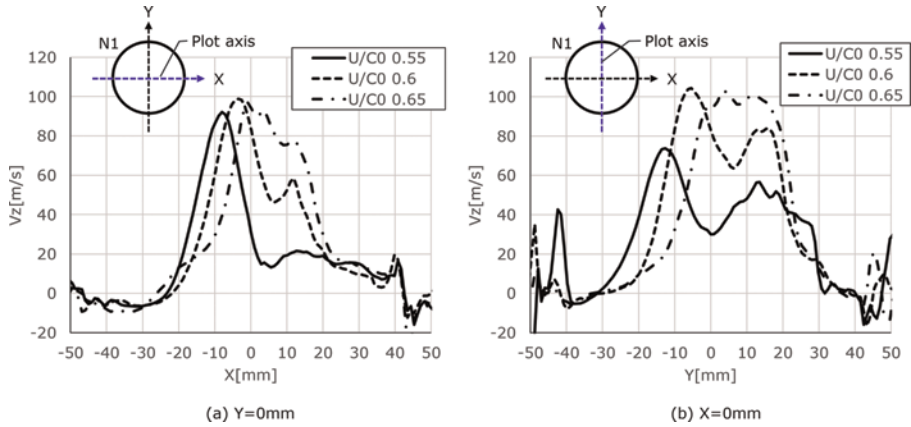
Figure 10. V_z distribution along X axis and Y axis at N1.

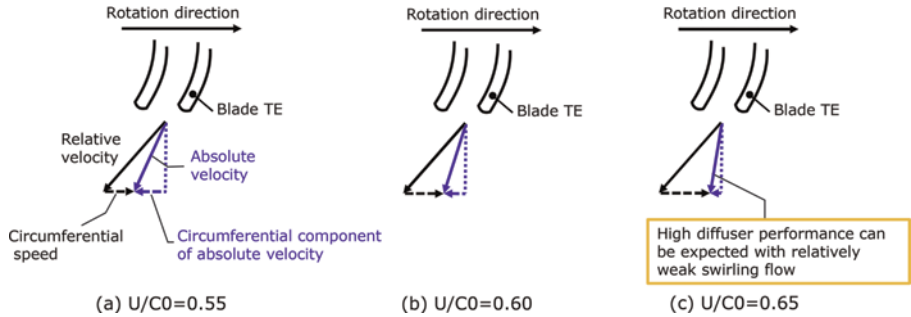(a) U/C0=0.55   (b) U/C0=0.60   (c) U/C0=0.65

Figure 11. Illustrations of the wheel exit velocity triangle.

3.2   Diffuser performance analysis by PIV and wall static pressure measurement

To quantitatively discuss the diffuser performance under U/C_0 conditions, C_{pr} is evaluated by the results of PIV measurement at N1 and wall static pressure measurements. Figure 12 shows the velocity evaluation area. The evaluation area is set to avoid measurement failure sections near the wall. V_x, V_y and V_z are evaluated in the area, and V is calculated by an equation below.

$$V = \sqrt{V_x^2 + V_y^2 + V_z^2}$$

Due to the relatively small circumferential velocity, the absolute flow velocity is evaluated to be minimum at $U/C_0 = 0.65$, which is close to the efficiency peak. On the other hand, when the velocity ratio is lower than $U/C_0 = 0.65$, the absolute velocity tends to increase as the circumferential velocity increases.

270

The V_z evaluation results are compared with the measured mass flow rate in Figure 13. The mass flow rate increases at lower U/C_0 conditions. However, comparing the conditions of $U/C_0 = 0.65$, V_z is almost the same under the condition of $U/C_0 = 0.60$, and V_z decreases further under the condition of $U/C_0 = 0.55$. This indicates that the flow distribution outside the evaluation area can be increased as the U/C_0 decreases.

Evaluation result of C_{pr} of the diffuser is shown in Figure 14. C_{pr} is evaluated by the following equation.

$$C_{pr} = \frac{P_s - P_{sl}}{P_t - P_{sl}}$$

In general, P_t is defined at the diffuser inlet and C_{pr} describes how the diffuser recovers static pressure from the dynamic pressure at the diffuser inlet. However, because PIV measurement at the diffuser inlet is difficult due to layout constraints, P_t is defined by the following equation. The density ρ is evaluated by the static pressure and temperature measured at the downstream of the PIV measurement section.

$$P_t = P_{s6} + \frac{\rho V^2}{2}$$

From the evaluation results of Group 1, the diffuser C_{pr} is evaluated as the highest under the condition of $U/C_0 = 0.65$. Focusing on the distribution of C_{pr} in Group 1, the rate of increase of C_{pr} decreases between No. 4 and No. 5 at $U/C_0 = 0.55$ and $U/C_0 = 0.60$. This may be due to the separation of flow between these measurement points, which reduces the effective flow area. The extended low velocity region in the low velocity ratio condition shown in Figure 9 may be caused by the transport of flow separation occurring between these measurement points.

These measurements show that even under low U/C_0 conditions (U/C_0 of 0.55 and 0.60), the decrease in C_{pr} at measurement point No.6 is within 0.03 points. Although there are technical challenges in inhibiting flow separation, the diffuser can maintain robust performance as measured in this study.
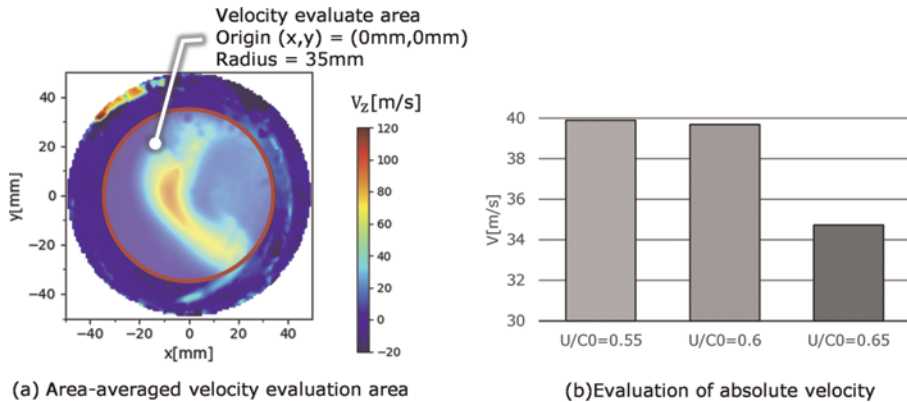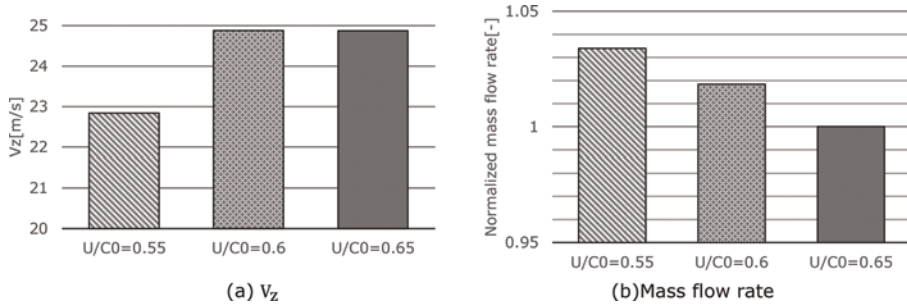

(a) Area-averaged velocity evaluation area   (b)Evaluation of absolute velocity

Figure 12. Area-averaged velocity evaluation area.

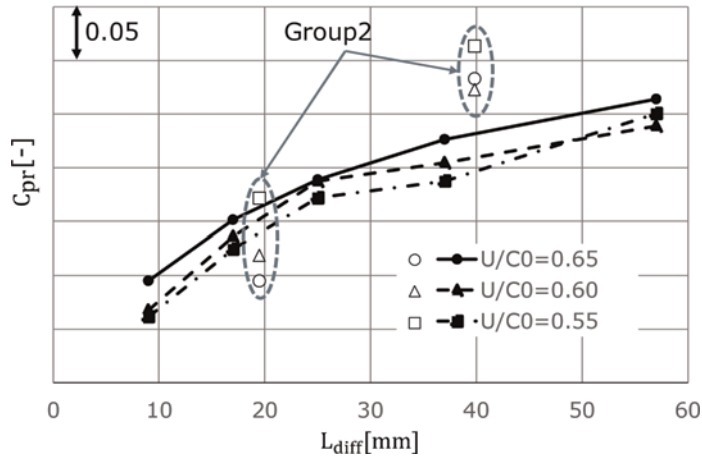**Figure 13. Evaluation of V_z and measured mass flow rate.**

Figure 14. Evaluation of the diffuser C_{pr} (L_{diff} is listed in Table 3).

3.3 PIV measurement results at N2

The measurement results at N2 are shown in Figure 15. The figure shows that at $U/C_0 =$ 0.55 and 0.60, the flow from the turbine wheel expands and diffuses more compared to N1. This indicates that the diffuser performance is relatively U/C_0 of 0.55 and 0.60 conditions, while the flow less expands at $U/C_0 = 0.65$ condition. "Low swirl and high V_z region" will be discussed later.
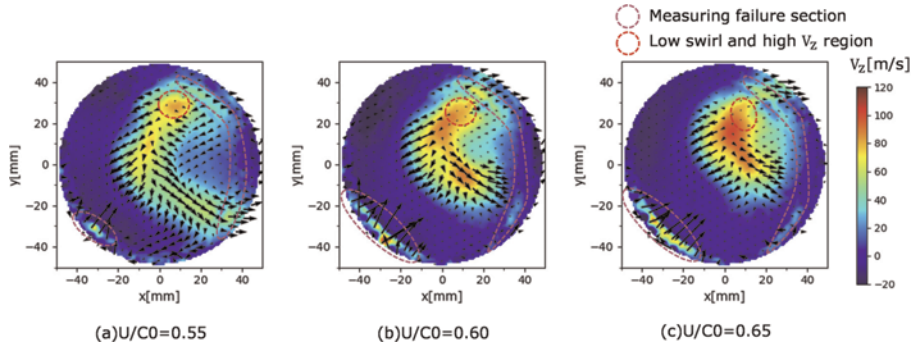
Figure 15. V_z contour and tangential vectors at N2.

3.4 PIV measurement results at N3 and N4

The measurement results at N3 are shown in Figure 16. The vectors at N3 indicates that the flow at the diffuser outlet tends to expand radially, especially in U/C_0 of 0.55 conditions. The results at N4 are shown in Figure 17. As a result, it is found that in $U/C_0 = 0.55$ condition, a low velocity region develops downstream of $Z = -40$mm, and the bulk flow deviates to the +Y side. This may be caused by blockage on the -Y side of the measuring tube due to relatively strong swirling flow at the diffuser outlet. However, because the measuring tube used in this study is not long enough to equalize the flow field at the outlet, it may be caused by the flow distribution at the outlet of the measuring section.

Illustration of flow field in the measurement section is shown in Figure 18. Focusing on flow transport between N1 and N2, PIV measurement captures the expansion of the clockwise bow-shaped region. On the other hand, source of low swirl and high V_z region in N2 are not captured in N1. Considering that High V_z region is captured near +Y sidewall of N3 at U/C_0 of 0.55, the source may be in N1 and measurement failure region. Due to the measurement failure sections, the source is not clearly measured under U/C_0 of 0.60 and 0.65.
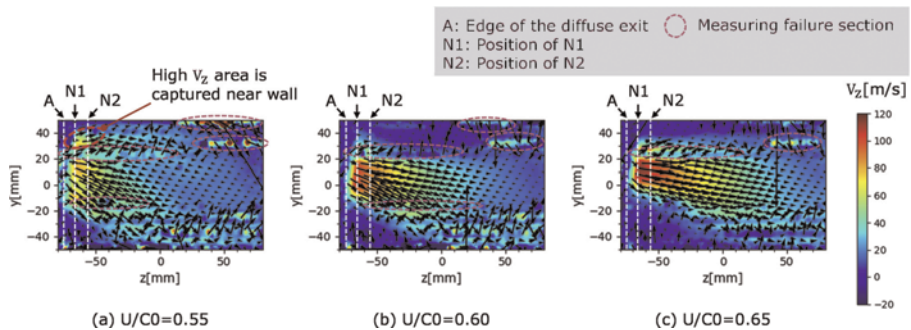

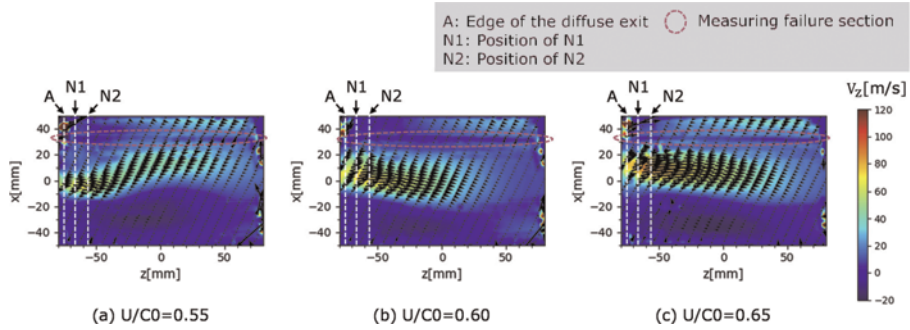Figure 16. V_z contour and tangential vectors at N3.

273

Figure 17. V_z contour and tangential vectors at N4.
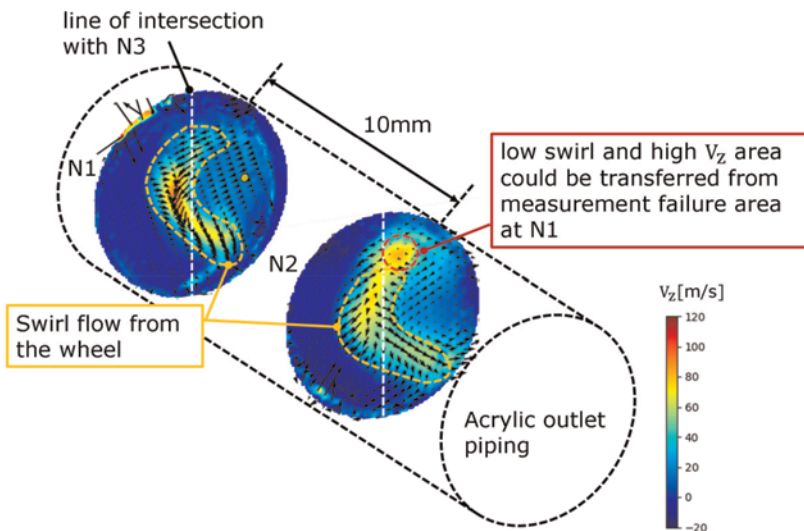

Figure 18. Illustration of flow field in the measurement section (Contours are results under $U/C_0 = 0.55$ condition).

4   CONCLUSIONS

A twin-scroll turbine for an automotive turbocharger with a non-axisymmetric diffuser is studied by PIV and wall static pressure measurements at $U/C_0 = 0.55$, 0.60, and 0.65. The outline of this study is as follows.

- These measurements show that even under low U/C0 conditions, the C_{pr} reduction at the diffuser outlet is within 0.03 points. Although there are technical challenges in suppressing flow separation under low U/C0 conditions, the diffuser can maintain robust performance as measured in this study.
- From the measurements at $U/C_0 = 0.55$ and 0.60, it is found that between $L_{diff} = $ 25 mm and 37 mm, blockage due to flow separation could occur and diffuser performance could be degraded. Resolution of this blockage could lead to improved turbine performance under low velocity ratio conditions.

5   FUTURE WORKS

Based on the measurement results in this study, the accuracy of the CFD model will be improved. The improved model will then be used to optimize turbine design. In addition, as mentioned above, a new series of measurements is conducted under partial admission conditions that are very important to the performance of the twin scroll turbine.

NOMENCLATURE

CFD	Computational Fluid Dynamics
C_0	Spouting velocity
C_p	Specific heat at constant pressure
C_{pr}	Static pressure recovery coefficient
D_3	Inlet diameter of turbine wheel
D_4	Outlet diameter of turbine wheel
N	Number of revolutions
PIV	Particle Image Velocimetry
π	Pi
Π_{ts}	Total to static pressure ratio (P_{tin}/P_{sout})
P	Static pressure
P_t	Total pressure
T_t	Total temperature at turbine inlet
U	Circumferential speed
V	Velocity
κ	Specific heat ratio
ρ	Static density
Subscripts	
1	Wall static pressure measurement point No.1
6	Wall static pressure measurement point No.6
in	Turbine inlet
out	Turbine outlet
x	X direction
y	Y direction
z	Z direction

REFERENCES

[1] Singh *et al.*, "Effect of Inlet Swirl on the Performance of Wide-Angled Annular Diffusers", *Indian Journal of Engineering & Materials Sciences*", Vol.1, pp.63–69 (1994)

[2] Blanco *et al.*, "Performance Analysis of an Axial Exhaust Diffuser Downstream of an Un-shrouded Turbine", *WIT Transactions on Engineering Sciences*, Vol.82 (2014)

[3] Yeo *et al.*, "Laser Velocity Measurements in a Twin-Entry Vaneless Radial Turbocharger Turbine", *JSME International Journal, Series B*, Vol.37, No.4(1994)

[4] Osako *et al.*, "Study on Internal Flow of Radial Turbine Rotating Blades for Turbochargers", *Mitsubishi Heavy Industries technical review*, Vol.38, No.4(2001)

[5] Nakamura *et al.*, *"Unsteady Internal Flow and Loss Mechanism of a Turbocharger Turbine Under Pulsating Flow Condition"*, Turbomachinery (2020).

[6] Kawabata, "Flow Behavior In Exhaust Diffuser Of Radial Turbine", Hosei university departmental bulletin paper (2015).

[7] Hasler, *"Optimisation of Wastegate Bypass Flow Reintroduction for Increased Turbine Stage Efficiency"*, https://www.cummins.com/sites/default/files/files/brochures/turbos/turbine-efficiency-improvements-using-design-for-improved-wastegate-flow.pdf. Accessed 28/11/2022.

[8] Osako *et al.*, "Development of Twinscroll Turbine for Automotive Turbochargers using Unsteady Numerical Simulation", *Mitsubishi Heavy Industries technical review*, Vol.50,No.1(2013)

[9] *The visualization Society of Japan*, [PIV handbook 2nd edition], "PIV handobukku dai ni ban" (in Japanese),Morikita Publishing Co., Ltd(2002)

[10] Morita *et al.*, *"Performance of a Twin Scroll Turbine for an Automotive Turbocharger Under Full-Admission and Partial-Admission"*, Turbomachinery Vol.45, No.2(2017)

Author index